APPLIED COMPUTATIONAL ELECTROMAGNETICS SOCIETY JOURNAL

August 2016
Vol. 31 No. 8
ISSN 1054-4887

The ACES Journal is abstracted in INSPEC, in Engineering Index, DTIC, Science Citation Index Expanded, the Research Alert, and to Current Contents/Engineering, Computing & Technology.

The illustrations on the front cover have been obtained from the research groups at the Department of Electrical Engineering, The University of Mississippi.

EMERITUS EDITORIAL ASSISTANTS

AUGUST 2016 REVIEWERS

THE APPLIED COMPUTATIONAL ELECTROMAGNETICS SOCIETY

JOURNAL

Vol. 31 No. 8 August 2016

TABLE OF CONTENTS

Analysis and Optimization of Elliptic Ridged Waveguide with FDFD Technique and PSO Algorithm
Alessandro Fanti, Marco Simone, and Luisa Deias 860

A Comparison between Vector Algorithm and CRSS Algorithms for Indoor Localization using Received Signal Strength
Huthifa A. Obeidat, Yousif A. S. Dama, Raed A. Abd-Alhameed, Yim F. Hu, Rami Qahwaji, James M. Noras, and Steven M. R. Jones 868

Efficient Stochastic FDTD Algorithm with Optimized GPU Acceleration
Athanasios N. Papadimopoulos, Georgios G. Pyrialakos, Nikolaos V. Kantartzis, and Theodoros D. Tsiboukis 877

New Equivalent Circuit Analysis and Synthesis for Broadband Composite Right/Left-Handed Transmission Line Metamaterials
Na Kou, Yan Shi, and Long Li 884

Derivation of the Resonant Frequency of Rectangular Dielectric Resonator Antenna by the Perturbation Theory
Saeed Fakhte and Homayoon Oraizi 894

Analytic Expressions of Some Statistics in Radar Target Recognition Based on Late Time Representation
Joon-Ho Lee, Young-Ik Choi, Jung-Min Seo, and Byung-Kwon Son 901

Research on Terahertz Wave Reflection and Transmission of Carbon Nanotubes Slab Using FDTD
Mao Y. Wang, Hai L. Li, Yu L. Dong, Gui P. Li, Cui L. Zhong, and Jun Xu 908

A Novel Approach of High Resolution Imaging using Modified Excitation Signal for Ground Penetration Radar (GPR) Applications
Homayoun Ebrahimian, Mohammad Ojaroudi, and Sajjad Ojaroudi 914

Dynamical Chiral Metamaterial with Giant Optical Activity and Constant Chirality Over a Certain Frequency Band
Faruk Karadağ, İbrahim Çömez, Furkan Dinçer, Mehmet Bakır, and Muharrem Karaaslan 919

UWB Slot Antenna with Band-Notched Property with Time Domain Modeling based on Genetic Algorithm Optimization
Javad Zolghadr, Yuanli Cai, and Nasser Ojaroudi 926

A Novel Wideband End-Fire Conformal Antenna Array Mounted on a Dielectric Cone
Zengrui Li, Longdan Tan, Xiaole Kang, Jianxun Su, Qingxin Guo, Yaoqing (Lamar) Yang, and Junhong Wang 933

Analysis of Radiation Characteristics of Conformal End-Fire Antenna Mounted on a Large Conducting Cylinder
Ping Wang 943

A Low Profile, Broadband Linearly and Circularly Polarized Cavity Backed Antenna Using Halved-Dual Mode SIW Cavity
Seyed A. Razavi and Mohammad H. Neshati 953

A Compact Disc-Shaped Printed Antenna Using Parasitic Element on Ground Plane for Super Wideband Applications
Md. M. Islam, Mohammad R. I. Faruque, and Mohammad T. Islam 960

Asymmetrical Single Cell Multiband Uni-Planar Mushroom Resonant Antenna
Navid Amani and Amir Jafargholi 970

A Dual Frequency Monopole Antenna with Double Spurlines for PCS and Bluetooth Applications
Niwat Angkawisittpan and Apirat Siritaratiwat 976

Full-Wave Analysis of Indoor Electromagnetic Pollution from Base-Station Antennas
Xunwang Zhao, Zhongchao Lin, Huanhuan Zhang, Sio-Weng Ting, and Yu Zhang 982

Palladium Decorated SWCNTs Sensor for Detecting Methane at Room Temperature Based on UWB-RFID
Jian Liu and Ping B. Li 989

Transformer-Based Dual-Mode VCO for Multi-Mode Multi-Standard Receiver
Xiangning Fan, Xiaoyang Shi, and Li Tang 997

Design of a 0.7~1.5 GHz Wideband Power Amplifier in 0.18-μm CMOS Process
Xiangning Fan, Zhou Yu, Jiakai Lu, and Zaijun Hua 1003

Analysis and Optimization of Elliptic Ridged Waveguide with FDFD Technique and PSO Algorithm

Alessandro Fanti, Marco Simone, and Luisa Deias

Department of Electrical and Electronic Engineering
University of Cagliari, 09123, Piazza d'Armi, Cagliari, Italy
{alessandro.fanti, marco.simone, luisa.deias }@diee.unica.it

Abstract ─ A new design technique for elliptic ridged and sectoral waveguides is presented. The PSO technique has been employed, using FDFD to compute the propagation data of the guide. Conflicting requirements of wide bandwidth and high power handling capability are taken both into account with a suitable objective function.

Index Terms ─ Cutoff frequency, elliptical ridged waveguide analysis, finite difference frequency domain, microwave components, microwave filters, optimization, PSO, ridged waveguides, waveguide modes.

I. INTRODUCTION

In many applications, microwave propagation structures with high power handling capabilities and low-losses are required. The most effective structures which satisfy these requests are metallic hollow waveguides (WG). The modal structure [1] of WG propagation implies that WGs can be used only as long as single mode propagation takes place. Moreover, the propagation of each mode is high-pass and dispersive. Therefore, the useful bandwidth of a given WG is relatively narrow. The most popular approach to increase significantly the bandwidth, retaining all the useful WG properties, is the use of ridged waveguides R-WG [2].

First studies on R-WGs were made by Cohn [3], who showed how rectangular ridge waveguides have a lower cutoff frequency and a greater bandwidth compared to a standard rectangular waveguide with the same dimensions. Then Hopfer [4] analysed the microwave properties of single and double ridge waveguide, such as cut-off frequency, bandwidth, attenuation and power handling: in particular he showed that a ridge structure provides a larger bandwidth but, on the other hand, it has a reduced power handling capability. Transverse resonance technique [5] has been the first approach of analysis of rectangular R-WG, [2] despite its reduced accuracy. Application of ridged circular waveguides, ridged elliptic waveguides (REW) and sectoral elliptic waveguides (SEW) [6] can be found in many components like filters, matching networks, orthomode transducers, polarizers and circulators that are widely used in satellite and terrestrial communication systems [7]-[11]. Low-cost design, small size, and optimum performance of these components are essential to satisfy today's stringent payload requirements.

An analytical, closed form solution exists also for elliptic waveguides, and has been found by Chu [12] since the 30's. Unfortunately, the field distribution is described by the Mathieu functions [13], whose numerical evaluation is very cumbersome. The best approach seems the expansion of those functions in a series of (more tractable) Bessel functions [14]. In [15], the cutoff wavelengths have been computed efficiently applying by the method of fundamental solutions. In [16], using Mathieu functions and their addition theorem, was presented the general exact solution for evaluation the cutoff frequency in eccentric elliptical waveguides.

Aim of this work is to devise a FDFD [17]-[20] approach for SEW [21] and REW homogeneous elliptic waveguides, tailored to the structure, but as simple as the standard one in the formulation. Use of a suitable elliptical grid (which perfectly fits the waveguide boundary) allows to evaluate the SEW and REW modes with the required accuracy using order of magnitude less sampling points than the standard approach of FDFD [22], namely the use of a rectangular grid with a staircase approximation of the boundary. In addition a REW configuration have been effectively optimized through a synergic use of PSO and the FDFD, aiming at the best trade trade-off of the different requirements of bandwidth and power handling.

II. DESCRIPTION OF FDFD TECNIQUE

The TE and TM modes of waveguide can be calculated [1] by solving the eigenvalue equation $\nabla_t^2\phi = -k_t^2\phi$, with the boundary conditions (BC) $\partial\phi/\partial n = 0$ for TE modes and $\phi = 0$ for TM modes. In the eigenvalue equation ϕ is a scalar potential and k_t is

Submitted On: February 27, 2015
Accepted On: Novenber 8, 2015

the "transverse eigenvalue", from which the propagation constant and the characteristic impedance can be obtained. Apart some canonical geometries, this eigenvalue problem must be solved numerically. Probably, the most effective approach is FDFD [23], i.e., the direct discretization of the problem on a suitable grid. Such a technique has been shown to be well suitable to ridge waveguide through proper approximations of the equation and the boundary conditions (BC). A rectangular lattice of sampling points is a very accurate grid for rectangular and staircase ridges [23], whereas it reduces a curvilinear geometry to a staircase approximate structure. Since the analysis presented in this paper is focused on elliptic boundaries, a set of sampling points in elliptic coordinate has been considered (Fig. 1).

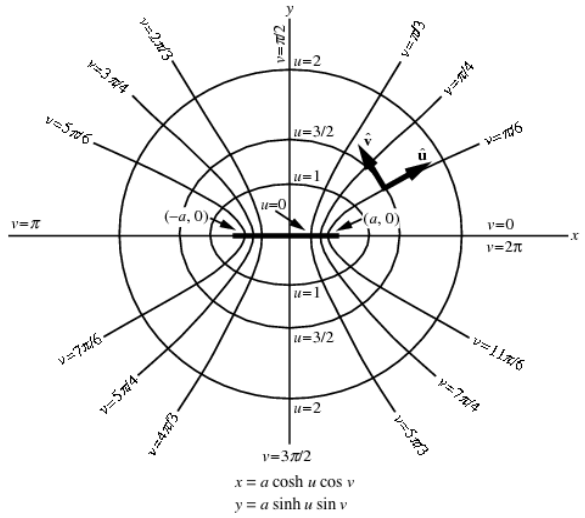

Fig. 1. Geometry of the elliptic coordinates [24].

Let's define Δu, Δv the spacing steps, and $\phi_{pq} = \phi(p\Delta u, q\Delta v)$. The elliptical grid is characterized by a number of points n_u and n_v respectively along the axes u and v. The Helmholtz equation takes the form:

$$\frac{1}{a^2\left(\sinh^2 p\Delta u + \sin^2 q\Delta v\right)} \cdot \left[\frac{\partial^2\phi}{\partial u^2} + \frac{\partial^2\phi}{\partial v^2}\right]_{pq} = -k_t^2\phi_{pq}. \quad (1)$$

For each internal point P (see Fig. 2) is simpler to discretize the term in brackets (1) using a fourth-order Taylor expansion,

$$\phi_B = \phi_P + \left.\frac{\partial\phi}{\partial u}\right|_P \cdot(-\Delta u) + \frac{1}{2}\left.\frac{\partial^2\phi}{\partial u^2}\right|_P \cdot(-\Delta u)^2 + \frac{1}{6}\left.\frac{\partial^3\phi}{\partial u^3}\right|_P \cdot(-\Delta u)^3 + \frac{1}{24}\left.\frac{\partial^4\phi}{\partial u^4}\right|_P \cdot(-\Delta u)^4, \quad (2)$$

$$\phi_N = \phi_P + \left.\frac{\partial\phi}{\partial u}\right|_P \cdot(-2\Delta u) + \frac{1}{2}\left.\frac{\partial^2\phi}{\partial u^2}\right|_P \cdot(-2\Delta u)^2 + \frac{1}{6}\left.\frac{\partial^3\phi}{\partial u^3}\right|_P \cdot(-2\Delta u)^3 + \frac{1}{24}\left.\frac{\partial^4\phi}{\partial u^4}\right|_P \cdot(-2\Delta u)^4, \quad (3)$$

$$\phi_D = \phi_P + \left.\frac{\partial\phi}{\partial u}\right|_P \cdot(\Delta u) + \frac{1}{2}\left.\frac{\partial^2\phi}{\partial u^2}\right|_P \cdot(\Delta u)^2 + \frac{1}{6}\left.\frac{\partial^3\phi}{\partial u^3}\right|_P \cdot(\Delta u)^3 + \frac{1}{24}\left.\frac{\partial^4\phi}{\partial u^4}\right|_P \cdot(\Delta u)^4, \quad (4)$$

$$\phi_Q = \phi_P + \left.\frac{\partial\phi}{\partial u}\right|_P \cdot(2\Delta u) + \frac{1}{2}\left.\frac{\partial^2\phi}{\partial u^2}\right|_P \cdot(2\Delta u)^2 + \frac{1}{6}\left.\frac{\partial^3\phi}{\partial u^3}\right|_P \cdot(2\Delta u)^3 + \frac{1}{24}\left.\frac{\partial^4\phi}{\partial u^4}\right|_P \cdot(2\Delta u)^4, \quad (5)$$

leading to:

$$\left.\frac{\partial^2\phi}{\partial u^2}\right|_P = \frac{1}{12\Delta u^2}\cdot\left(16\phi_B + 16\phi_D - \phi_N - \phi_Q - 30\phi_P\right). \quad (6)$$

By repeating the same for the v direction:

$$\left.\frac{\partial^2\phi}{\partial v^2}\right|_P = \frac{1}{\Delta v^2}\cdot\left(16\phi_H + 16\phi_G - \phi_A - \phi_C - 30\phi_P\right), \quad (7)$$

an approximation of the term in square brackets is obtained:

$$\left[\frac{\partial^2\phi}{\partial u^2} + \frac{\partial^2\phi}{\partial v^2}\right] = \frac{16}{12\Delta v^2}\cdot\phi_H + \frac{16}{12\Delta v^2}\cdot\phi_G - \frac{1}{12\Delta v^2}\cdot\phi_A - \frac{1}{12\Delta v^2}\cdot\phi_C + \frac{16}{12\Delta u^2}\cdot\phi_B + \frac{16}{12\Delta u^2}\cdot\phi_D - \frac{1}{12\Delta u^2}\cdot\phi_N - \frac{1}{12\Delta u^2}\cdot\phi_Q - \frac{30}{12}\left(\frac{1}{\Delta u^2} + \frac{1}{\Delta v^2}\right)\cdot\phi_P, \quad (8)$$

which provides an approximation of the Helmholtz equation suitable to the FDFD's application.

Due to geometric singularities, Equation (8) is not applicable in the two foci, in the segment of points between them and in the external points.

For a generic point P in the segment joining the two foci, it is possible to integrate $\nabla_t^2\phi = -k_t^2\phi$:

$$\int \nabla_t^2\phi dS = -k_t^2\int \phi dS\theta, \quad (9)$$

and apply the Gauss theorem:

$$\int_{\Gamma_F} \frac{\partial\phi}{\partial n}\cdot dl = -k_t^2\int_{S_F}\phi dS, \quad (10)$$

wherein S_F is the cell surface, and Γ_F is the cell boundary.

The grid presents two types of boundary points, the

radial ones (Fig. 3 (a)) and the angular ones (Fig. 3 (b)).

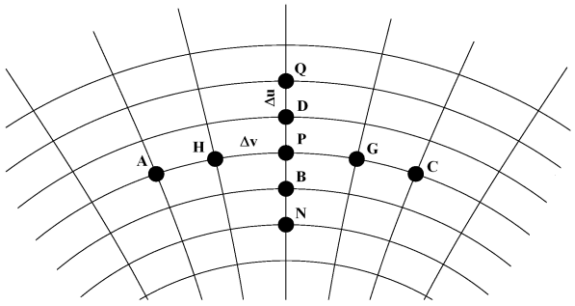

Fig. 2. Internal point of the elliptic coordinates grid TE and TM.

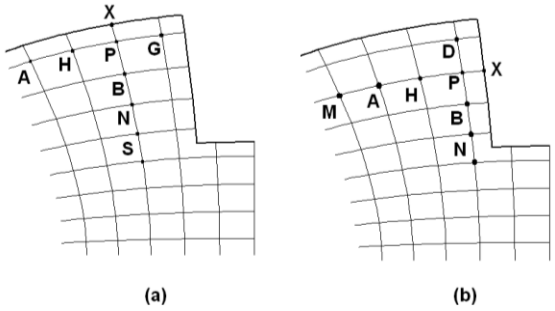

Fig. 3. (a) Radial boundary point P, and (b) angular boundary point P.

Both the boundary points request the same enforcement of the TE boundary conditions, so only the radial one will be considered. The point X in Fig. 3 (a) is not a discretization point, so the application of the Taylor expansion would require the computation of $\phi(u)$ outside the sampling region. Therefore a different approach has been devised using either ϕ_X to enforce the boundary condition $\frac{\partial\phi}{\partial n}=0$.

By considering an "edge" sampling point P (Fig. 3 (a)), the second derivative in u direction can be written as follows:

$$\left.\frac{\partial^2\phi}{\partial u^2}\right|_P \cong \sum_{i=B,N,S} F_i\left(\phi_i-\phi_P\right)= \\ =\left[T_1\left.\frac{\partial\phi}{\partial u}\right|_P+T_2\left.\frac{\partial^2\phi}{\partial u^2}\right|_P+T_3\left.\frac{\partial^3\phi}{\partial u^3}\right|_P+T_4\left.\frac{\partial^4\phi}{\partial u^4}\right|_P\right], \quad (11)$$

where:

$$T_1=\sum_{i=B,N,S}F_i\cdot\Delta u_i,\ T_2=\sum_{i=B,N,S}A_i\cdot\Delta u_i^2,$$
$$T_3=\sum_{i=B,N,S}F_i\cdot\Delta u_i^3,\ T_4=\sum_{i=B,N,S}F_i\cdot\Delta u_i^4,$$

are linear combination of the unknown coefficient F_i, and B,N,S is the points used in the expression of coefficient B.

Now can be expanded $\partial\phi/\partial u=0$ using a Taylor series:

$$\left.\frac{\partial\phi}{\partial u}\right|_X \simeq \left.\frac{\partial\phi}{\partial u}\right|_P+\left.\frac{\partial^2\phi}{\partial u^2}\right|_P\cdot\left(\frac{\Delta u}{2}\right)+ \\ +\frac{1}{2}\left.\frac{\partial^3\phi}{\partial u^3}\right|_P\cdot\left(\frac{\Delta u}{2}\right)^2+\frac{1}{6}\left.\frac{\partial^4\phi}{\partial u^4}\right|_P\cdot\left(\frac{\Delta u}{2}\right)^3=0, \quad (12)$$

which can be solved for $\left.\frac{\partial\phi}{\partial u}\right|_P$. Its expression can be used to replace the first term in the right hand side of Equation (11):

$$\left(T_2-T_1\frac{\Delta u}{2}\right)\cdot\left.\frac{\partial^2\phi}{\partial u^2}\right|_P+\left(T_3-T_1\frac{\Delta u^2}{8}\right)\cdot\left.\frac{\partial^3\phi}{\partial u^3}\right|_P+ \\ +\left(T_4-T_1\frac{\Delta u^3}{48}\right)\left.\frac{\partial^4\phi}{\partial u^4}\right|_P. \quad (13)$$

Equation (13) is an approximation of $\frac{\partial^2\phi}{\partial u^2}$ if:

$$T_2-T_1\frac{\Delta u}{2}=1,\ T_3-T_1\frac{\Delta u^2}{8}=0,\ T_4-T_1\frac{\Delta u^3}{48}=0,$$

and coefficients F_i are given by the solution of the linear system (13), so (6) is replaced, in this case by:

$$\left.\frac{\partial^2\phi}{\partial u^2}\right|_P=\frac{1}{24\Delta u^2}\cdot\left(21\phi_B+3\phi_N-\phi_S-23\phi_P\right), \quad (14)$$

and the Equation (8) became:

$$\frac{21}{24\Delta u^2}\phi_B+\frac{3}{24\Delta u^2}\phi_N-\frac{1}{24\Delta u^2}\phi_S+ \\ +\frac{\phi_H}{\Delta v^2}+\frac{\phi_G}{\Delta v^2}-\left(\frac{23}{24\Delta u^2}+\frac{2}{\Delta v^2}\right)\phi_P\cong-k_t^2\phi_P^2, \quad (15)$$

A significant advantage of the present approach is that TM modes can be computed on the same TE grid, at variance of the standard approach [22], which calls for two different sets of sampling points, to cope with the different BC (2). To get the TM modes on the same grid, as TE, only the BC needs to be changed to, which becomes $\phi_X=0$ (see Fig. 3 (a)). This BC can be enforced by expressing the potential in X has been approximated through Taylor:

$$\phi_X=\phi_P+\left.\frac{\partial\phi}{\partial u}\right|_P\cdot\left(\frac{\Delta u}{2}\right)+\frac{1}{2}\left.\frac{\partial^2\phi}{\partial u^2}\right|_P\cdot\left(\frac{\Delta u}{2}\right)^2+ \\ +\frac{1}{6}\left.\frac{\partial^3\phi}{\partial u^3}\right|_P\cdot\left(\frac{\Delta u}{2}\right)^3+\frac{1}{24}\left.\frac{\partial^4\phi}{\partial u^4}\right|_P\cdot\left(\frac{\Delta u}{2}\right)^4, \quad (16)$$

and set $\phi_X=0$. The second derivative in P (17) is obtained by adding (11) and (16), and solving the linear system (13):

$$\left.\frac{\partial^2\phi}{\partial u^2}\right|_P = \frac{7}{3\Delta u^2}\phi_B - \frac{2}{5\Delta u^2}\phi_N + \frac{1}{21\Delta u^2}\phi_S - \frac{16}{3\Delta u^2}\phi_P \,. \quad (17)$$

The final expression is obtained from the combination of (7) and (17) into (8):

$$\begin{aligned} &\frac{7}{3\Delta u^2}\phi_B - \frac{2}{5\Delta u^2}\phi_N + \frac{1}{21\Delta u^2}\phi_S + \\ &\frac{1}{3\Delta v^2}\phi_G + \frac{5}{3\Delta v^2}\phi_H - \frac{2}{15\Delta v^2}\phi_A + \\ &-\left(\frac{4}{\Delta v^2} + \frac{16}{3\Delta u^2}\right)\phi_P \cong -k_t^2\phi_P^2 \end{aligned} \quad . \quad (18)$$

Of course all other points can be dealt with in the same way as for TE modes.

III. DESCRIPTION OF PSO

PSO is an iterative algorithm designed to find out the solution of optimization problems, very efficient in solving multidimensional problems in a large variety of applications. It has been proposed first by Kennedy and Eberhart [25] for non-linear functions optimization and neural network training. Later on, it has been introduced in electromagnetic research for antenna design [26]-[29], and subsequently it has been applied to artificial ground plane for surface wave antennas [30], microstrip antennas [31]-[33], linear and planar array geometry [34]-[35], log-periodic array dipole antennas, aperture antennas and so on.

PSO takes inspiration from the animal kingdom, in particular from the group movement in search of a common objective. The algorithm consists of a swarm randomly initialized inside a predetermined solution space, which represents the set of the admissible solution for the problem. The quality of the solution is measured through a suitable objective function, associated with each position in the solution space. The choice of the objective function is a key point of every PSO procedure, since it must be accurately defined to well describe the requests of the problem. The group of particles moves iteratively inside the solution space, trying to reach the position which represents the optimal solution, corresponding to the minimum value of the objective function. The movement of each individual is based on its own instinct, on the memory of its path and on the iterations with the other individuals. Each particle is described by a vector of variables x, which are the coordinates of the solution space and, at the same time, the parameters to be optimized. In the j-th iteration, the i-th particle is characterized by its position $x_{i,j}$ (19) and velocity $v_{i,j}$ (20). Next position, direction and velocity of the single particle are updated according to its position and velocity at the previous step, the best solution found by the particle in its path (personal best, *p*) and the best solution found by the whole swarm (global best, *g*):

$$x_{i,j} = x_{i,j-1} + v_{i,j}, \quad (19)$$

$$\begin{aligned} v_{i,j} = w\cdot v_{i,j-1} + c_1\cdot r_1\cdot(p_{i,j} - x_{i,j-1}) + \\ +c_2\cdot r_2\cdot(g_{i,j} - x_{i,j-1}) \end{aligned}, \quad (20)$$

w scales the velocity component at the same direction of the previous step (inertia weight), r_1, r_2 are two random numbers between 0.0 and 1.0 which simulate the random component of the swarm behaviour, c_1, c_2 provide a weight between the pull of *g* and *p*: low values allow particles to roam far from target positions before being attracted to, whereas high values provide movements more strongly orientated to target. Eberhart suggested that the best choice for c_1 and c_2 is 2.0 [36] for most of applications. In general, velocity is applied to position updating for a time-step Δt which is set to 1 in this work.

The algorithm main steps (Fig. 4) are:

1. Initialization of swarm position and velocity.
2. Systematic particles movement in the solution space. For each particle:
   a) Fitness evaluation (*g*, *p* update)
   b) Velocity update
   c) Position update (swarm movement).
3. Iteration of point 2 until a stop criterion (convergence or maximum number of iterations) is reached.

The objective function shown in Fig. 4 contains the electromagnetic problem and evaluates the propagation characteristics of the ridge WG, whose parameters are variable to be optimized and thus the PSO particles' coordinates.

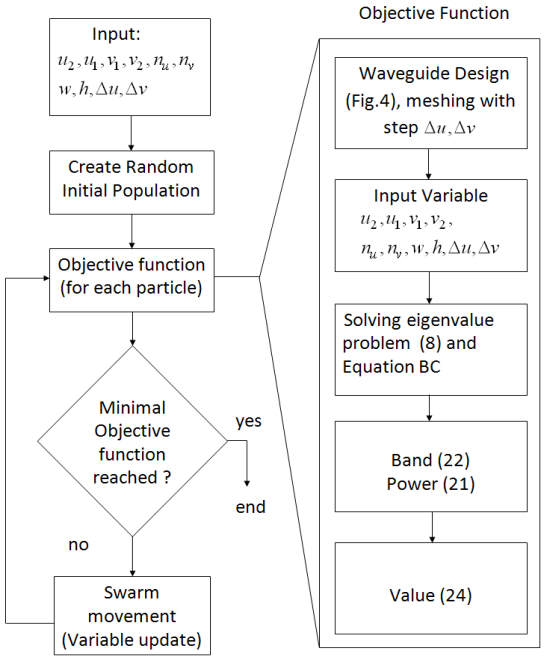

Fig. 4. PSO block diagram.

IV. PARAMETER REW AND SEW

The implementation of an optimization algorithm starts from the definition of the optimization variables, which define the solution space through their constraints. In our case, the variables are the geometrical dimensions of all the ridges (width w and height h) and the horizontal spacing s between them, therefore they constitute the solution space.

The chosen objective function includes both the bandwidth of the simple mode propagation regime, and the maximum power flux. These data can be obtained by the computation of the eigenvalues of the REW (or SEW) section. This is performed by the FDFD described in Section II, after a suitable discretization of the section has been performed. Once the eigenvalue problem is solved we have both the scalar potential and the eigenvalue for the first modes of the guide. From the former, by numerical derivatives, we can compute the mode field [1]. The smallest two eigenvalues k_{TE1}, k_{TE2} gives directly the WG bandwidth. The bandwith is equal to:

$$BW = f_{TE2} - f_{TE1} = \frac{\tilde{c}}{2\pi}\left(k_{TE2} - k_{TE1}\right), \qquad (21)$$

where f_{TE1} and f_{TE2} are respectively, the first and second cut-off frequencies of the TE modes of the SEW and c is the free-space light-speed. The knowledge of the mode distribution allows to compute the power flux P through a transverse section of a SEW or REW using its relationship with the total energy for unit length W_{EM} [4]:

$$P = W_{EM} \cdot \frac{k_z c}{k_0} = \frac{1}{\sqrt{\varepsilon_0 \mu_0}} \cdot \frac{\lambda_0}{\lambda_g} \cdot \frac{\varepsilon_0}{2} \cdot \int_S E^2 dS \,. \qquad (22)$$

The electric field in the integral is computed by the E-field distribution on the transverse section given by the FDFD. This distribution is normalised so that max |E| is equal to the field at the dielectric breakdown (E_{BD}), so (3) actually gives the maximum power.

Then an appropriate objective function is devised to select the best-suited solution for the trade-off request between a large bandwidth (21) and a large power flux (22).To devise the objective function, the ratio between the actual SEW properties and the rectangular WG ones are considered. This is done for bandwidth and high power handling capability (PHC):

$$R_B = \frac{BW_{rect}}{BW_{SEW}} \qquad R_P = \frac{P_{rect}}{P_{SEW}} \quad , \qquad (23)$$

where BW_{rect}, BW_{SEW} and P_{rect}, P_{SEW} are, respectively, the bandwidth, the PHC of R-WG [37] and SEW. The power flux (P) computed from (21) depends on E_{BD} so, as the field distribution in (21) is normalized, R_P is evaluated at the same maximum field in the WG.

The objective functions is:

$$f_p(k) = \left|\frac{R_P}{k} - 1\right| + R_B^2 \,. \qquad (24)$$

This objective function allows to maximize the PHC with the constraint of bandwidth a k-times reduction in the PHC (24). The configuration has been tested with 20 particles in the swarm, with constant accelerations equal to c1 = c2 = 2. The BW has been optimized with respect to a power reduction by a factor 2 and 3, thus considering $f_p(2)$ and $f_p(3)$.

V. RESULTS

A. FDFD validation

The FDFD for elliptic ridge waveguide described in the previous sections has been extensively validated, to evaluate its accuracy and effectiveness. In the simulations presented in this section we will consider first a sector of elliptic ridged waveguide (see Fig. 5) and then a ridged sector. All dimensions have been normalized to the minor semi-axis of the ellipse.

The FDFD procedure has been assessed against the analytical results of [38]. The resulting eigenvalue problem has been solved using standard MATLAB routines, on a PC with two Intel Xeon E5504 CPUs@2.00 GHz, 48 GB RAM, OS: MS Windows 7 Professional. The results are shown in the next tables. It appears that an FDFD approach provides a very high accuracy: the difference with respect to the analytic accurate data presented in [38] is smaller than 0.02% in most cases.

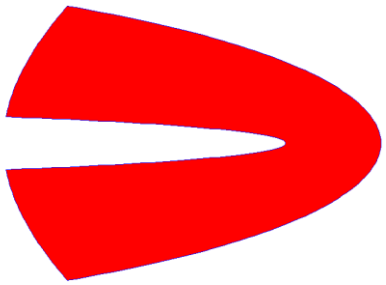

Fig. 5. Elliptic sectoral guide $u \in (u_1, u_2)$, $v \in (v_1, v_2)$, with $u_1 = 0.1$, $u_2 = 0.5$ and $v_1 = -50°$, $v_2 = 50°$.

The total time spent by the FDFD approach is given by the matrix filling time and by the eigenvalue and eigenvectors extraction. For example, for a grid with $\Delta u = 0.0040$, $\Delta v = 0.0009$ and 1010000 points, the filling matrix time is 2,07 sec and the time to extract eigenvalue and eigenvectors is 93.02 sec. The k_t normalized with respect to the focal length, of the first three modes are shown in Table 1.

In Fig. 6, left, we shown the contour plots of the

potential eigenfunctions for the first three TE modes (corresponding to the data of Table 1).

In order to show the flexibility of this approach, a different ridged sector has been considered. Only the eigenfunctions has been reported, since no analytic data are available.

Table 1: Analytical [38] and FDFD k_t, for the guide of Fig. 5. $\Delta u = 0.00563$, $\Delta v = 0.00017$

Modes	$k_t \cdot a$ [38]	$k_t \cdot a$ (our)
1TE	2.6564	2.6564
2TE	6.8370	6.8370
3TE	9.5446	9.5448
1TM	14.2832	14.2831
2TM	14.2995	14.2999
3TM	19.5616	19.5594

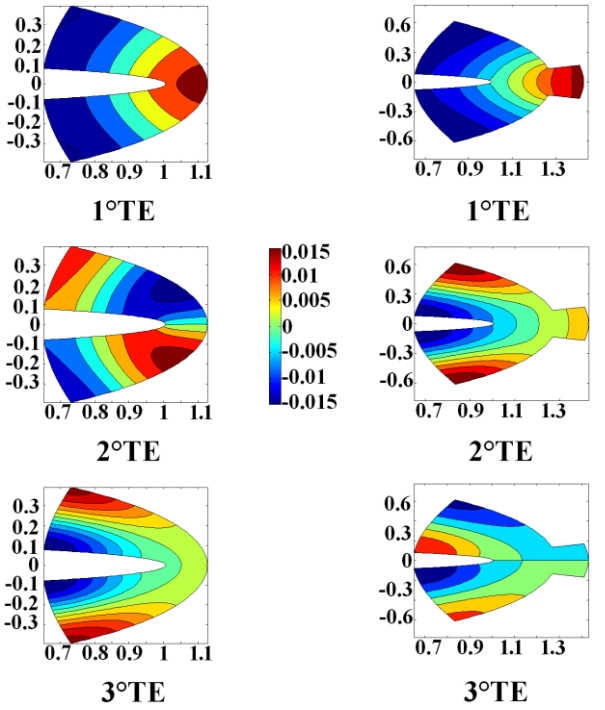

Fig. 6. Lowest-order eigenvectors for the examples presented. (a) Left: structure of Fig. 4. (b) Right: ridged sectoral guide with $u_1 = 0.1$, $u_2 = 0.74$, $v_1 = -50°$, $v_2 = 50°$ and $u_3 = 0.1$, $u_4 = 0.9$, $v_3 = -10°$, $v_4 = 10°$.

B. Constraints and optimal dimensions

The correct scaling of the variables has been obtained by choosing as variables the ratio to the upper ridge part and by imposing the constraints shown in Table 2. In the Table 3 summarize the optimal dimensions and the performance of the considered structure of Fig. 7. The structure SEW (Fig. 7) require six variables in the PSO algorithm.

Table 2: Constraints for staircase SEW

$w_1 = w$	
$w_2 = Aw_1$	A∈[0.01:0.99]
$w_3 = Bw_2$	B∈[0.01:0.99]
$h_1 = Ch_2$	C∈[0.01:0.99]
$h_2 = Dh_3$	D∈[0.01:0.99]
$h_2 = h$	
$6\Delta v h_{u,v} \le w \le (v_2 - v_1) h_{u,v} - 4\Delta v h_{u,v}$	
$4\Delta v h_{u,v} \le w_2$	
$2\Delta v h_{u,v} \le w_3$	
$\Delta u h_{u,v} \le h_1$	
$2\Delta u h_{u,v} \le h_2$	
$3\Delta u h_{u,v} \le h_3 \le (u_2 - u_1) h_{u,v} - 2\Delta u h_{u,v}$	

Table 3: Optimal Dimension of SEW.

Objective Function	$w_1 / h_{u,v}$	$w_2 / h_{u,v}$	$w_3 / h_{u,v}$	
$f_p(2)$	1.19	1.17	1.15	
$f_p(3)$	4.72	1.02	0.99	
Objective Function	$h_1 / h_{u,v}$	$h_2 / h_{u,v}$	$h_3 / h_{u,v}$	*BW* (*GHz*)
$f_p(2)$	0.01	0.02	0.09	3.55
$f_p(3)$	0.01	0.09	0.94	3.86

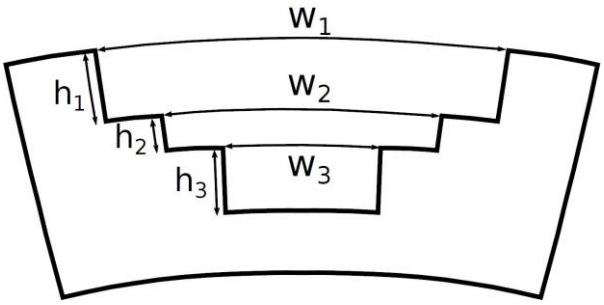

Fig. 7. A typical SEW with $u_1 = 0.1$, $u_2 = 0.5$ and $v_1 = -5°$, $v_2 = +5°$.

VI. CONCLUSION

An approach to the FDFD computation of modes of SEW and REW have been presented. An elliptic mesh has been used in order to avoid staircase approximations of the boundary. The presented results show both the flexibility of the method, as well its simplicity for the computation for TE and TM modes in SEW and REW. Moreover the effectiveness of PSO in the geometrical optimization of a SEW has been illustrated.

ACKNOWLEDGMENT

Marco Simone gratefully acknowledges Sardinia Regional Government for the financial support of his Ph.D. scholarship (P.O.R. Sardegna F.S.E. Operational Programme of the Autonomous Region of Sardinia, European Social Fund 2007-2013 - Axis IV Human Resources, Objective l.3, Line of Activity l.3.1.).

The authors would like to thank George Evers for making freely available its MATLAB PSO Research Toolbox which has been used for simulations.

This work was supported in part by Regione Autonoma della Sardegna under contract CRP-49231 (CUP C45E120000200002).

REFERENCES

[1] R. E. Collin, *Field Theory of Guided Waves*, 2nd ed., New York, IEEE Press, 1991.

[2] J. Helszajn, *Ridge Waveguides and Passive Microwave Components*, London, IEE, 2000.

[3] S. B. Cohn, "Properties of ridged waveguide," *Proceedings of the IRE*, vol. 35, pp. 783-788, August 1947.

[4] S. Hopfer, "The design of ridge waveguide," *IRE Transactions on Microwave Theory and Techniques*, vol. MTT-3, pp. 20-29, October 1955.

[5] R. Sorrentino, *Transverse Resonance Technique*, in Numerical Techniques for Microwave and Millimeter Wave Passive Structures, Chapter 11, New York, John Wiley, 1989.

[6] A. A. El-Sherbiny, "Cutoff wavelengths of ridged, circular, and elliptic guides," *IEEE Transactions on Microwave Theory and Techniques*, MTT-21, pp. 7-12, January 1973.

[7] A. E. Williams and A. E. Atia, "Dual-mode canonical waveguide filters," *IEEE Transactions on Microwave Theory and Techniques*, vol. 25, no. 12, pp. 1021-1026, December 1977.

[8] R. Behe and P. Brachat, "Compact duplexer-polarizer with semicircular waveguide," *IEEE Transactions on Antennas and Propagation*, vol. 39, pp. 1222-1224, August 1991.

[9] B. V. de la Filolie and R. Vahldieck, "Coaxial and circular waveguide band-pass filters using printed metal inserts," *IEEE MTT-S International Microwave Symposium Digest*, pp. 905-908, Albuquerque, New Mexico, June 1992.

[10] J. Huang, R. Vahldieck, and H. Jin, "Computer-aided design of circular ridged waveguide evanescent-mode bandpass filters using the FDTLM method," *IEEE MTT-S International Microwave Symposium Digest*, pp. 459-462, Atlanta, GA, June 1993.

[11] U. Balaji and R. Vahldieck, "Mode matching analysis of circular-ridged waveguide discontinuities," *IEEE Transactions on Microwave Theory and Techniques*, vol. 46, pp. 191-195, February 1998.

[12] L. J. Chu, "Electromagnetic waves in elliptic hollow pipes of metal," *Journal of Applied Physics*, vol. 9, pp. 583-591, September 1938.

[13] N. Marcuvitz, *Waveguide Handbook*, Peregrinius, London, 1986.

[14] J. G. Kretzschmar, "Wave propagation in hollow conducting elliptical waveguides," *IEEE Transactions on Microwave Theory and Techniques*, vol. 18, iss. 9, pp. 547-554, September 1970.

[15] D. L. Young, S. P. Hu, C. W. Chen, C. M. Fan, and K. Murugesan, "Analysis of elliptical waveguides by the method of fundamental solutions", *Microwave and Optical Technology Letters*, vol. 44, pp. 552-558, February 2005.

[16] G. P. Zouros, "Exact cutoff wave numbers of composite elliptical metallic waveguides," *IEEE Transactions on Microwave Theory and Techniques*, vol. 61, iss. 9, pp. 3179-3186, September 2013.

[17] A. Fanti, G. Mazzarella, G. Montisci, and G. A. Casula, "VFD approach to the computation TE and TM modes in elliptic waveguide on TM grid," *Applied Computational Electromagnetics Society (ACES) Journal*, vol. 28, no. 12, pp. 1205-1212, December 2013.

[18] C. S. Lavranos and G. A. Kyriacou, "Eigenvalue analysis of curved waveguides employing FDFD method in orthogonal curvilinear co-ordinates," *IEE Electronics Letters*, vol. 42, no. 12, pp. 702-704, June 2006.

[19] C. S. Lavranos and G. A. Kyriacou, "Eigenvalue analysis of curved waveguides employing an orthogonal curvilinear frequency-domain finite-difference method," *IEEE Transactions on Microwave Theory and Techniques*, vol. 57, iss. 3, pp. 594-611, March 2009.

[20] G. Tsogkas, D. Georgios, J. A. Roumeliotis, and S. P. Savaidis. "Cutoff wavelengths of elliptical metallic waveguides," *IEEE Transactions on Microwave Theory and Techniques*, vol. 57, iss. 10, pp. 2406-2415, October 2009.

[21] A. Fanti, L. Deias, G. A. Casula, and G. Montisci, "A fourth order FDFD approach for the analysis of sectorial elliptic waveguides," *Applied Computational Electromagnetics Society (ACES) Journal*, vol. 30, no. 5, pp. 488-495, May 2015.

[22] A. Fanti and G. Mazzarella, "Curvilinear finite difference approach to the computation of modes of Circular and Elliptic Waveguides," *IEEE Proc. Int. Conf. on Applied Electromagnetics and Communications, (ICECom 2010), Dubrovnik*, Croazia, 20-23 September 2010.

[23] M. N. O. Sadiku, *Numerical Techniques in Electromagnetics*, Boca Raton, CRC Press, 2001.

[24] http://mathworld.wolfram.com/EllipticCylindricalCoordinates.html

[25] J. Kennedy and R. Eberhart, "Particle swarm

optimization," *Proceedings of IEEE International Conference on Neural Networks*, vol. 4, pp. 1942-1948, Perth Wash, Australia, November 1995.

[26] J. Robinson, S. Sinton, and Y. Rahmat-Samii, "Particle swarm, genetic algorithm, and their hybrids: optimization of a profiled corrugated horn antenna," *IEEE Antennas and Propagation Society International Symposium 2002*, vol. 1, pp. 314-317, San Antonio, Texas, June 2002.

[27] J. Robinson and Y. Rahmat-Samii, "Particle swarm optimization in electromagnetics," *IEEE Transactions on Antennas and Propagation*, vol. 52, iss. 2, pp. 397-407, February 2004.

[28] N. Jin and Y. Rahmat-Samii, "Particle swarm optimization for antenna designs in engineering electromagnetics," *Journal of Artificial Evolution and Applications*, vol. 2008, no. 9, 2008.

[29] H. Wu, J. Geng, R. Jin, J. Qiu, W. Liu, J. Chen, and S. Liu, "An improved comprehensive learning particle swarm optimization and its application to the semiautomatic design of antennas," *IEEE Transactions on Antennas and Propagation*, vol. 57, iss. 10, pp. 3018-3028, October 2009.

[30] E. Carrubba, A. Junge, F. Marliani, and A. Monorchio, "Particle swarm optimization for multiple dipole modeling of space equipment," *IEEE Transactions on Magnetics*, vol. 50, iss. 12, pp. 1-10, December 2014.

[31] Y. Choukiker, S. K. Behera, D. Mishra, and R. K. Mishra, "Optimization of dual band microstrip antenna using PSO," *Applied Electromagnetics Conference (AEMC)*, Kolkata, India, pp. 1-4, December 2009.

[32] A. A. Minasian and T. S. Bird, "Particle swarm optimization of microstrip antennas for wireless communication systems," *IEEE Transactions on Antennas and Propagation*, vol. 61, iss. 12, pp. 6214-6217, December 2013.

[33] A. Deb, J. S. Roy, and B. Gupta, "Performance comparison of differential evolution, particle swarm optimization and genetic algorithm in the design of circularly polarized microstrip antennas," *IEEE Transactions on Antennas and Propagation*, vol. 62, iss. 8, pp. 3920-3928, August 2014.

[34] M. M. Khodier and C. G. Christodoulou, "Linear array geometry synthesis with minimum side lobe level and null control using particle swarm optimization," *IEEE Transactions on Antennas and Propagation*, vol. 53, iss. 8, part 2, pp. 2674-2679, August 2005.

[35] D. Cao, A. Modiri, G. Sureka, and K. Kiasaleh, "DSP implementation of the particle swarm and genetic algorithms for real time design of thinned array antennas," *IEEE Antennas Wireless Propagation Letter*, vol. 11, pp. 1170-1173, 2012.

[36] R. C. Eberhart and Y. Shi, "Particle swarm optimization: Development, applications and resources," *Proceedings of the 2001 Congress on Evolutionary Computation*, COEX Seoul, Korea, vol. 1, pp. 81-86, May 2001.

[37] M. Simone, A. Fanti, and G. Mazzarella, "Ridge waveguide optimization with PSO algorithm," *Journal of Electromagnetic Waves and Applications*, vol. 2, iss. 29, pp. 199-209, February 2015.

[38] G. Amendola, G. Di Massa, and G. Angiulli, "Elliptic-hyperbolical waveguides," *Journal of Electromagnetic Waves and Applications*, vol. 14, iss. 11, pp. 1473-1487, 2000.

Alessandro Fanti received the Laurea degree in Electronic Engineering and Ph.D. degree in Electronic Engineering and Computer Science from the University of Cagliari, Cagliari, Italy, in 2006 and 2012, respectively. He urrently holds a post-doc scholarship for design of microwave components. His research activity involves the use of numerical techniques for modes computation of guiding structures, optimization techniques, analysis and design of waveguide slot arrays, analysis and design of patch antennas.

Marco Simone graduated in Electronic Engineering at the University of Cagliari on 2011 and currently is a Ph.D. student in Electronic Engineering and Informatics at University of Cagliari. His research activity involves the use of optimization techniques for microwave devices.

Luisa Deias received the Laurea degree in Electronic Engineering and Ph.D. degree in Electronic Engineering and Computer Science from the University of Cagliari, Cagliari, Italy, in 2002 and 2006, respectively. She worked as Post-doctoral Fellow in the Electro-magnetic Group at the University of Cagliari from 2006 to 2013. Her research interests include numerical techniques in electromagnetism, metamaterial analysis and optimization, microwave components and antennas analysis and design.

A Comparison between Vector Algorithm and CRSS Algorithms for Indoor Localization using Received Signal Strength

Huthifa A. Obeidat [1], Yousif A. S. Dama [1,2], Raed A. Abd-Alhameed [1], Yim F. Hu [1], Rami Qahwaji [1], James M. Noras [1], and Steven M. R. Jones [1]

[1] School of Engineering and Informatics
University of Bradford, Bradford, UK, BD7 1DP
H.A.Obeidat@student.bradford.ac.uk, r.a.a.abd@Bradford.ac.uk, R.S.R.Qahwaji@bradford.ac.uk, j.m.noras@Bradford.ac.uk, s.m.r.Jones@Bradford.ac.uk

[2] Department of Telecommunication Engineering, An Najah National University, Nablus, Palestine
yasdama@najah.edu

Abstract ─ A comparison is presented between two indoor localization algorithms using received signal strength, namely the vector algorithm and the Comparative Received Signal Strength (CRSS) algorithm. Signal values were obtained using ray tracing software and processed with MATLAB to ascertain the effects on localization accuracy of radio map resolution, number of access points and operating frequency. The vector algorithm outperforms the CRSS algorithm, which suffers from ambiguity, although that can be reduced by using more access points and a higher operating frequency. Ambiguity is worsened by the addition of more reference points. The vector algorithm performance is enhanced by adding more access points and reference points while it degrades with increasing frequency provided that the statistical mean of error increased to about 60 cm for most studied cases.

Index Terms ─ CRSS, indoor localization, ray tracing, RSS.

I. INTRODUCTION

Indoor localization is the process of locating an object within a building, ideally with high accuracy and low computational effort [1]. Localization using Received Signal Strength (RSS) aims to establish a one-to-one relationship between the target location and the measured data [2]: as the distance between the target node and the receiver increases, the signal generally becomes weaker. Knowledge of the radio attenuation helps to establish the relationship between distance and RSS, a process known as radio mapping [2].

RSS-based localization techniques offer low cost, and low sensitivity to the bandwidth and undetected paths [3, 4]. On the other hand, they are sensitive to shadowing, low SNR, and non-line-of-sight propagation, with errors increasing with resulting rapid power attenuation [5].

It is noteworthy that actual distance does not always scale linearly with the RSS value, especially in indoor environments, where obstacles may reduce the strength of the signal, thus giving a false indication that the target is far away from the transmitter [6-8]. Deployment of AP, taking into account environmental features, enhances the localization accuracy [9]. The variability of RSS measurements is due to many factors [10, 11]:

- the orientation of the receiver;
- temporal factors - readings differ throughout the day because of the people movements;
- human factors since 50% of the human body is water;
- interference factors due to having devices operating in the same channel, although by using different channels the correlation becomes trivial.

Using wireless sensor networks for localization purposes brings the advantages of continuous monitoring, low cost, and a capability to work unattended, even for years [12]. However, some problems can arise as those devices operate at 2.4 GHz, and may experience interference with devices such as microwave ovens and Bluetooth devices, with a resulting increase in error probability [6].

There are many different RSS–based algorithms used for indoor localization, including radio frequency (RF) fingerprinting, one of the best-known algorithms [12-14]. This has two phases. In the off-line or training phase, predetermined points are chosen. At each location, the system collects RSS values from the access points, either experimentally which will consume effort, time and cost, or using ray-tracing software, whereby the system builds a database of RSS with locations. This database is called a radio map [15]. The software takes account only of approximate building information, and

Submitted On: February 25, 2015
Accepted On: January 9, 2016

details are ignored. This introduces more error in comparison with measurement data.

In the on-line phase, RSS measurements are collected from unknown locations, and then values are compared with the existing radio map. The closest match to the database is taken as the best estimate of the target location [15].

The present research work compares two indoor localization algorithms based on RF-fingerprinting, the vector algorithm and the Comparative Received Signal Strength (CRSS) algorithm. It extends previous work [16, 17]: here, we have adopted lower operating frequencies. Section II offers a brief explanation of the methodology, and then Section III sets out the environment and specifications of the study. Finally, Section IV presents a discussion of the results.

II. VECTOR AND CRSS ALGORITHMS

In our investigation, the relative benefits and drawbacks of two localization algorithms were investigated. The first algorithm, the vector algorithm, uses a vector of received signal strength readings measured at the reference point from the different access points within the facility. The readings are arranged according to the access point order.

Vectors from the reference points are stored in the database, and the test node vector is compared with the database, by calculating the Euclidean distance between the test vector and the database vectors. The smallest Euclidean distance represents the closest reference point to the test node.

The second algorithm is the CRSS algorithm. We extend the work done by authors in [18], whereby the vectors of the previous approach are converted into constraint matrices, which comprise the database of the radio map. Test node readings also are converted into a matrix, and then the Euclidean distance between this test node matrix and the database matrices is calculated, where again the smallest distance indicates the closest reference location to the test node.

In the initial off-line phase, $R_i(x, y)$ is the RSS from the transmitter or access point i at tag location (x, y). The elements of this matrix depend on RSS values, as shown:

$$M_\alpha(x,y) = \left[\mathrm{c_{ij}}(x,y)\right]. \quad i,j = 1,2,\dots,\alpha, \tag{1}$$

$$\mathrm{c_{ij}}(x,y) = \begin{cases} +1 & \mathrm{R_i}(x,y) > \mathrm{R_j}(x,y) \\ -1 & \mathrm{R_i}(x,y) < \mathrm{R_j}(x,y), \\ 0 & \mathrm{R_i}(x,y) = \mathrm{R_j}(x,y) \end{cases} \tag{2}$$

$$\mathrm{c_{ij}}(x,y) = 0 \ \ for\ all\ i = j, \tag{3}$$

where $M_\alpha(x, y)$ is the constructed matrix, and $c_{ij}(x, y)$ compares the RSS access point for access point i with that for access point j. (x, y) is the location for the mobile which is considered to be known. The following example illustrates the method: assuming there are three APs, the RSS values received at the RP located at (x, y) are [-20 dBm, -12 dBm, -14 dBm]. The first row compares the power received from the first AP with the other AP readings as explained in Equation (2), the second row compares the power received from the second AP with the RSS values from the other APs, etc. The resultant matrix is:

$$M_3(x,y) = \begin{bmatrix} 0 & -1 & -1 \\ 1 & 0 & 1 \\ 1 & -1 & 0 \end{bmatrix}. \tag{4}$$

In the on-line phase, the radio map is constructed just as in the off-line phase, except that the location of the test devices is estimated by comparing the constraint matrix of a tag with those in the radio map. The closest matrix is the one with the smallest Euclidean distance, thus the corresponding location for the closest matrix is taken to be the closest location to the tag.

The inherent redundancy that exists in each constraint matrix (i.e., insensitivity to the absolute RSS values) gives rise to an acceptable performance for the positioning algorithm and makes the system more robust.

In this work, we assume that the tags operate a protocol that avoids collision, so that in the case of multiple tags there will be no cross talk.

This study is based on a simple scenario without clutter, in order to clarify the relative merits of the proposed algorithms. We initially investigate a single room without clutter; further studies will examine the multipath fading arising from clutter.

III. SIMULATION AND RESULTS

A. The CRSS algorithm

A severe drawback of the CRSS algorithm was exposed during the analysis of the results obtained in the project, termed "the ambiguity problem".

While generating the CRSS radio map, it was noted that some RPs have identical same constraint matrices, in that although each RP is likely to have unique power readings, the relative power readings are found frequently to coincide.

The generated matrix does not depend on the absolute RSS readings only, but also on the descending order of the received power readings of the APs. Thus, a test area may divide into regions in which all the RPs located in that region can be represented by identical matrices.

Consider a test area with three APs with RSS values: [x dBm, y dBm, z dBm]: we sort them according to these values, giving 13 possible arrangements as shown in the Table 1.

This means that if this test area has 20 RPs, then in the best case the area can be represented by 13 matrices, or even fewer. As shown above, this algorithm is dependent on the number of RPs and APs.

In the localization process, a test point will create a matrix based on its RSS readings, using which the Euclidean distance is calculated. Because we are interested in the elements with the same matrix indices the Euclidean distance is estimated as in following:

$$e = \sqrt{\sum_{i=1}^{N}\sum_{j=1}^{N}(c_{ij} - t_{ij})^2}, \quad (5)$$

where c_{ij} represents the elements in a radio map matrix c in row i and column j, and t_{ij} represents the corresponding element in the on-line matrix t.

Some RPs have identical matrices, and consequently, more than one RP will appear as closest to the test point. This problem is termed *ambiguity*. Figure 1 illustrates an example; four RPs appear equally closest to the test point, as their corresponding matrices have the same Euclidean distance to the test point matrix.

The effect of the ambiguity problem becomes worse if closest matrix is the same matrix for more than one RP. This can arise when RPs have similar propagation environments as shown in Tables 2, 3, 4 and 5: when more than one RP has the same matrix, the phenomenon is called similarity.

Table 1: Possible arrangements for RRS data from three APs

1	$x > y > z$	7	$y > x > z$
2	$x > z > y$	8	$y > z > x$
3	$x > y = z$	9	$y > x = z$
4	$x = y > z$	10	$y = z > x$
5	$x = z > y$	11	$z > x > y$
6	$x = y = z$	12	$z > y > x$
13	$z > x = y$		

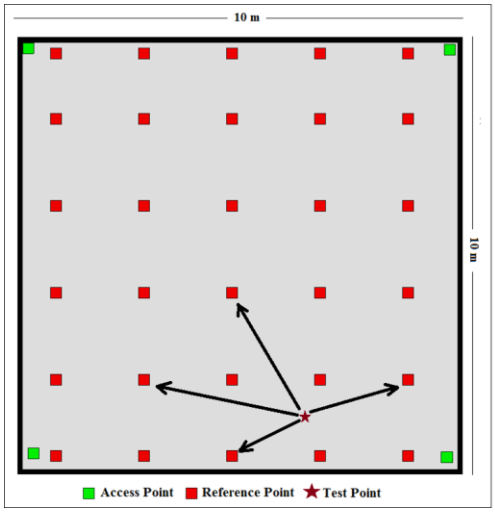

Fig. 1. Ambiguity example for a test area.

Table 2: Similarity in CRSS matrices for three APs at 200 MHz

No. of RPs	4	9	20	30
Unique Matrices	4	3	0	0
Matrix for 2 RPs	0	0	2	0
Matrix for 3 RPs	0	2	2	0
Matrix for 4 RPs	0	0	0	1
Matrix for 5 RPs	0	0	2	4
Matrix for 6 RPs	0	0	0	1

Table 3: Similarity in CRSS matrices for four APs at 200 MHz

No. of RPs	4	9	20	30
Unique Matrices	4	7	11	8
Matrix for 2 RPs	0	1	3	5
Matrix for 3 RPs	0	0	1	4

Table 4: Similarity in the CRSS matrices for three APs at 400 MHz

No. of RPs	4	9	20	30
Unique Matrices	4	4	0	0
Matrix for 2 RPs	0	1	2	1
for 3 RPs	0	1	1	0
for 4 RPs	0	0	2	1
for 5 RPs	0	0	1	2
for 6 RPs	0	0	0	1
for 7 RPs	0	0	0	0
for 8 RPs	0	0	0	1

Table 5: Similarity in the CRSS matrices for four APs at 400 MHz

No. of RPs	4	9	20	30
Unique Matrices	4	7	10	15
Matrix for 2 RPs	0	1	5	7
Matrix for 3 RPs	0	0	0	1

The example in Fig. 2 helps more clearly to explain these tables. Consider the similarity in the CRSS matrices for twenty RPs, four APs and 200 MHz as in Table 3: among the RPs, 11 of them have distinct matrices, while in 3 pairs of RPs each shares the same matrix. Finally, another 3 RPs generate the same matrix.

Inspection of the identical matrices shows them to be in adjacent location in groups of 2, 3, 4… etc. as also shown in the other tables.

Increasing the number of RPs tends to worsen the effect of ambiguity, with more RPs having the same constraint matrix. Table 3 shows the effect of increasing RPs in a test area with four APs and an operating frequency of 200 MHz. With only four RPs, all four generated matrices are unique, but with nine RPs two RPs share the same matrix while the other seven have unique matrices. With twenty RPs, three pairs of RPs share the same matrix, with a further triplet of three RPs having one matrix in common. The thirty RP case is even worse, with ten RPs sharing five matrices in pairs and twelve RPs sharing four matrices, i.e., four sets of triplet RPs with a matrix in common.

Similarity in CRSS matrices is affected by the number of APs used in the system, as the matrix size will correspondingly increase. Table 3 shows the similarity in the generated matrices using four APs for the same test area and the same operating frequency.

The difference between the cases of four APs and three APs is obvious; adding more APs reduces the

similarity in the generated matrices. From the previous tables, it can be seen that adding more APs will reduce similarity, while adding more RPs will increase similarity.

Results obtained when changing the frequency from 200 MHz to 400 MHz are shown in Tables 4 and 5, which show that the similarity is reduced as the frequency increased.

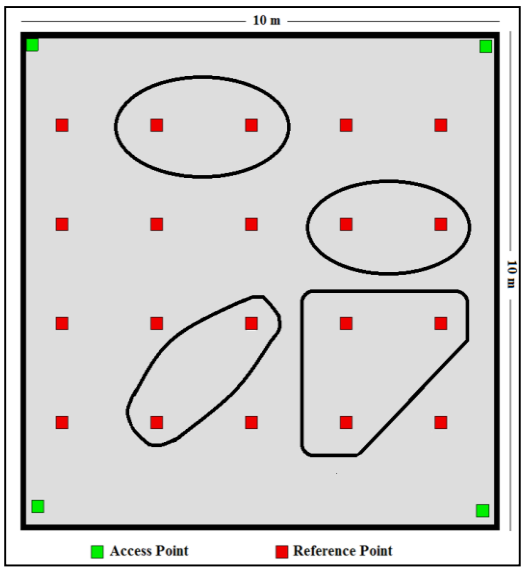

Fig. 2. Example of similarity.

Ambiguity need not always have negative consequences, namely if the estimated locations surrounded the test point. Rather than identifying the test point as close to a certain RP, it would be located within a specific area.

However, throughout all the experiments such a thing rarely happened. It is true that with increasing frequency, the similarity in the generated matrices will be less, but this does not mean that localization performance is thereby improved: a test point considered to be close to fewer RPs using 400 MHz does not mean that these RPs are closer than those estimated at 200 MHz, as shown in Fig. 3.

The localization process includes the calculation of the Euclidean distance between all the matrices in the database and choosing the one representing the least error. As a result, more matrices may have the same Euclidean distance, therefore, more RPs will be considered as the closest RP. There have been sincere efforts to characterize the effect of the ambiguity analytically, however, the results show randomness in the number of the linked RPs to the test point as Fig. 4 shows. Based on results obtained from one experiment, this shows the number of the closest RPs using different radio map resolution. The similarity in the twenty RPs is less relatively when compared to the system with thirty RPs, but still this does not necessarily mean that the ambiguity effect will be less. Moreover, even if the number of the estimated "closest locations" is less, this does mean that an estimated location lies closest to the test point, as depicted previously in Fig. 3.

The ambiguity problem is a severe drawback of the CRSS algorithm, which jeopardizes the system's credibility, despite claims that it outperforms the vector algorithm due to the redundancy in the information embedded within the matrix [2]. A similar analysis was conducted for a more elaborate scenario including a number of rooms adjoining a corridor on a single floor of the author's recent work [19] as shown in Fig. 5, and similar conclusions have been drawn.

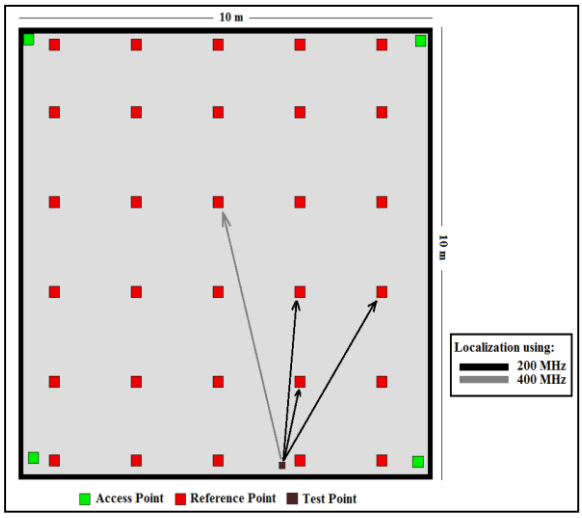

Fig. 3. Less ambiguity does not imply better localization.

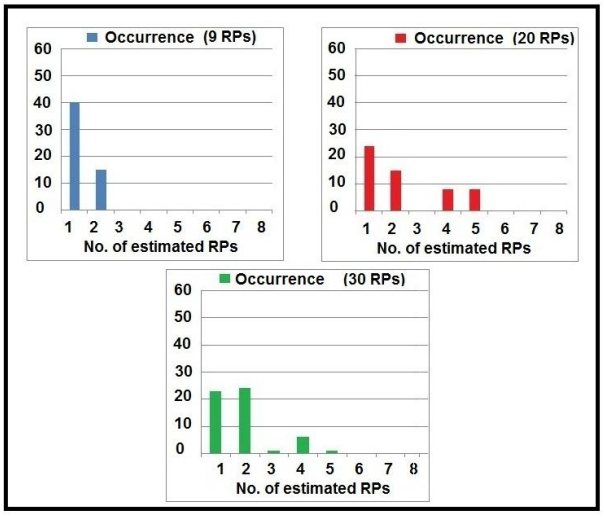

Fig. 4. The number of estimated RPs in the CRSS using different sets of radio maps.

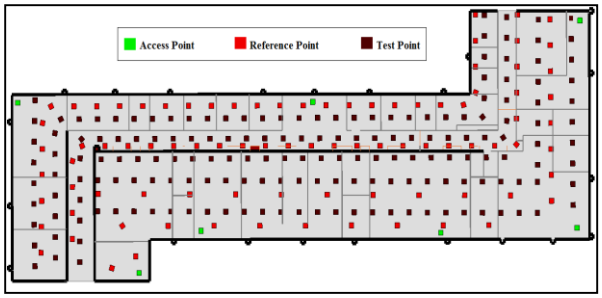

Fig. 5. The 3rd floor of the Chesham Building, University of Bradford.

As the present work shows that the CRSS algorithm is unreliable, in the following we consider the vector algorithm only.

B. The vector algorithm

This algorithm is deemed successful as long as the estimated location is the closest to the actual location of the mobile terminal. When the estimated RP is not closest to the actual location of the mobile terminal, then the algorithm is said to have failed. The percentage of correctly estimated locations gives the *success rate*.

Figure 6 shows the localization performance for the vector algorithm using three APs and different radio map resolutions. The performance is enhanced as the number of the RPs increases; e.g., P(Error $\leq$ 2 m) was about 0.26 for the four RP system, and increased gradually up to 0.8 for the thirty RP system.

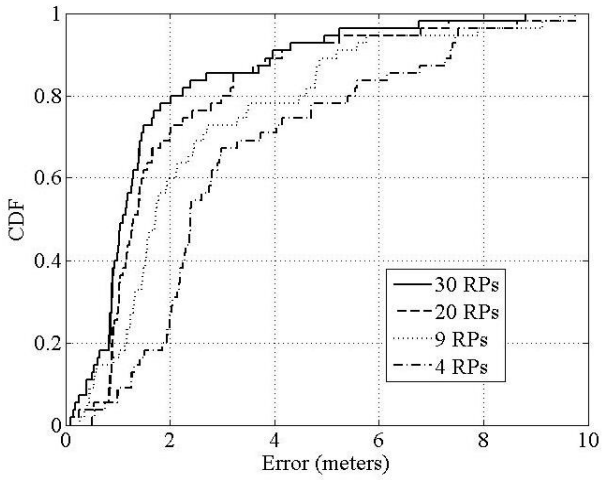

Fig. 6. Localization error for the vector algorithm using three APs, at 200 MHz.

The statistical mean of error was also reduced as shown in Fig. 7. Moreover, the performance shows more stability as the number of RPs increases; error deviation was reduced and the high error estimates were less common. For thirty, twenty, nine and four RPs the error for 85% of locations was less than (2.7, 3.2, 4.8, 6.15) m respectively. Thus, increasing the number of RPs improves localization and enhances stability.

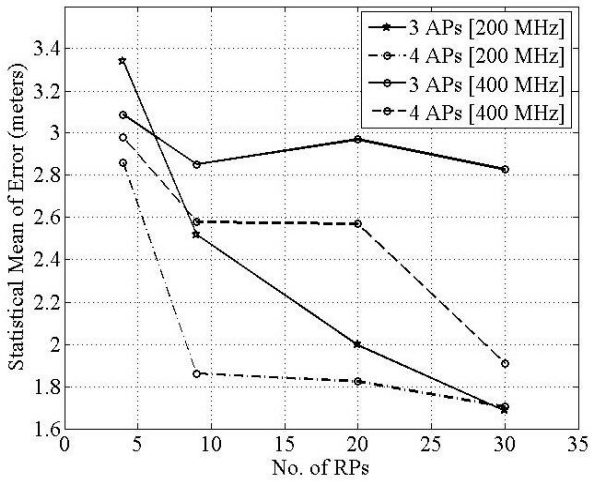

Fig. 7. Statistical mean error for the vector algorithm.

Figure 7 shows the statistical mean error for the vector algorithm using three and four APs at different frequencies. The figure shows that the overall performance of the algorithm is poor for low-resolution radio maps. It improves gradually as the number of APs and RPs in the system increases. The system performance at 200 MHz improves steadily until it reaches a maximum level of accuracy. As shown in the metrics in Table 6, the algorithm performance does not give satisfactory accuracy at 400 MHz except for the system that used thirty RPs and four APs. In general, the performance at 200 MHz is significantly better than at 400 MHz, however high-resolution radio maps and adequate numbers of APs will improve the algorithm's performance to acceptable levels.

Table 6: Success rates for different sets of RPs, APs and frequencies

No. of APs	No. of RPs	200 MHz	400 MHz
3 APs	4 RPs	65%	67%
	9 RPs	58%	47%
	20 RPs	49%	32%
	30 RPs	49%	32.7%
4 APs	4 RPs	78%	72%
	9 RPs	72%	58%
	20 RPs	58%	54%
	30 RPs	52%	61%

It can be noted that the success rate decreases as the number of RPs increases, as shown in Table 6, although the localization error improved. This can be justified thus: the algorithm is considered successful when the estimated location is the closest RP to the test point.

When the number of RPs in the radio map is limited, the RPs will be large distances away, and it is expected that they will be exposed to different fading parameters, so it will be easier for the algorithm to estimate the closest RP. However, as the number of RPs increases, they become closer to each other, and they will have more similar propagation environments, and thus comparable RSS readings. It will be more difficult for the algorithm to estimate the closest RP, and therefore the error will be enhanced.

Figure 8 shows the localization performance using four APs for different numbers of RPs, showing the outstanding performance of the algorithm especially with a high-resolution radio map, and they underline the importance of the number of APs in determining the overall system performance. They also suggest that even low-resolution systems could provide a system with good accuracy as long as there were an adequate number of APs in the system. If we exclude the 4 RPs system, the algorithm shows stability and robustness, with deviations constant for the other systems. The most interesting result obtained is the performance of the localization using nine RPs, which is almost the same as for those using twenty and thirty RPs in the 0-2 m window, and outperforms them slightly in the 2-4 m window. For thirty, twenty, nine and four RPs the error for 85% of locations was less than (3.37, 3.2, 2.28, 5.385) m respectively. This may be considered as the optimum system, which has good performance metrics with only a few RPs used.

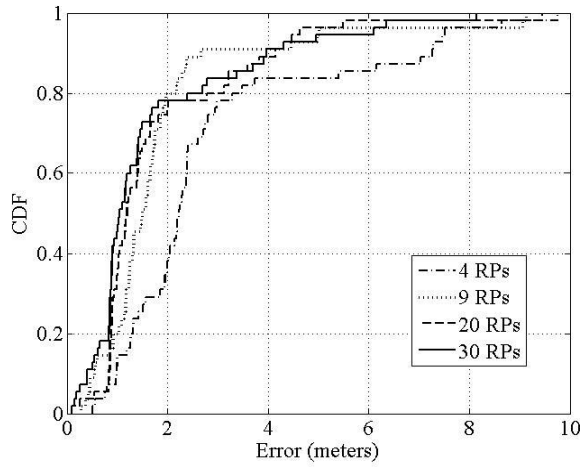

Fig. 8. Localization error for the vector algorithm using four APs, at 200 MHz.

Figure 9 shows a localization error comparison between the three AP and four AP systems. The four AP system shows better performance, with a success rate enhanced from 58% to 74%. The statistical mean of error was improved from 2.52 m to 1.86 m. Standard deviation was reduced from 2.12 m to 1.7 m. The error performances of the two systems are almost the same in the 0-1 m window, but they do vary in the 1-2 m window.

P(Error $\leq$ 2 m) for three RPs was about 0.6 whereas it was around 0.8 for the four RP system. This accuracy is satisfactory for many applications. The effect of adding an extra AP to the system is obvious as all the metrics reflect enhancement in performance.

Figure 10 shows the localization performance for the vector algorithm using three and four APs with a radio map resolution of thirty RPs. The success rate was enhanced from 49% to 52%, and the mean error has changed slightly from 1.68 m to 1.7 m. Standard deviation remained the same at 1.68 m. The performance of the two systems is effectively identical. It is clear that increasing the number of RP points will make the need for more APs less. In addition, increasing the number of RPs will enhance the performance of localization but the enhancement obtained may become insignificant, as the accuracy will saturate at a certain level.

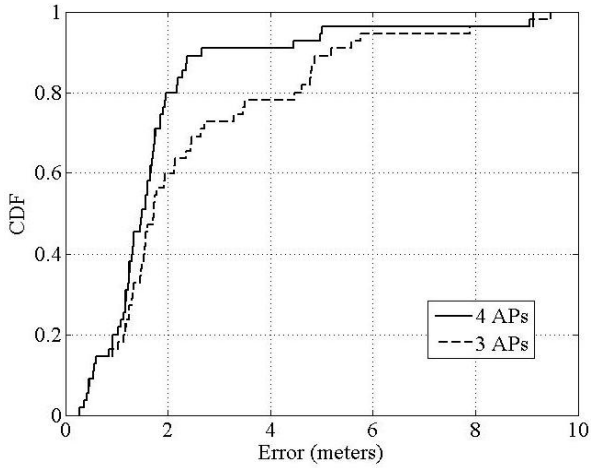

Fig. 9. Localization error for the vector algorithm using nine RPs.

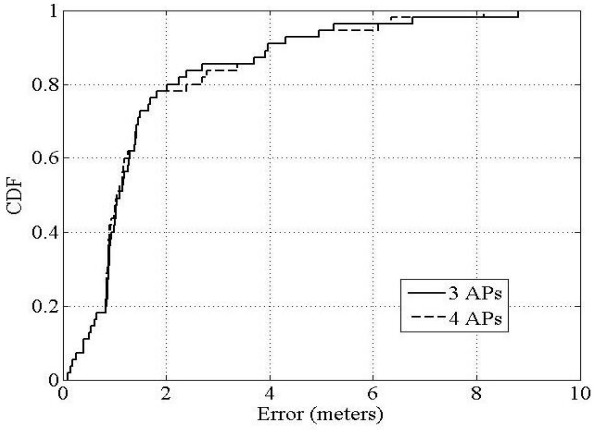

Fig. 10. Localization error for the vector algorithm using twenty RPs, at 200 MHz.

As mentioned above, two operating frequencies, 200 MHz and 400 MHz, were used to conduct the experiments. In general, the localization performance with 200 MHz is better. A justification for such results can be found in propagation theory. When a signal travels in space over a surface, as well as the direct wave there is also a ground wave traveling with it. Due to the different paths that the signals take, a phase shift of 180 degrees occurs every $\lambda/2$, leading to destructive interference and thus reduced power at those points. For example, at 400 MHz, this happens every 0.375 m, so test points at such locations will be completely irrelevant to the RP measurements. As the power readings in the area around the RP will change significantly, mapping the received power vector with the location will result in weaknesses in RSS-based algorithms. At 200 MHz, cancellation occurs every 0.75 m and so the fluctuation in power readings is slower than with 400 MHz.

Figure 11 shows the performance of the vector algorithm for two different operating frequencies and a radio map resolution of twenty RPs. The algorithm performance with 200 MHz is clearly better than with 400 MHz. The error for 85% of locations was less than 3.2 m (three and four APs at 200 MHz), 6.3m (three APs at 400 MHz) and 6.6m (four APs at 400 MHz). Moreover, Table 7 shows that the algorithm performance at 200 MHz with the use of three APs only is better than its performance with the use of four APs at 400 MHz provided that the statistical mean of error increased to about 60 cm for most studied cases. These results emphasize the importance of the operating frequency in determining the algorithm performance.

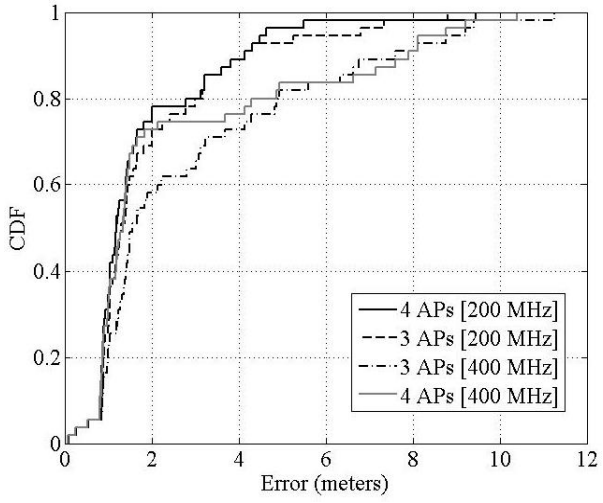

Fig. 11. Localization error at 200 MHz and 400 MHz, for twenty RPs.

Table 7: Performance metrics of the vector algorithm for 200 MHz and 400 MHz

No. of APs	Metric	200 MHz	400 MHz
3 APs	Success rate	49%	32.7%
	Mean	2 m	2.97 m
	Standard deviation	1.75 m	2.27 m
4 APs	Success rate	58%	54%
	Mean	1.82 m	2.57 m
	Standard deviation	1.61 m	2.75 m

IV. CONCLUSIONS

The paper compares two indoor localization algorithms using received signal strength, the vector algorithm, and the CRSS algorithm. The experiment was carried out at 200 MHz and 400 MHz, and the localization performance was tested for different numbers of access points (AP), and for different numbers of reference points (RP). In the vector algorithm, increasing the number of RPs enhances the localization process up to a certain limit, while increasing the number of APs will also result in better performance. Experiments show that increasing the number of RPs will compensate for a reduction in the number of APs, which seems to be attractive commercially. The CRSS algorithm suffers from ambiguity since more than one RP may have the same matrix, and increasing the number of RPs will only make the ambiguity worse. Reducing the number of the APs will increase the algorithm's ambiguity.

It is noted that a lower frequency is better for localization than a higher one. Based on the experimental results the vector algorithm is better in terms of accuracy, cost, and effort.

ACKNOWLEDMENT

The authors would like to acknowledge support from the TSB-KTP project grant No. 008734 with the Seven Technologies Group, Leeds, United Kingdom.

REFERENCES

[1] Z. Yang and Y. Liu, *Location, Localization, and Localizability Location-Awareness Technology for Wireless Networks*. 1st ed., New York, United States: Springer, 2011.

[2] K. Pour and D. Kasper, "A robust model-based approach to indoor positioning using signal strength," in *Personal, Indoor and Mobile Radio Communications, 2008. PIMRC 2008. IEEE 19th International Symposium on*, Cannes, pp. 1-5, 2008.

[3] H. Ahn, and W. Yu, "Environmental-adaptive RSSI-based indoor localization," *Automation Science*

and Engineering, IEEE Transactions on, vol. 6, no. 4, pp. 626- 633, Oct. 2009.

[4] S. A. Kharidia, Q. Ye, S. Sampalli, J. Cheng, H. Du, and L. Wang, "HILL: A hybrid indoor localization scheme," in *Mobile Ad-hoc and Sensor Networks (MSN), 2014 10th International Conference on*, pp. 201-206, 19-21 Dec. 2014.

[5] D. Munoz, F. Bouchereasus, and C. Caldera, *Position Location Techniques and Applications*. 1st ed., Burlington, United States: Academic Press, 2009.

[6] A. Ladd, "On the feasibility of using wireless ethernet for indoor localization," *Robotics and Automation, IEEE Transactions on*, vol. 20, no. 3, pp. 555-559, June 2004.

[7] D. Moeinfar, H. Shamsi, and F. Nafar, "Design and implementation of a low-power active RFID for container tracking at 2.4 GHz frequency," *Advances in Internet of Things*, vol. 2, no. 2, pp. 13-22, 2012 [Online]. Available: DOI:10.4236/ait.2012.22003

[8] Y. Cui, Q. Wang, H. Yuan, X. Song, X. Hu, and L. Zhao, "Relative localization in wireless sensor networks for measurement of electric fields under HVDC transmission lines," *Sensors*, vol. 15, no. 2, pp. 3540-3564, Feb. 2015 [Online]. Available: http://dx.doi.org/10.3390/s150203540

[9] Y. Chapre, P. Mohapatra, S. Jha, and A. Seneviratne, "Received signal strength indicator and its analysis in a typical WLAN system (short paper)," in *Local Computer Networks (LCN), 2013 IEEE 38th Conference on*, pp. 304-307, 21-24 Oct. 2013.

[10] L. Xu, F. Yang, Y. Jiang, L. Zhang, C. Feng, and N. Bao, "Variation of received signal strength in wireless sensor network," in *Advanced Computer Control (ICACC), 2011 3rd International Conference on*, pp. 151-154, 18-20 Jan. 2011.

[11] K. Ullah, I. V. Custodio, N. Shah, and E. dos Santos Moreira, "An experimental study on the behavior of received signal strength in indoor environment," in *Frontiers of Information Technology (FIT), 2013 11th International Conference on*, pp. 259-264, 16-18 Dec. 2013.

[12] M. Shchekotov, "Indoor localization methods based on Wi-Fi lateration and signal strength data collection," in *Open Innovations Association (FRUCT), 2015 17th Conference of*, pp. 186-191, 20-24 Apr. 2015.

[13] T. Chuenurajit, S. Phimmasean, and P. Cherntanomwong, "Robustness of 3D indoor localization based on fingerprint technique in wireless sensor networks," in *Electrical Engineering/ Electronics, Computer, Telecommunications and Information Technology (ECTI-CON), 2013 10th International Conference on*, pp. 1-6, 15-17 May 2013.

[14] M. Bshara, U. Orguner, F. Gustafsson, and L. Van Biesen, "Fingerprinting localization in wireless networks based on received-signal-strength measurements: A case study on WiMAX networks," in *Vehicular Technology, IEEE Transactions on*, vol. 59, no. 1, pp. 283-294, Jan. 2010.

[15] L. Xie, Y. Wang, and X. Xue, "A new indoor localization method based on inversion propagation model," *6th International Conference on in Wireless Communications Networking and Mobile Computing (WiCOM), 2010*, Chengdu, China, pp. 1-4, 2010.

[16] Y. A. S. Dama, H. Hammad, R. Zaid, R. Zaid, R. A. Abd-Alhameed, and P. S. Excell, "A comparison between vector algorithm and CRSS algorithm for indoor localization," *IET conference on Ninth CEM International Conference on Computation in Electromagnetics*, Imperial College, London, UK, session 3, P3-4, pp. 1-2, 31 Mar.-01 Apr. 2014.

[17] H. A. Obeidat, R. A. Abd-Alhameed, J. M. Noras, S. Zhu, T. Ghazaany, N. T. Ali, and E. Elkhazmi, "Indoor localization using received signal strength," in *Design and Test Symposium (IDT), 2013 8th International*, pp. 1-6, 16-18 Dec. 2013.

[18] K. Pour and J. Perez, "Robust indoor positioning based on received signal strength," *2nd International Conference on, Birmingham in Pervasive Computing and Applications, 2007. ICPCA 2007*, UK, pp. 693-698, 2007.

[19] H. A. Obeidat, W. Shuaieb, H. Alhassan, K. Samarah, M. Abousitta, R. A. Abd-Alhameed, S. M. R. Jones, and J. M. Noras, "Location based services using received Signal Strength algorithms," *Internet Technologies and Applications (ITA), 2015*, pp. 411-413, 8-11 Sept. 2015.

Huthaifa Obeidat was born in Jordan, he received his B.Sc. degree in Electrical Engineering from Jordan University of Science and Technology 2011, he was awarded M.Sc. degree in Personal Mobile and Satellite Communication from the University of Bradford 2013. Since then, he worked as Lecturer in Communication and Electronics department at Jerash University in Jordan. Currently he is a Ph.D. student at the University of Bradford. His research interests include Radiowave Propagation, Antenna and Location Based Services.

Yousef Dama is an Assistant Professor in Telecommunications Engineering at An-Najah National University, Palestine. He received his B.Sc. in Electrical Engineering from An-Najah National University, Palestine, in 2005, M.Sc. degree in Personal Mobile and Satellite Communications from University of Bradford, UK, in 2006, and his Ph.D. in Broadband Wireless Systems Engineering from University of Bradford, UK, in 2013. He has published about 40 academic journals and referred conference papers. His current research interests includes diversity techniques, space time coded orthogonal frequency division multiplexing, Propagation channel modelling, and spatial envelope correlation of MIMO system for broadband wireless systems and novel localization applications.

Raed A. Abd-Alhameed is Professor of Electromagnetic and Radio Frequency Engineering at the University of Bradford, UK. Currently, he is the Leader of the RF, Antenna Design and Electromagnetic Research in the School of Engineering and Informatics, Bradford University. He is Principal Investigator for several funded projects from EPSRC, EU, TSB, RDP and has led several successful knowledge transfer programmes for Pace PLC, YW PLC, Datong of Seven Technologies Group, WiMAC and ITEG Ltd. He has published over 400 academic journal and conference papers and is co-author of three books and several book chapters. Abd-Alhameed is a Fellow of the Institution of Engineering and Technology, Fellow of Higher Education Academy, and a Chartered Engineer in the U.K.

Fun Hu is Professor of Wireless Communications Engineering at University of Bradford, UK. Hu has received considerable funding support through participations and contributions to many flagship projects funded by the UK funding councils, EU, ESA and TSB. Her major research is in integrated mobile, wireless and satellite communication networks with particular applications to vehicular communications networks including aircrafts and trains. She is the Head of the Future Ubiquitous Research Group and has published over 100 papers in scientific journals and international conferences, and co-authored 1 book, edited two books and contributed to 5 book chapters.

Rami Qahwaji is Professor of Visual Computing at Bradford University. His research interests include: 2D/3D image processing, machine learning, signal processing and the design of machine vision systems with proven track record in the fields of satellite imaging, medical imaging, data visualisation and applied data mining working with various medical and industrial collaborators. He led the development of software systems that are being used by NHS, NASA, European Space Agency and other companies. His research has been funded by EPSRC, EU, NHS, ERDF, ESA, TSB, Yorkshire Forward, and has over 120 refereed publications. Qahwaji is Fellow of the Institution of Engineering and Technology, Charted Engineer and Fellow of the Higher Education Academy.

James Noras is a Senior Lecturer in the School of Engineering and Informatics at the University of Bradford, UK, and has published 59 journal papers and 93 conference papers, in fundamental semiconductor physics, analogue and digital circuit design, digital signal processing and RF system design and evaluation. His main research interests are now in digital system design and implementation, DSP and coding for communication systems, and localization algorithms for mobile systems. Noras is a Member of the Institute of Physics and a Chartered Physicist.

Steve Jones is a Senior Lecturer in the School of Engineering and Informatics at the University of Bradford. He has worked on a wide variety of projects in the area of satellite slant-path propagation (e.g., 10 GHz bistatic-scatter, 11/14 GHz scintillation and ice depolarization with Olympus) and mobile radio propagation (notably Mobile VCE and TEAMS projects). He served as an Associate Editor for the IEEE Transactions on Antennas and Propagation 2004-8. Recently, he has worked on multiple-antenna technologies, signal processing, localization and propagation modelling for broadband wireless access systems.

Efficient Stochastic FDTD Algorithm with Optimized GPU Acceleration

Athanasios N. Papadimopoulos, Georgios G. Pyrialakos, Nikolaos V. Kantartzis, and Theodoros D. Tsiboukis

Department of Electrical and Computer Engineering
Aristotle University of Thessaloniki, 54124 Thessaloniki, Greece
{papadian, pyrialak, kant, tsibukis}@auth.gr

Abstract ─ A 3-D curvilinear stochastic finite-difference time-domain (S-FDTD) technique on modern graphics processing units (GPUs) is introduced in this paper for complex media with high levels of statistically-variable heterogeneities. The novel accelerated methodology develops a robust covariant/contravariant dual-grid tessellation and estimates the mean value and standard deviation of field components during only a single run. In this way, notably accurate and stable estimations can be very rapidly and economically obtained, unlike the usual multiple-realization staircase Monte-Carlo FDTD schemes. These merits are successfully verified via realistic microwave setups with highly-varying media uncertainties, where the featured algorithm is shown to overwhelm the typical exceedingly resource consuming approaches.

Index Terms ─ Curvilinear coordinates, graphics processing units (GPUs), media uncertainties, Monte-Carlo schemes, statistical modeling, stochastic-FDTD method.

I. INTRODUCTION

Recently, an escalating research interest has arisen in the area of non-deterministic electromagnetic problems. Due to their abruptly-random media features, such applications are too complex for a conventional treatment; thus they are usually treated via the Monte-Carlo (MC) approach [1]. However, the large number of realizations and unduly resources actually prohibit its applicability to real-world 3-D (or even 2-D) arrangements. To mitigate these defects, several efficient alternatives have been proposed. Specifically, in [2] a stochastic finite-difference time-domain (S-FDTD) method is presented in Cartesian coordinates, while [3] follows a single-run approach for precise field statistics. Also, [4] launches an FDTD-based polynomial chaos expansion along with the proper basis functions and [5] derives a stochastic finite integration technique for electrokinetics. Despite the obvious profits, though, diverse issues are to be resolved, like the remarkable system demands and the manipulation of curved structures.

In this paper, a generalized S-FDTD method is developed via advanced graphics processing units (GPUs), for the accurate and fast analysis of electromagnetic problems with uncertainties in their constitutive and geometrical parameters. The new 3-D algorithm presents a covariant/contravariant metrics concept, based on a properly modified rendition of [6], for dual curved meshes to compute the mean value and standard deviation of electric and magnetic fields in just a single realization, unlike existing MC-FDTD techniques. For additional acceleration, the proposed method is programmed through the compute unified device architecture (CUDA) platform, which exploits the parallelized features of modern GPUs. Hence, very rapid and precise simulations are attained, whereas the detrimental lattice reflection errors, owing to staircase approximations, are drastically minimized. The prior advantages are substantiated via realistic microwave structures with complex curved parts, stochastic geometries as well as random electric permittivity, conductivity, and magnetic permeability. Numerical results reveal the accuracy and stability of the featured formulation, compared to the MC-FDTD outcomes, and its significant speedup over serialized implementations.

II. THE CURVILINEAR S-FDTD METHOD

The S-FDTD algorithm is derived for a general coordinate system, where we consider the covariant $\mathbf{a}_1$, $\mathbf{a}_2$, $\mathbf{a}_3$ and contravariant $\mathbf{a}^1$, $\mathbf{a}^2$, $\mathbf{a}^3$ bases for the electric, **E**, and magnetic field, **H**, vectors [6, 7]. This implies that in our formulation, there are four sets of components: (i) two covariant, i.e., (e_1, e_2, e_3), (h_1, h_2, h_3) and (ii) two contravariant i.e., (e^1, e^2, e^3), (h^1, h^2, h^3), for the **E** and **H** field components, respectively. In addition, for the case of unbounded computational domains, the convolution perfectly matched layer (CPML) absorbing boundary condition [8] is employed. Bearing in mind the above considerations, we apply operator $\mathcal{L}$ (representing the mean value M or variance σ^2) to Maxwell equations. For illustration, the e_1 covariant component is given by:

Submitted On: February 27, 2015
Accepted On: June 17, 2016

$$\mathcal{L}\left\{e_1\big|_{i+1/2,j,k}^{n+1}\right\}=\mathcal{L}\left\{D_{\mathrm{A}}\big|_{i+1/2,j,k}e_1\big|_{i+1/2,j,k}^{n}\right.$$
$$+\frac{D_{\mathrm{B}}\big|_{i+1/2,j,k}}{\sqrt{g}\Delta a_2}\left(h^3\big|_{i+1/2,j+1/2,k}^{n+1/2}-h^3\big|_{i+1/2,j-1/2,k}^{n+1/2}+\zeta_{e_{12}}\big|_{i+1/2,j,k}^{n+1/2}\right)$$
$$\left.-\frac{D_{\mathrm{B}}\big|_{i+1/2,j,k}}{\sqrt{g}\Delta a_3}\left(h^2\big|_{i+1/2,j,k+1/2}^{n+1/2}-h^2\big|_{i+1/2,j,k-1/2}^{n+1/2}+\zeta_{e_{13}}\big|_{i+1/2,j,k}^{n+1/2}\right)\right\} \quad (1)$$

where g is the Jacobian determinant of the g_{rs} system metrics (for r, s = 1,2,3) and Δa_r the spatial step along the a_r covariant direction. Also, D_{A} and D_{B} are coefficients that include the uncertainties of media constitutive parameters and ζ the covariant CPML terms. For example, the ζ_{12} component in (1) is expressed as:

$$\mathcal{L}\left\{\zeta_{e_{12}}\big|_{i+1/2,j,k}^{n+1/2}\right\}=\mathcal{L}\left\{R\,\zeta_{e_{12}}\big|_{i+1/2,j,k}^{n-1/2}\right.$$
$$\left.+S\left(h^3\big|_{i+1/2,j+1/2,k}^{n+1/2}-h^3\big|_{i+1/2,j-1/2,k}^{n+1/2}\right)\right\}, \quad (2)$$

with R and S accumulating the tunable CPML features [7] along the a_r covariant direction. Furthermore, the contravariant components of (1) are calculated via a dual-mesh metrics interpolation, which requires the covariant terms toward the other two directions. Indicatively, the h^3 component is provided in (3) (bottom of page).

Next, to consider all random media uncertainties, the Delta method [9], [10] is incorporated. The specific approach uses a Taylor series expansion on each side of (1) and (2). So, for a first-order approximation [2], the mean value and variance of a function $f(y_1,y_2,\ldots,y_n)$ of multiple random variables $y_1,y_2,\ldots,y_n$ are, respectively,

$$M\{f(y_1,y_2,\ldots,y_n)\}\approx f(m_{y_1},m_{y_2},\ldots,m_{y_n}), \quad (4)$$

$$\sigma^2\{f(y_1,y_2,\ldots,y_n)\}\approx\sum_{i=1}^{n}\sum_{j=1}^{n}\frac{\partial f}{\partial y_i}\frac{\partial f}{\partial y_j}\bigg|_{m_{y_1},m_{y_2},\ldots,m_{y_n}}$$
$$\cdot M\{(y_i-m_{y_i})(y_j-m_{y_j})\}, \quad (5)$$

for $m_{y1},m_{y2},\ldots,m_{yn}$ the mean values of $y_1,y_2,\ldots,y_n$, which, herein, are the e_r, h_r, e^r, h^r components and the four media parameters, i.e., electric permittivity ε, magnetic permeability μ, conductivity $\bar{\sigma}$ and magnetic losses $\bar{\rho}$.

As (4) implies, the mean value update equations share a similar form to those of the FDTD method, after substituting all stochastic parameters in the latter with their mean values. It is deduced from (6) that variance terms include covariance components of two random variables, given by $\mathrm{Cov}\{y_1,y_2\}=\rho_{y_1,y_2}\sigma\{y_1\}\sigma\{y_2\}$, for ρ the correlation coefficient. In fact, ρ varies between 0 and 1, with values near unity revealing a strong correlation. Observing the covariances in (1)-(3), we may derive that ρ must be practically equal to unity. This is evident for field components and ζ terms, which are highly correlated, as they exist at very proximate time intervals. Thus, an instructive linear expansion of these terms, i.e., $\sigma\{y_1\pm y_2\}=\sqrt{(\sigma\{y_1\}\pm\sigma\{y_2\})^2}$ is extracted. In this paper, the standard deviation of all stochastic parameters does not exceed the 10% of the analogous mean value; a threshold which is deemed very realistic for our simulations. In this context, we acquire (6) for the standard deviation of e_1 (bottom of page) and

$$h^3\big|_{i,j,k}^{n+1/2}=g_{33}h_3\big|_{i,j,k}^{n+1/2}+\frac{g_{31}}{4}\left(h_1\big|_{i+1/2\,j,k+1/2}^{n+1/2}+h_1\big|_{i+1/2,j,k-1/2}^{n+1/2}+h_1\big|_{i-1/2,j,k+1/2}^{n+1/2}+h_1\big|_{i-1/2,j,k-1/2}^{n+1/2}\right)$$
$$+\frac{g_{31}}{4}\left(h_2\big|_{i,j+1/2,k+1/2}^{n+1/2}+h_1\big|_{i,j+1/2,k-1/2}^{n+1/2}+h_1\big|_{i,j-1/2,k+1/2}^{n+1/2}+h_1\big|_{i,j-1/2,k-1/2}^{n+1/2}\right). \quad (3)$$

$$\sigma\left\{e_1\big|_{i+1/2,j,k}^{n+1}\right\}=\frac{2m_\varepsilon-m_{\bar{\sigma}}\Delta t}{2m_\varepsilon+m_{\bar{\sigma}}\Delta t}\sigma\left\{e_1\big|_{i+1/2,j,k}^{n}\right\}+\frac{4\Delta t\left(m_{\bar{\sigma}}\rho_{\varepsilon,e_1}\sigma\{\varepsilon\}-m_\varepsilon\rho_{\bar{\sigma},e_1}\sigma\{\bar{\sigma}\}\right)}{\left(2m_\varepsilon+m_{\bar{\sigma}}\Delta t\right)^2}M\left\{e_1\big|_{i+1/2,j,k}^{n}\right\}$$
$$+\frac{D\big|_{i+1/2,j,k}}{\sqrt{g}\Delta a_2}\left[\sigma\left\{h^3\big|_{i+1/2,j+1/2,k}^{n+1/2}\right\}-\sigma\left\{h^3\big|_{i+1/2,j-1/2,k}^{n+1/2}\right\}+\sigma\left\{\zeta_{e_{12}}\big|_{i+1/2,j,k}^{n+1/2}\right\}\right.$$
$$\left.-G(h^3)\big|_{i+1/2,j,k}\left(M\left\{h^3\big|_{i+1/2,j+1/2,k}^{n+1/2}\right\}-M\left\{h^3\big|_{i+1/2,j-1/2,k}^{n+1/2}\right\}\right)+G(\zeta_{e_{12}})\big|_{i+1/2,j,k}M\left\{\zeta_{e_{12}}\big|_{i+1/2,j,k}^{n+1/2}\right\}\right]$$
$$+\frac{D\big|_{i+1/2,j,k}}{\sqrt{g}\Delta a_3}\left[\sigma\left\{h^2\big|_{i+1/2,j,k-1/2}^{n+1/2}\right\}-\sigma\left\{h^2\big|_{i+1/2,j,k+1/2}^{n+1/2}\right\}+\sigma\left\{\zeta_{e_{13}}\big|_{i+1/2,j,k}^{n+1/2}\right\}\right.$$
$$\left.-G(h^2)\big|_{i+1/2,j,k}\left(M\left\{h^2\big|_{i+1/2,j,k+1/2}^{n+1/2}\right\}-M\left\{h^2\big|_{i+1/2,j,k-1/2}^{n+1/2}\right\}\right)+G(\zeta_{e_{13}})\big|_{i+1/2,j,k}M\left\{\zeta_{e_{13}}\big|_{i+1/2,j,k}^{n+1/2}\right\}\right], \quad (6)$$

for $D\big|_{i+1/2,j,k}=\dfrac{2\Delta t}{2m_\varepsilon+m_{\bar{\sigma}}\Delta t}$ and $G(P)\big|_{i+1/2,j,k}=\dfrac{2\rho_{\varepsilon,P}\sigma\{\varepsilon\}+\rho_{\sigma,P}\sigma\{\bar{\sigma}\}\Delta t}{2m_\varepsilon+m_{\bar{\sigma}}\Delta t}$, (7)

$$\sigma\left\{\zeta_{e_{12}}\Big|_{i+1/2,j,k}^{n+1/2}\right\} = R\sigma\left\{\zeta_{e_{12}}\Big|_{i+1/2,j,k}^{n-1/2}\right\} + S\left[\sigma\left\{h^3\Big|_{i+1/2,j+1/2,k}^{n+1/2}\right\} - \sigma\left\{h^3\Big|_{i+1/2,j-1/2,k}^{n+1/2}\right\}\right], \quad (8)$$

with similar formulas for the other quantities. In (6) and (7), $m_\varepsilon, m_{\bar{\sigma}}, \sigma\{\varepsilon\}, \sigma\{\bar{\sigma}\}$ are the mean value and standard deviation of ε and $\bar{\sigma}$, while $\rho_{\varepsilon,L}, \rho_{\bar{\sigma},L}$ are the cross-correlation coefficients between component P (here $P = h^2, h^3, \zeta_{e_{12}}, \zeta_{e_{13}}$) and material parameter. Moreover, (7) shows that to obtain σ, one has to evaluate the mean value of **E** and **H** components via (4) at the previous time-step. This does not permit the extraction of either the mean value or standard deviation alone, due to the coupling of (4) and (6). So, the formulation requires twice the usual FDTD system resources. In contrast, the MC-FDTD scheme focuses on the computed fields, whose uncertainties are found by samples over the total number of simulations. As a result, its overhead is analogous to this (usually very large) number, yet obligatory for a viable approximation of the ideal normal distribution. Finally, since the typical Courant criterion in Cartesian coordinates is affected by the curvilinear formalism, the stability throughout our paper is guaranteed by the generalized Courant condition [7]:

$$\Delta t \le \left[c \sup\left(\sqrt{\sum_r^3 \sum_s^3 g^{rs}}\right)\right]^{-1}, \quad (9)$$

pertinent to handle non-uniform lattices, as the ones implemented herein. In (9), sup(.) denotes the maximum value in the entire *i*, *j*, *k* domain and g^{rs} is a metric that is the inverse of g_{rs}. Notice that all of our studies have been proven completely stable, even for very detailed grids or very long simulation times.

III. OPTIMAL GPU IMPLEMENTATION

For our curvilinear simulations, we develop the full 3-D code based on the CUDA 6.0 platform [11]-[13] to exploit modern GPUs. This decision is favored from the parallelization potential of the S-FDTD method, which offers substantial acceleration. Our algorithm allows the fully independent execution of update equations at each grid node during a single time-step. Thus, we assign one or more such nodes to the various independent execution flows of the hardware, to get the maximum performance via a comprehensive optimization process that will be discussed. In CUDA independent processes called threads, are arranged in an algorithmic 3-D "grid". Such a structure provides these threads with unique coordinates and allows the manipulation of the actual space coordinates in the domain. To this aim, we assign specific memory addresses from our 3-D matrix (i.e., the electromagnetic field space) to specific thread coordinates, for the entire space and connect nearby memory addresses with equally adjacent threads.

Emphasis should be given to the handling of wraps, groupings of 32 threads that although, by their nature, perform 32 individual parallel executions, they are issuing a common command for all the involved execution flows at the same time. This leads to inefficient algorithms, where incorporation of branching below a 32 thread interval lead to serialization in the execution flow. Threads are also organized into larger structures called blocks that may have up to three dimensions in a local grid of thread coordinates. All wraps that reside inside each block are assigned to the same streaming multiprocessor (SM) in the hardware; so making use of the same local memories (shared memory, L1 cache, etc.) and the same schedulers. Lastly, the concept of "kernel", a CUDA function executed on the GPU, must be considered. Through kernels we can create our grid and block structure, control the hardware, and use the different local memories available per block. A flow chart of our algorithm is given in Fig. 1, while its key realization features are summarized as follows.

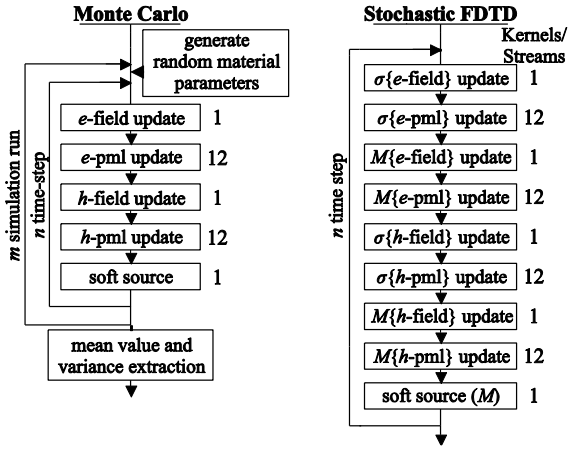

Fig. 1. Flow chart for the GPU realization of the MC-FDTD and the proposed curvilinear S-FDTD method.

A. Kernel size and register usage

According to our analysis, a grouping of 32×16 threads-per-block has been found to guarantee very good performance in Cartesian grids. The complexity of the curvilinear S-FDTD algorithm did, however, require extensive treatment of kernel variables, yielding an optimal 24×16 grid. Although in the simple case of fully orthogonal meshes, the use of one kernel for each of the FDTD updates suffices, we observed that a multi-kernel implementation (exploiting streams as discussed later) is more beneficial for the curvilinear S-FDTD algorithm. Regarding the surrounding CPML layers, four different kernels for each side (two for electric and two for magnetic components), running simultaneously via streams, are necessary for the additional calculations (due to the extra CPML terms) to be completed.

B. Use of streams

Aiming at the highest parallelization, we resort – at various points – to the use of streams. They refer to independent flow sequences, defined outside a kernel and passed as an argument when the latter is called. Also, they allow kernels, likely not to interfere or share cross-dependences, to be executed concurrently; something impossible in their default state, so avoiding unnecessary serializations. Thanks to them, we can partially achieve the simultaneous execution of the main routine and the CPML kernels, resulting in about 72% less overall computational time, as illustrated in Fig. 2.

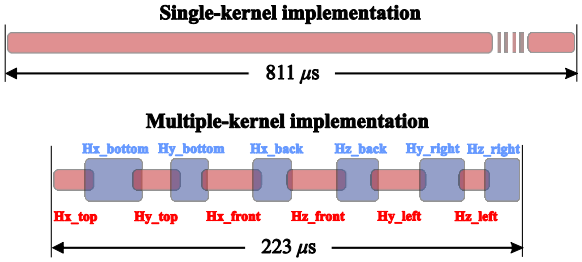

Fig. 2. Efficiency differences between single- and multiple-kernel realizations for the CPML update.

C. Memory considerations

In our realization, the global memory is used for the storage of the main components and the CPML variables. Special attention has been paid to the suitable matrix alignment in memory, which ensures that adjacent threads in the kernels access similarly-placed elements. Only when this occurs, transfers of 32 elements from global memory (in the case of floats) are conducted in a single memory access cycle (i.e., "coalesced access"). For the CPML, specific grid alignments are selected, because a simplistic implementation of a unique kernel for all CPML areas would render coalesced access unfeasible. This is due to the use of a small grid along the perpendicular (with respect to the CPML) directions, which does not allow the assign of the first grid dimension to the first dimension of CPML auxiliary field matrices. However, the latter action is required for memory coalescing. A simple, yet inefficient, solution could use a full size grid, which would introduce large numbers of idle threads. So, the division of the algorithm into individual parts with different grids, that exploit streams, appears as the optimal choice.

D. Use of atomics

Atomics are necessary for the simultaneous update of elements at the grid corners. Figure 3 clarifies the correction provided in our algorithm by this idea, when the race between concurrent threads is likely to produce undesirable miscalculations (the case of top/bottom CPMLs is shown in Fig. 3). So, correct updating is ensured without causing any performance degradation.

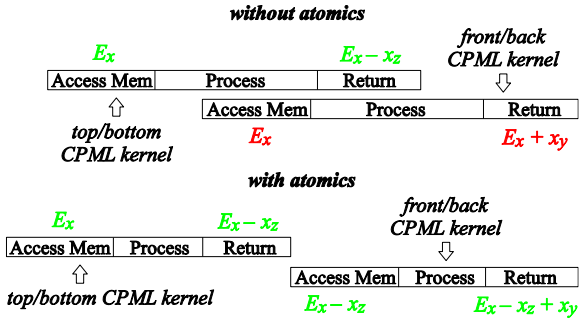

Fig. 3. Illustration of the error that can arise during parallel CPML updates and its mitigation via atomics (x_y and x_z refer to terms at the CPML corner regions).

IV. NUMERICAL RESULTS

The performance of the proposed algorithm is validated in terms of complicated microwave structures with real-world stochastic media parameters. Such uncertainties are normally encountered at their substrate, copper parts and geometry, possibly created during the manufacturing process. Furthermore, comparisons are conducted with an MC-FDTD scheme, which needs the large number of almost 10^4 FDTD realizations, whereas all infinite domains are terminated by an 8-cell CPML.

A. Koch-shaped fractal microstrip

Let us study the Koch fractal microstrip filter of Fig. 4, which suppresses particular frequencies with a reduced size. Its dimensions are given in [14] and all statistical constitutive/geometric parameters of its copper parts and substrate are obtained from the Ventec™ and Isola™ Corporation datasheets. Therefore, for the substrate: m_ε = 4.4, $\sigma\{\varepsilon\}$ = 0.088, $m_{\bar{\sigma}} = 3.427$ mS/m, $\sigma\{\bar{\sigma}\} = 0.07$ mS/m, while for its height h: m_h = 15 mm and $\sigma\{h\}$ = 0.3 mm. On the other hand, for the copper parts, we have $m_{\bar{\sigma}} = 58.6$ S/m and $\sigma\{\bar{\sigma}\} = 0.17$ S/m. Figures 5 and 6 present the E_x mean value and standard deviation, as derived from the MC-FDTD technique (mesh: 203×407×117 cells and total CPU computational time: 62.57 hours) and our algorithm (mesh: 101×201×51 cells and total CPU computational time: 22.92 min). Note that all calculations are performed across a straight horizontal line at the center of filter's top side. As discerned, the agreement between the two methods is promising, whereas the convergence of the standard deviation outcomes (Fig. 6) is very satisfactory. However, it is stated that as $\rho \to 1$, the S-FDTD technique tends to overestimate the solution, as also discussed in [2], [3]. Furthermore, in the inlet snapshot of Fig. 5, we illustrate the mean value of the current distribution atop the filter, while Fig. 7 summarizes the significant GPU acceleration of our algorithm for various lattices via two NVIDIA™ models. Similar deductions can be drawn for the *S*-parameters of Fig. 8.

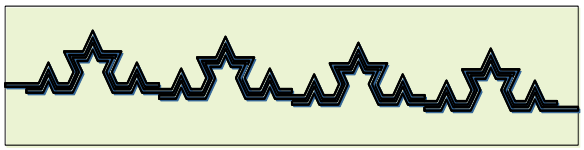

Fig. 4. A second-order Koch-shaped microstrip filter.

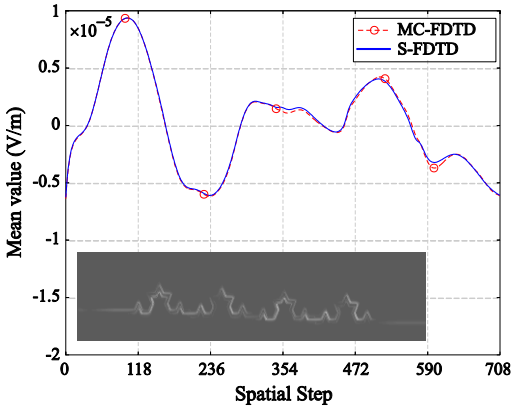

Fig. 5. Mean value of the E_x component for the Koch-shaped fractal filter at 2 GHz (inlet snapshot gives the mean value of the current distribution at the top side).

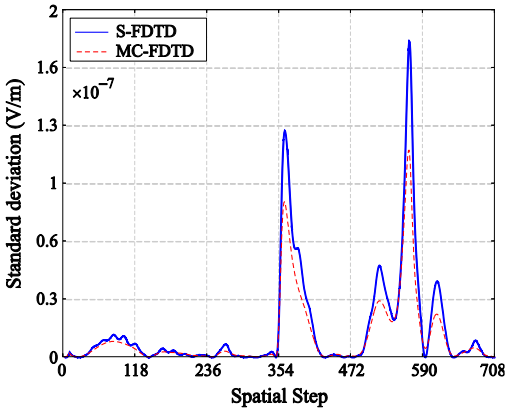

Fig. 6. Standard deviation of the E_x component for the Koch-shaped fractal filter at 2 GHz.

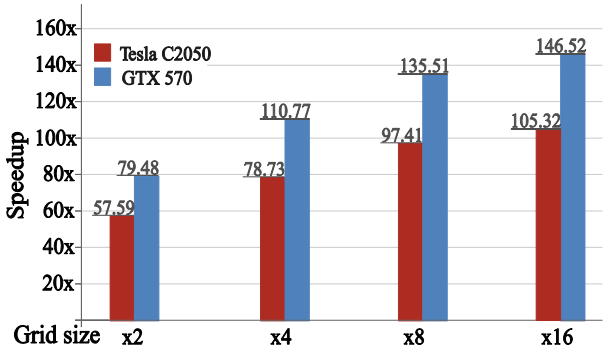

Fig. 7. GPU acceleration of the proposed method.

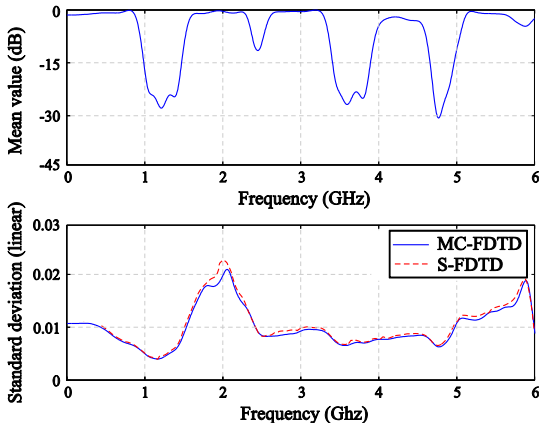

Fig. 8. Mean value and standard deviation of the *S*-parameters for the Koch-shaped fractal filter.

B. Compact wideband resonator filter

The second application is the compact wideband filter of Fig. 9, with a folded multiple-mode resonator [15]. For the same stochastic constitutive/geometric parameters as in the previous problem, the basic dimensions are selected as: L_1 = 18.8 mm, L_2 = 5.8 mm, L_3 = 9 mm, L_4 = 5 mm, w_1 = 2.27 mm, w_2 = 5.5 mm, w_3 = 0.4 mm, g_1 = 1 mm, g_2 = 0.4 mm, g_3 = 0.21 mm, and H = 4 mm. This realistic setup (mesh: 273×107×49 cells and total CPU computational time: 36.27 min) leads to the single-run current distribution mean value of Fig. 10, at the filter's top side, which is very smooth, unlike the one of the MC-FDTD method (mesh: 511×263×105 cells and total CPU computational time: 71.34 hours) through an extremely large number of multiple realizations. Finally, the accuracy of our algorithm are successfully substantiated through the *S*-parameters of Fig. 11, again evaluated during only a single realization.

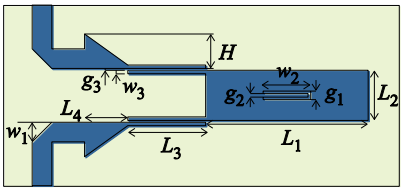

Fig. 9. Top-view of the compact wideband filter with a folded multi-mode resonator.

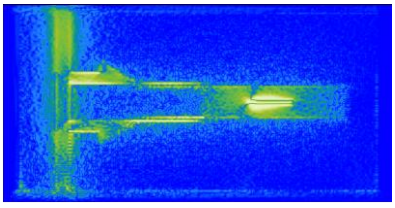

Fig. 10. Snapshot of the current distribution mean value at the top side of the compact wideband filter.

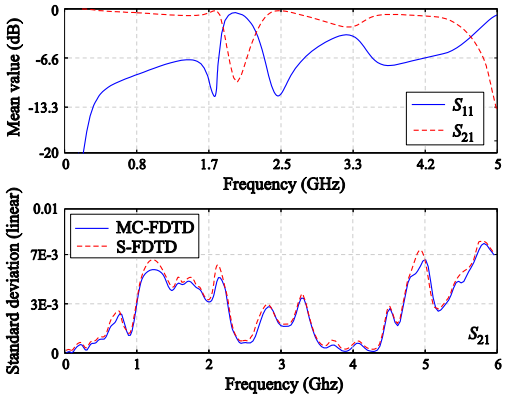

Fig. 11. Mean value and standard deviation of the *S*-parameters for the compact wideband filter.

V. CONCLUSION

A 3-D curvilinear S-FDTD method has been presented in this paper for statistically heterogeneous materials regarding their constitutive/geometric parameters. The new scheme launches a covariant/contravariant concept, while its single-run GPU rendition is more than 100× faster than existing techniques. So, accurate outcomes can be very rapidly and cost-effectively derived.

ACKNOWLEDGMENT

This research has been co-financed by the EU and Greek funds through Research Program: Aristeia.

REFERENCES

[1] F. Hastings, J. Schneider, and S. Broschat, "A Monte-Carlo FDTD technique for rough surface scattering," *IEEE Trans. Antennas Propag.*, vol. 43, no. 11, pp. 1183-1191, 1995.

[2] S. Smith and C. Furse, "Stochastic FDTD for analysis of statistical variation in EM fields," *IEEE Trans. Antennas Propag.*, vol. 60, no. 7, pp. 3343-3350, 2012.

[3] T. Tan, A. Taflove, and V. Backman, "Single realization stochastic FDTD for weak scattering waves in biological random media," *IEEE Trans. Antennas Propag.*, vol. 61, pp. 818-828, 2013.

[4] A. Austin and C. Sarris, "Efficient analysis of geometrical uncertainty in the FDTD method via polynomial chaos with application to microwaves," *IEEE Trans. Microw. Theory Tech.*, vol. 61, no. 12, pp. 4293-4301, 2013.

[5] L. Codecasa and L. Di Rienzo, "Stochastic finite integration technique formulation for electro-kinetics," *IEEE Trans. Magn.*, vol. 50, no. 2, pp. 7014104(1-4), 2014.

[6] M. Fusco, "FDTD algorithm in curvilinear coordinates [EM scattering]," *IEEE Trans Antennas Propag.*, vol. 38, no. 1, pp. 76-89, 1990.

[7] A. Taflove and S. Hagness, *Computational Electrodynamics: The Finite-Difference Time-Domain Method*. Artech House, Norwood, 2005.

[8] M Inman, A. Elsherbeni, J. Maloney, and B. Baker, "Practical implementation of a CPML for GPU accelerated FDTD," *ACES J.*, vol. 23, no. 1, pp. 16-22, 2008.

[9] S. Lalléchère, P. Bonnet, I. El Baba, and F. Paladian, "An electromagnetic compatibility problem via unscented transform and stochastic collocation methods," *ACES J.*, vol. 27, no. 12, pp. 94-101, 2012.

[10] J. Ochoa and A. Cangellaris, "Macro-modeling of electromagnetic domains exhibiting geometric and material uncertainty," *ACES J.*, vol. 27, no. 2, pp. 80-87, 2012.

[11] V. Demir and A. Elsherbeni, "CUDA based FDTD implementation," *ACES J.*, vol. 25, no. 4, pp. 303-314, 2010.

[12] V. Demir and A. Elsherbeni, "CUDA-OpenGL interoperability to visualize electromagnetic fields calculated by FDTD," *ACES J.*, vol. 27, no. 2, pp. 206-214, 2012.

[13] N. Takada, T. Shimobada, N. Masuda, and T. Ito, "Improved performance of FDTD computation using a thread block constructed as a 2-D array with CUDA," *ACES J.*, vol. 25, no. 12, pp. 1061-1069, 2012.

[14] W. Chen and G. Wang, "Effective design of novel compact fractal-shaped microstrip coupled-line filters for suppression of the second harmonic," *IEEE Microw., Wireless Compon. Lett.*, vol 19, no. 2, pp. 74-76, 2009.

[15] H. Wang, Q. Chu, and J. Gong, "A compact wideband microstrip filter using folded multiple-mode resonator," *IEEE Microw. Wireless Compon. Lett.*, vol. 19, no. 5, pp. 287-289, 2009.

Athanasios N. Papadimopoulos is pursuing his Ph.D. degree in the Aristotle University of Thessaloniki, Greece, since 2014. His research focuses on numerical techniques, graphene forms and semi-analytical Green's function methods.

Georgios G. Pyrialakos is pursuing his Ph.D. degree in the Aristotle University of Thessaloniki, Greece, since 2013. His research aims at computational methods, hardware acceleration, advanced microwave components and metamaterials.

Nikolaos V. Kantartzis serves as an Associate Professor in the Aristotle University of Thessaloniki, Greece, since 2010. His research interests include EMC modeling, numerical methods, graphene, metamaterials, contemporary microwave applications, and enhanced antenna systems.

Theodoros D. Tsiboukis is a Professor Emeritus in the Aristotle University of Thessaloniki, Greece. His interests involve computational electromagnetics, energy methods, EMC applications, metamaterials, antennas, and waveguides. Tsiboukis has been the recipient of several awards and is a member of various societies and chambers.

New Equivalent Circuit Analysis and Synthesis for Broadband Composite Right/Left-Handed Transmission Line Metamaterials

Na Kou, Yan Shi, and Long Li

School of Electronic Engineering
Xidian University, Xi'an 710071, Shaanxi, China
kouna02091322@126.com, shiyan@mail.xidian.edu.cn, and lilong@mail.xidian.edu.cn

Abstract ─ This paper proposes a new equivalent circuit analysis and synthesis method for the broadband composite right/left-handed transmission line (CRLH TL) and Dual-CRLH (DCRLH) TL metamaterials. In order to consider magnitude and phase of S-parameter of the CRLH/DCRLH TL element simultaneously, a pseudo-inverse technique is first implemented to extract the primary equivalent circuit. By using the filter synthesis technique, the retrieval primary equivalent circuit is further transformed to a typical band-pass/band-stop filter circuit as the secondary equivalent circuit. With two-step retrieval procedure, the response of the secondary equivalent circuit can more accurately agree with that of CRLH/DCRLH TL unit cell, compared with the sole use of the pseudo-inverse technique or the filter synthesis technique. Based on the equivalent circuit models, the topological structure and parameters of CRLH/DCRLH TL can be effectively synthesized for a given center frequency and bandwidth. Numerical results are given to demonstrate good performance of the proposed analysis and synthesis methods.

Index Terms ─ Composite right/left handed transmission line (CRLH TL), Dual-CRLH (DCRLH) TL, equivalent circuit, filter synthesis, pseudo-inverse, two-step retrieval procedure.

I. INTRODUCTION

Electromagneitc metamaterials are artificial effectively homogeneous electromagnetic structures, which exhibit unusual electromagnetic properties not found in natural media. One of physical realization of the metamaterials is based on composite right/left-handed transmission line (CRLH TL) [1]-[3]. Compared with resonant left-handed (LH) metamaterials, the CRLH TL is broad-band and low-loss. Up to now, many different types of the CRLH TLs including Dual CRLH (DCRLH) TL [4], [5], simplified CRLH TL [6] and extended CRLH TL [7] were reported. Due to unprecedented properties and performances, various CRLH-based components, antennas and system applications have been developed [8-13].

When designing the CRLH TL structure, a large number of periodic cells are usually cascaded to achieve special performance. However, analyzing the multi-cell of CRLH TL often needs to use full-wave electromagnetic simulations, and thus plenty of computational resource and time are consumed. By contrast, the equivalent circuit (EC) analysis of the CRLH TL structure is more efficient and costs less computational resource. As a result, we need to extract the relatively precise equivalent circuit of the CRLH TL unit cell firstly, and then the equivalent circuit of multi-cell CRLH TL structure can be obtained to flexibly synthesize new CRLH metamaterial structures. The CRLH TL unit cell is often categorized as a series inductor (L_R), series capacitor (C_L), shunt inductor (L_L), and shunt capacitor (C_R), and exhibits a band-pass filter, in the sense that it has left-handed (LH) high-pass with low-frequency stop-band and right-handed (RH) low-pass with high-frequency stop-band. Most of methods, such as an unwrapping method [1], a calibration method based on transmission matrix [14], etc., have been developed to extract the propagation constant of the CRLH TL structure. However, those methods cannot be implemented to solve the equivalent circuit of the CRLH TL unit cell. The filter technique [15] can be used to extract the equivalent circuit of the CRLH TL structure according to its band-pass response. But the specific phase response of the CRLH TL structure distinguishes itself from the conventional filters which are generally designed to meet the magnitude specifications. In fact, the phase response is a key parameter in the filter design. For example, the phase of S_{21} can be used to calculate the group delay of the filter [15]. A pseudo-inverse method [16] has been proposed to extract the equivalent circuit of a CRLH TL unit cell to simultaneously meet magnitude and phase responses. By transforming *S*-parameters of a CRLH TL unit cell obtained by full-wave simulation or measurement to *ABCD* parameters of the corresponding lumped LC circuit, the capacitance and inductance in the lumped LC circuit can be solved. But by use of the pseudo-inverse matrix, the retrieval lumped LC circuit can only

Submitted On: August 17, 2015
Accepted On: February 11, 2016

roughly feature electromagnetic responses of the CRLH TL structures.

This paper presents a new method to extract the equivalent circuits of the CRLH TL and DCRLH TL unit cells which combine the aforementioned pseudo-inverse method and filter synthesis technique. The new method combines the advantages of the two traditional extraction methods which owns good performance to meet both the magnitude and phase responses. The pseudo-inverse method is first implemented to obtain the primary equivalent circuit according to both magnitude and phase of the scattering parameters of the CRLH TL and DCRLH TL unit cells. In order to further improve retrieval accuracy, the primary equivalent circuit is transformed to typical band-pass/band-stop filter circuit as the secondary equivalent circuit according to the filter synthesis technique. Numerical results show that the scattering parameter responses solved by the extracted circuit and the original unit cell agree well with each other. Furthermore, three CRLH TL cells are cascaded to verify the accuracy of the equivalent circuit, results shows the *S*-parameters of the cascaded equivalent circuit agrees well with that of the three-cell CRLH TL structure. Finally, a typical CRLH TL structure with specific feature is synthesized by use of the equivalent circuit. Numerical results also show a good agreement between the equivalent circuit and the CRLH TL structure.

II. PSEUDO-INVERSE TECHNIQUE TO EXTRACT PRIMARY EQUIVALENT CIRCUIT OF CRLH AND DCRLH TL UNIT CELL FROM S PARAMETERS

The equivalent circuit model of a CRLH unit cell can be featured by the impedance and admittance from the lumped elements L_R, C_L, L_L, and C_R, as shown in Fig. 1. Complex *S*-parameters of the CRLH unit cell at *N* distinct frequency points can be obtained by full-wave simulation or measurement. In order to approximate the *S* parameters of the CRLH TL unit cell by using its equivalent circuit model as accurately as possible, the two-step retrieval procedure is implemented. The parameter extraction of the lumped elements in the primary equivalent circuit is achieved by implementing the pseudo-inverse method. First we convert the *S* parameters of a CRLH TL unit cell to *ABCD* parameters. Specifically, the *ABCD* parameters of the unit cell are related to its *S* parameters as follows [17], [18]:

$$A=\frac{(1+S_{11})(1-S_{22})+S_{12}S_{21}}{2S_{21}}, \tag{1}$$

$$B=Z_0\frac{(1+S_{11})(1+S_{22})-S_{12}S_{21}}{2S_{21}}, \tag{2}$$

$$C=\frac{(1-S_{11})(1-S_{22})-S_{12}S_{21}}{2Z_0S_{21}}, \tag{3}$$

$$D=\frac{(1-S_{11})(1-S_{22})-S_{12}S_{21}}{2S_{21}}. \tag{4}$$

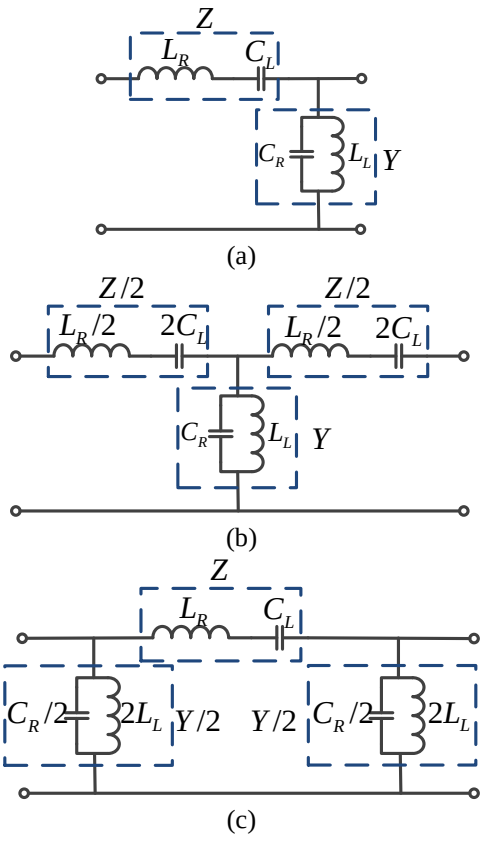

Fig. 1. The equivalent lumped LC circuits of the CRLH TL unit cell: (a) asymmetrical network, (b) symmetrical T-network, and (c) symmetrical π-network.

Second, we solve the *ABCD* parameters according to the equivalent circuit model of the CRLH unit cell. The equivalent circuit of a classical CRLH TL unit cell includes three types such as asymmetrical network, symmetrical T-network and symmetrical π-network [1], as shown in Fig. 1. Corresponding to three kinds of the equivalent circuits, the *ABCD* parameters can be expressed as follows:

$$\begin{bmatrix} A & B \\ C & D \end{bmatrix}=\begin{bmatrix} 1+ZY & Z \\ Y & 1 \end{bmatrix}, \tag{5}$$

$$\begin{bmatrix} A & B \\ C & D \end{bmatrix}=\begin{bmatrix} 1+\frac{ZY}{2} & Z(1+\frac{ZY}{4}) \\ Y & 1+\frac{ZY}{2} \end{bmatrix}, \tag{6}$$

$$\begin{bmatrix} A & B \\ C & D \end{bmatrix}=\begin{bmatrix} 1+\frac{ZY}{2} & Z \\ Y(1+\frac{ZY}{4}) & 1+\frac{ZY}{2} \end{bmatrix}, \tag{7}$$

where the impedance parameter Z and admittance parameter Y are:

$$Z = j(\omega L_R' - \frac{1}{\omega C_L'}), \tag{8}$$

$$Y = j(\omega C_R' - \frac{1}{\omega L_L'}). \tag{9}$$

Here we have $L_R' = L_R$, $C_R' = C_R$, $L_L' = L_L$, and $C_L' = C_L$ for three types of the equivalent lumped circuits. It can be seen from (5)-(7) that $Y = C$ and $Z = B$ for the asymmetrical network, $Y = C$ and $Z = 2B/(A+1)$ for the symmetrical T-network, and $Z = B$ and $Y = 2C/(A+1)$ for the symmetrical π-network, respectively.

The third step is to extract the parameters of L_R, C_L, L_L, and C_R from the parameters Z and Y. Substituting the S parameters at N distinct frequency points into (1)-(4) and inserting the resultant $ABCD$ parameters into (5)-(9), the parameters Z and Y can be obtained as follows:

$$\begin{bmatrix} Z(\omega_1) \\ Z(\omega_2) \\ \vdots \\ Z(\omega_N) \end{bmatrix} = \begin{bmatrix} j\omega_1 & -\frac{j}{\omega_1} \\ j\omega_2 & -\frac{j}{\omega_2} \\ \vdots & \vdots \\ j\omega_N & -\frac{j}{\omega_N} \end{bmatrix} \begin{bmatrix} L_R' \\ \frac{1}{C_L'} \end{bmatrix}, \tag{10}$$

$$\begin{bmatrix} Y(\omega_1) \\ Y(\omega_2) \\ \vdots \\ Y(\omega_N) \end{bmatrix} = \begin{bmatrix} j\omega_1 & -\frac{j}{\omega_1} \\ j\omega_2 & -\frac{j}{\omega_2} \\ \vdots & \vdots \\ j\omega_N & -\frac{j}{\omega_N} \end{bmatrix} \begin{bmatrix} C_R' \\ \frac{1}{L_L'} \end{bmatrix}. \tag{11}$$

Introducing the matrix,

$$W = \begin{bmatrix} j\omega_1 & -\frac{j}{\omega_1} \\ j\omega_2 & -\frac{j}{\omega_2} \\ \vdots & \vdots \\ j\omega_N & -\frac{j}{\omega_N} \end{bmatrix}, \tag{12}$$

(10) and (11) can be rewritten as:

$$[Z] = [W] \begin{bmatrix} L_R' \\ \frac{1}{C_L'} \end{bmatrix}, \tag{13}$$

$$[Y] = [W] \begin{bmatrix} C_R' \\ \frac{1}{L_L'} \end{bmatrix}. \tag{14}$$

Solving (13) and (14) by using the pseudo-inverse technique, the lumped parameters of the equivalent circuit can be obtained as follows:

$$\begin{bmatrix} L_R' \\ \frac{1}{C_L'} \end{bmatrix} = [W]^+ [Z], \tag{15}$$

$$\begin{bmatrix} C_R' \\ \frac{1}{L_L'} \end{bmatrix} = [W]^+ [Y], \tag{16}$$

in which $[\ ]^+$ denotes the matrix pseudo-inverse. Similar procedure can be implemented for a DCRLH TL unit cell. Three types of the equivalent circuits of the DCRLHTL unit cell are shown in Fig. 2.

The impedance Z and admittance Y for the DCRLH TL unit cell can be written in terms of the lumped elements as follows:

$$\frac{1}{Z} = j(\omega C_L' - \frac{1}{\omega L_R'}), \tag{17}$$

$$\frac{1}{Y} = j(\omega L_L' - \frac{1}{\omega C_R'}), \tag{18}$$

where $L_R'=L_R$, $C_R'=C_R$, $L_L'=L_L$, and $C_L'=C_L$ for three types of the equivalent lumped circuits.

Similarly inserting the S parameters at N distinct frequency points into (1)-(7), (17) and (18), we have:

$$\begin{bmatrix} \frac{1}{Z} \end{bmatrix} = [W] \begin{bmatrix} C_L' \\ \frac{1}{L_R'} \end{bmatrix}, \tag{19}$$

$$\begin{bmatrix} \frac{1}{Y} \end{bmatrix} = [W] \begin{bmatrix} L_L' \\ \frac{1}{C_R'} \end{bmatrix}. \tag{20}$$

With the pseudo-inverse technique, (19) and (20) can be solved as:

$$\begin{bmatrix} C_L' \\ \frac{1}{L_R'} \end{bmatrix} = [W]^+ \begin{bmatrix} \frac{1}{Z} \end{bmatrix}, \tag{21}$$

$$\begin{bmatrix} L_L' \\ \frac{1}{C_R'} \end{bmatrix} = [W]^+ \begin{bmatrix} \frac{1}{Y} \end{bmatrix}. \tag{22}$$

According to (15), (16), (21) and (22), the lumped capacitance and inductance of the primary equivalent circuits of the CRLH TL and DCRLH TL unit cells can

be obtained.

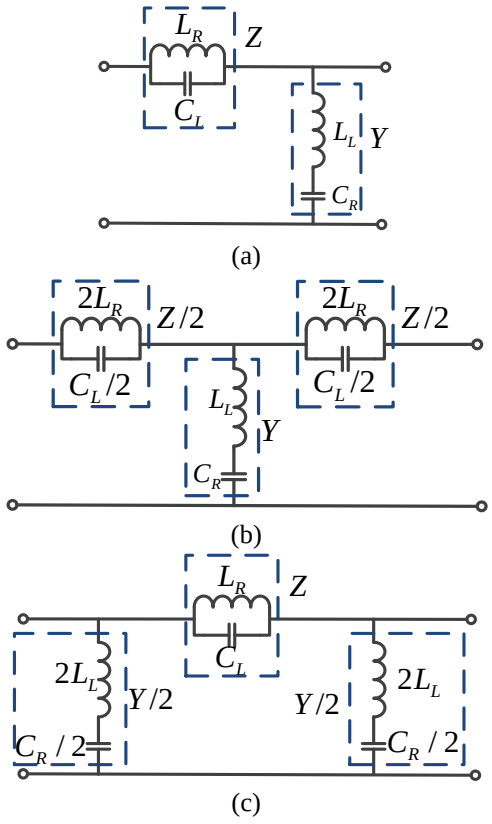

Fig. 2. The equivalent lumped LC circuits of the DCRLH TL unit cell: (a) asymmetrical network, (b) symmetrical T-network, and (c) symmetrical π-network.

III. FILTER SYNTHESIS TECHNIQUE TO EXTRACT SECONDARY EQUIVALENT CIRCUIT OF CRLH AND DCRLH TL UNIT CELL

The pseudo-inverse method can simultaneously approximate the magnitude and phase of *S* parameters of the CRLH and DCRLH TL unit cells. However, the retrieval equivalent circuit model roughly features the electromagnetic responses of the CRLH and DCRLH TL unit cells due to the use of the matrix pseudo-inverse. On the other hand, according to viewpoint of the filter design, the *S*-parameter responses of the CRLH TL unit cell demonstrate the band-pass characteristics, while those of DCRLH TL unit cell show the band-stop characteristics. Hence, a filter synthesis procedure can be introduced into the primary equivalent circuit to improve its approximation accuracy. First, we determine low-pass prototype of the primary equivalent circuit. Second, the resultant low-pass prototype is employed to re-synthesize the desirable band-pass or band-stop responses.

Considering the band-pass characteristics of the CRLH TL unit cell, its primary equivalent circuit is chosen as the symmetrical T network, as shown in Fig. 1 (b), and the corresponding low-pass prototype is shown in Fig. 3.

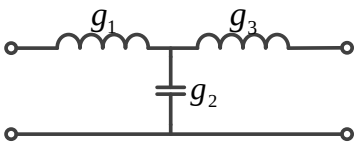

Fig. 3. The low-pass prototype.

According to the band-pass-to-low-pass transformation, we can obtain:

$$g_1 = g_3 = \frac{L_R}{2} \cdot \frac{2\pi f_0 \cdot FBW}{Z_0}, \tag{23}$$

$$g_2 = \frac{1}{L_L} \cdot \frac{Z_0 \cdot FBW}{2\pi f_0}, \tag{24}$$

where f_0 is the central frequency of the band-pass response, *FBW* is the corresponding fractional bandwidth, and Z_0 is the source impedance of the circuit. Following the band-pass synthesis procedure in terms of the coupled resonator cavity filter, as shown in Fig. 4 (a), all parameters can be determined as follows [15]:

$$L = \frac{1}{2\pi f_0}, \tag{25}$$

$$C = \frac{1}{2\pi f_0}, \tag{26}$$

$$K_{01} = K_{34} = \sqrt{\frac{FBW \cdot Z_0}{g_1}}, \tag{27}$$

$$K_{12} = K_{23} = \frac{FBW}{\sqrt{g_1 \cdot g_2}}. \tag{28}$$

Similarly for the DCRLH TL unit cell, the band-stop-to-low-pass transformation is employed, and the parameters in the low-pass prototype shown in Fig. 3 are obtained as:

$$g_1 = g_3 = \frac{L_R}{2} \cdot \frac{2\pi f_0}{FBW \cdot Z_0}, \tag{29}$$

$$g_2 = \frac{1}{L_L} \cdot \frac{Z_0}{2\pi f_0 \cdot FBW}. \tag{30}$$

With the band-stop synthesis procedure in terms of the coupled resonator cavity filter, as shown in Fig. 4 (b), we can get all parameters as follows:

$$L = \frac{1}{2\pi f_0}, \tag{31}$$

$$C = \frac{1}{2\pi f_0}, \tag{32}$$

$$\frac{1}{J_{01}} = \frac{1}{J_{34}} = \sqrt{g_1 \cdot FBW \cdot Z_0}, \tag{33}$$

$$\frac{1}{J_{12}} = \frac{1}{J_{23}} = \frac{FBW}{\sqrt{g_1 \cdot g_2}}. \tag{34}$$

It is worthwhile pointing out that the use of the filter synthesis procedure can better meet the magnitude characteristics of the *S* parameters of the CRLH and DCRLH TL unit cells, irrespective of their phase information.

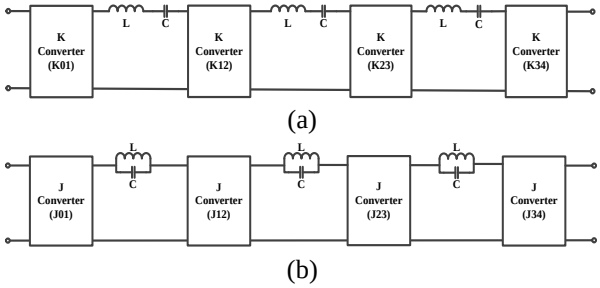

Fig. 4. The coupling resonator cavity filter circuit: (a) band-pass filter and (b) band-stop filter.

With the developed two-step retrieval procedure, the secondary equivalent circuit in terms of the coupled resonator cavity filter can accurately feature the electromagnetic responses of the CRLH/DCRLH TL unit cell. Figure 5 shows the flow chart of whole retrieval procedure.

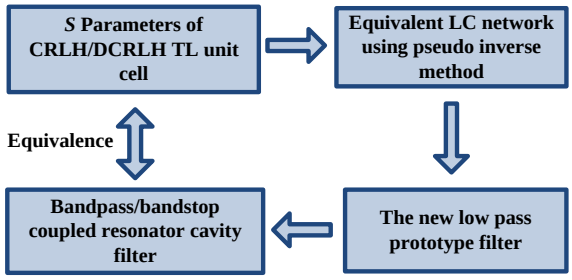

Fig. 5. The flow chart of the proposed two-step retrieval method.

IV. SYNTHESIS OF THE CRLH AND DCRLH TL UNIT CELLS

According to above discussion, we can know that the coupled resonator cavity filter obtained by the two-step retrieval method has nearly the same *S*-parameter responses in magnitude and phase as the CRLH and DCRLH TL unit cells. Hence, given the desirable center frequency and fractional bandwidth, we can synthesize the CRLH and DCRLH TL unit cell structures using the inverse two-step retrieval procedure. The flow chart of the synthesize procedure is shown in Fig. 6.

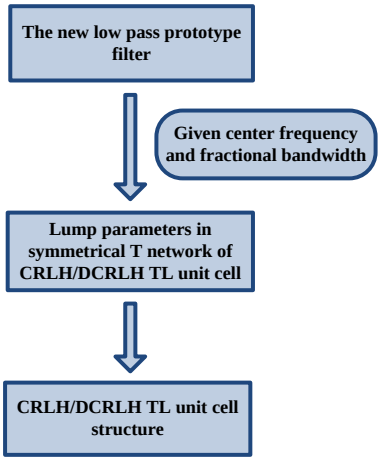

Fig. 6. The flow chart of the synthesis procedure of the CRLH/DCRLH TL unit cell.

According to the low-pass prototype of the CRLH and DCRLH TL unit cells shown in Fig. 3, the lumped elements L_R, C_L, L_L, and C_R in the primary equivalent circuit can be determined, when the operating center frequency and the fractional bandwidth are given. Specifically, according to (23) and (24), the lumped elements for the CRLH TL unit cell are:

$$L_R = \frac{2Z_0 \cdot g_1}{2\pi f_0 \cdot FBW}, \tag{35}$$

$$L_L = \frac{Z_0 \cdot FBW}{2\pi f_0 \cdot g_2}, \tag{36}$$

$$C_L = \frac{1}{(2\pi f_0)^2 \cdot L_R}, \tag{37}$$

$$C_R = \frac{1}{(2\pi f_0)^2 \cdot L_L}. \tag{38}$$

Similarly according to (29) and (30), the lumped elements for the DCRLH TL unit cell are:

$$L_R = \frac{FBW \cdot 2Z_0 \cdot g_1}{2\pi f_0}, \tag{39}$$

$$L_L = \frac{1}{g_2} \cdot \frac{Z_0}{2\pi f_0 \cdot FBW}, \tag{40}$$

$$C_L = \frac{1}{(2\pi f_0)^2 \cdot L_R}, \tag{41}$$

$$C_R = \frac{1}{(2\pi f_0)^2 \cdot L_L}. \tag{42}$$

Once these lumped elements are solved, we can design the geometries of the CRLH and DCRLH TL unit cells by the computer-aided design method. A general design optimization and modeling of microwave circuits is space-mapping optimization algorithm [19], which can automatically mate the equivalent circuits of the CRLH and DCRLH TL unit cells with their

corresponding structures. Besides, for some classical structures of the CRLH and DCRLH TL unit cells, for example the CRLH TL unit cell consisting of the interdigital capacitors and stub inductors shorted to the ground plane by a via [20], [21], some approximately empirical formula can be employed to fast achieve the design.

V. NUMERICAL RESULTS AND DISCUSSIONS

In this section, some CRLH and DCRLH TL structures are presented to show good performance of the proposed two-step retrieval method.

A. Example of the CRLH TL Structure

As the first example, consider a typical CRLH TL structure composed of interdigital capacitors and stub inductors shorted to the ground plane by a via [19], as shown in Fig. 7. The geometry parameters of the CRLH TL structure are given in Table 1. The pseudo-inverse method, the conventional filter synthesis method and the proposed two-step retrieval method have been implemented to extract the equivalent circuits of the CRLH unit cell, as shown in Fig. 8. Here, according to the band-pass response of the CRLH TL structure, we choose f_0=4 GHz and FBW=1.125, and the parameters in the corresponding low-pass prototype circuit can be obtained as $g_1 = g_3 = 0.5055$, $g_2 = 1.9355$. Figure 9 shows the S-parameter comparison between the pseudo-inverse method, the filter synthesis method and two-step retrieval method. It can be seen from Fig. 9 that among three retrieval methods, two-step retrieval method can obtain the best equivalent circuit to match the magnitude and phase of S_{21}.

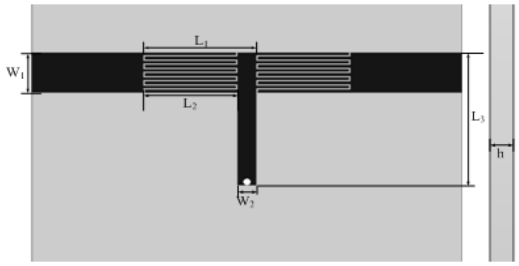

Fig. 7. Microstrip implementation of the CRLH TL unit cell.

Table 1: Parameters of the CRLH TL Unit Cell

Parameters	mm
L_1	6.10
L_2	5.00
L_3	8.00
W_1	2.40
W_2	1.00
H	1.00

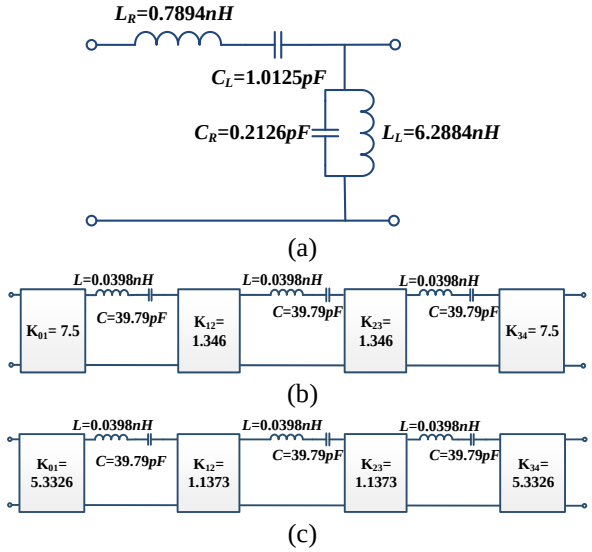

Fig. 8. Equivalent circuits of the CRLH TL unit cell: (a) the pseudo-inverse method, (b) filter synthesis method, and (c) two-step retrieval method.

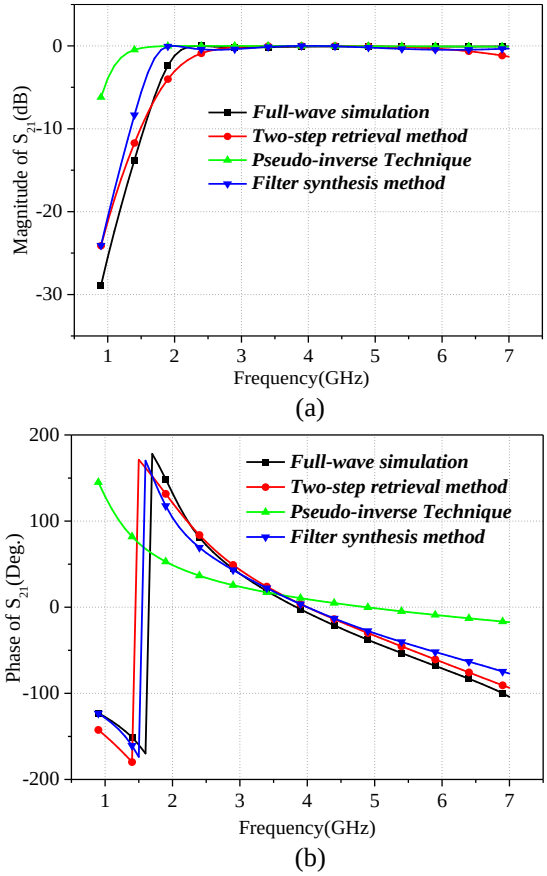

Fig. 9. S-parameter comparison of the equivalent circuits of the CRLH TL between the pseudo-inverse method, filter synthesis method and two-step retrieval method: (a) magnitude of S_{21} and (b) phase of S_{21}.

Furthermore, three CRLH TL unit cells is cascaded for a wider band-pass response, as shown in Fig. 10. Three kinds of the equivalent circuits obtained by three retrieval methods are cascaded to realize the equivalent circuits of the cascading CRLH TL structure, respectively. Figure 11 shows *S*-parameter comparison between three retrieval methods. It can be seen that the cascading equivalent circuit obtained by the two-step retrieval method can best match the cascading CRLH TL structure according to *S*-parameter response in magnitude and phase.

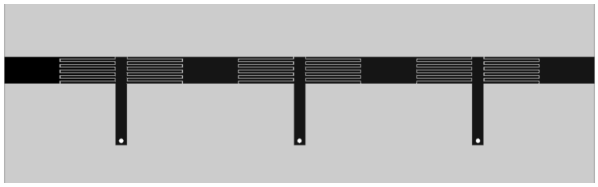

Fig. 10. Topology structure of the 3-cell CRLH TL structure.

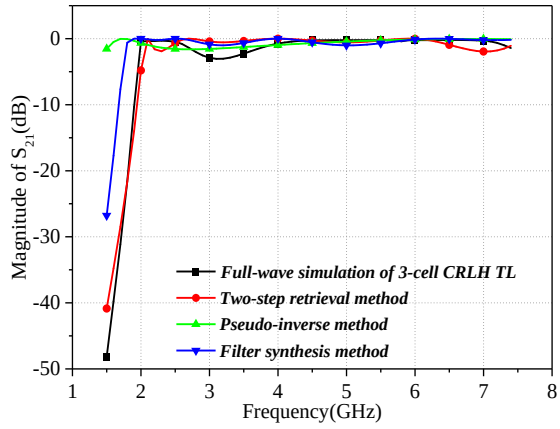

(a)

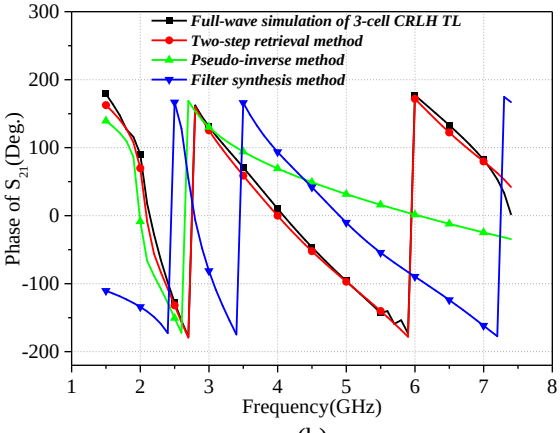

(b)

Fig. 11. *S*-parameter comparison of the 3-cell CRLH TL structure and couple resonator cavity filter: (a) magnitude of S_{21} and (b) phase of S_{21}.

B. Example of the DCRLH TL structure

Next, a microstrip implementation of the DCRLH TL structure [22] is considered. The unit cell consists of one interdigital capacitor paralleled by two high impedance stubs and four series branches of the plane capacitors and stubs, as shown in Fig. 12. The dimension of the DCRLH TL unit cell is given in Table 2. We use the pseudo-inverse method, the filter synthesis method, and the two-step retrieval method to extract the equivalent circuits of the DCRLH TL unit cell, respectively, as shown in Fig. 13. Considering the band-stop response of the DCRLH TL unit cell, we choose f_0=4.7 GHz and *FBW*=0.87 in this example. The obtained parameters in the low-pass prototype circuit are $g_1 = g_3$=0.5676 and g_2 =1.5986.

Table 2: Parameters of the DCRLH TL Unit Cell

Parameters	mm
L_1	10.0
L_2	6.00
L_3	2.00
L_4	2.80
W_1	2.80
W_2	0.75
W_3	3.50
H	1.00

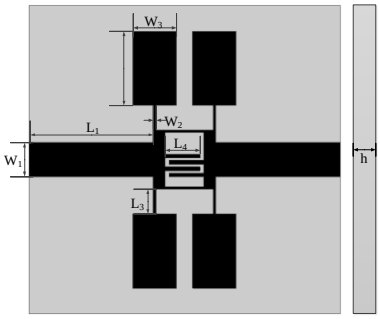

Fig. 12. Microstrip implementation of the DCRLH TL unit cell.

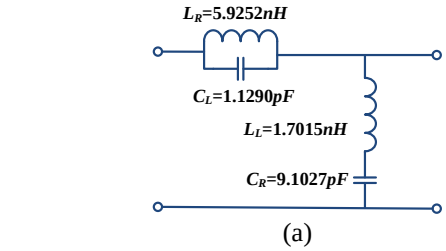

(a)

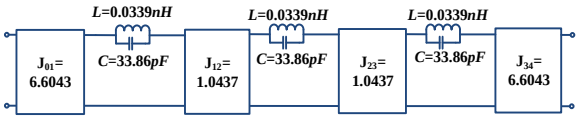

(b)

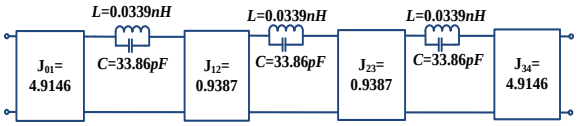

(c)

Fig. 13. Equivalent circuits of the DCRLH TL unit cell: (a) the pseudo-inverse method, (b) filter synthesis method, and (c) two-step retrieval method.

Due to the simultaneous use of the pseudo-inverse and the filter synthesis techniques, the *S*-parameter responses of the equivalent circuit extracted by the two-step retrieval method agree well with that of the original DCRLH TL unit cell, as shown in Fig. 14.

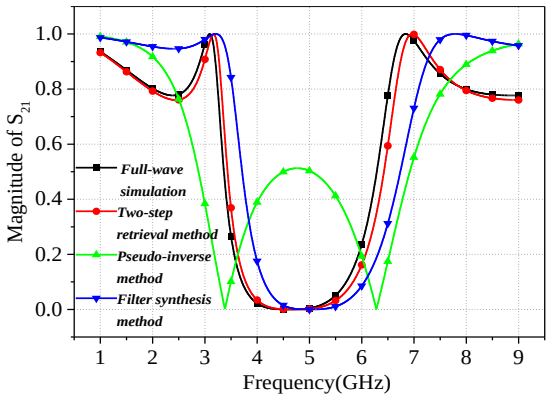

(a)

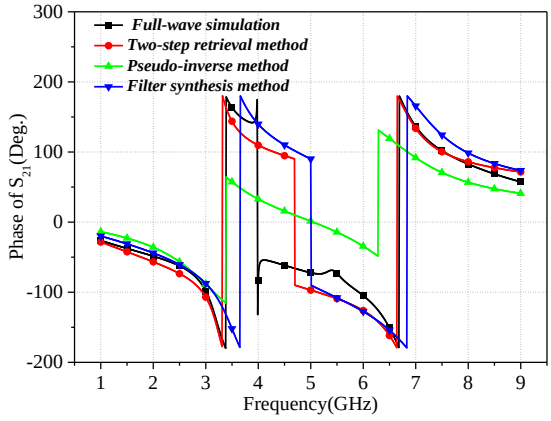

(b)

Fig. 14. *S*-parameter comparison of the equivalent circuits of the CRLH TL unit cell between the pseudo-inverse method, filter synthesis method and two-step retrieval method: (a) magnitude of S_{21} and (b) phase of S_{21}.

C. Synthesis of the CRLH TL structure

Finally, we design a CRLH TL unit cell with the operating center frequency of 10 GHz, and the fractional bandwidth of 0.6. For simplicity, the CRLH TL structure same as the first example is chosen, as shown in Fig. 15.

Hence, the parameters in the low-pass prototype circuit are same as those in the first example, e.g., $g_1 = g_3 = 0.5055$ and $g_2 = 1.9355$. According to (35)-(38), the lumped elements L_R, C_L, L_L, and C_R can be solved as 0.6704 *nH*, 0.1305 *pF*, 0.2467 *nH*, and 1.0 *pF*, respectively. Considering approximation empirical formula of the CRLH TL structure [1], i.e.,

$$L_L = \frac{Z_0}{\omega_0}\tan(\beta L_3), \tag{43}$$

$$C_L = (\varepsilon_r + 1)L_2[-2A_1 + A_2] \quad (pF), \tag{44}$$

$$A_1 = 4.409\tanh[0.55(\frac{h}{W_1})^{0.45}]\cdot 10^{-6}(pF/\mu m), \tag{45}$$

$$A_2 = 9.92\tanh[0.52(\frac{h}{W_1})^{0.5}]\cdot 10^{-6}(pF/\mu m), \tag{46}$$

where Z_0 and β represent the characteristic impedance and the propagation constant of the microstrip line, respectively, the geometries of the CRLH unit cell can be obtained, as shown in Table 3. For comparison, the two-step retrieval method is implemented to obtain the equivalent circuit of the CRLH TL unit cell, as shown in Fig. 16. Figure 17 shows the comparison between *S* parameter of the designed CRLH unit cell obtained by the full-wave simulations and that of the equivalent circuit extracted by the two-step retrieval method, in a good agreement with each other.

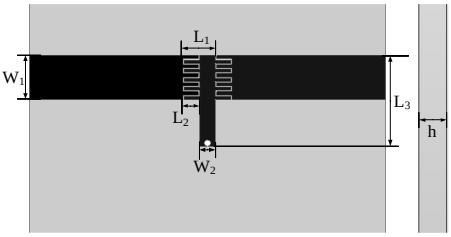

Fig. 15. Topology structure of the designed CRLH TL unit cell.

Table 3: Parameters of the DCRLH TL Unit Cell

Parameters	mm
L_1	1.05
L_2	0.55
L_3	3.00
W_1	1.45
W_2	0.50
H	1.00

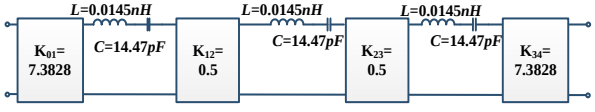

Fig. 16. Couple resonator cavity filter circuit of the designed CRLH TL unit cell.

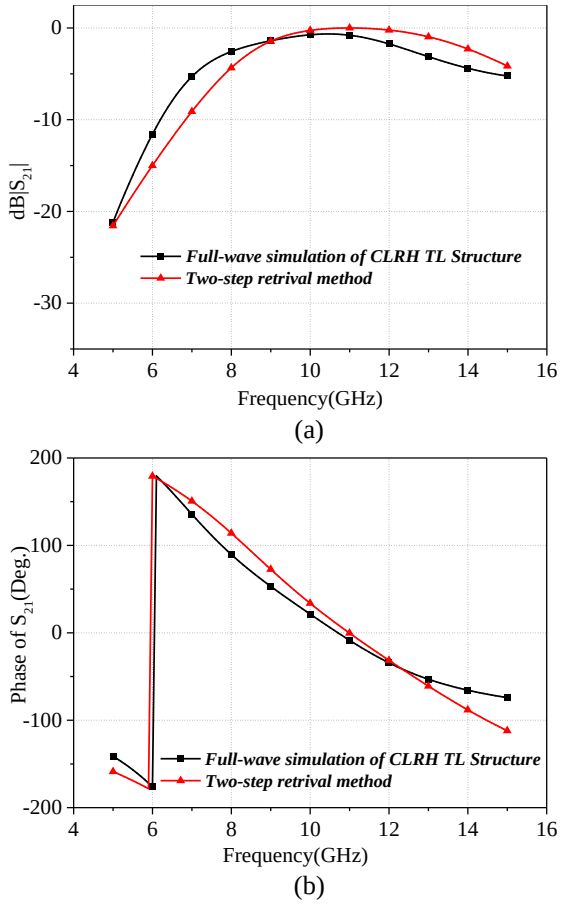

Fig. 17. *S*-parameter comparison of the designed CRLH TL unit cell and the coupled resonator cavity filter: (a) magnitude of S_{21} and (b) phase of S_{21}.

VI. CONCLUSION

The two-step retrieval method to extract the equivalent circuits of the CRLH TL and DCRLH TL unit cells is proposed. The new extraction procedure combines the pseudo-inverse technique and the filter synthesis method based on the coupled resonator cavity filter, of which the electromagnetic responses can be equivalent to the bandpass of the CRLH TL unit cell and bandstop of the DCRLH TL unit cell. The equivalent circuit obtained by the two-step retrieval method can better match the magnitude and phase of *S* parameters from the original CRLH and DCRLH TL unit cells. Based on the equivalent circuit models, the topological structure and parameters of CRLH/DCRLH TL can be effectively synthesized for a given center frequency and bandwidth. The proposed method makes the analysis and synthesis of the metamaterial-based CRLH TL structures more accurate and efficient.

ACKNOWLEDGMENT

This work is partly supported by National Natural Science Foundation of China under Contract No. 51477126, and partly supported by Natural Science Basic Research Plan in Shaanxi Province of China (No. 2013JZ019), Technology Innovation Research Project of the CETC, and Fundamental Research Funds for the Central Universities (K5051202051, SPSZ021409, and SPSZ031410).

REFERENCES

[1] C. Caloz and T. Itoh, *Electromagnetic Metamaterials: Transmission Line Theory and Microwave Applications*. New Jersey: Wiley and IEEE Press, 2005.

[2] A. Lai, T. Itoh, and C. Caloz, "Composite right/left-handed transmission line metamaterial," *IEEE Microwave Magazine*, vol. 5, pp. 34-50, 2004.

[3] A. Sanada, C. Caloz, and T. Itoh, "Characteristics of the composite right/left-handed transmission lines," *IEEE Microwave Wireless Compon. Lett.*, vol. 14, pp. 68-70, 2004.

[4] C. Caloz and H. V. Nguyen, "Novel broadband conventional and dual composite right/left-handed (C/D-CRLH) metamaterials: properties, implementation and double-band coupler application," *Applied Physics A*, vol. 87, pp. 309-316, 2007.

[5] C. Caloz, "Dual composite right/left-handed (D-CRLH) transmission line metamaterial," *IEEE Microwave Wireless Compon. Lett.*, vol. 16, no. 11, pp. 585-587, 2006.

[6] X. Q. Lin, R. P. Liu, X. M. Yang, J. X. Chen, X. X. Yin, Q. Cheng, and T. J. Cui, "Arbitrarily dual-band components using simplified structures of conventional CRLH TLs," *IEEE Trans. Microwave Theory Techn.*, vol. 54, no. 7, pp. 2902-2909, 2006.

[7] L. Qiang, Y. J. Zhao, W. Zhao, Q. Sun, and B. Liu, "Extended dual composite right/left-handed transmission line," *Microw. Opt. Technol. Lett.*, vol. 52, no. 12, pp. 2838-2840, 2010.

[8] S. C. Chiu, L. Y. O. Yang, C. P. Lai, and S. Y. Chen, "Compact CRLH asymmetric-CPS resonant antenna with frequency agility," *IEEE Trans. Antenna Propagation*, vol. 62, pp. 527-534, 2014.

[9] S. C. Chiu, C. P. Lai, and S. Y. Chen, "Compact CRLH CPW antennas using novel termination circuits for dual-band operation at zeroth-order series and shunt resonances," *IEEE Trans. Antenna Propagation*, vol. 61, pp. 1071-1080, 2013.

[10] C. J. Lee, K. M. K. H. Leong, and T. Itoh, "Composite right/left-handed transmission line based compact resonant antennas for RF module integration," *IEEE Trans. Antenna Propagation*, vol. 54, pp. 2283-2291, 2006.

[11] Y. J. Chi and F. C. Chen, "CRLH leaky wave antenna based on ACPS technology with 180° horizontal plane scanning capability," *IEEE Trans.*

Antenna Propagation, vol. 61, pp. 571-577, 2013.

[12] A. A. Ibrahim and A. M. E. Safwat, "Microstrip-fed monopole antennas loaded with CRLH unit cells," *IEEE Trans. Antennas Propagation*, vol. 60, pp. 4027-4036, 2012.

[13] C. Y. Liu, Q. X. Chu, and J. Q. Huang, "A planar D-CRLH transmission line structure and its application to leaky-wave antenna," *2010 9th International Symposium on Antennas Propagation and EM Theory (ISAPE)*, pp. 345-348, 2010.

[14] N. Dolatsha, M. Shahabadi, and R. Dehbashi, "Via-free CPW-based composite right/left-handed transmission line and a calibration approach to determine its propagation constant," *J. Electromagn. Waves Appl.*, vol. 22, pp. 1599-1606, 2008.

[15] J. S. Hong and M. J. Lancaster, *Microstrip Filters for RF/Microwave Applications*. New York: John Wiley & Sons, 2001.

[16] R. K. Gulati, "*Equivalent Circuit Modeling of Transmission Line Metamaterial Unit Cells*," Master thesis, University of New South Wales, 2013.

[17] D. M. Pozar, *Microwave Engineering*. 3rd Edition, New York: John Wiley & Sons, 2004.

[18] N. Kou, Y. Shi, and L. Li, "An improved equivalent circuit model for C/D CRLH TL metamaterials," *International Microwave Workshop Series on Advanced Materials and Processes for RF and THz Applications*, Suzhou, China, July 1-3, 2015.

[19] S. Koziel, Q. S. Cheng, and J. W. Bandler, "Space mapping," *IEEE Microwave Magazine*, pp. 105-122, 2008.

[20] C. Caloz, A. Sanada, and T. Itoh, "A novel composite right/left-handed coupled-line directional coupler with arbitrary coupling level and broad bandwidth," *IEEE Trans. Microwave Theory Tech.*, vol. 52, pp. 980-992, 2004.

[21] C. M. Wu and T. Itoh, "A re-radiating CRLH-transmission line leaky wave antenna using distributed amplifiers," *2009 Asia Pacific Microwave Conference*, pp. 1998-2001, 2009.

[22] C. Caloz and T. Itoh, "Novel microwave devices and structures based on the transmission line approach of meta-materials," *IEEE MTT-S International Microwave Symposium*, vol. 1, pp. 195-198, 2003.

Derivation of the Resonant Frequency of Rectangular Dielectric Resonator Antenna by the Perturbation Theory

Saeed Fakhte and Homayoon Oraizi

Department of Electrical Engineering and Center of Excellence in Railway Transportation
Iran University of Science and Technology, Tehran, 16846-13114, Iran
saeedfakhte@elec.iust.ac.ir, h_oraizi@iust.ac.ir

Abstract ─ Based on the concept of perturbation theory, a modification to the dielectric waveguide model (DWM) is presented for the calculation of resonant frequency of rectangular dielectric resonator antenna (DRA). A large number of simulations are performed using commercial software and the results are compared between those of the DWM and the proposed method. Finally, the accuracy of proposed method is validated by the experimental data available in the literature. Differences between the measured and theoretical resonant frequencies vary by less than 2%.

Index Terms ─ Dielectric waveguide model, dielectric resonator antenna, perturbation theory, Q-factor, resonant frequency.

I. INTRODUCTION

Recently, dielectric resonator antennas (DRA) have received much attention owing to their numerous attractive characteristics, such as light weight, low profile and high radiation efficiency [1-6]. Rectangular shape is the most versatile due to its fabrication simplicity and improved degree of freedom compared to other shapes such as cylindrical or hemispherical shapes.

For the calculation of resonant frequencies and Q-factors of dielectric resonators, several methods have been reported. These methods include the closed cavity method with perfect magnetic conductor (PMC) walls [7], the dielectric waveguide model (DWM) [7], and the surface integral equation incorporated with the method of moments [8,9]. The perturbation correction to the DWM for characterizing the $TE^{z}_{01\delta}$ mode of cylindrical dielectric resonators has been reported [7]. This idea is used to improve the accuracy of DWM for estimating the resonant frequency of the rectangular DRA.

Various comparisons amongst the measured resonant frequencies and Q-factors of rectangular DRAs to those predicted using the dielectric waveguide model (DWM) have been carried out [10-12,14].

In this paper, the perturbation theory is applied to improve the accuracy of determination of the rectangular DRA resonant frequency using DWM. In fact, parts of stored electric and magnetic energies exist outside the DRA volume, which are neglected in the first-order DWM.

There are some differences between [7] and the proposed work. First, in [7] a cylindrical DRA is investigated whereas here a rectangular DRA is assumed. Second is that, in [7] a mode with non-broadside radiation pattern is studied and here a mode with broadside radiation pattern is examined. Observe that the Marcatili and EDC methods have already been used to improve the accuracy of DWM by using the electromagnetic fields outside the rectangular DRA [17]. However, the proposed method leads to more accurate results. The proposed perturbation method also provides an improvement for the calculation of Q-factor of rectangular DRAs. It is verified by comparison with the simulation and experimental data available in the literature.

II. THEORY

A rectangular dielectric resonator antenna (RDRA), whose dimensions are a×b×d/2 is located on a large ground plane (Fig. 1). The DRA has a relative dielectric constant of ε_r. By applying the image theory, the ground plane is removed and the procedure results in an isolated RDRA having dimensions $a \times b \times d$. The field components of TE^{y}_{111} mode inside the resonator have already been derived [18, Eq. (4)]. The resonance frequency f_o is obtained from the following transcendental equation [10]:

$$k_y \tan(\frac{k_y b}{2}) = \sqrt{(\varepsilon_r - 1)k_0^2 - k_y^2},$$
$$k_x^2 + k_y^2 + k_z^2 = \varepsilon_r k_0^2, \quad (1)$$
$$k_x = \frac{\pi}{a}, k_z = \frac{\pi}{d},$$

where k_0 is the free space wave number at resonance frequency f_0 and other parameters are shown in Fig. 1.

Figure 2 shows a dielectric waveguide having a rectangular cross section of width a in the x-direction, height d in the z-direction with waves propagating in the y-direction. To model DRA, the waveguide is truncated

Submitted On: January 3, 2016
Accepted On: May 21, 2016

along the y-direction at ±b/2.

To improve the model, the same electric and magnetic fields inside DRA (as for the first order DWM) are retained and the PMC walls are removed. The tangential electric fields at the resonator surfaces in the x- and z-directions are continuous. They exponentially decrease outside DRA in free space. Also, the fields in the dashed regions in Fig. 2 are assumed to be zero. The extended DRA model consists of five regions, as shown in Fig. 2.

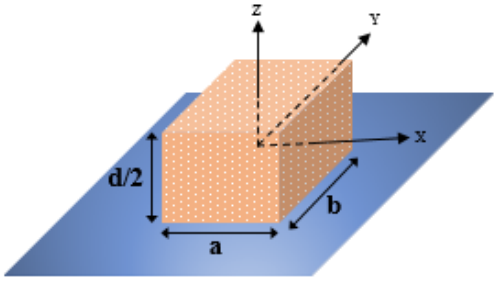

Fig. 1. 3D view of the isolated DR antenna configuration.

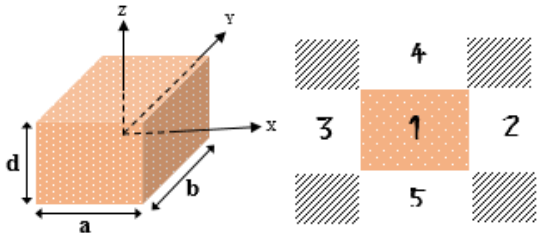

(a) (b)

Fig. 2. (a) 3D view of the truncated dielectric waveguide model, and (b) cross-sectional view.

The fields outside the dielectric resonator must be of evanescent form. Therefore, the potential function of TE^{y}_{111} mode for $|x| > a/2$ takes the following form:

$$\psi_2^y = B\cos(\mathrm{k}_y y)\cos(\mathrm{k}_z z)\,\mathrm{e}^{-\alpha_2|x|}. \quad (2)$$

Then,

$$E_{x2,3} = -Bk_z\cos(\mathrm{k}_y y)\sin(\mathrm{k}_z z)\,\mathrm{e}^{-\alpha_2|x|}, \quad (3.a)$$

$$E_{y2,3} = 0, \quad (3.b)$$

$$E_{z2,3} = \pm B\alpha_2\cos(\mathrm{k}_y y)\cos(\mathrm{k}_z z)\,\mathrm{e}^{-\alpha_2|x|}, \quad (3.c)$$

$$H_{x2,3} = \frac{\pm B\alpha_2}{j\omega\mu_0}k_y\sin(\mathrm{k}_y y)\cos(\mathrm{k}_z z)\,\mathrm{e}^{-\alpha_2|x|}, \quad (3.d)$$

$$H_{y2,3} = \frac{B(\mathrm{k}_0^2-\mathrm{k}_y^2)}{j\omega\mu_0}\cos(\mathrm{k}_y y)\cos(\mathrm{k}_z z)\,\mathrm{e}^{-\alpha_2|x|}, \quad (3.e)$$

$$H_{z2,3} = \frac{Bk_yk_z}{j\omega\mu_0}\sin(\mathrm{k}_y y)\sin(\mathrm{k}_z z)\,\mathrm{e}^{-\alpha_2|x|}, \quad (3.f)$$

where

$$\alpha_2 = \sqrt{(\varepsilon_r - 1)\mathrm{k}_0^2 - k_x^2}. \quad (4)$$

Also, for $|z| > d/2$ let,

$$\psi_4^y = C\cos(\mathrm{k}_x x)\cos(\mathrm{k}_y y)\,\mathrm{e}^{-\alpha_4|z|}. \quad (5)$$

Then,

$$E_{x4,5} = \mp C\alpha_3\cos(\mathrm{k}_x x)\cos(\mathrm{k}_y y)\,\mathrm{e}^{-\alpha_4|z|}, \quad (6.a)$$

$$E_{y4,5} = 0, \quad (6.b)$$

$$E_{z4,5} = Ck_x\sin(\mathrm{k}_x x)\cos(\mathrm{k}_y y)\,\mathrm{e}^{-\alpha_4|z|}, \quad (6.c)$$

$$H_{x4,5} = \frac{Ck_xk_y}{j\omega\mu_0}\sin(\mathrm{k}_x x)\sin(\mathrm{k}_y y)\,\mathrm{e}^{-\alpha_4|z|}, \quad (6.d)$$

$$H_{y4,5} = \frac{C(\mathrm{k}_0^2-\mathrm{k}_y^2)}{j\omega\mu_0}\cos(\mathrm{k}_x x)\cos(\mathrm{k}_y y)\,\mathrm{e}^{-\alpha_4|z|}, \quad (6.e)$$

$$H_{z4,5} = \frac{\pm Ck_y\alpha_3}{j\omega\mu_0}\cos(\mathrm{k}_x x)\sin(\mathrm{k}_y y)\,\mathrm{e}^{-\alpha_4|z|}, \quad (6.f)$$

where

$$\alpha_4 = \sqrt{(\varepsilon_r - 1)\mathrm{k}_0^2 - k_z^2}. \quad (7)$$

In [18, Eq. (4)], the tangential components of the magnetic field are functions of $\cos(k_x x)$ and $\cos(k_z z)$, that vanish at x=±a/2 and z=±d/2 in agreement with the location of the PMC walls. On the other hand, the calculated H fields in the exterior regions consist of three components as H_x, H_y and H_z shown in Equations (3) and (6). The comparison of these components with those of [18, Eq. (4)], indicates that the tangential components of magnetic field are not continuous, whereas the transverse components are continuous. As an approximation, the tangential (XZ and YZ planes) components of magnetic field and transverse (XZ plane) components of electric fields in the exterior region are set equal to zero [7]. Also, as another approximation, it is assumed that the regions outside of the DR (regions 2, 3, 4 and 5) are bounded by PMC walls. The reason for this is that the energies in $(|y| > b/2, |x| > a/2)$ and $(|y| > b/2, |z| > d/2)$ regions are not considered in calculations. So, in $(|y| < b/2, |x| > a/2)$ and $(|y| < b/2, |z| > d/2)$ regions, y=±b/2 walls are considered as PMC walls. First, for calculation of the stored energies outside of the DRA, it is assumed that $k_y = n\pi/b$. Then, in the final formula the value of k_y which is obtained by DWM method was used. For an outward perturbation at a place of large electric field in a cavity, the resonant frequency increases [13].

The fields inside and outside the unperturbed DR cavity at the resonant frequency f_o are denoted by (E_{in}, H_{in}) and (E_{out}, H_{out}), respectively. Then,

$$\frac{f - f_0}{f_0} \approx \frac{\int_{\Delta v}(\mu|H_{out}|^2 - \varepsilon|E_{out}|^2)\,\mathrm{dv}}{\int_{v_0}(\mu|H_{in}|^2 + \varepsilon|E_{in}|^2)\,\mathrm{dv}}. \quad (8)$$

Equation (8) can be written in terms of stored energies as follows:

$$\frac{f-f_0}{f_0}=\frac{\Delta W_m-\Delta W_e}{W_m+W_e}, \tag{9}$$

where ΔW_m and ΔW_e are the changes in the stored magnetic energy and electric energy, respectively, due to the shape perturbation, and W_e+W_m is the total stored energy in the DRA. In Equation (9), the numerator represents the difference of the stored magnetic and electric energies in regions 2, 3, 4 and 5, whereas the denominator represents the sum of both energies in region 1.

The integrals for the stored energies in separate regions can be calculated analytically:

$$\Delta W_m-\Delta W_e=\frac{\varepsilon_0 b(k_y^2-k_0^2)}{16k_0^2}A^2\left[\frac{k_x^2 d}{\alpha_2}+\frac{k_z^2 a}{\alpha_4}\right], \tag{10}$$

$$W_e+W_m=\frac{\varepsilon_0\varepsilon_r abdA^2}{16}\left(1+\frac{\sin(k_y b)}{k_y b}\right)(k_x^2+k_z^2). \tag{11}$$

Substituting Equations (10) and (11) into Equation (9), we get:

$$f_{pert}=f_o+df, \tag{12}$$

where

$$df=f_o\frac{\left(\frac{k_y}{k_0}\right)^2-1}{\varepsilon_r ad}\cdot\frac{1}{1+\frac{\sin(k_y b)}{k_y b}}\times\frac{\frac{k_x^2 d}{\sqrt{(\varepsilon_r-1)k_0^2-k_x^2}}+\frac{k_z^2 a}{\sqrt{(\varepsilon_r-1)k_0^2-k_z^2}}}{k_x^2+k_z^2}. \tag{13}$$

Hence, by adding *df* to the resonant frequency calculated by DWM, the more accurate result for the resonant frequency of DRA can be obtained. Further, the radiation Q-factor of TE_{111}^y mode is determined in [10]:

$$Q_{rad}=\frac{\varepsilon_r\pi^4}{256(\varepsilon_r-1)^2k_0^5 abd}\times\frac{1+\sin c(k_y b)}{\sin c^2(k_y b/2)}.(k_x^2+k_z^2). \tag{14}$$

The Q-factor accuracy can be improved by substituting the corrected theoretical value of resonant frequency, f_{pert}, in Equation (14) and is labeled Q_{pert}^{rad}.

III. RESULTS AND DISCUSSION

To examine the accuracy of the proposed method in predicting the resonant frequency and Q factor of an isolated rectangular DRA, the calculated resonant frequencies were compared with the experimentally measured results in the literature, as well as with those computed from the eigenmode solver of ANSOFT HFSS 13. The eigenmode solver gives resonant frequency and field distribution of all the modes, which can be excited in DRA. Note that, in this solver the feed network is completely ignored. So, the results of the other simulation softwares, which consider the effects of the feed network (namely CST and HFSS driven modal), are slightly different from the eigenmode solvers. So, since the dielectric waveguide model (DWM) does not consider the effects of the feed network, the theoretical results should be compared with the eigenmode solvers.

Note that, the results of DRA excited by microstrip line and probe are affected by the presence of the feed and differ from the measured results of the isolated DRA. In Table 1, the theoretical and simulated results of resonant frequencies for TE_{111}^y mode of a DRA having dimensions b/a=0.5, d/a=0.9, and design resonant frequency f_o=5 GHz are presented, where the values of b/a, d/a, and resonant frequency are constant but the dielectric constant of the DRA varies.

The errors of the proposed modified model and the dielectric waveguide model (DWM) from the simulated resonant frequencies are denoted by:

$$\Delta f_{pert}=\frac{f_{pert}-f_{HFSS}}{f_{HFSS}}, \tag{15}$$

$$\Delta f_{DWM}=\frac{f_{DWM}-f_{HFSS}}{f_{HFSS}}, \tag{16}$$

$$\Delta f_{EDC}=\frac{f_{EDC}-f_{HFSS}}{f_{HFSS}}, \tag{17}$$

$$\Delta f_{Marc}=\frac{f_{Marc}-f_{HFSS}}{f_{HFSS}}, \tag{18}$$

where f_{HFSS} is the resonant frequency calculated by the Eigenmode solver of Ansoft HFSS, f_{DWM} is the resonant frequency calculated by DWM, f_{EDC} is the resonant frequency calculated by the EDC method, f_{Marc} is the resonant frequency calculated by the Marcatili method and f_{pert} is the resonant frequency calculated by the perturbation method. Observe that, the resonant frequencies calculated by DWM are lower than the simulated values by about 2% to 6.5%. The perturbational correction to DWM by the modified theoretical results are applied for the examples of Table 1. Observe that, the resonant frequencies calculated by the proposed model are more accurate than those of DWM, EDC and Marcatili. Also, the percentage difference between the calculated and simulated results of resonant frequencies and Q factors for both the DWM and the perturbation method are plotted in Fig. 3 (a) and defined as:

$$|\Delta f|=\frac{f_{calculated}-f_{simulation}}{f_{simulation}}, \tag{19}$$

$$|\Delta Q| = \frac{Q_{rad}^{calculated} - Q_{rad}^{HFSS}}{Q_{rad}^{HFSS}}. \quad (20)$$

Note that, the term "calculated" is referred to DWM and perturbation methods. The values of $|\Delta f|$ and $|\Delta Q|$ of TE_{111}^{y} mode of an isolated rectangular DRA are plotted versus b/a in Fig. 3 (a) for ε_r=90, d/a=0.6, and f_o=2.4 GHz and versus d/a in Fig. 3 (b) for ε_r=90, b/a=0.6, and f_o=2.4 GHz. The values plotted in Figs. 3 (b) and (c) have been computed for arbitrary but a high value of dielectric constant, ε_r=90. Observe in Fig. 3 (b) that, as the value of the geometrical parameter b/a grows the differences between the results of DWM and simulations tend to be lower. $|\Delta f|$ for the perturbation method is always lower than that of DWM, but the $|\Delta Q|$ for DWM is more accurate for high values of b/a. Also, observe in Fig. 3 (b) that, for d/a>0.3 the results computed from the perturbation method are closer to the simulated results than those calculated by DWM.

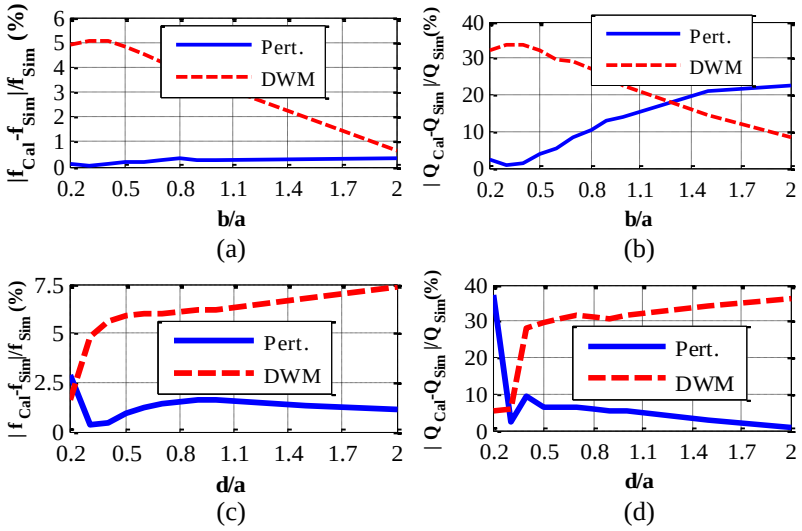

Fig. 3. The percentage difference between calculated and simulated resonant frequencies and Q factor versus: (a) aspect ratio, b/a, for ε_r=90, d/a=0.6, and f_0=2.4 GHz; (b) aspect ratio, d/a, for ε_r=90, b/a=0.6, and f_0=2.4 GHz.

Table 1: Theoretical and simulated resonant frequencies of TE_{111}^{y} mode of an isolated rectangular DRA. (b/a=0.5, d/a=0.9, f_{DWM}=5 GHz), frequency unit: GHz

ε_r	a (mm)	f_{DWM}	f_{HFSS}	f_{pert}	$f_{Marcatili}$	f_{EDC}	Δf_{DWM}	Δf_{pert}	$\Delta f_{Marcatili}$	Δf_{EDC}
10	17.75	5	5.102	5.2	4.82	4.71	-2%	1.9%	-5.53%	-7.68%
20	12.62	5	5.205	5.234	4.92	4.87	-3.9%	0.6%	-5.48%	-6.44%
30	10.33	5	5.255	5.245	4.95	4.91	-4.8%	-0.2%	-5.80%	-6.57%
40	8.95	5	5.28	5.25	4.96	4.93	-5.3%	-0.6%	-6.06%	-6.63%
50	8.01	5	5.301	5.253	4.97	4.95	-5.7%	-0.9%	-6.24%	-6.62%
60	7.31	5	5.317	5.255	4.97	4.96	-6%	-1.2%	-6.53%	-6.71%
70	6.77	5	5.325	5.257	4.98	4.96	-6.1%	-1.3%	-6.48%	-6.85%
80	6.34	5	5.334	5.258	4.98	4.97	-6.3%	-1.4%	-6.64%	-6.82%
90	5.98	5	5.338	5.259	4.98	4.97	-6.3%	-1.5%	-6.71%	-6.89%
100	5.67	5	5.346	5.259	4.98	4.97	-6.5%	-1.6%	-6.85%	-7.03%

These discrepancies between the results of DWM and simulation are due to the neglected stored energies outside the DRA volume. Figures 4 (a) and (b) show the ratio of the total stored energy outside (in regions 2-5) and inside the DRA, $(W_e + W_m)_{out}/(W_e + W_m)_{in}$, versus the geometrical parameters b/a, d/a, and ε_r, respectively.

Observing the stored energies ratio as a function of b/a, we conclude that increasing b/a decreases the exterior stored energies in an appreciable way. Thus, the improvement of the accuracy of DWM for higher values of b/a (Fig. 3 (a)) is logical. When the parameter d/a is increased this energy ratio starts increasing (Fig. 4 (b)). Observe in Fig. 3 (b) that the error increase of DWM is expected.

Some experimental results for the resonant frequencies and Q factors of an isolated rectangular DRA are available [10,14, and 15]. To reveal the superiority of the proposed model over the first-order DWM, the errors

of these two models from measurement are considered in another example. In Table 2, the theoretical resonant frequencies and Q-factors calculated by the perturbation theory, DWM, EDC and Marcatili are compared with measured results. Observe that the corrected values of the resonant frequency and radiation Q-factor are much closer to the reported measured data. Differences between the measured and theoretical resonant frequencies vary between 0.47% to 1.94%. Also, the theoretical Q-factor may differ from the measured values from 2.74% to 8.82%.

The theoretical studies for arbitrary shaped antennas were focused on the bounds on the Q-factor of them. So, as our best knowledge, there is not any accurate closed form formula for determining the Q-factor of an arbitrary shaped dielectric antenna. For example, assuming that the DRA fabricated from a material of dielectric constant ε_r and has a radiation efficiency of 100%, then the Q-factor can be expressed by [19]:

$$Q = \frac{1 + 3(\frac{\pi}{\sqrt{\varepsilon_r}})^2}{(\frac{\pi}{\sqrt{\varepsilon_r}})^3 \left[1 + (\frac{\pi}{\sqrt{\varepsilon_r}})^2\right]}. \quad (21)$$

The calculated results by this formula are also listed in Table 2. Observe that, there are considerable difference between these results and those of measurement.

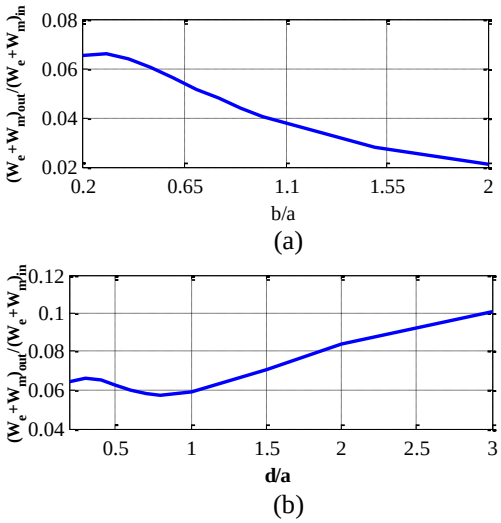

Fig. 4. The ratio of stored electric and magnetic energies in regions 2, 3, 4 and 5 to stored energies inside the DRA versus: (a) aspect ratio, b/a, for ε_r=90, d/a=0.6, and f_0=2.4 GHz; (b) aspect ratio, d/a, for ε_r=90, b/a=0.6, and f_0=2.4 GHz.

Table 2: Comparison of theoretical resonant frequency and radiation Q factor of rectangular DR with experimental results for TE^{y}_{111} mode of DRA. Frequency unit: GHz

Ref.		[10]	[10]	[10]	[15]	[16]	[16]	[16]	[16]
Dimensions	ε_r	79.46	37.84	37.84	37.84	100	100	100	100
	a (mm)	7.45	8.6	8.77	8.6	10	10	12.7	10
	b (mm)	2.98	2.58	3.51	8.6	10	10	12.7	5
	d (mm)	7.45	8.6	8.77	2.58	4	2	2	2
Experiment	f_{exp}	4.673	6.322	5.684	10.28	4.57	7.97	7.72	8.5
	Q_{rad}^{Exp}	95	28.5	31.5	-	-	-	-	-
Perturbation	f_{per}	4.582	6.256	5.619	10.37	4.36	7.93	7.78	8.46
	Q_{rad}^{pert}	99.62	29.28	34.28	20.22	114.36	86.26	67.06	72.4
DWM	f_{DWM}	4.35	5.93	5.34	10.16	4.22	7.76	7.67	8.02
	Q_{DWM}^{rad}	128.9	37.98	44.07	17.14	105.3	37.28	24.57	60.6
Marcatili	f_{Marc}	4.33	5.9	5.30	9.75	4.18	7.58	7.43	7.9
EDC	f_{EDC}	4.31	5.84	5.26	9.75	4.17	7.58	7.43	7.9
Simulation	f_{sim}	4.647	6.28	5.65	10.14	4.38	7.83	7.65	8.42
Q_Bound	Q_{rad}^{Bound}	27.9	10.61	10.61	10.61	38.05	38.05	38.05	38.05
Error (%)	Δf_{DWM}	-7	-6.1	-6.1	-1.17	-7.7	-2.63	-0.65	-5.65
	ΔQ_{rad}^{DWM}	35.47	32.98	39.68	-	-	-	-	-
	Δf_{pert}	-1.94	-1.04	-1.14	0.88	-4.6	-0.5	0.78	-0.47
	ΔQ_{rad}^{pert}	4.86	2.74	8.82	-	-	-	-	-
	Δf_{Marc}	-7.34	-6.68	-6.76	-5.16	-8.54	-4.89	-3.76	-7.06
	Δf_{EDC}	-7.77	-7.62	-7.46	-5.16	-8.75	-4.89	-3.76	-7.06
	Δf_{sim}	-0.56	-0.67	-0.60	-1.37	-4.24	-1.77	-0.91	-0.95

To inspect the accuracy of the perturbation method in calculating the resonant frequency of a rectangular DRA compared to other methods, the calculated resonant frequencies were compared with the measured results, as well as those computed by the methods mentioned in the [17]. In this paper, a more comprehensive DWM method

reported that does not neglect fields outside of DRA. In Tables 3 and 4, the theoretical resonant frequencies of the samples calculated by the Marcatili method, EDC method [17], and proposed method and measured results are presented.

Note that, in [17] it has been mentioned that the TE^{x}_{mnl} mode of the structure is equivalent to the $TE^{x}_{m,2n-1,l}$ mode of an isolated resonator of height $2b$. Observe that, the resonant frequencies of fundamental modes calculated by the proposed method are generally more accurate than those of the Marcatili and EDC methods, but the results of EDC and Marcatili methods for higher order modes are more accurate than those obtained by the proposed method. The results of the eigenmode solver of HFSS are also given in Table 4. Observe that, there is some difference between the results of simulation and measurement. This could be due to the effects of the feeding structure used in the experimental setup. However, the maximum error of the perturbation method is less than 6.5%. Comparison with the simulation results shows that the maximum error is even lower. Note that, the Marcatili and EDC methods [17] are taken into account the fields outside the DRA.

Table 3: Comparison of theoretical resonant frequency and radiation Q factor of rectangular DR with experimental results and the results of the [17]. a=d=6 mm, ε_r=37.1

Mode	b (mm)	Resonant Frequencies (GHz)						Difference with Experiment, %				
		DWM	Marcatili	EDC	Proposed	Sim.	Exp.	DWM	Marcatili	EDC	Proposed	Sim.
TE^{y}_{111}	4	6.96	6.89	6.86	7.27	7.32	7.27	-4.36	-5.2	-5.6	0	0.69
$TE^{x}_{111}, TE^{z}_{111}$	4	8	7.89	7.86	8.25	8.27	8.20	-2.47	-3.8	-4.1	0.61	0.85
TE^{y}_{111}	3	7.43	7.34	7.33	7.8	7.85	7.91	-6.26	-7.2	-7.3	-1.39	-0.76
$TE^{x}_{111}, TE^{z}_{111}$	3	9.72	9.52	9.46	10.01	9.95	9.97	-2.54	-4.5	-5.1	0.4	-0.20

Table 4: Comparison of theoretical resonant frequency of rectangular DR with experimental results and the results of the [17] for higher order modes. a=d=6 mm, ε_r=37.1

Mode	Dimension (mm)			Resonant Frequency (GHz)						Error (%)				
	a	2b	d	DWM	Prop.	Sim.	EDC	Marc.	Exp.	Δf_{DWM}	Δf_{pert}	Δf_{Sim}	Δf_{EDC}	$\Delta f_{Marc.}$
TE^{x}_{131}	*12*	*20*	*8*	8.66	8.69	8.44	8.41	8.45	8.30	4.24	4.59	1.67	1.32	1.79
TE^{x}_{131}	*8*	*24*	*10*	7.62	7.74	7.54	7.41	7.46	7.29	4.43	5.99	3.37	1.63	2.31
TE^{x}_{132}	*8*	*20*	*12*	10.21	10.28	10.03	9.99	10.02	9.7	5.12	5.81	3.35	2.95	3.25
TE^{x}_{132}	*12*	*20*	*8*	12.62	12.57	12.18	12.17	12.22	12.01	4.95	4.56	1.41	1.32	1.73
TE^{x}_{132}	*10*	*24*	*8*	12.25	12.25	11.85	11.68	11.80	11.62	5.28	5.28	1.96	0.51	1.54
TE^{x}_{132}	*12*	*16*	*10*	11.90	11.88	11.54	11.53	11.66	11.25	5.62	5.45	2.54	2.46	3.58
TE^{x}_{231}	*8*	*20*	*12*	10.52	11.08	10.84	10.31	10.43	10.40	1.15	6.33	4.14	-0.87	0.29
TE^{x}_{231}	*8*	*24*	*10*	10.11	10.74	10.52	9.91	10.02	10.25	-1.38	4.67	2.60	-3.37	-2.27
TE^{x}_{231}	*12*	*16*	*10*	10.6	10.96	10.70	10.28	10.43	10.40	1.9	5.24	2.84	-1.16	0.29

IV. CONCLUSION

In this paper the perturbation theory is applied to the dielectric waveguide model which is utilized for determining the resonant frequency and radiation Q factor of rectangular dielectric resonator antennas. The results obtained by this method are much closer to the simulated and measured ones compared to other reported methods.

REFERENCES

[1] S. Fakhte, H. Oraizi, and M. H. Vadjed-Samiei, "A high gain dielectric resonator loaded patch antenna," *Progress In Electromagnetics Research C*, vol. 30, pp. 147-158, 2012.

[2] S. Fakhte, H. Oraizi, R. Karimian, and R. Fakhte, "A new wideband circularly polarized stair-shaped dielectric resonator antenna," *IEEE Trans. Antennas Propag.*, vol. 63, no. 4, pp. 1828-1832, Apr. 2015.

[3] S. Fakhte, H. Oraizi, and R. Karimian, "A novel low cost circularly polarized rotated stacked dielectric resonator antenna," *IEEE Antennas and Wireless Propag. Lett.*, vol. 13, pp. 722-725, Apr. 2014.

[4] K. W. Leung, E. H. Lim, and X. S. Fang, "Dielectric resonator antennas: From the basic to the aesthetic," *Proc. IEEE*, vol. 100, no. 7, pp. 2181-2193, July 2012.

[5] A. Petosa and A. Ittipiboon, "Dielectric resonator antennas: A historical review and the current state of the art," *IEEE Antennas and Propagation Magazine*, vol. 52, no. 5, pp. 91-116, Oct. 2010.

[6] Q. Lai, G. Almpanis, C. Fumeaux, H. Benedickter, and R. Vahldieck, "Comparison of the radiation efficiency for the dielectric resonator antenna and the microstrip antenna at Ka band," *IEEE Trans. Antennas and Propag.*, vol. 56, no. 11, pp. 3589-

3592, 2008.
[7] D. Kajfez and P. Guillon, Eds., *Dielectric Resonators*. Artech House, Norwood, MA, 1986.
[8] A. W. Glisson, D. Kajfez, and J. James, "Evaluation of modes in dielectric resonators using a surface integral equation formulation," *IEEE Trans. Microwave Theory Tech*., vol. 31, pp. 1023-1029, 1983.
[9] A. A. Kishk, M. R. Zunoubi, and D. Kajfez, "A numerical study of a dielectric disk antenna above grounded dielectric substrate," *IEEE Trans. Antennas Propagat*., vol. 41, pp. 813-821, 1993.
[10] R. K. Mongia and A. Ittipiboon, "Theoretical and experimental investigations on rectangular dielectric resonator antennas," *IEEE Trans. Antennas Propag.*, vol. 45, no. 9, pp. 1348-1356, Sept. 1997.
[11] C. Trueman, et al., "Computation and measurement of the resonant frequencies and Q-factors of high permittivity dielectric resonators," *Symposium on Antenna Technology and Applied Electromagnetics ANTEM 94 Digest*, Ottawa, Canada, pp. 395-402, Aug. 1994.
[12] Y. M. M. Antar, D. Cheng, G. Seguin, B. Henry, and M. G. Keller, "Modified waveguide model (MWGM) for rectangular dielectric resonator antenna (DRA)," *Microwave and Optical Technology Letters*, vol. 19, no. 2, pp. 158-160, Oct. 1998.
[13] J. A. Kong, *Electromagnetic Wave Theory*. Wiley Interscience, 1990.
[14] C. W. Trueman, S. R. Mishra, C. L. Larose, and R. K. Mongia, "Resonant frequencies and Q factors of dielectric parallelepipeds," *IEEE Transactions Instrumentation and Measurement*, vol. 44, pp. 322-325, 1995.
[15] R. K. Mongia, A. Ittibipoon, and M. Cuhaci, "Low profile dielectric resonator antennas using a very high permittivity material," *Electron. Lett*., vol. 30, no. 17, pp. 1362-1363, 1994.
[16] Y. Liu, H. Liu, M. Wei, and S. Gong, "A low-profile and high-permittivity dielectric resonator antenna with enhanced bandwidth," *IEEE Antennas and Wireless Propag. Lett*., vol. 14, pp. 791-794, Mar. 2015.
[17] R. K. Mongia, "Theoretical and experimental resonant frequencies of rectangular dielectric resonators," *IEE Proc.-H*, vol. 139, pp. 98-104, 1992.
[18] S. Maity and B. Gupta, "Closed form expressions to find radiation patterns of rectangular dielectric resonator antennas for various modes," *IEEE Trans. Antenna and Propag*., vol. 62, no. 12, pp. 6524-6527, Oct. 2014.
[19] A. Petosa, *Dielectric Resonator Antenna Handbook*. Norwood, MA, Artech House, 2007.

Saeed Fakhte was born in Amlash, Iran, in 1987. He received the B.Sc. degree from the Sharif University of Technology, Tehran, Iran, in 2009, the M.Sc. degree from the Iran University of Science and Technology (IUST), Tehran, Iran, in 2012, and is currently working toward the Ph.D. degree in Electrical Engineering at IUST. Currently, he is a Visiting Scholar at the Politecnico di Torino, Torino, Italy. His research interests are in various areas of electrical engineering, such as dielectric resonator antenna design, metamaterials and the application of numerical methods in electromagnetics and antennas.

Homayoon Oraizi received the B.E.E. degree from the American University of Beirut, Beirut, Lebanon, in 1967, and the M.Sc. and Ph.D. degrees in Electrical Engineering from Syracuse University, Syracuse, NY, in 1969 and 1973, respectively. From 1973 to 1974, he was a Teacher with the K.N. Tousi University of Technology, Tehran, Iran. From 1974 to 1985, he was with the Communications Division, Iran Electronics Industries, Shiraz, Iran, where he was engaged in various aspects of technology transfer mainly in the field of HF/VHF/UHF communication systems. In 1985, he joined the school of Electrical Engineering, Iran University of Science and Technology, Tehran, Iran, where he is currently an Exemplary Professor of Electrical Engineering. From July 2003 to August 2003, he spent a two-month term as a Fellow of the Japan Society for the Promotion of Science with Tsukuba University, Ibaraki, Japan. From August 2004 to February 2005, he spent a six-month sabbatical leave at Tsukuba University. He has authored or co-authored over 300 papers in international journals and conferences. He has authored and translated several textbooks in Farsi. He was listed in the 1999 Who's Who in the World. His research interests are in the area of numerical methods for antennas, microwave devices, and radio wave propagation. Oraizi is a Fellow of the Electromagnetic Academy.

Analytic Expressions of Some Statistics in Radar Target Recognition Based on Late Time Representation

Joon-Ho Lee [1*], Young-Ik Choi [2], Jung-Min Seo [1], and Byung-Kwon Son [1]

[1] Information & Communication Engineering
Sejong University, 98, Kunja-dong, Kwangjin-ku, Seoul, 143-747 Korea
joonhlee@sejong.ac.kr*, jmseo93@gmail.com, hellosbk@nate.com

[2] EW (Electronic Warfare) R&D Lab
LIG Nex1 Co., Ltd., 333, Pangyo-ro, Bundang-gu, Seongnam-si, Gyeonggi-do, 463-400 Korea
youngik.choi@lignex1.com

Abstract — In this paper, we consider the projection of the late time response of an unknown radar target onto the column space and the left null space of the matrix whose entries are from the natural frequencies of the specific radar target. We get explicit expressions for the projection onto the column space, the projection onto the left null space, the square of projection onto the column space and the square of the projection onto the left null space. Also, we note that the norm of the defined projection onto the column space and the norm of the defined projection onto the left null space are Ricean distributed, and that the square of the norm of the projection onto the column space and the square of the norm of the projection onto the left null space are chi-square distributed. Accordingly, we give analytic expressions of the mean and the variance of the Ricean distribution and those of the chi-square distribution.

Index Terms — Chi-square distribution, late time response, projection onto the column space, projection onto the left null space, radar target recognition, Ricean distribution.

I. INTRODUCTION

There has been much research on the radar target recognition based on the natural frequencies [1-4]. In [3], the authors show the explicit expression for the mean and the variance of the square of the norm of the projection onto the left null space.

In this paper, we present explicit expressions for the defined projection onto the column space, projection onto the left null space, the square of the projection onto the column space and the square of the projection onto the left null space. In addition, we also present the analytic expressions for the mean and the variance of the norm of the defined projection onto the column space and the projection onto the left null space and those of the square of the norm of the projection onto the column space and the square of the norm of the projection onto the left null space.

The difference between this paper and [3] are the following. In [3], we only considered the square of the norm of the projection onto the left null space. In this paper, we considered the square of the norm of the projection onto the column space, the norm of the projection onto the column space and the norm of the projection onto the left null space as well as the square of the norm of the projection onto the left null space. In addition, in deriving the explicit expression of the projection, there is some difference in applying the Cramer's rule between [3] and this paper.

II. THE PROJECTION ONTO THE COLUMN SPACE AND THE PROJECTION ONTO THE LEFT NULL SPACE

It can be easily shown that, from the late time representation based on the natural frequencies, the late time response can be written as [3], $n=1,\cdots,N,$:

$$y_n = \sum_{i=1}^{M} c_i z_i^{\,n} + h_n, \tag{1}$$

where N is the number of the sampled late time response and M is the number of the natural frequencies. $h_n, n=1,\ldots,N,$ is the zero-mean Gaussian noise associated with $y_n, n=1,\ldots,N.$ $z_i, i=1,\ldots,M,$ is the z-plane natural frequencies of the target. In the noiseless case where $h_n, n=1,\ldots,N,$ is equal to zero, (1) reduces to:

$$u_n = \sum_{i=1}^{M} c_i z_i^{\,n}, \tag{2}$$

where $u_n, n=1,\ldots,N,$ is the noiseless late time response.

In matrix form, (1) can be written as:

$$\mathbf{y} = \mathbf{Z}\mathbf{c}, \tag{3}$$

where $\mathbf{Z}, \mathbf{y}$ and $\mathbf{c}$ are defined as:

Submitted On: November 24, 2014
Accepted On: May 1, 2016

$$Z_{mn} = z_n^m, \tag{4}$$

$$\mathbf{y} = \begin{bmatrix} y_1 & y_2 & \cdots & y_N \end{bmatrix}^T, \tag{5}$$

$$\mathbf{c} = \begin{bmatrix} c_1 & c_2 & \cdots & c_M \end{bmatrix}^T. \tag{6}$$

Since N is larger than M, the least squares solution of (3) can be written as

$$\hat{\mathbf{c}} = \left(\mathbf{Z}^H\mathbf{Z}\right)^{-1}\mathbf{Z}^H\mathbf{y}. \tag{7}$$

Using (7) in the right-hand side of (3), we have,

$$\mathbf{Z}\hat{\mathbf{c}} = \mathbf{Z}\left(\mathbf{Z}^H\mathbf{Z}\right)^{-1}\mathbf{Z}^H\mathbf{y}. \tag{8}$$

We note that the projection onto the column space matrix onto the column space of the matrix $\mathbf{Z}$ is defined as:

$$\mathbf{P}_Z \equiv \mathbf{Z}\left(\mathbf{Z}^H\mathbf{Z}\right)^{-1}\mathbf{Z}^H. \tag{9}$$

Using (9) in (8) enables us to write (8) as:

$$\mathbf{Z}\hat{\mathbf{c}} = \mathbf{Z}\left(\mathbf{Z}^H\mathbf{Z}\right)^{-1}\mathbf{Z}^H\mathbf{y} = \mathbf{P}_\mathbf{Z}\mathbf{y}. \tag{10}$$

The projection onto the left null space can be defined by subtracting the projection onto the column space of $\mathbf{y}$ onto the column space of $\mathbf{Z}$ from the noisy late time response $\mathbf{y}$:

$$\mathbf{y} - \mathbf{Z}\hat{\mathbf{c}} = \left(\mathbf{I} - \mathbf{P}_\mathbf{Z}\mathbf{y}\right) = \mathbf{P}_\mathbf{Z}^{\perp}\mathbf{y}, \tag{11}$$

where (9) is used and $\mathbf{P}_\mathbf{Z}^{\perp} \equiv \mathbf{I} - \mathbf{P}_\mathbf{Z}$ is called the projector onto the left null space of $\mathbf{Z}$.

III. EXPLICIT EXPRESSIONS FOR THE PROJECTION ONTO THE COLUMN SPACE AND THE PROJECTION ONTO THE LEFT NULL SPACE

From (4), the m-th row and the n-th column of $\mathbf{Z}^H\mathbf{Z}$ can be written as:

$$\left(\mathbf{Z}^H\mathbf{Z}\right)_{mn} = \sum_{i=1}^{N}\left(z_m^* z_n\right)^i \quad m = 1,\cdots,M \quad n = 1,\cdots,M. \tag{12}$$

If we use the cofactor expansion along the n-th column of the matrix $\mathbf{Z}^H\mathbf{Z}$, we have,

$$\det \mathbf{Z}^H\mathbf{Z} = \sum_{m=1}^{M}\left(\sum_{i=1}^{N}\left(z_m^* z_n\right)^i (-1)^{m+n}\det \mathbf{L}_{m,n}\right), \tag{13}$$

where $\mathbf{L}_{m,n}$ is the $(M-1)\times(M-1)$ matrix formed by removing from $\mathbf{Z}^H\mathbf{Z}$ its m-th row and n-th column.

From (1) and (4), $\mathbf{Z}^H\mathbf{y}$ can be written as:

$$\mathbf{Z}^H\mathbf{y} = \begin{bmatrix} \sum_{i=1}^{N} z_1^{*i} y_i & \sum_{i=1}^{N} z_2^{*i} y_i & \cdots & \sum_{i=1}^{N} z_M^{*\,i} y_i \end{bmatrix}^T. \tag{14}$$

$\mathbf{B}_n$ is defined by replacing the n-th column of the matrix $\mathbf{Z}^H\mathbf{Z}$ by $\mathbf{Z}^H\mathbf{y}$ for $n = 1,\cdots,M$:

$$\mathbf{B}_n = \begin{bmatrix} \sum_{i=1}^{N}\left(z_1^* z_1\right)^i & \cdots & \sum_{i=1}^{N}\left(z_1^* z_{n-1}\right)^i & \sum_{i=1}^{N}\left(z_1^*\right)^i y_i & \sum_{i=1}^{N}\left(z_1^* z_{n+1}\right)^i & \cdots & \sum_{i=1}^{N}\left(z_1^* z_M\right)^i \\ \vdots & \ddots & \vdots & \vdots & \vdots & \ddots & \vdots \\ \sum_{i=1}^{N}\left(z_M^* z_1\right)^i & \cdots & \sum_{i=1}^{N}\left(z_M^* z_{n-1}\right)^i & \sum_{i=1}^{N}\left(z_M^*\right)^i y_i & \sum_{i=1}^{N}\left(z_M^* z_{n+1}\right)^i & \cdots & \sum_{i=1}^{N}\left(z_M^* z_M\right)^i \end{bmatrix}. \tag{15}$$

The determinant of matrix $\mathbf{B}_n$ can be obtained from the cofactor expansion along the first column of the matrix $\mathbf{B}_n$:

$$\det \mathbf{B}_n = \sum_{m=1}^{M}\left(\left(\sum_{i=1}^{N}\left(z_m^*\right)^i y_i\right)(-1)^{m+n}\det \mathbf{L}_{m,n}\right). \tag{16}$$

Using the Cramer's rule, the explicit expression of the least squares solution in (7) is:

$$\hat{c}_n = \frac{\det \mathbf{B}_n}{\det \mathbf{Z}^H\mathbf{Z}} \quad n = 1,\cdots,M. \tag{17}$$

Note that, in [3], the authors applied the Cramer's rule to obtain $\left(\mathbf{Z}^H\mathbf{Z}\right)^{-1}\mathbf{Z}^H$, not to obtain $\left(\mathbf{Z}^H\mathbf{Z}\right)^{-1}\mathbf{Z}^H\mathbf{y}$. In this paper, the Cramer's rule is used to obtain $\left(\mathbf{Z}^H\mathbf{Z}\right)^{-1}\mathbf{Z}^H\mathbf{y}$. What is desirable in this new approach is that we can get expressions which are more compact, intuitive and insightful than those given in [3].

By substituting (13) and (16) in (17), we get

$$\hat{c}_n = \frac{\det \mathbf{B}_n}{\det \mathbf{Z}^H\mathbf{Z}} = \frac{\sum_{m=1}^{M}\left(\left(\sum_{i=1}^{N}\left(z_m^*\right)^i y_i\right)(-1)^{m+n}\det \mathbf{L}_{m,n}\right)}{\sum_{m=1}^{M}\left(\sum_{i=1}^{N}\left(z_m^* z_n\right)^i (-1)^{m+n}\det \mathbf{L}_{m,n}\right)}. \tag{18}$$

Using (18) in (10), we have,

$$\mathbf{Z}\hat{\mathbf{c}} = \begin{bmatrix} \sum_{n=1}^{M} z_n \dfrac{\sum_{m=1}^{M}\left(\left(\sum_{i=1}^{N}\left(z_m^*\right)^i y_i\right)(-1)^{m+n}\det \mathbf{L}_{m,n}\right)}{\sum_{m=1}^{M}\left(\sum_{i=1}^{N}\left(z_m^* z_n\right)^i (-1)^{m+n}\det \mathbf{L}_{m,n}\right)} \\ \vdots \\ \sum_{n=1}^{M} z_n{}^N \dfrac{\sum_{m=1}^{M}\left(\left(\sum_{i=1}^{N}\left(z_m^*\right)^i y_i\right)(-1)^{m+n}\det \mathbf{L}_{m,n}\right)}{\sum_{m=1}^{M}\left(\sum_{i=1}^{N}\left(z_m^* z_n\right)^i (-1)^{m+n}\det \mathbf{L}_{m,n}\right)} \end{bmatrix}. \tag{19}$$

The implicit expression of the norm of the projection onto the column space is,

$$\left\|\mathbf{P}_\mathbf{Z}\mathbf{y}\right\| = \left\|\mathbf{Z}\left(\mathbf{Z}^H\mathbf{Z}\right)^{-1}\mathbf{Z}^H\mathbf{y}\right\|. \tag{20}$$

From (19) and (20), the corresponding explicit expression of the norm of the projection onto the column space is,

$$\left\|\mathbf{P}_\mathbf{Z}\mathbf{y}\right\| = \sqrt{\sum_{j=1}^{N}\left(\sum_{n=1}^{M} z_n{}^j \frac{\sum_{m=1}^{M}\left(\left(\sum_{i=1}^{N}\left(z_m^*\right)^i y_i\right)(-1)^{m+n}\det \mathbf{L}_{m,n}\right)}{\sum_{m=1}^{M}\left(\sum_{i=1}^{N}\left(z_m^* z_n\right)^i (-1)^{m+n}\det \mathbf{L}_{m,n}\right)}\right)^2}. \tag{21}$$

Similarly, the implicit expression of the square of the norm of the projection onto the column space is,

$$\left\|\mathbf{P}_\mathbf{Z}\mathbf{y}\right\|^2 = \left\|\mathbf{Z}\left(\mathbf{Z}^H\mathbf{Z}\right)^{-1}\mathbf{Z}^H\mathbf{y}\right\|^2. \tag{22}$$

From (19) and (22), the explicit expression of the

square of the norm of the projection onto the column space is,

$$\left\|\mathbf{P}_{\mathbf{Z}}\mathbf{y}\right\|^2=\sum_{j=1}^{N}\left(\sum_{n=1}^{M}z_n{}^{j}\frac{\sum_{m=1}^{M}\left(\left(\sum_{i=1}^{N}\left(z_m^{*}\right)^{i}y_i\right)(-1)^{m+n}\det\mathbf{L}_{m,n}\right)}{\sum_{m=1}^{M}\left(\sum_{i=1}^{N}\left(z_m^{*}z_n\right)^{i}(-1)^{m+n}\det\mathbf{L}_{m,n}\right)}\right)^2. \tag{23}$$

Using the same approach to get (21) and (23), the explicit expressions of $\left\|\mathbf{P}_{\mathbf{Z}}^{\perp}\mathbf{y}\right\|$ and $\left\|\mathbf{P}_{\mathbf{Z}}^{\perp}\mathbf{y}\right\|^2$ can be written as:

$$\left\|\mathbf{P}_{\mathbf{Z}}^{\perp}\mathbf{y}\right\|=\sqrt{\sum_{j=1}^{N}\left(y_j-\sum_{n=1}^{M}z_n{}^{j}\frac{\sum_{m=1}^{M}\left(\left(\sum_{i=1}^{N}\left(z_m^{*}\right)^{i}y_i\right)(-1)^{m+n}\det\mathbf{L}_{m,n}\right)}{\sum_{m=1}^{M}\left(\sum_{i=1}^{N}\left(z_m^{*}z_n\right)^{i}(-1)^{m+n}\det\mathbf{L}_{m,n}\right)}\right)^2}, \tag{24}$$

$$\left\|\mathbf{y}-\mathbf{Z}\hat{\mathbf{c}}\right\|^2=\sum_{j=1}^{N}\left(y_j-\sum_{n=1}^{M}z_n{}^{j}\frac{\sum_{m=1}^{M}\left(\left(\sum_{i=1}^{N}\left(z_m^{*}\right)^{i}y_i\right)(-1)^{m+n}\det\mathbf{L}_{m,n}\right)}{\sum_{m=1}^{M}\left(\sum_{i=1}^{N}\left(z_m^{*}z_n\right)^{i}(-1)^{m+n}\det\mathbf{L}_{m,n}\right)}\right)^2, \tag{25}$$

which is supposed to be Ricean-distributed and chi-square distributed, respectively [5].

IV. ANALYTIC EXPRESSIONS FOR THE MEAN AND THE VARIANCE

A. Analytic expressions for the statistics of the projection onto the column space

A sum of the squares of independent Gaussian random variables is chi-square distributed, and the degree of freedom of the chi-square random variable is the number Gaussian random variables. In $\left\|\mathbf{P}_{\mathbf{Z}}\mathbf{y}\right\|^2=\sum_{i=1}^{M}w_i^2$, $\left\|\mathbf{P}_{Z}\mathbf{y}\right\|^2$ is expressed as a sum of square of M Gaussian random variables, which implies that $\left\|\mathbf{P}_{Z}\mathbf{y}\right\|^2$ is chi-square distributed with the degree of freedom M.

In [3], the mean and the variance of $\left\|\mathbf{P}_{\mathbf{Z}}^{\perp}\mathbf{y}\right\|^2$ have been derived. Adopting the scheme presented in [3], the mean and variance of $\left\|\mathbf{P}_{\mathbf{Z}}\mathbf{y}\right\|^2$ are expressed as:

$$\mathrm{Mean}\left(\left\|\mathbf{Z}\left(\mathbf{Z}^H\mathbf{Z}\right)^{-1}\mathbf{Z}^H\mathbf{y}\right\|^2\right)=\mathrm{Mean}\left(\sum_{i=1}^{M}w_i^2\right)=M\sigma^2+\sum_{i=1}^{M}\mu_{w_i}^2, \tag{26}$$

$$\mathrm{Var}\left(\left\|\mathbf{Z}\left(\mathbf{Z}^H\mathbf{Z}\right)^{-1}\mathbf{Z}^H\mathbf{y}\right\|^2\right)=\mathrm{Var}\left(\sum_{i=1}^{M}w_i^2\right)=2M\sigma^4+4\sigma^2\sum_{i=1}^{M}\mu_{w_i}^2, \tag{27}$$

where w_i is the *i*-th entry of $\mathbf{w}=\mathbf{V}^T\mathbf{y}$ and μ_{w_i} is the expected value of w_i. Note that $\mathbf{V}$ is defined from $\mathbf{P}_{\mathbf{Z}}=\mathbf{V}\Lambda\mathbf{V}^T$.

The norm of the projection onto the column space is equal to:

$$\left\|\mathbf{P}_{\mathbf{Z}}\mathbf{y}\right\|=\sqrt{\sum_{i=1}^{M}w_i^2}. \tag{28}$$

Since $\left\|\mathbf{P}_{\mathbf{Z}}\mathbf{y}\right\|^2=\sum_{i=1}^{M}w_i^2$ is chi-square distributed, it follows that $\left\|\mathbf{P}_{\mathbf{Z}}\mathbf{y}\right\|=\sqrt{\sum_{i=1}^{M}w_i^2}$ is Ricean distributed [5].

From the moment of Ricean distribution, we can obtain the mean and the variance of (28) [5]:

$$\mathrm{Mean}(\left\|\mathbf{P}_{\mathbf{Z}}\mathbf{y}\right\|)=\sqrt{2}\sigma\exp\left(-\frac{\sum_{i=1}^{M}\mu_{w_i}^2}{2\sigma^2}\right)\frac{\Gamma\left[\frac{1}{2}(M+1)\right]}{\Gamma\left[\frac{1}{2}M\right]}{}_1F_1\left(\frac{1}{2}(M+1),\frac{1}{2}M;\frac{\sum_{i=1}^{M}\mu_{w_i}^2}{2\sigma^2}\right), \tag{29}$$

$$\mathrm{Var}(\left\|\mathbf{P}_{\mathbf{Z}}\mathbf{y}\right\|)=2\sigma^2\exp\left(-\frac{\sum_{i=1}^{M}\mu_{w_i}^2}{2\sigma^2}\right)\frac{\Gamma\left[\frac{1}{2}(M+2)\right]}{\Gamma\left[\frac{1}{2}M\right]}{}_1F_1\left(\frac{1}{2}(M+2),\frac{1}{2}M;\frac{\sum_{i=1}^{M}\mu_{w_i}^2}{2\sigma^2}\right)-\left[\mathrm{Mean}\left(\left\|\mathbf{Z}\left(\mathbf{Z}^H\mathbf{Z}\right)^{-1}\mathbf{Z}^H\mathbf{y}\right\|\right)\right]^2, \tag{30}$$

where $\mathrm{Mean}\left(\left\|\mathbf{Z}\left(\mathbf{Z}^H\mathbf{Z}\right)^{-1}\mathbf{Z}^H\mathbf{y}\right\|\right)$ is given in (29), and Γ is the gamma function. ${}_1F_1(\alpha,\beta,\gamma)$ is the hypergeometric function.

B. Analytic expressions for the statistics of the projection onto the left null space

In $\left\|\mathbf{P}_{\mathbf{Z}}^{\perp}\mathbf{y}\right\|^2=\sum_{i=1}^{N-M}w_i^2$, $\left\|\mathbf{P}_{\mathbf{Z}}^{\perp}\mathbf{y}\right\|^2$ is expressed as a sum of square of N-M Gaussian random variables, which implies that $\left\|\mathbf{P}_{\mathbf{Z}}^{\perp}\mathbf{y}\right\|^2$ is chi-square distributed with the degree of freedom N-M.

It is shown in [3] that the mean and the variance of $\left\|\mathbf{P}_{\mathbf{Z}}^{\perp}\mathbf{y}\right\|^2$ are expressed as:

$$\mathrm{Mean}\left(\left\|\left(\mathbf{I}-\mathbf{F}\left(\mathbf{F}^H\mathbf{F}\right)^{-1}\mathbf{F}^H\right)\mathbf{y}\right\|^2\right)=\mathrm{Mean}\left(\sum_{i=1}^{N-M}w_i^2\right)=(N-M)\sigma^2+\sum_{i=1}^{N-M}\mu_{w_i}^2, \tag{31}$$

$$\mathrm{Var}\left(\left\|\left(\mathbf{I}-\mathbf{F}\left(\mathbf{F}^H\mathbf{F}\right)^{-1}\mathbf{F}^H\right)\mathbf{y}\right\|^2\right)=\mathrm{Var}\left(\sum_{i=1}^{N-M}w_i^2\right)=2(N-M)\sigma^4+4\sigma^2\sum_{i=1}^{N-M}\mu_{w_i}^2, \tag{32}$$

where w_i is the *i*-th entry of $\mathbf{w}=\mathbf{V}^T\mathbf{y}$ and μ_{w_i} is the expected value of w_i. Note that $\mathbf{V}$ is defined from $\mathbf{P}_{\mathbf{Z}}^{\perp}=\mathbf{V}\Lambda\mathbf{V}^T$.

The norm of the projection onto the left null space can be written as:

$$\left\|\mathbf{P}_{\mathbf{Z}}^{\perp}\mathbf{y}\right\|=\sqrt{\sum_{i=1}^{N-M}w_i^2}. \tag{33}$$

Comparing (28) and (33), we can see that

$\left\|\mathbf{P}_{\mathbf{Z}}^{\perp}\mathbf{y}\right\| = \sqrt{\sum_{i=1}^{N-M} w_i^2}$ is also Ricean distributed with M in (28) replaced by $N-M$ in (33) and the corresponding mean and the variance can be written as [5]:

$$\text{Mean}\left(\left\|\mathbf{P}_{\mathbf{Z}}^{\perp}\mathbf{y}\right\|\right) = \sqrt{2}\sigma \exp\left(-\frac{\sum_{i=1}^{N-M}\mu_{w_i}^2}{2\sigma^2}\right)\frac{\Gamma\left[\frac{1}{2}(N-M+1)\right]}{\Gamma\left[\frac{1}{2}(N-M)\right]}\,{}_1F_1\left(\frac{1}{2}(N-M+1),\frac{1}{2}(N-M);\frac{\sum_{i=1}^{N-M}\mu_{w_i}^2}{2\sigma^2}\right), \tag{34}$$

$$\text{Var}\left(\left\|\mathbf{P}_{\mathbf{Z}}^{\perp}\mathbf{y}\right\|\right) = 2\sigma^2 \exp\left(-\frac{\sum_{i=1}^{N-M}\mu_{w_i}^2}{2\sigma^2}\right)\frac{\Gamma\left[\frac{1}{2}(N-M+2)\right]}{\Gamma\left[\frac{1}{2}(N-M)\right]}\,{}_1F_1\left(\frac{1}{2}(N-M+2),\frac{1}{2}(N-M);\frac{\sum_{i=1}^{N-M}\mu_{w_i}^2}{2\sigma^2}\right) - \left[\text{Mean}\left(\left\|\left(\mathbf{I}-\mathbf{F}\left(\mathbf{F}^H\mathbf{F}\right)^{-1}\mathbf{F}^H\right)\mathbf{y}\right\|\right)\right]^2. \tag{35}$$

V. NUMERICAL RESULTS

For the square of the norm of the projection onto the column space, we validate (23), (26) and (27) by evaluating (23) and (22) using the Monte Carlo simulation, and calculate the mean of (23) and the mean of (22) to see whether they are equal to (26). Also, we evaluate the variance of (23) and the variance of (22) to see whether they are consistent with (27).

For the square of the norm of the projection onto the left null space, to show that (25), (31) and (32) are all valid we make the Monte Carlo simulation for (25) and check whether the mean of (25) is equal to (31). Also, we check whether the variance of (25) is equal to (32).

For the norm of the projection onto the column space, we validate (21), (29) and (30) by evaluating (21) and (20) using the Monte Carlo simulation, and calculate the mean of (21) and the mean of (20) for checking whether they are all equal to (29). Also, we calculate the variance of (21) and the variance of (20) to see whether they are all equal to (30).

For the norm of the projection onto the left null space, to show that (24), (34) and (35) are all correct, we evaluate (24) via the Monte Carlo simulation and check whether the mean of (24) is equal to (34). Also, we check whether the variance of (24) is consistent with (35).

The lengths of the thin wires used for the numerical simulation are equal to 1.0 meter, 0.9 meter and 0.8 meter.

In evaluating $\left\|\mathbf{P}_{\mathbf{Z}}\mathbf{y}\right\|$, $\left\|\mathbf{P}_{\mathbf{Z}}^{\perp}\mathbf{y}\right\|$, $\left\|\mathbf{P}_{\mathbf{Z}}\mathbf{y}\right\|^2$ and $\left\|\mathbf{P}_{\mathbf{Z}}^{\perp}\mathbf{y}\right\|^2$, $\mathbf{Z}$ in (4) corresponds to 1.0 meter long wire, and $\mathbf{y} = \begin{bmatrix} y_1 & y_2 & \cdots & y_N \end{bmatrix}^T$ can be the late time response of 0.8 meter, 0.9 meter or 1.0 meter. Scattering data are generated using the singularity expansion method (SEM) representation for the thin wires of 1.0 meter, 0.9 meter and 0.8 meter with incidence angle of 40 degrees. That is, the correct target is the thin wire of $L = 1.0$ m, and the wrong targets are the thin wires of $L = 0.9$ m and $L = 0.8$ m. The radii of all the wires are equal to $L/200$.

For noise simulation, each point of the SEM-based wire transient response is perturbed with Gaussian noise. We consider the various signal-to-noise ratios (SNRs) of SNR = 0, 5 and 10 dB. The details on how to make numerical simulations can be found in [3]. We use the late time transient responses of thin wires of 0.8 meter, 0.9 meter and 1.0 meter and the z-plane natural frequencies of the correct target of 1.0 m. The z-plane natural frequencies for the thin wire of 1.0 meter, $z_i, i = 1,\cdots,6$, are $0.9617 \pm j1.5464, 0.9445 \pm j2.4621$ and $0.9321 \pm j3.8925$ [3].

In Fig. 1, the line with legend 'Analytic' are from (26). The lines with legends 'Simulation: Implicit' and 'Simulation: Explicit' are given from the averages of the Monte Carlo simulation of (22) and (23). The line with legend 'Analytic' are from (26), and those with legends 'Simulation: Implicit' and 'Simulation: Explicit' are given from the variances of (22) and (23) via the Monte Carlo simulation in Fig. 2.

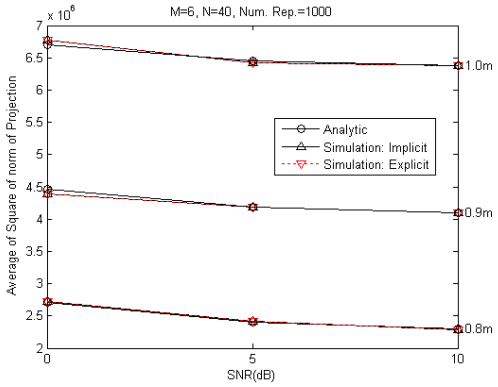

Fig. 1. Average of square of norm of projection onto the column space ($M = 6, N = 40$).

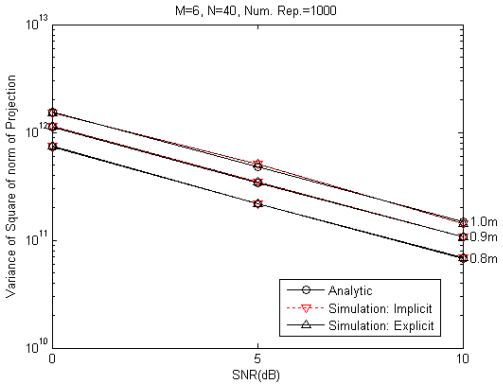

Fig. 2. Variance of square of norm of projection onto the column space ($M = 6, N = 40$).

In Fig. 3, the result with legend 'Analytic' are from (31), and those with legends 'Simulation: Implicit' and 'Simulation: Explicit' are given from the averages of the Monte Carlo simulation of (25). In Fig. 4, the line with legend 'Analytic' are given by (32), and those with legends 'Simulation: Implicit' and 'Simulation: Explicit' are given from the variances of the Monte Carlo simulation of (25).

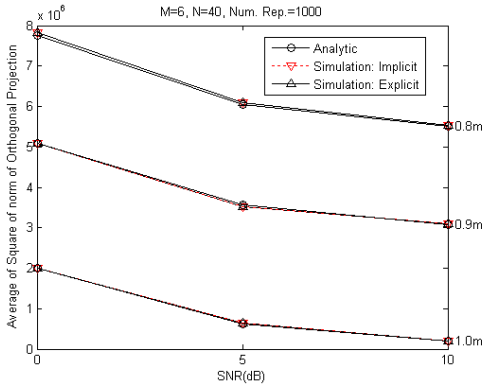

Fig. 3. Average of square of norm of projection onto the left null space ($M = 6, N = 40$).

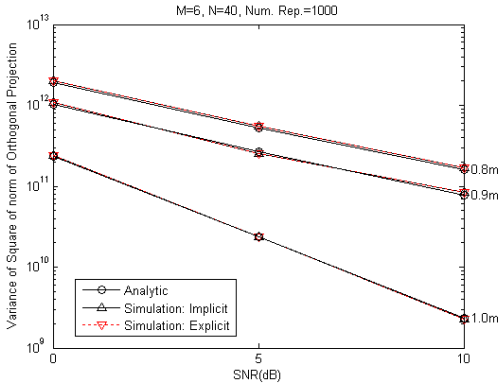

Fig. 4. Variance of square of norm of projection onto the left null space ($M = 6, N = 40$).

In Fig. 5, the line with legend 'Analytic' are from (29), and those with legends 'Simulation: Implicit' and 'Simulation: Explicit' are given from the averages of the Monte Carlo simulation corresponding to (20) and (21). In Fig. 6, the line with legend 'Analytic' are from (30), and those with legends 'Simulation: Implicit' and 'Simulation: Explicit' are given from the variances of the Monte Carlo simulation of (20) and (21).

In Fig. 7, the line with legend 'Analytic' are from (34), and those with legends 'Simulation: Implicit' and 'Simulation: Explicit' are given from the averages of the Monte Carlo simulation of (24). The result with legend 'Analytic' are from (35), and those with legends 'Simulation: Implicit' and 'Simulation: Explicit' are calculated from the variances of the Monte Carlo simulation of (24) in Fig. 8.

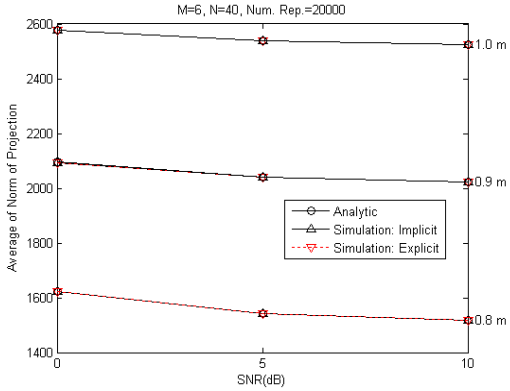

Fig. 5. Average of norm of projection onto the column space ($M = 6, N = 40$).

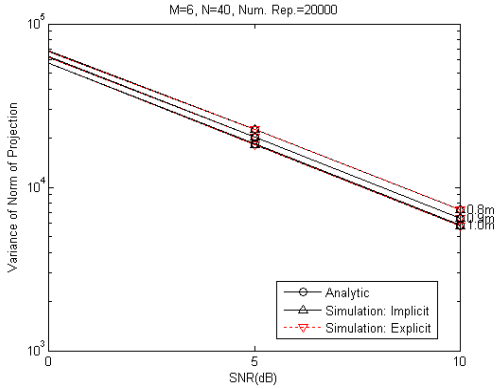

Fig. 6. Variance of norm of projection onto the column space ($M = 6, N = 40$).

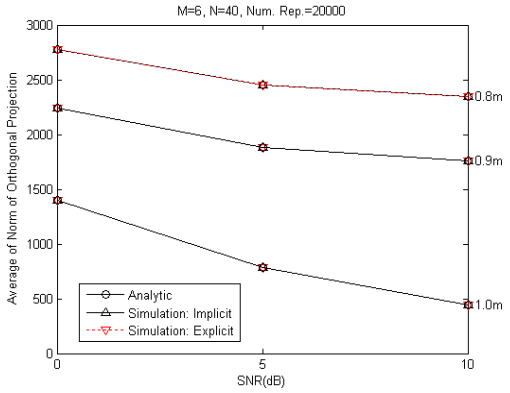

Fig. 7. Average of norm of projection onto the left null space ($M = 6, N = 40$).

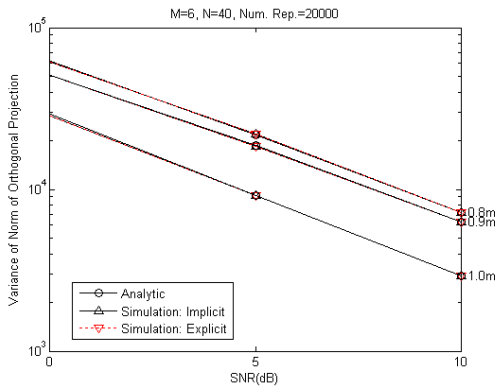

Fig. 8. Variance of norm of projection onto the left null space ($M = 6, N = 40$).

In Fig. 5, we can observe the following:

- In Fig. 5, the norm of the projection onto the column space of the correct target of 1.0 m is small enough to recognize the correct target compared with that for the wrong targets of 0.9 m and 0.8 m.
- As SNR increases, the norm of the projection onto the column space of the correct target decreases significantly, which is favorable for the recognition of the correct target.
- As the number of natural frequencies increases, the norm of the projection onto the column space of the correct target increases and those for the wrong target decrease, which improves the performance of the radar target recognition with an increase of the number of the natural frequencies. Since the results in Fig. 1 are for the square of the norm of the projection onto the column space of $\mathbf{Z}$ of the late time response and those in Fig. 5 are the norm of the projection onto the column space of $\mathbf{Z}$ of the late time response, the observation for Fig. 5 is also true for Fig. 1.

In Fig. 7, we can see the following:

- The norm of the projection onto the left null space of the matrix $\mathbf{Z}$ corresponding to the correct target of length 1.0 meter is large enough to recognize the correct target compared with that for the wrong targets of length 0.9 meter and 0.8 meter.
- As SNR increases, the norm of the projection onto the left null space for the correct target decreases significantly, which is favorable for the recognition of the correct target.
- As the number of natural frequencies increases, the norm of the projection onto the left null space for the correct target decrease and those for the wrong target increase, which improves the performance of the radar target recognition with an increase of the number of the natural frequencies. Since the results in Fig. 3 are for the square of the norm of the projection onto the left null space of $\mathbf{Z}$ of the late time response and those in Fig. 7 are the norm of the projection onto the left null space of $\mathbf{Z}$ of the late time response, the observation for Fig. 7 is also true for Fig. 3.

VI. CONCLUSION

The mean and the variance of the square of the norm of the projection onto the column space are given in (26) and (27), respectively, and those of the square of the norm of the projection onto the left null space are given in (31) and (32), respectively.

The mean and the variance of the norm of the projection onto the column space are given in (29) and (30), respectively, and those of the square of the norm of the projection onto the left null space are given in (34) and (35), respectively.

(23), (26) and (27) are verified in Figs. 1-2, and (25), (31) and (32) are verified in Figs. 3-4. In Figs. 5-6, the validity of (21), (29) and (30) is shown. Figures 7-8 show the validity of (24), (34) and (35).

From the numerical results, for the square of the norm of the projection onto the column space, it has been confirmed that the mean and the variance of the norm of the projection onto the column space can be available from the derived expressions in (26) and (27) without actually performing the Monte Carlo simulations which require many evaluations of (22) or (23). In addition to the square of the norm of the projection onto the column space, it is also true for the norm of the projection onto the column space, the square of the norm of the projection onto the left null space, and the norm of the projection onto the left null space.

ACKNOWLEDGMENT

This research was supported by Basic Science Research Program through the National Research Foundation of Korea (NRF) funded by the Ministry of Education (2013R1A1A2A10012245).

REFERENCES

[1] D. Blanco, D. Ruiz, E. Alameda-Hernandez, M. C. Carrion, "Extinction pulses synthesis for radar target discrimination using /spl beta/-splines, new E-pulse conditions," *IEEE Trans. Antennas and Propagation*, vol. 54, pp. 1577-1585, Sep. 2006.

[2] J. Chauveau, N. de Beaucoudrey, and J. Saillard, "Selection of contributing natural poles for the characterization of perfectly conducting targets in resonance region," *IEEE Trans. Antennas and Propagation*, vol. 55, pp. 2610-2617, Sep. 2007.

[3] J.-H. Lee and H.-T. Kim, "Radar target recognition basd on late time representation: Closed-form expression for criterion," *IEEE Trans. Antennas and Propagation*, vol. 54, pp. 2455-2462, Sep. 2006.

[4] J.-H. Lee, H.-J. Moon, and S.-H. Jeong, "Numerically efficient determination of the optimal threshold in natural frequency-based radar target

recognition," *IEEE Transactions on Antennas and Propagation*, vol. 62, no. 11 pp. 5889-5894, 2014.

[5] J. H. Proakis, *Digital Communications*. New York: McGraw-Hill, 2001.

Research on Terahertz Wave Reflection and Transmission of Carbon Nanotubes Slab Using FDTD

Mao Y. Wang [1], Hai L. Li [1], Yu L. Dong [1], Gui P. Li [1], Cui L. Zhong [2], and Jun Xu [1]

[1] School of Physical Electronics
University of Electronic Science and Technology of China, Cheng du, 610054, China
wmybrimlhl@163.com, hailong703@163.com, yldong@uestc.edu.cn, lgp@uestc.edu.cn, xujun@uestc.edu.cn

[2] Department of Electrical and Computer Engineering
Shenzhen Institutes of Advanced Technology, Chinese Academy of Sciences, Shenzhen, 518055, China
zhongcuilin@hotmail.com

Abstract ─ Terahertz wave reflection and transmission of carbon nanotubes slab are investigated in this paper. The wave and current equations that describe characters of terahertz wave in dispersive carbon nanotubes (CNTs) are presented and discretized by using the auxiliary differential equation (ADE) in the finite-difference time-domain method (FDTD), because the permittivity of CNTs are frequency-dependent. The ADE-FDTD method and program's efficiency is proved by the reference's analytical method. Numerical results show that the transmission coefficient of single wall carbon nanotubes (SWCNTs) does not show distinct peaks and dips at Terahertz frequency. The multiple transmitted pulses of silicon dioxide bi-covered with SWCNTs are observed. The electromagnetic interference (EMI) shielding effect of SWCNTs, double wall carbon nanotubes (DWCNTs) and Hydrogen doped CNTs are compared.

Index Terms ─ Auxiliary differential equation (ADE), carbon nanotubes, dispersive, finite-difference time-domain (FDTD), permittivity.

I. INTRODUCTION

Nowadays, carbon nanotubes (CNTs) [1-8] and grapheme, which are advanced engineering materials with unique structures and electrical properties, have attracted much attention. CNTs can be classified as single wall (SW), double wall (DW) and multiwall (MW) carbon nanotubes and modified as hydrogen (H) doped CNTs [5] and so on. CNTs [9-12] have some potential microwave, Terahertz (THz) wave, and optical applications, such as hydrogen storage devices, antennas, interconnects, electrochemical capacitors, and lightweight electromagnetic shields etc.

The electromagnetic interference shielding effectiveness [13-14] of carbon nanotubes structure at THz frequency regime has not yet been considerable studied. CNTs have the compound properties of metallic and semiconductor. The complex and frequency dispersive permittivity of CNTs at THz frequency regime are affected by the number of tube walls, thickness, aspect ratio, filling factor, and geometrical factor during the growth. Analytical and numerical methods [14-20] have been developed to investigate the electromagnetic characteristic of carbon nanotubes such as semi-classical approach [14], method of moments (MoM) [15], and finite-difference time-domain (FDTD) method [17-23] etc. FDTD method is a popular algorithm to predict the properties of materials in arbitrary shapes. Compared to other modeling approaches, FDTD method can study not only carbon nanotubes are made of hollow and long carbon cylindrical molecules, but also CNTs are equivalent to dispersive media. For simulating equivalent CNTs, the computational memory and cost requirement of auxiliary differential equation (ADE) FDTD method is relatively lower than shift operator [19], recursive convolution method and Z-transform methods and is generally used to simulate dispersive media.

In this paper, the electromagnetic interference shielding effectiveness of SWCNTs, DWCNTs and H-doped CNTs at THz frequency are computed with the ADE-FDTD method. Firstly, the ADE-FDTD method for dispersive Drude-Lorentzian model of carbon nanotubes is deduced. Then the accuracy of ADE-FDTD method and program is verified by analytical method in the reference [24]. The interaction of terahertz wave with stratified media containing single wall carbon nanotubes is simulated. The reflection and transmission coefficients for medium covered by SWCNTs, DWCNTs and H-doped CNTs are compared to discuss their application in EMI shielding.

II. ADE-FDTD FORMULA

As in Ref. [4], an extended Drude-Lorentzian model can be used to simulate the relative dispersive permittivity

Submitted On:July 26, 2015
Accepted On: June 16, 2016

of carbon nanotubes at THz frequency [25], i.e.,

$$\varepsilon_r = \varepsilon_c - \frac{\omega_p^2}{\omega(\omega - \mathrm{j}\Gamma)} + \frac{\omega_{p1}^2}{-\omega^2 + \mathrm{j}\omega\Gamma_1 + \omega_1^2}, \quad (1)$$

where ε_c is the dielectric constant at infinite frequency. ω_p, ω_1, and ω_{p1} represent the electron plasma, phonon and oscillator frequency, respectively. Γ and Γ_1 are relaxation rate and spectral width, respectively.

The frequency-dependent constitutive relation for CNTs can be characterized as:

$$\boldsymbol{D}=\varepsilon_r\varepsilon_0\boldsymbol{E} = \varepsilon_c\varepsilon_0\boldsymbol{E} + \boldsymbol{P} + \boldsymbol{P}_1, \quad (2)$$

where the polarization intensities $\boldsymbol{P}$ and $\boldsymbol{P}_1$ are:

$$\boldsymbol{P} = \varepsilon_0\omega_p^2\boldsymbol{E} / [(\mathrm{j}\omega)^2 + \Gamma\mathrm{j}\omega], \quad (3)$$

$$\boldsymbol{P}_1 = \varepsilon_0\omega_{p1}^2\boldsymbol{E} / [(\mathrm{j}\omega)^2 + \Gamma_1\mathrm{j}\omega + \omega_1^2]. \quad (4)$$

By applying the transform relation ($\mathrm{j}\omega \rightarrow \partial/\partial t$) between frequency domain and time domain, we obtain:

$$\partial^2\boldsymbol{P} / \partial t^2 + \Gamma\partial\boldsymbol{P} / \partial t = \varepsilon_0\omega_p^2\boldsymbol{E}, \quad (5)$$

$$\partial^2\boldsymbol{P}_1 / \partial t^2 + \Gamma_1\partial\boldsymbol{P}_1 / \partial t + \omega_1^2\boldsymbol{P}_1 = \varepsilon_0\omega_{p1}^2\boldsymbol{E}. \quad (6)$$

By defining the induced electric currents $\boldsymbol{J}$ and $\boldsymbol{J}_1$,

$$\boldsymbol{J} = \partial\boldsymbol{P} / \partial t, \quad (7)$$

$$\boldsymbol{J}_1 = \partial\boldsymbol{P}_1 / \partial t. \quad (8)$$

The electromagnetic field and current equations discretized with the ADE-FDTD method for the CNTs are:

$$\nabla\times\boldsymbol{E} = -\mu\partial\boldsymbol{H} / \partial t, \quad (9)$$

$$\nabla\times\boldsymbol{H} = \varepsilon_c\varepsilon_0\partial\boldsymbol{E} / \partial t + \boldsymbol{J} + \boldsymbol{J}_1 + \boldsymbol{J}_s, \quad (10)$$

$$\partial^2\boldsymbol{J} / \partial t^2 + \Gamma\partial\boldsymbol{J} / \partial t = \varepsilon_0\omega_p^2\partial\boldsymbol{E} / \partial t, \quad (11)$$

$$\partial^2\boldsymbol{J}_1 / \partial t^2 + \Gamma_1\partial\boldsymbol{J}_1 / \partial t + \omega_1^2\boldsymbol{J}_1 = \varepsilon_0\omega_{p1}^2\partial\boldsymbol{E} / \partial t, \quad (12)$$

where $\boldsymbol{J}_s$ is the free current source.

The standard grid, leapfrog in time approach is used to discrtize the Eqs. (9)-(12). The electric field and electric current are sampled at the cell edge for integer and half integer time steps, respectively. The magnetic field is sampled at the cell center for half integer time steps. If $\partial/\partial x$=0 and $\partial/\partial y$=0, the iterative fields and currents for a one-dimensional (1D) CNTs slab are:

$$H_y^{n+\frac{1}{2}}(i+\frac{1}{2}) = H_y^{n-\frac{1}{2}}(i+\frac{1}{2}) - \frac{\Delta t}{\mu\Delta z}\left[E_x^n(i+1) - E_x^n(i)\right], \quad (13)$$

$$E_x^{n+1}(i) = E_x^n(i) + \frac{\Delta t}{\varepsilon_c\varepsilon_0\Delta z}\left\{\begin{array}{l}\left[H_y^{n+\frac{1}{2}}(i+\frac{1}{2}) - H_y^{n+\frac{1}{2}}(i-\frac{1}{2})\right] \\ -[J_x^{n+\frac{1}{2}}(i) + J_{x1}^{n+\frac{1}{2}}(i) + J_s^{n+\frac{1}{2}}(i)]\Delta z\end{array}\right\}, \quad (14)$$

$$J_{x1}^{n+\frac{3}{2}}(i) = \alpha_{x1}J_{x1}^{n+\frac{1}{2}}(i) + \beta_{x1}J_{x1}^{n-\frac{1}{2}}(i) + \gamma_{x1}\left[E_x^{n+1}(i) - E_x^{n-1}(i)\right], \quad (15)$$

$$J_x^{n+\frac{3}{2}}(i) = \alpha_x J_x^{n+\frac{1}{2}}(i) + \beta_x J_x^{n-\frac{1}{2}}(i) + \gamma_x\left[E_x^{n+1}(i) - E_x^{n-1}(i)\right], \quad (16)$$

where

$$\alpha_{x1} = \frac{4-2\Delta t^2\omega_1^2}{2+\Gamma_1\Delta t},\ \beta_{x1} = \frac{\Gamma_1\Delta t-2}{2+\Gamma_1\Delta t},\ \gamma_{x1} = \frac{\varepsilon_0\omega_{p1}^2\Delta t}{2+\Gamma_1\Delta t},$$

$$\alpha_x = \frac{4}{2+\Gamma\Delta t},\ \beta_x = \frac{\Gamma\Delta t-2}{2+\Gamma\Delta t},\ \gamma_x = \frac{\varepsilon_0\omega_p^2\Delta t}{2+\Gamma\Delta t}. \quad (17)$$

The power reflection, transmission, and absorption coefficients in decibel scale are:

$$R_{\mathrm{dB}} = 20\lg R, \quad (18)$$

$$T_{\mathrm{dB}} = 20\lg T, \quad (19)$$

$$A_{\mathrm{dB}} = 10\lg(1-|R|^2-|T|^2). \quad (20)$$

III. NUMERICAL RESULTS

In the following section, FDTD numerical results about Terahertz wave reflection and transmission of stratified media containing various carbon nanotubes are illustrated. The EMI shielding effectiveness, which is generally dependent upon various material parameters characterized by CNTs' aspect ratio, filling factor, geometrical factor and working frequency etc. are discussed below.

To validate the auxiliary differential equation finite-difference time-domain method introduced above, Fig. 1 illustrates the reflection and transmission coefficients for one-layer single wall carbon nanotubes slab. The spatial discretization size is δ=0.1 μm and the time step size is $\Delta t=\delta/2c$. The incident differential Gaussian pulse in the time domain is $E_i(t)= \{(t-t_0)\cdot\exp[-4\pi(t-t_0)^2/\tau^2]\}/\tau^2$. The pulse peak occurs at t_0=120Δt. The pulse width of the pulse is influenced by the constant τ=150Δt.

If no special instructions in this paper, the material parameters in Eq. (1) for SWCNTs [4] are ε_c=8.41, ω_p=2π×23 THz, ω_{p1}=2π×38.9 THz, ω_1=2π×5.9 THz, Γ=2π×24.5 THz, Γ_1=2π×29.6 THz. The CNTs' thickness is 10 μm. The reflection and transmission coefficients computed with analytical propagation matrix method in Ref. [4] and the ADE-FDTD method reach a good agreement in Fig. 1. Though the peak value of the reflection coefficient occur at 0.916 THz, the transmission coefficient for a 10-μm-thick SWCNTs slab does not show obvious peaks and troughs at 0.3-2.5 THz in Fig. 1. The variation trend is consistent with the experimental results in Ref. [9].

Figure 2 gives the ADE-FDTD method simulated the terahertz wave transmission coefficient and the time domain waveform of 1mm depth silicon dioxide (SiO_2) and silicon dioxide bi-covered by 15 μm depth SWCNTs respectively. The permittivity for SiO_2 is presumed constant ε_r=4 [26].

As shown in Fig. 2 (a), the SWCNTs can make the transmission coefficient greatly decrease. The single

wall carbon nanotubes demonstrate high efficiency shielding at terahertz frequency range. The sampling points of the transmission time-domain waveform E_y in Fig. 2 (b) are 5δ away from the media boundary between SWCNTs and vacuum. Several transmitted pulses produced by the multi-reflection phenomena in the stratified media can be seen in Fig. 2 (b).

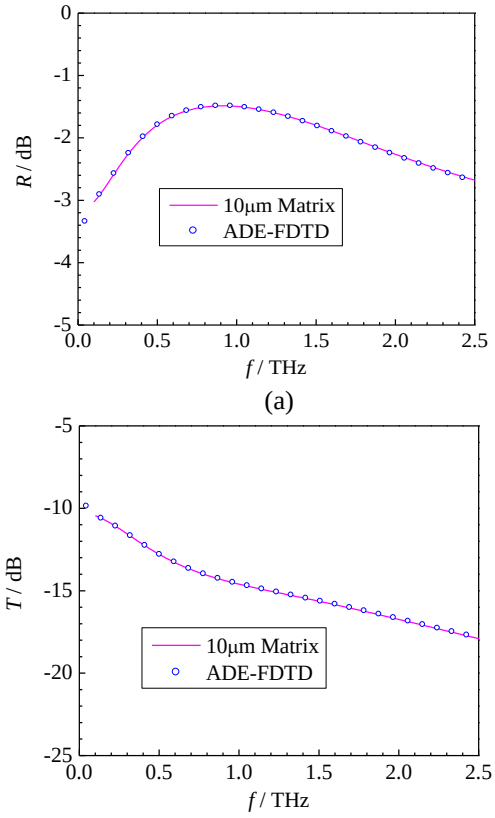

Fig. 1. Reflection and transmission coefficients for one-layer SWCNTs. (a) Reflection coefficient and (b) transmission coefficient.

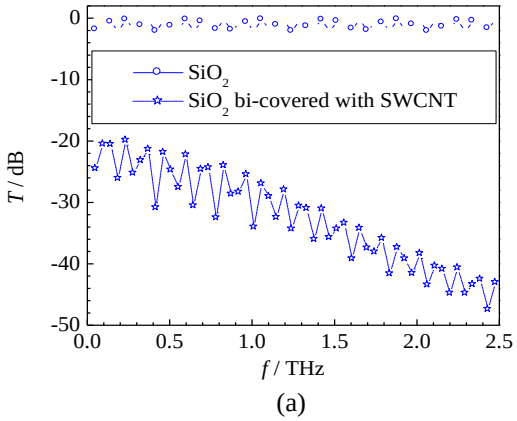

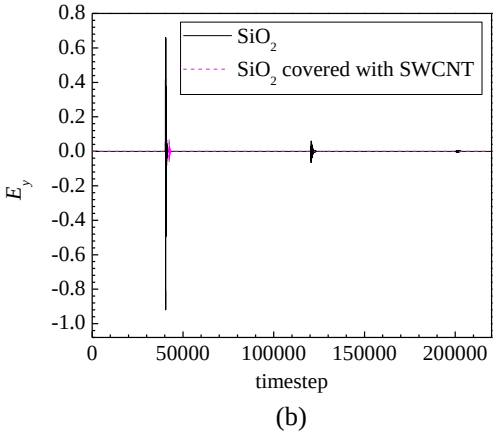

Fig. 2. FDTD predicted THz wave transmission of silicon dioxide bi-covered with SWCNTs. (a) Transmission coefficient and (b) normalized time domain waveform.

Figure 3 compares the ADE-FDTD method calculated electromagnetic scattering of 100 μm depth silicon dioxide (SiO_2) [26] whose ε_r=4 bi-covered with SWCNTs, DWCNTs, and H-doped CNTs. The thickness of each CNTs layer is 10 μm. The material parameters for DWCNTs [4] are ε_c=5.76, $\omega_p=2\pi\times10.5$ THz, $\omega_{p1}=2\pi\times32.2$ THz, $\omega_1=2\pi\times5.5$ THz, $\Gamma=2\pi\times24.3$ THz, $\Gamma_1=2\pi\times23.3$ THz and for H-doped CNTs [5] are ε_c=6.25, $\omega_p=2\pi\times7.42$ THz, $\Gamma=2\pi\times34.29$, $\omega_{p1}=2\pi\times4.69$ THz, $\omega_1=2\pi\times1.53$ THz, $\Gamma_1=2\pi\times3.27$ THz.

Because the permittivity and conductivity [2] of SWCNTs are larger than those of DWCNTs and H-doped CNTs discussed in this paper, the reflection coefficient of silicon dioxide bi-covered with SWCNTs is larger than those with DWCNTs and H-doped CNTs. Compared to the transmission coefficient of one layer SWCNTs in Fig. 1 (b), the transmission coefficient of SiO_2 bi-covered with SWCNTs in Fig. 3 (b) shows several peaks and dips originating from the silicon dioxide substrate in the Terahertz region.

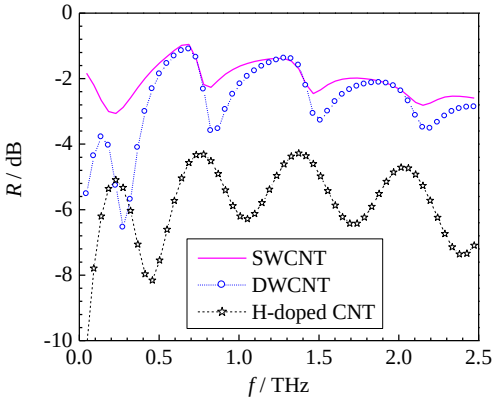

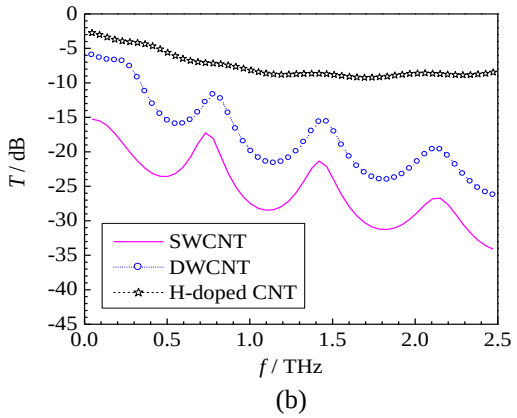

(b)

Fig. 3. FDTD predicted Terahertz wave reflection and transmission coefficients of silicon dioxide bi-covered with SWCNTs, DWCNTs, and H-doped CNTs. (a) reflection coefficient and (b) transmission coefficient.

IV. CONCLUSION

In this paper, terahertz wave reflection and transmission of carbon nanotubes slab is investigated with auxiliary differential equation in Finite-Difference Time-Domain method. The extended Drude-Lorentzian model in the frequency domain is used to simulate dispersive carbon nanotubes. The wave and current equations for CNTs are got with the transform relation between frequency domain and time domain and discretized using Yee's scheme. After the validity of method and program, ADE-FDTD method predicted Terahertz wave reflection and transmission of silicon dioxide bi-covered with SWCNTs, DWCNTs and H-doped CNTs are compared. The local resonances of the transmission coefficient associated with the material parameters of silicon dioxide substrate result in some oscillations. The computed results show that impedance mismatch and loss characteristic of SWCNTs make the transmission coefficient of silicon dioxide decrease. The SWCNTs demonstrates good electromagnetic interference shielding effectiveness.

ACKNOWLEDGMENT

This work is supported by the National Natural Science Foundation of China (41304119, 41104097), and the Fundamental Research Funds for the Central Universities (ZYGX2015J039, ZYGX2015J041, ZYGX2015J037).

REFERENCES

[1] M. F. De Volder, S. H. Tawfick, R. H. Baughman, and A. J. Hart, "Carbon nanotubes: present and future commercial applications," *Science*, vol. 339, no. 6119, pp. 535-539, 2013.

[2] X. Y. He and X. N. Fu, "Simulation investigation on optical and electrical properties of carbon nanotube in terahertz region," *Commun. Theor. Phys.*, vol. 51, no. 1, pp. 161-164, 2009.

[3] E. Dadrasnia and H. Lamela, "Optical and electrical characterization of carbon nanotubes by terahertz spectroscopy: comparison between modeling and experimental results," *Proc. of SPIE*, vol. 8096, no. 80963P, pp. 1-6, 2011.

[4] I. Maeng, C. Kang, S. J. Oh, J. H. Sonb, K. H. An, and Y. H. Lee, "Terahertz electrical and optical characteristics of double-walled carbon nanotubes and their comparison with single-walled carbon nanotubes," *Appl. Phys. Lett.*, vol. 90, no. 5, pp. 051914, 1-4, 2007.

[5] C. Kang, I. H. Maeng, S. J. Oh, S. C. Lim, K. H. An, Y. H. Lee, and J. H. Son, "Terahertz optical and electrical properties of hydrogen-functionalized carbon nanotubes," *Phys. Rev. B*, vol. 75, no. 8, pp. 085410, 1-5, 2007.

[6] Z. R. Wu, L. Wang, Y. T. Peng, A. Young, S. Seraphin, and H. Xin, "Terahertz characterization of multi-walled carbon nanotube films," *Journal of Applied Physics*, vol. 103, no. 9, pp. 094324, 1-6, 2008.

[7] J. Lloyd-Hughes and T. Jeon, "A review of the terahertz conductivity of bulk and nano-materials," *Journal of Infrared, Millimeter and Terahertz Waves*, vol. 33, no. 9, pp. 871-925, 2012.

[8] L. Ren, C. L. Pint, A. K. Wójcik, T. Arikawa, Y. Takemoto, K. Takeya, I. Kawayama, A. A. Belyanin, M. Tonouchi, R. H. Hauge, and J. Kono, "Anisotropic terahertz dynamics of highly-aligned single-walled carbon nanotubes," *Terahertz Science and Technology*, vol. 3, no. 1, pp. 26-32, 2010.

[9] J. T. Hong, D. J. Park, J. Y. Moon, S. B. Choi, J. K. Park, F. Rotermund, J. Y. Park, S. Lee, and Y. H. Ahn, "Terahertz wave applications of single-walled carbon nanotube films with high shielding effectiveness," *Applied Physics Express*, vol. 5, no. 1, pp. 015102, 1-3, 2012.

[10] X. J. Feng, W. X. Huang, Y. Luo, J. Zhang, and Y. X. Zhang, "Terahertz spectroscopic investigation of MWNTs and MWNTS/Mica," *Chinese Journal of Sensors and Actuators*, vol. 23, no. 4, pp. 453-457, 2010.

[11] W. Abdelli, X. Mininger, L. Pichon, and H. Trabelsi, "Impact of composite materials on the shielding effectiveness of enclosures," *The Applied Computational Electromagnetics Society*, vol. 27, no. 4, pp. 369-375, 2012.

[12] M. A. Seo, J. H. Yim, Y. H. Ahn, F. Rotermund, D. S. Kim, S. Lee, and H. Lim, "Terahertz electromagnetic interference shielding using single-walled carbon nanotube flexible films," *Applied Physics Letters*, vol. 93, no. 23, pp. 231905, 1-3, 2008.

[13] Y. Huang, N. Li, Y. F. Ma, F. Du, F. F. Li, X. B.

He, X. Lin, H. J. Gao, and Y. S. Chen, "The influence of single-walled carbon nanotube structure on the electromagnetic interference shielding efficiency of its epoxy composites," *Carbon*, vol. 45, no. 8, pp. 1614-1621, 2007.

[14] J. A. Berres and G. W. Hanson, "Multiwall carbon nanotubes at RF-THz frequencies: scattering, shielding, effective conductivity, and power dissipation," *IEEE Transactions on Antennas and Propagation*, vol. 59, no. 8, pp. 3098-3103, 2011.

[15] A. I. Sotiropoulos, I. V. Plegas, S. Koulouridis, and H. T. Anastassiu, "Scattering properties of carbon nanotube arrays," *IEEE Transactions on Electromagnetic Compatibility*, vol. 54, no. 1, pp. 110-117, 2012.

[16] M. Y. Wang, C. W. Qiu, J. Xu, Y. L. Dong, H. Zheng, and H. L. Li, "Mie series for electromagnetic scattering of chiral metamaterials sphere," *Journal of Systems Engineering and Electronics*, vol. 22, no. 6, pp. 885-891, 2011.

[17] M. Y. Wang, G. P. Li, M. Zhou, R. Wang, C. L. Zhong, J. Xu, and H. Zheng, "The effect of media parameters on wave propagation in a chiral metamaterials slab using FDTD," *International Journal of Numerical Modelling: Electronic Networks, Devices and Fields*, vol. 27, no. 1, pp. 109-121, 2014.

[18] L. Hai, M. F. Pantoja, S. G. Garcia, A. R. Bretones, and R. G. Martin, "An FDTD thin-wire model for modeling carbon nanotube dipoles at THz regime," *IEEE Antennas and Wireless Propagation Letters*, vol. 11, pp. 708-711, 2012.

[19] L. Q. Li, Y. X. Shi, F. Wang, and B. Wei, "SO-FDTD method of analyzing the reflection and transmission coefficient of weakly ionized dusty plasma layer," *Acta Phys. Sin.*, vol. 61, no. 12, pp. 125201, 1-5, 2012.

[20] S. G. Zhou, H. L. Li, L. Y. Fu, and M. Y. Wang, "Preliminary study on active modulation of polar mesosphere summer echoes with the radio propagation in layered space dusty plasma," *Plasma Science and Technology*, vol. 18, no. 6, pp. 607-610, 2016.

[21] A. Z. Elsherbeni and V. Demir, *The Finite-Difference Time-Domain Method For Electromagnetics With MATLAB Simulations*. SciTech Publishing, 2009.

[22] M. Y. Wang, H. L. Li, D. L. Gao, L. Gao, J. Xu, and C. W. Qiu, "Radiation pressure of active dispersive chiral slabs," *Opt. Express*, vol. 23, no. 13, pp. 16546-16553, 2015.

[23] K. Han, P. Freeman, H. Y. Han, J. Hamar, and J. F. Stack Jr., "Finite-difference time-domain modeling of ultra-high frequency antennas on and inside the carbon fiber body of a solar-powered electric vehicle," *The Applied Computational Electromagnetics Society*, vol. 29, no. 6, 2014.

[24] D. B. Ge, *Electromagnetic Wave Theory*. Xidian University Press, Xian, 1997.

[25] E. Dadrasnia, S. Puthukodan, and H. Lamela, "Terahertz electrical conductivity and optical characterization of composite nonaligned single- and multiwalled carbon nanotubes," *Journal of Nanophotonics*, vol. 8, no. 1, pp. 083099, 1-10, 2014.

[26] K. S. Lee, T. M. Lu, and X. C. Zhang. "Tera tool terahertz time-domain spectroscopy is a highly sensitive optical tool for dielectric and optical property characterization of thin film at terahertz frequency," *IEEE Circuits & Devices Magazine*, vol. 17, no. 5, pp. 23-28, 2002.

Mao Yan Wang was born in Shandong, China, 1979. She is currently an Associate Professor with University of Electronic Science and Technology of China (UESTC). Her research interests include millimeter wave circuit and systems, computation electromagnetic, and terahertz.

Hai Long Li was born in Shandong, China, in 1979. He is currently an Associate Professor with UESTC. His research interests include dusty plasma and high-power microwave technique.

Yu Liang Dong was born in Sichuan, China, 1972. He is currently an Associate Professor with UESTC. His research interests include millimeter wave hybrid integrated technology, millimeter wave communication and radar RF technology.

Gui Ping Li was born in Shanxi, China, 1974. She is currently a Lecturer with UESTC. Her research interests include microwave and millimeter-wave circuit and systems etc.

Cui Lin Zhong was born in Hunan, China, 1975. His current research interests include microwaves, antenna techniques, radio technology of wireless communication and radar.

Jun Xu was born in 1963. He is currently a Professor with UESTC. His research interests include millimeter wave hybrid integrated technology, communication and radar RF technology.

A Novel Approach of High Resolution Imaging using Modified Excitation Signal for Ground Penetration Radar (GPR) Applications

Homayoun Ebrahimian [1], Mohammad Ojaroudi [2], and Sajjad Ojaroudi [3]

[1] Department of Electrical Engineering
Ardabil Branch, Islamic Azad University, Ardabil, Iran
ebrahimian@iauardabil.ac.ir

[2] Department of Electric and Electronic Engineering
Ankara University, Ankara, Turkey
ojaroudi@ankara.edu.tr

[3] Young Researchers and Elite Club
Germi Branch, Islamic Azad University, Germi, Iran
s.ojaroudi.p@gmail.com

Abstract ─ In this paper a modified Gaussian pulse stimulus is employed to improve the accuracy of underground pipe localizing for 2D visualization of GPR results. This pulse shaping puts more energy at higher frequencies in contrast with conventional Gaussian in GPR. Hence, a wider bandwidth is available to achieve higher accuracy for precise spatial localization. Two dimensional simulations of GPR profiles over ground surface with and without conduits run with the finite-difference time-domain (FDTD) program GPRMAX are presented to validate the accuracy of the proposed method. Results from these surveys showed decent structural recovery of a small pipe similar in structure to that of the modeled ones. Finally, the dense surveys served as a benchmark to compare interpretations taken with the same surveys at lower spatial resolutions and profiles with 2D-only processing methods in order to understand errors in analysis and interpretation that are possible from 2D surveys.

Index Terms ─ Finite Difference Time Domain (FDTD), Gaussian Pulse, Ground Penetrating Radar (GPR), Pulse Shape Modulation (PSM).

I. INTRODUCTION

Ground penetrating radar is a type of nondestructive testing (NDT) techniques which uses electromagnetic waves to investigate the composition of non-conducting materials either when searching for buried objects or when measuring their internal structure. Information that can be obtained from GPR includes the depth, orientation, size and shape of buried objects, and the density and water content of soils [1]. The GPR performance is associated with the electrical and magnetic properties of local soil and buried targets. The choice of the central frequency and the bandwidth of the GPR are the key factors in the GPR system design. Although the higher frequencies are needed for better resolution and detailed echo to determine small size objects, the lower frequencies are preferred to detect something buried too deep because of the dramatically increased attenuation of the soil with increasing frequency. Thus, the pulsed GPR is used in order to benefit from both low and high frequencies. The pulsed GPR systems acquire pulse response in time domain directly.

A challenging problem in GPR is resolution improvement. Typically, if a GPR system has insufficient resolution, small or closely-spaced targets may be smoothed together into a single aberration in the waveform. This effect may not only obscure some targets, but it also may lead to inaccurate reflection readings. Rise time, settling time and pulse aberrations of the stimulus signal can also significantly affect a GPR system's resolution [2]-[3]. Also, many factors contribute to the accuracy of a GPR results. These factors include the GPR system's impulse response, probe and interconnect reflections and material losses, impulse amplitude accuracy, baseline correction and the accuracy of the reference reflection used in the measurements.

In this paper, we explore the advantages of generating a novel stimulus, similar to the traditional signal but instead of an impulse like (Gaussian) signals, a modified signal using new codes will be employed. The advantage conferred by "high resolution GPR" is that more energy is available at higher frequencies than with conventional step or impulse GPR, subsequently a relatively higher bandwidth and higher accuracy in

Submitted On: December 31, 2014
Accepted On: May 1, 2016

identifying the reflected voltage is achieved [4-5]. Simulated results using GPRMAX software are presented to validate the effectiveness of the proposed method for precisely calculating the time-dependent location of underground targets. The GPRMAX2D is electromagnetic wave software for GPR modelling [6]. It is based on FDTD method. In this work, we choose this simulator because of its simplicity of use and rapidity. The modified GPR code has a wider bandwidth that leads to higher accuracy localization of the various buried targets. Therefore, the GPR results in modified case follow the reference buried target more closely than does the ordinary GPR results with Gaussian pulse.

II. THEATRICAL BACKGROUND AND IMPLEMENTATION OF GPR IMAGING

This section describes the reflected voltage of microstrip discontinuity using the proposed stimulus signals and compares it with simulated reflected voltage obtained using ideal impulse and step GPRs. In order to illustrate the proposed method performance, a step-slit microstrip discontinuity with the listed design parameters were simulated (Fig. 1 (a)), and the GPR results of the input impedance for both using full-wave analysis using full wave GPR results using GPRMAX2D simulation tools are presented and discussed [7]-[8]. The proposed GPR test field with circular cylindrical pipe located underground is shown in Fig. 1 (a). Figure 1 (b) present the scan B which represents the passing over a zone in which simulated GPR was buried in horizontally position (a) and the result obtained by simulation (b). It can be observed that in the case of real measurements, the image is very noisy, containing, in addition, clutters. Using the specific technology of ultrasound examinations, the image from Fig. 1 (b) is a B scan made from 171 raw data A-scan type using GPRMAX2D.

The GPR characteristics for the proposed ground surface with pipe with Gaussian pulse as stimuli in Fig. 1 (b), obviously ideal impulse provides excellent time localization, corresponding to an extremely broad frequency bandwidth in the frequency domain. Typically, for ideal impulse excitation we can calculate exactly the amount of reflected energy at an interface as follows:

$$\Gamma_{1,2} = \frac{\sqrt{\varepsilon_{r1}} - \sqrt{\varepsilon_{r2}}}{\sqrt{\varepsilon_{r1}} - \sqrt{\varepsilon_{r2}}}, \quad (1)$$

where Γ is the reflection coefficient and ε_{r1} and ε_{r2} are the dielectric constants. Similarly, for ideal impulse excitation signal we can calculate precisely the thickness of a layer as follows:

$$d_i = \frac{C.t_i}{\left(2\sqrt{\varepsilon_{r,i}}\right)}, \quad (2)$$

where d_i is the thickness of layer i, t_i the total travel time through that layer, C is the speed of light and $\varepsilon_{r,i}$ the dielectric constant of the layer where L is the transmission line length, and ε_r is the relative permittivity of substrate. The penetration depth of GPR waves (in a low-loss medium) can be approximated as:

$$\delta(m) = 25\lambda = 25\frac{c}{f\sqrt{\varepsilon_r}}. \quad (3)$$

The vertical resolution (in a low-loss medium) is given roughly as:

$$R = \delta/100. \quad (4)$$

Ideal impulse provides excellent time localization, corresponds to an extremely broad frequency bandwidth in the frequency domain. For ideal impulse as excitation signal we can calculate exactly locations of discontinuities as follows, but in practice one can see that the waveform is distorted after the reflection and propagation. Because GPR receives signals already reflected from some distance, the time needed for passing the way back to the object and forth is longer than in a case when the antenna is situated slightly above the examined object. Because of this the cross-section of a pipe will be presented in the reading as a hyperbole.

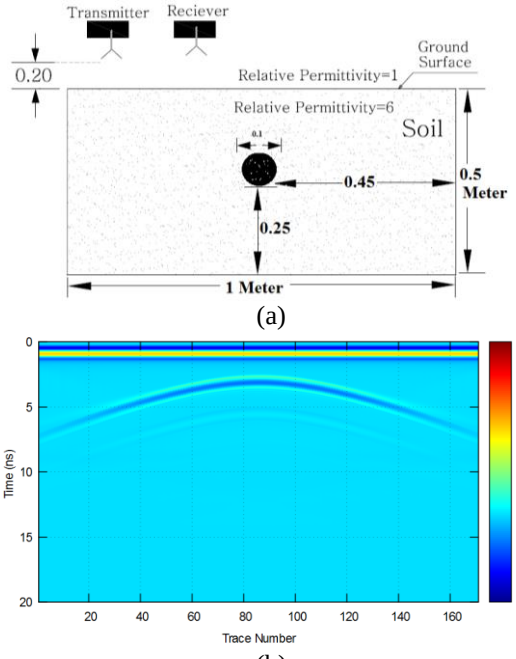

Fig. 1. Configuration of the proposed GPR test field with circular cylindrical pipe located underground, (a), scan B which represents the hyperbolic reflection from the pipe using GPRMAX 2D (b).

III. MODIFIED EXCITATION SIGNAL GENERATION BASED ON GAUSSIAN PULSE DERIVATIVES

The Gaussian pulse function $G(t,\tau)$ is part of a standard set of functions [9]. It is worth to note that

Gaussian pulses remain Gaussian distribution when they pass through any linear systems. A general formula of Gaussian pulse is shown in Equation (5), in which τ is a time constant. Gaussian monocycle is the first derivative of the Gaussian pulse and Gaussian doublet is the second derivative of a Gaussian pulse [10]. The general formulas for Gaussian monocycle and normalized Gaussian doublet are shown in Equations (6) and (7) respectively. These three signals with their spectrums are shown in Fig. 2 (a):

$$G(t,\tau) = e^{-\left(\frac{t-t_0}{\tau}\right)^2}, \tag{5}$$

$$\frac{dG(t,\tau)}{dt} = -\frac{t-t_0}{\tau} e^{-\left(\frac{t-t_0}{\tau}\right)^2}, \tag{6}$$

$$\frac{d^2G(t,\tau)}{dt^2} = \left[1-4\pi\left(\frac{t-t_0}{\tau}\right)^2\right] e^{-2\pi\left(\frac{t-t_0}{\tau}\right)^2}. \tag{7}$$

The Gaussian derivative functions have many interesting properties and will be reviewed here. When we take derivatives with respect to t (i.e., time derivatives) of the Gaussian function repetitively, we see a pattern emerging of a polynomial of increasing order, multiplied with the original (normalized) Gaussian function again. Examples are given for Gaussian derivative functions from order 0 up to order 2 (note the marked increase in amplitude for higher order of differentiation) are shown in Fig. 2. Figure 2 (b) shows normalized power spectra for Gaussian derivative filters, where the normalized power spectra shows it indicates that higher order of differentiation means a higher center frequency for the band-pass filter.

The Gaussian function itself is a common factor of all these higher order derivatives. We extract the polynomials by dividing the expression by the Gaussian function. These polynomials are the Hermite polynomials. They emerge from the following definition:

$$\frac{\partial^n e^{-t^2}}{\partial t^n} = (-1)^n H_n(t) e^{-t^2}. \tag{8}$$

The function $H_n(t)$ is the Hermite polynomial, where n is called the polynomial order. When we make the substitution $t \to \frac{t}{(\tau\sqrt{2})}$, we get the following relation between the Gaussian function $G(t,\tau)$ and its derivatives:

$$\frac{\partial^n G(t,\tau)}{\partial t^n} = (-1)^n \frac{1}{(\tau\sqrt{2})^n} H_n\left(\frac{t}{\tau\sqrt{2}}\right) G(t,\tau). \tag{9}$$

The amplitude of the Hermite polynomials explodes for large t, but the Gaussian envelope suppresses any polynomial function behavior. No matter how high the polynomial order is, the exponential function always dominates.

In this study, a novel method for designing a new excitation signal with high resolution characteristic for GPR is presented and illustrated in Fig. 3. A schematic of our new pulse shaping method, indicates that the system is comprised of three parts: differentiator, summation, and differentiator multiplier. The overall operation is generally given by M_N and represented by:

$$M_N(t) = \sum_{n=0}^{N} P_n . \frac{\partial^n G(t,\tau)}{\partial^n t}. \tag{10}$$

Specifically, formulas (11) and (12) show two examples of UWB pulses that can be used as stimulus waveforms in this study. Figure 4 shows these pulses with ordinary Gaussian pulse:

$$M_1(t) = p_0 . x(t) + p_1 \frac{dx(t)}{dt}, \tag{11}$$

with $p_0 = 1$ and $p_1 = 1$. M_1 provides the closest functional fit to the types of pulse shapes produced by our experimental hardware. Meanwhile, M_2 represents the third order of proposed method we called it waveform:

$$M_2(t) = p_0 . x(t) + p_1 \frac{dx(t)}{dt} + p_2 \frac{d^2x(t)}{dt^2}, \tag{12}$$

with $p_0 = 1$, $p_1 = 1$ and $p_2 = -1$.

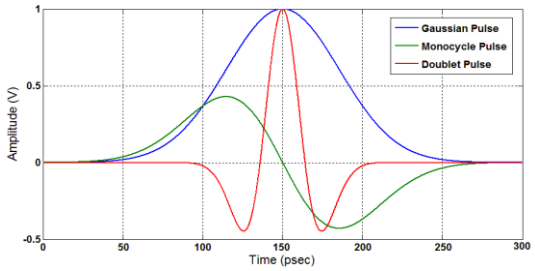

(a)

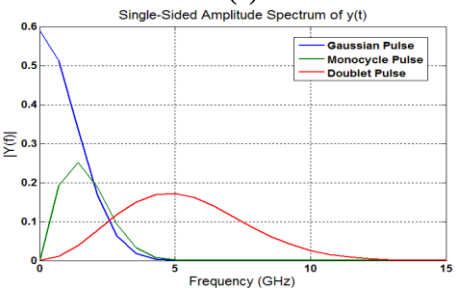

(b)

Fig. 2. Excitation waveforms used in the GPR simulations: (a) Gaussian pulse, monocycle pulse and normalized doublet pulse, and (b) frequency spectrum of each pulse. Gaussian derivative kernels act like band-pass filters [10].

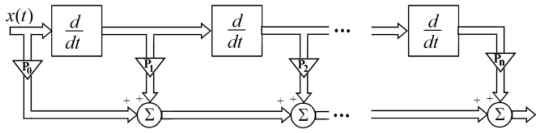

Fig. 3. The proposed schematic related to new excitation signal method.

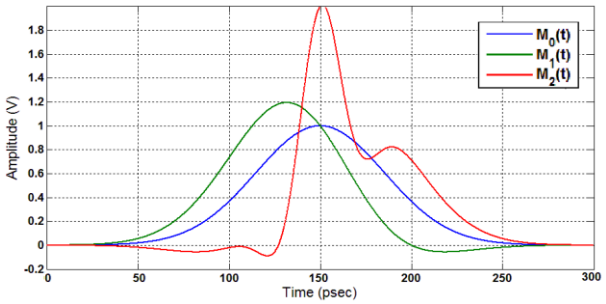

Fig. 4. The three first orders of stimulus signals generated by the proposed method used in the step GPR simulations.

IV. THE PROPOSED PULSE PERFORMANCE IN GPR RESULTS

Through processing raw data, simulated result by using GPRMAX, the image is achieved and shown in Fig. 5. Figure 5 shows the original image, before image signal processing using the excitation signals shown in Fig. 2 (a). The black and white lines are from the strong direct wave and surface reflection. Under them, three different metal objects are clearly distinguished. But the PVC pipe's image is not clear. Also, several small scatters were founded. According to the resolution, the depth resolution in the vertical plane and the distance resolution between two objects can be considered. The depth resolution of the ten of centimeters is obtained. The reason of lower depth resolution is that the lower frequency range is used. The measurements show that the developed UWB-GPR system has a good ability in detecting buried metal object, even small targets of several centimeters.

To improve the resolution of the GPR results and to show the effects of the proposed excitation signal generation method on these improvements, Fig. 5 shows the simulated reflection waveform with different shapes of our proposed excitation signal observed at the receiver. The corresponding results generated by M_1 and M_2 stimuli are shown in this figure. Two cases are studied for modified codes GPR. Using higher order coded stimulus leads better similarity to the ideal case. It is clearly shown to that GPR results with this proposed excitation signal have very good localization resolution and the peak amount errors at the center of discontinuities locations from ideal GPR results are small in this case in our simulation [11]. It is apparent from this figure, Fig. 6, that the energy in the modified GPR reflection exceeds the energy in the conventional GPR reflection. Additionally, in order to show the performance of the proposed method in multiple and complicated objects case, Fig. 7 shows another example with a pair of horizontal buried objects. As shown in Fig. 7, the modified GPR results follow the target more closely than does the ordinary step GPR results. Figures 6 and 7 indicate a discrepancy between simulated data and ideal results. This discrepancy is multi-reflection and assembly tolerances. The time characteristics for the GPR results are summarized in Table 1.

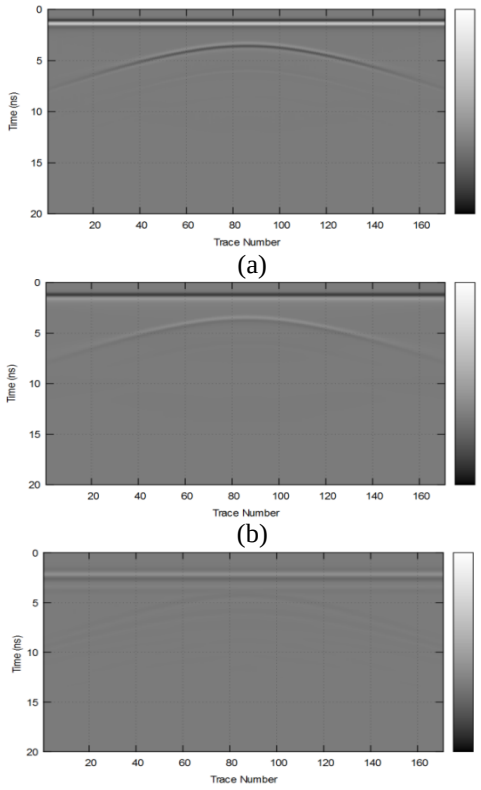

Fig. 5. GPR images before image signal processing using: (a) Gaussian, (b) monocycle, and (c) double.

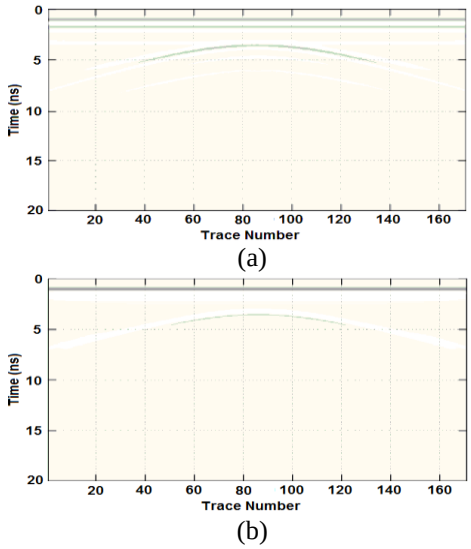

Fig. 6. GPR images after using the proposed method: (a) the first order, and (b) the second order.

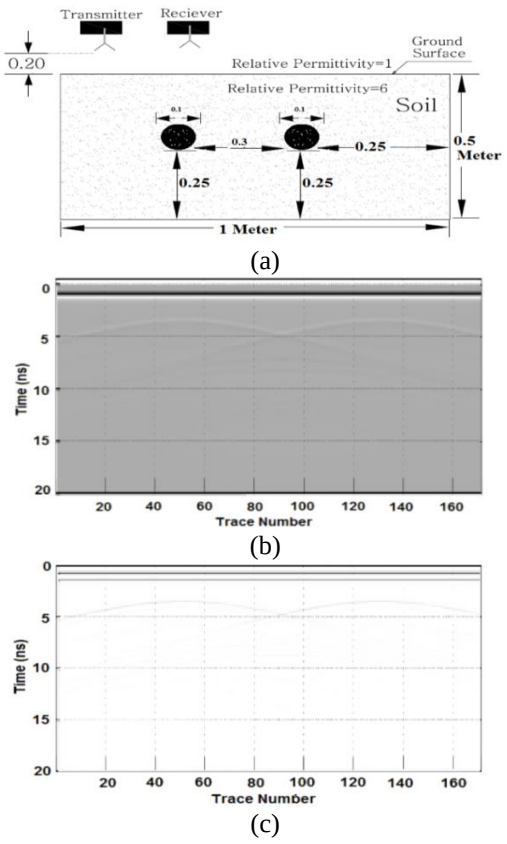

Fig. 7. (a) Configuration of the proposed GPR test field with a pair of horizontal circular cylindrical pipe located underground, (b) using conventional Gaussian pulse which represents the hyperbolic reflection from the pipes, and (c) after using the second order of the proposed method.

Table 1: The GPR characteristics of the proposed method in comparison with the ideal results

Parameter	Theoretical	M0(t)	M1(t)	M2(t)
$\Gamma_{1,2}$	-0.420	-0.39	-0.405	-0.41
d_1 (m)	0.1	0.23	0.17	0.14

V. CONCLUSION

In this paper, we present novel approach for high resolution GPR system that we designed a modified Gaussian pulse stimulus to improve the accuracy of localizing underground pipe for 2D visualization of GPR results. For the simulation the finite-difference time-domain (FDTD) program GPRMAX is used. Results obtained by our GPR system prove that our system has a good ability to finding buried targets with 1 cm resolution. The proposed modified GPR is very practical as it is based on more realistic signals rather than assuming ideal impulses. Additionally, our 2D visualization method proves that it possible to easily distinguish other buried objects. But there is one more reason why our program for 2D visualization is still in progress and improvement. Namely, we are aware that we are dealing, by the current method, with a lot of data that has to be processed in order to visualize buried objects.

REFERENCES

[1] I. Giannakis, A. Giannopoulos, and C. Warren, "A realistic FDTD numerical modeling framework of ground penetrating radar for landmine detection," in *IEEE Journal of Selected Topics in Applied Earth Observations and Remote Sensing*, vol. 9, no. 1, pp. 37-51, Jan. 2016.

[2] Z. Lin and W. Jiang, "Ground penetrating radar B-scan data modeling and clutter suppression," *2015 Fifth International Conference on Instrumentation and Measurement, Computer, Communication and Control (IMCCC)*, Qinhuangdao, pp. 397-402, 2015.

[3] S. Tan, H. Zhou, and L. Xiang, "An automatic framework using space-time processing and TR-MUSIC for subsurface imaging," *Ground Penetrating Radar (GPR), 14th International Conference on*, Shanghai, 2012, pp. 286-290, 2012.

[4] M. Ojaroudi, "Cognitive UWB imaging radar based on new approaches in cognitive visual neuroscience," *Advanced Radar Systems Journal*, vol. 3, pp. 1-7, Dec. 2014.

[5] M Ojaroudi, E. Mehrshahi, and A. Fathy, "A novel approach for the design of modified excitation signal using a narrow pulse generator for high-resolution time domain reflectometry applications," *Microwave and Optical Technology Letters*, vol. 56, no. 12, pp. 2987-2990, 2014.

[6] A. Giannopoulous, "Modelling ground penetrating radar by GprMax," *Science Direct*, pp. 755-762, 2 Aug. 2005.

[7] GPRMAX 3D/2D Software, copyright by Antonis Giannopoulos, 2005.

[8] C. Warren, A. Giannopoulos, and I. Giannakis, "An advanced GPR modelling framework: The next generation of gprmax," *Advanced Ground Penetrating Radar (IWAGPR), 8th International Workshop on*, Florence, 2015, pp. 1-4, 2015.

[9] G. E. Andrews, R. A. Askey, and R. Roy, *Special Functions*. Cambridge University Press, Cambridge, 2000.

[10] C. M. Bender and S. A. Orszag, *Advanced Mathematical Methods for Scientists and Engineers*. McGraw-Hill, New York, 1978.

[11] J. S. Lee and C. Nguyen, "Uniplanar picosecond pulse generator using step-recovery diode," in *Electronics Letters*, vol. 37, iss. 8, pp. 504-506, Apr. 2001.

Dynamical Chiral Metamaterial with Giant Optical Activity and Constant Chirality Over a Certain Frequency Band

F. Karadağ [1], İ. Çömez [1], F. Dinçer [2], M. Bakır [3], and M. Karaaslan [4]

[1] Department of Physics
Cukurova University, Adana, 01030, Turkey
fkaradag@cu.edu.tr, icomez2003@yahoo.com

[2] Department of Electrical Engineering
Kilis 7 Aralık University, Turkey
furkandincer@kilis.edu.tr

[3] Department of Informatics
Mustafa Kemal University, Turkey
mbakir@mku.edu.tr

[4] Department of Electrical and Electronic Engineering
Iskenderun Technical University, Turkey
muharrem.karaaslan@iste.edu.tr

Abstract ─ We demonstrate numerically and experimentally a dynamical chiral metamaterial that uniaxially creates giant optical activity and circular dichroism. In addition, the structure gives a high negative refractive index due to the large chirality. The proposed chiral metamaterial includes four L attached cross (FLAC) wire strips and offers a simple geometry, flexibility and more efficient results for chiral metamaterial applications such as polarization rotator, EM filter and so on. The experimental results are in a good agreement with the numerical simulation. It can be seen that FLAC wire strips based chiral metamaterial can also be used to achieve natural-small chirality with a constant value in a wide frequency range between 3.5-4.5 GHz. This is also another crucial feature of the structure. Therefore, the proposed chiral metamaterial with constant chirality value can be used to design novel EM devices such as polarization converter, anti-reflection filters for a certain frequency range.

Index Terms ─ Dynamical chiral metamaterials, natural-small chirality, optical activity, wide band.

I. INTRODUCTION

Metamaterials (MTMs) are defined as artificial electromagnetic (EM) materials that are rapidly developing as a research area due to having many potential application areas such as diffraction-limit breaking [1], cloaking [2], super lens [3], sensing [4, 5], absorber [6] and chiral metamaterial [7, 8]. Chiral media have received considerable attention in the recent years due to their potential applications in the fields of electromagnetic, microwave, and millimeter wave frequencies. The reason is that the chiral media shows exotic and individual properties such as giant optical activity and negative refraction. They are also MTMs made up of unit cells without mirror symmetry planes [9-14]. Giant optical activity is also realized by using gold nanostructures in the visible frequency range [15]. The broadband achievement of large optical activity is demonstrated in microwave regime by metamaterial with hybrid elements composed of twisted pairs of cross-shaped meta-atoms and their complements [16]. Conditions for the phase velocity to be directed opposite to the direction of power flow in a Faraday chiral medium are investigated and derived for a plane wave propagation in an arbitrary direction. It is observed that the phase velocity can be directed in the reverse direction to the power flow which provides that the gyrotropic parameter of the ferrite component medium is sufficiently large compared with the corresponding nongyrotropic permeability parameters [17]. It is also demonstrated that bright-bright, dark-dark, and dark-bright vector solitons can be formed in a spectral subregime in which one of the two Beltrami components exhibits a negative real refractive index when nonlinearity is ignored and the chirality parameter is sufficiently large [18, 19]. The optical theorem for an obstacle excited by a plane and a spherical wave mixed radiation-scattering theorems expressing the extinction cross section by means of the

Submitted On: February 1, 2016
Accepted On: April 14, 2016

secondary Beltrami field at the dipole's location is investigated [20]. In all these studies, general properties of chiral medium are theoretically derived dislikeness with the proposed structure in this study. The proposed study gives opportunities to the researchers to realize the mentioned theoretical outputs.

The major advantage of chiral MTMs over natural materials is that the macroscopic parameters can be designed to have desired values [14, 21]. This advantage provides the ability to control electromagnetic waves. Chiral media have different responses for a left circularly polarized (LCP, -) wave and a right circularly polarized (RCP, +) wave due to the intrinsic chiral asymmetry of the medium refractive index. This phenomenon is caused by the cross-coupling effect between the electric and magnetic fields through a chiral medium. These two circularly polarized waves then combine at the chiral-end and propagate out from the chiral media as an elliptically polarized wave based on circular dichroism. This ability is called as optical activity. κ describes chirality parameter and the strength of the cross-coupling effect, so that it is one of the constitutive relations of a chiral medium. Basically, chirality parameter is defined as the geometric property of a structure onto its mirror image. Chirality is also connected to the refractive index,

$$n^{\pm} = \sqrt{\varepsilon_r \mu_r} \pm \kappa. \quad (1)$$

They are characterized by the quantity of chirality,

$$\kappa = (n_+ - n_-)/2, \quad (2)$$

where n_+/n_- is the refractive index of the RCP or LCP waves and high chirality leads to negative refractive index. Furthermore, there are some studies on chiral metamaterials in literature [22-34]. Natural like chirality over a certain frequency band and strong optically active chiral metamaterials are also investigated in literature with different types of inclusions [31, 32]. Small chirality is achieved by rectangular split ring resonators in the same frequency band with the proposed metamaterial in this study but it doesn't demonstrate that the same resonators can be used to obtain huge values of chirality admittance [31].

In this study, we designed both numerically and experimentally FLAC wire strips based chiral MTM. In conventional chiral metamaterial studies, chirality based negative index of refraction, giant optical activity and very large circular dichroism is the main subject. The object of these studies is to realize both huge polarization conversion and negative refraction by using metamaterials with high chirality admittance. Unlike the mentioned conventional chiral metamaterial studies in literature, the suggested structure has very flexible feature because of its dynamical properties which provide mechanical tunability and present natural-small chirality with constant value in a wide frequency range between 3.5-4.5 GHz together with other conventional metamaterial potentials such as negative index of refraction, giant optical activity and very large circular dichroism. This is also another crucial feature of the structure comparing to the other literature studies. This provides to design novel EM devices such as polarization converter, anti-reflection filters for a certain frequency range [25-29]. Firstly, we designed a dynamical chiral MTM structure. When we changed arm-lengths of the structure, we observed that our dynamic chiral MTM structure has very flexible feature and it can also be used as a frequency shifter (because of the mechanical tunability). The parametric study is then realized by CST Microwave Studio (based on finite integration technique) to get the dimensions necessary for giant chirality between the frequency ranges of 1-6 GHz. Secondly, we measured the fabricated chiral MTM structures for 1-6 GHz by Rohde & Schwarz vector network analyzer (VNA) and microwave horn antennas. We evaluated and compared the simulation and experimental results. Obtained results show that experimental results are in a good agreement with the numerical simulation. Besides, the strong chirality and negative refractive index due to this strong chirality are obtained. In addition, the proposed dynamical chiral metamaterial has natural-small chirality with a constant value at a wide range of frequency between 3.5-4.5 GHz.

The organization of this paper is as follows. In Section II, the experiment and simulation of the chiral MTM structure based on FLAC wire strips-based chiral structure is proposed, the experimental and simulation methods are presented. In Section III, generalization of the idea and designs of chiral structures are introduced. Finally, summary and conclusions are provided in Section IV.

II. EXPERIMENT AND SIMULATION SETUP

The resonant behavior of the proposed structure is achieved by the geometry dependent capacitive elements such as gaps and strips. EM interaction between strips and gaps can be arranged by playing with the geometrical configuration of the structure such as shape and size. This provides mechanical tunability for the suggested structure to obtain well optical activity as desired. The main purpose of this geometry is to provide simpler structure that offers more flexibility and reliability on the control of incident EM wave polarization and simplifies the manufacturing process.

Designed structure consists of wire strips and their mirror image which are patterned at the front and back side of a host dielectric substrate, respectively. In the present work the selected host material is FR-4; a high frequency laminate with a thickness of 1.6 mm, relative permittivity of 4.2, relative permeability of 1 and loss tangent of 0.02. The cross wire strip-shapes are made of copper with a thickness of 0.036 mm and electrical conductivity of $5.8x10^7\ S/m$. The dimensions of the structure are presented in Fig. 1 (a). After the designing phase, we fabricated dynamic chiral MTM sample

structure with print circuit board technique as shown in Fig. 1 (b). Samples are simulated with a commercial full-wave EM solver, CST Microwave Studio (Computer Simulation Technology GmbH, Darmstadt, Germany), which uses a finite integration technique to determine reflection and transmission properties. In addition, boundary conditions are assigned as unit-cell (side surfaces) and open add space (front and back surfaces) boundary conditions in the simulation.

The experimental measurement setup consists of a VNA and two microwave horn antennas as shown in Fig. 1 (c). Two microwave horn antennas are connected to the VNA to measure the S-parameters. In the measurements, one horn acts as a transmitter and the other one detects the transmitted or reflected wave. Firstly, free space measurement without the chiral structure is carried out and this measurement used as the calibration data for the VNA. The structure is then inserted into the experimental measurement setup and S-parameter measurements are performed as co-polar and cross-polar reflection/ transmission coefficients. Initially, the distance between the horn antennas and chiral slab is kept sufficiently large to eliminate unwanted near-field effects.

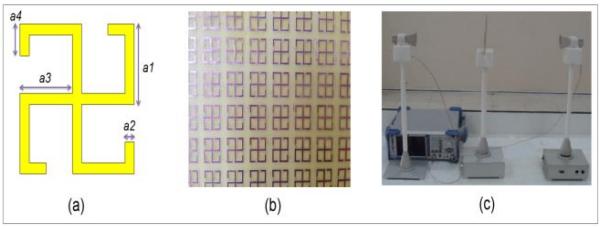

Fig. 1. (a) Schematic representation dimensions of one unit cell of the proposed resonator (a1=5.8 mm, a2=0.8 mm, a3=4.6 mm, a4=3.3 mm), (b) picture of the front side of the fabricated sample, and (c) a picture from the measurement setup.

III. NUMERICAL AND EXPERIMENTAL RESULTS OF THE PROPOSED STRUCTURE

Figure 2 shows the simulation and experimental results of the reflection coefficient (R), and transmission coefficients ($T+, T-$), as a function of frequency, respectively. The experimental results agree well with the numerical simulation. The transmission results for RCP ($T+$) and LCP ($T-$), split into two curves are obtained. There are two different resonance peak points in our structure. Dynamic structure of our chiral MTM provides this feature. It can be seen that the resonances are observed around the frequency of 3.1 and 5.6 GHz for transmission and reflection coefficients. The differentiation of the $T+$ and $T-$ provides optical activity, i.e., dynamical chirality due to the asymmetric resonance properties of the proposed structure.

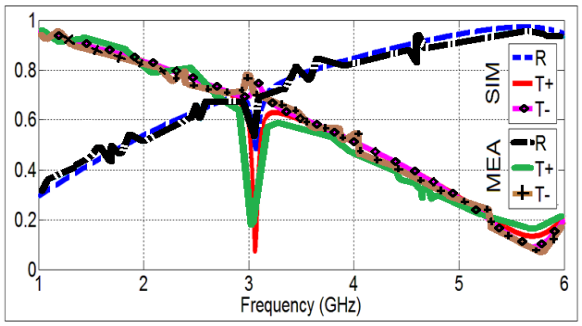

Fig. 2. Numerical and experimental results for $Abs\ (R)$, $Abs\ (T+)$, and $Abs\ (T-)$.

From the following retrieval results [22-34], the difference between the phases of RCP and LCP transmitted wave is characterized as the polarization azimuth rotation angle θ which is calculated by:

$$\theta = \frac{1}{2}[\arg(T_+) - arg(T_-)], \quad (3)$$

and demonstrated in Fig. 3 for simulation and experimental results, in order. Furthermore, we conclude that only at the resonance frequencies, the transmission spectra for the RCP and LCP waves are significantly different. This difference is due to the unmatched transmission behavior of RCP and LCP waves. Beside this, minor difference between RCP and LCP waves can be seen in the frequency range of 3.1-4.5 GHz. The small difference results in both minor asymmetric transmission and natural-small chirality. This difference between the amplitudes of two transmissions is characterized by ellipticity of the transmitted wave by the equation:

$$\eta = 0.5\tan^{-1}(|T_+|^2 - |T_-|^2)/(|T_+|^2 + |T_-|^2), \quad (4)$$

as shown in Fig. 4.

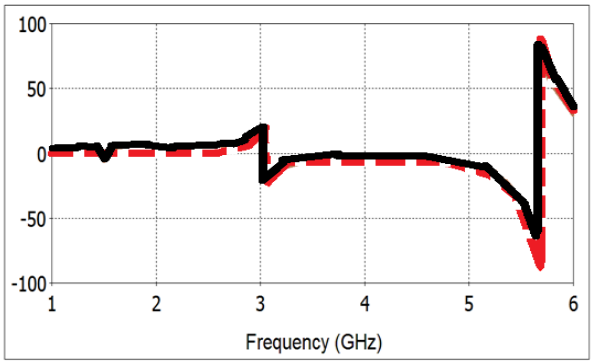

Fig. 3. Numerical (red-line) and experimental results (black-line) for theta (θ – degree).

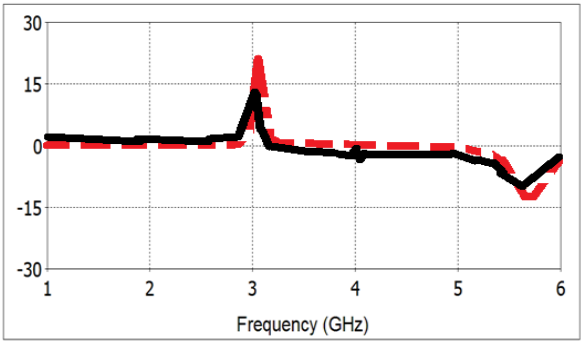

Fig. 4. Numerical (red-line) and experimental results (black-line) for ellipticity (η – degree).

Effective constitutive parameters are also evaluated using transmission and reflection parameters with retrieval formulas. These formulas can also be used to obtain chirality of the effective media from the RCP and LCP elements of the transmitted wave. The chirality κ can be obtained directly from the transmissions as:

$$Re(\kappa) = [\arg(T+) - \arg(T-) + 2m\pi]/(2k_0 d), \quad (5)$$

where k_0 is the wave vector in the vacuum, d is the thickness of the structure and m is an integer which guarantees the result to be physically meaningful. T_+ and T_- values are restricted by $-\pi < \arg(T_+) - \arg(T_-) + 2m\pi < \pi$ [22-34].

The average refractive index,

$$n = (n_L + n_R)/2, \quad (6)$$

and the impedance z can be obtained by using the traditional retrieval procedure by:

$$n_\pm = \frac{i}{k_0 d}\left\{\log\left[\frac{1}{T_\pm}(1 - \frac{\zeta-1}{\zeta+1}R)\right] \pm 2m\pi\right\}, \quad (7)$$

[25, 26] after taking the geometric average of transmission components with RCP and LCP transmitted wave ($T = \sqrt{T_+ T_-}$). In addition, the impedance can be extracted by:

$$\zeta = \pm\sqrt{\frac{(1+R)^2 - T_+ T_-}{(1-R)^2 - T_+ T_-}}. \quad (8)$$

The other retrieval parameters can then be calculated by $n_\pm = n \pm \kappa$, $\varepsilon = n/\zeta$, and $\mu = n\zeta$ [30-36]. Figures 5-7 show the retrieval results.

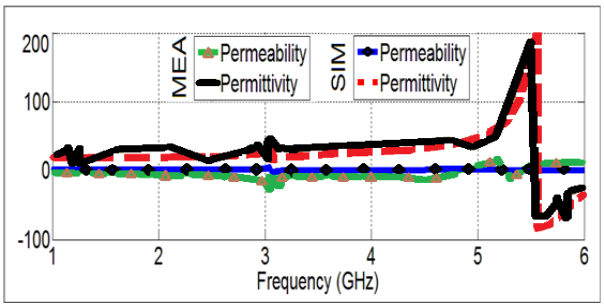

Fig. 5. Numerical and experimental results for permittivity and permeability values.

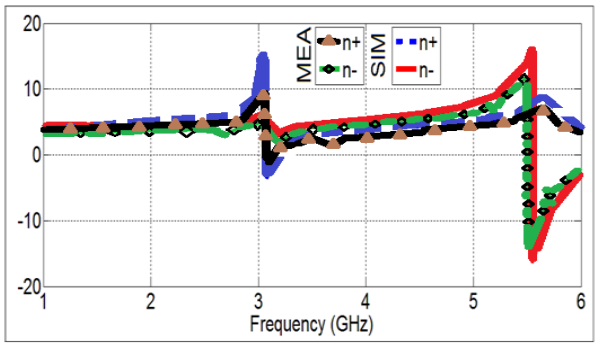

Fig. 6. Numerical and experimental results for n(+) and n(-) values.

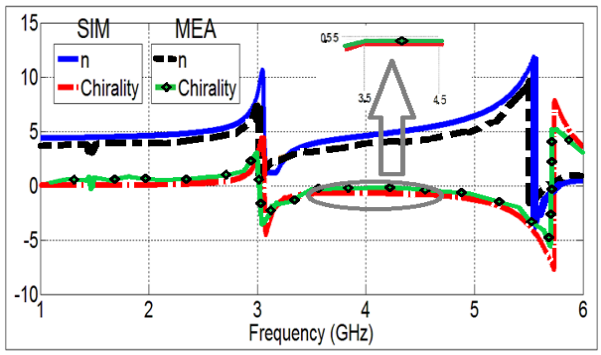

Fig. 7. Numerical and experimental results for n and chirality values.

It is clearly shown that the relative permeability is around 1 and small changes are observed around resonance frequencies. Besides, relative permittivity has also ripples around the resonance frequencies. The relative permittivity reduces to -95 at around the second resonance frequency. The RCP and LCP elements of effective index are shown in Fig. 6. The difference between them proves the asymmetric phenomena and optical activity of the overall structure.

The effective refractive index and chirality are shown in Fig. 7. Although the effective permittivity and permeability are not simultaneously negative at the second resonance frequency, the effective refractive index is negative. This is caused by the strong chirality at the same frequency. Beside this, another important phenomenon is the small-natural chirality observed between 3.1-4.5 GHz. A small-natural chirality phenomenon for chiral metamaterials has not been studied so far in the literature. The observed chirality is very small as natural chiral substances. Hence, this structure can be used in many applications such as polarization conversion, anti-reflection filter and so on. If the geometry of the dynamic chiral metamaterial is reduced to nanoscale, the proposed structure can be easily used as chiral sensor. One another advantage of

the proposed structure is constant value (~0.55) of the chirality for a wide range of frequency (3.5-4.5 GHz) (Inset in Fig. 7). Therefore, the proposed structure supposes polarization conversion with in all the frequencies in the range.

In order to show physical mechanism, we investigated the resonance electric field and surface current distributions for both resonance frequencies as presented in Figs. 8 and 9, respectively. As shown in Fig. 8, especially electric field distribution is strongly concentrated at the resonance frequency of 5.68 GHz according to the first resonance. However, electric field distributions are concentrated around the gaps due to EM interaction between layers. Moreover for Fig. 9, it can be seen that the magnetic field strongly concentrates at the resonance frequency of 3.08 GHz according to the second resonance frequency of 5.68 GHz. This situation verifies the character of the resonances as magnetic ones as indicated above. In addition, the intensity of the current is highly strengthened at the surface of the center resonators at the resonance. The surface current distribution at 5.68 GHz is particularly given to show their different characters.

It is well known that a material can only have chirality characteristics if it shows both electric and magnetic responses. It means that when electric field component is incident towards the structure, it results in magnetic response and vice versa. Since EM wave includes both electric and magnetic field components, it is not possible to decide exactly to the response of the structure. The magnetic response of the structure can be estimated by following the continuous current paths between front and backside inclusions of chiral metamaterial. Whereas the current distributions along centers of both front and back sided inclusions at 3.08 GHz is higher than that of 5.68 GHz, these currents are along the same direction. Therefore, this orientation does not contribute to the chirality admittance as well oriented inclusions. Whereas, the magnitude of the current is not high as the first one, both orientations are continuous and demonstrate instructive effect for 5.68 GHz. Hence, the chirality admittance is higher at this frequency value.

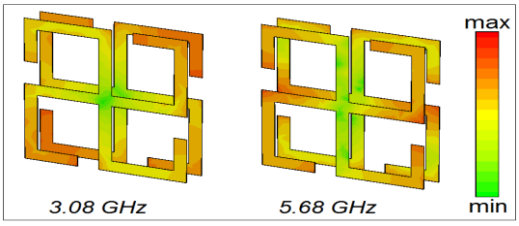

Fig. 8. Electric field distributions at the resonance frequencies.

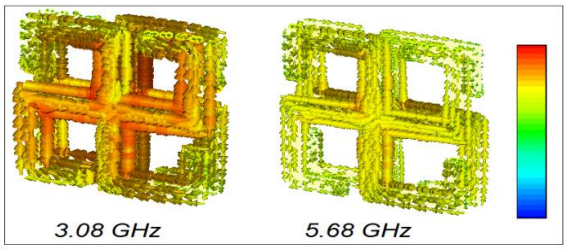

Fig. 9. Surface current distributions at the resonance frequencies.

IV. CONCLUSION AND DISCUSSION

In summary, we numerically and experimentally designed and studied a dynamical chiral MTM based on four L attached cross (FLAC) wire strips which has very simple geometry and features of wide-band chirality and mechanical tunability. The presented dynamic chiral design offers a much more efficient fabrication because of the feasible geometry. The experimental results are in a good agreement with the numerical simulation. This chiral MTM has very adaptable properties, including negative index of refraction due to chirality, giant optical activity and very large circular dichroism. Besides, the proposed chiral structure offers a natural-small chirality with a constant value at a wide frequency range between 3.5-4.5 GHz. This advantageous is the crucial point of the study. By using this property, it is possible to design polarization converter with constant amount in a wide range of frequency. In addition, the structure can be used as a sensor of chiral substances by placing between two layers of it. Therefore, the suggested dynamical chiral MTM has many potential applications in order to create configurable polarization rotator, sensors and so on.

ACKNOWLEDGMENT

This work is supported by the TUBITAK under Projects No: 113E290. One of the authors M. K. also acknowledges partial support from the Turkish Academy of Sciences.

REFERENCES

[1] J. S. Lih, J. S. Wang, M. C. Lu, Y. C. Huang, K. H. Chen, J. L. Chern, and L. E. Li, "Experimental realization of breaking diffraction limit by planar negative-index metamaterials in free space," *Europhys. Lett.*, vol. 69, pp. 544-549, 2005.

[2] J. B. Pendry, "A chiral route to negative refraction," *Science*, vol. 306, pp. 1353-1355, 2004.

[3] S. Tretyakov, I. Nefedov, A. Sihvola, S. Maslovski, and C. Simovski, "Waves and energy in chiral nihility," *J. Electromagn. Waves Appl.*, vol. 17, pp. 695-706, 2003.

[4] C. Monzon and D. W. Forester, "Negative refraction and focusing of circularly polarized waves in

optically active media," *Phys. Rev. Lett.*, vol. 95, pp. 123904-123908, 2005.

[5] S. Tretyakov, A. Sihvola, and L. Jylha, "Negative refractions and backward waves in biaxially anisotropic chiral media," *Phys. Condens. Matter.*, vol. 3, pp. 107-112, 2005.

[6] V. Yannopapas, "Circular dichroism in planar nonchiral plasmonic metamaterials," *J. Phys. Condens. Matter*., vol. 18, pp. 6883-6890, 2006.

[7] Z. Shuang, P. Yong-Shik, L. Jensen, L. Xinchao, Z. Weili, and Z. Xiang, "Negative refractive index in chiral metamaterials," *Phys. Rev. Lett*., vol. 102, pp. 023901-023908, 2009.

[8] F. Dincer, C. Sabah, M. Karaaslan, E. Unal, M. Bakir, and U. Erdiven, "Asymmetric transmission of linearly polarized waves and dynamically wave rotation using chiral metamaterial," *Progress In Electromagnetics Research*, vol. 140, pp. 227-239, 2013.

[9] K. Delihacioglu and S. Uckun, "Power reflection and transmission coefficients for meander L line polarizers with chiral slab," *ETRI Journal*, vol. 25, no. 1, pp. 41-48, 2003.

[10] D. Zarifi, M. Soleimani, and V. Nayyeri, "Dual- and multiband chiral metamaterial structures with strong optical activity and negative refraction," *IEEE Antennas and Wireless Propagation Letters*, vol. 11, pp. 334-337, 2012.

[11] C. Sabah and H. G. Roskos, "Design of a terahertz polarization rotator based on a periodic sequence of chiral-metamaterial and dielectric slabs," *Progress In Electromagnetics Research*, vol. 124, pp. 301-314, 2012.

[12] C. Sabah, "Multiband metamaterials based on multiple concentric open-ring resonators topology," *IEEE Journal of Selected Topics in Quantum Electronics*, vol. 19, pp. 8500808, 2013.

[13] F. Karadag and M. Karaaslan, "Artificial diamagnetic metamaterial loaded sub-wavelength waveguide with reduced bianisotropic effect: Design, fabrication and characterization," *Optoelectronics and Advanced Materials Rapid Communications*, vol. 3, no. 6, pp. 574-7, 2009.

[14] J. Zhou, J. Dong, B. Wang, T. Koschny, M. Kafesaki, and C. M. Soukoulis, "Negative refractive index due to chirality," *Physical Review B*, vol. 79, pp. 121104, 2009.

[15] M. Kuwata-Gonokami, et al., "Giant optical activity in quasi-two-dimensional planar nanostructures," *Phys. Rev. Lett*., vol. 95, 227401, 2005.

[16] K. Hannam, D. A. Powell, I. V. Shadrivov, and Y. S. Kivshar, "Broadband chiral metamaterials with large optical activity," *Phys. Rev. B*, vol. 89, 125105, 2014.

[17] T. G. Mackay and A. Lakhtakia, "Plane waves with negative phase velocity in Faraday chiral mediums," *Phys. Rev. E*, vol. 69, 026602, 2004.

[18] N. L. Tsitsas, A. Lakhtakia, and D. J. Frantzeskakis, "Vector solitons in nonlinear isotropic chiral metamaterials," *J. Phys.*, vol. 44, 435203, 2011.

[19] A. Lakhtakia, "Beltrami fields in chiral media," *World Scientific*, Singapore, 1994.

[20] C. Athanasiadis and N. L. Tsitsas, "Radiation relations for electromagnetic excitation of a layered chiral medium by an interior dipole," *J. Math. Phys.*, vol. 49, 013510, 2008.

[21] B. Wang, T. Koschny, and C. M. Soukoulis, "Wide-angle and polarization-independent chiral metamaterial absorber," *Physical Review B*, vol. 80, pp. 033108-4, 2009.

[22] R. Marques, L. Jelinek, and F. Mesa, "Negative refraction from balanced quasi-planar chiral inclusions," *Microw. Opt. Technol. Lett*., vol. 49, pp. 2606-9, 2007.

[23] F Dincer, M Karaaslan, O Akgol, E Unal, E Demirel, and C Sabah, "New generation planar chiral metamaterials with small and constant chirality over a certain frequency band," *Modern Physics Letters B*, vol. 29, no. 01, pp. 1450257, 2015.

[24] J. D. Baena, L. Jelinek, and R. Marques, "Towards a systematic design of isotropic bulk magnetic metamaterials using the cubic point groups of symmetry," *Phys. Rev. B.*, vol. 76, pp. 245115, 2007.

[25] C. Akturk, M. Karaaslan, E. Ozdemir, V. Ozkaner, F. Dincer, M. Bakir, and Z. Ozer, "Chiral metamaterial design using optimized pixelated inclusions with genetic algorithm," *Optical Engineering*, vol. 54 no. 3, pp. 035106-035106, 2015.

[26] R. Zhao, T. Koschny, and C. M. Soukoulis, "Chiral metamaterials: Retrieval of the effective parameters with and without substrate," *Optics Express*, vol. 18, no. 14, pp. 14553-67, 2010.

[27] I. Comez, M. Karaaslan, F. Dincer, F. Karadag, and C. Sabah, "Systematic analysis on the optical properties of chiral metamaterial slab for microwave polarization control," *Applied Computational Electromagnetics Society Journal*, vol. 30, no. 5, pp. 478-487, 2015.

[28] Z. Wu, B. Q. Zhang, and S. Zhong, "A double-layer chiral metamaterial with negative," *J. Electromagn. Waves Appl*., vol. 24, no. 7, pp. 983-992, 2010.

[29] F. Dincer, M. Karaaslan, E. Unal, O. Akgol, and C. Sabah, "Flexible chiral metamaterials with dynamically optical activity and high negative refractive index," *Modern Physics Letters B*, vol. 29, no. 18, pp. 1550087, 2015.

[30] M. C. K. Wiltshire, J. B. Pendry, and J. V. Hajnal, "Chiral swiss rolls show a negative refractive index," *Journal of Physics: Condensed Matter*, vol.

21, pp. 292201-5, 2009.
[31] Z. Li, R. Zhao, T. Koschny, M. Kafesaki, K. B. Alici, E. Colak, H. Caglayan, E. Ozbay, and C. M. Soukoulis, "Chiral metamaterials with negative refractive index based on four "U" split ring resonators," *Applied Physics Letters*, vol. 97, pp. 081901-3, 2010.
[32] F. Dincer, M. Karaaslan, O. Akgol, E. Unal, and C. Sabah, "Dynamic and tunable chiral metamaterials with wideband constant chirality over a certain frequency band," *Optik-International Journal for Light and Electron Optics*, vol. 126, no. 24, pp. 4808-4812, 2015.
[33] R. Zhao, L. Zhang, J. Zhou, T. Koschny, and C. M. Soukoulis, "Conjugated gammadion chiral metamaterial with uniaxial optical activity and negative refractive index," *Physical Review B*, vol. 83, pp. 035105, 2011.
[34] Z. Li, K. B. Alici, E. Colak, and E. Ozbay, "Complementary chiral metamaterials with giant optical activity and negative refractive index," *Applied Physics Letters*, vol. 98, pp. 161907-3, 2011.
[35] C. Sabah, F. Dincer, M. Karaaslan, O. Akgol, E. Demirel, and E. Unal, "New-generation chiral metamaterials based on rectangular split ring resonators with small and constant chirality over a certain frequency band," *IEEE Trans. Antennas Propagat.*, vol. 62, pp. 5745-5751, 2014.
[36] F. Dincer, M. Karaaslan, E. Unal, O. Akgol, and C. Sabah, "Chiral metamaterial structures with strong optical activity and their applications," *Optical Engineering*, vol. 53, 107101, 2014.

İbrahim Comez received the M.S. degree in Physics Department from the University of Cukurova, Adana, Turkey. He is currently studying Metamaterials and Chiral Media as a Ph.D. student. His research interests are metamaterials, solid state physics, cihral, and anisotropic media.

Muharrem Karaaslan received the Ph.D. degree in Physics Department from the University of Cukurova, Adana, Turkey, in 2009. He is the co-author of about 70 scientific contributions published in journals and conference proceedings. His research interest are applications of metamaterials, analysis and synthesis of antennas, and waveguides.

Faruk Karadag received the Ph.D. degree in Physics Department from the University of Çukurova, Adana, Turkey, in 2002. He is the co-author of about 25 scientific contributions published in international journals and conference proceedings. His research interest includes the applications of metamaterials, solid state physics, and anisotropic media.

Furkan Dincer received the B.Sc., M.Sc., and Ph.D. degrees in Electrical and Electronics Engineering from Sutcu Imam, Yuzuncu Yil and Mustafa Kemal Universities, Turkey. His research interests are related with the functional microwave structures and metamaterials.

UWB Slot Antenna with Band-Notched Property with Time Domain Modeling based on Genetic Algorithm Optimization

Javad Zolghadr [1], Yuanli Cai [1], and Nasser Ojaroudi [2]

[1] School of Electronic and Information Engineering, Xi'an Jiaotong University, Xi'an 710049, China
Javad.zolghadr@gmail.com, ylicai@mail.xjtu.edu.cn

[2] Young Researchers and Elite Club, Ardabil Branch, Islamic Azad University, Ardabil, Iran
n.ojaroudi@yahoo.com

Abstract ─ This paper presents a kind of band-notched slot antenna with time domain designing method for ultra-wideband (UWB) applications. The proposed antenna consists of a square radiating stub with a defected mircostrip feed-line using an M-shaped step impedance resonator (SIR) slot and a defected ground plane with a pair of inverted U-shaped slots. By cutting two inverted U-shaped slots in the ground plane, a new resonance at the higher frequencies is excited and hence much wider impedance bandwidth can be produced that. To generate a band-notched characteristic, we use an M-shaped slot at the feed-line. The proposed antenna can operate from 3.03 to 13.21 GHz with frequency band-notched function in 7.28-7.79 GHz to avoid interference from downlink of X-band satellite communication systems. To verify the validation of the proposed antenna an equivalent circuit based on time domain reflectometry (TDR) analysis is presented. In addition, the accuracy of the equivalent circuit models have been improved using Genetic algorithm optimization (GAP). Detailed simulation and numerical investigations are conducted to understand their behaviors and optimize for broadband operation. The proposed antenna exhibits almost omni-directional radiation patterns in UWB frequency range and could be used in wireless systems.

Index Terms ─ Band-notched function, GAP, microstrip-fed slot antenna, TDR analysis, UWB systems.

I. INTRODUCTION

In UWB communication systems, one of key issues is a design of compact antennas while providing wideband characteristic over the whole operating band [1]. Consequently, a number of planar antennas with different geometries have been experimentally characterized [2-5] and automatic design methods have been developed to achieve the optimum planar shape. Moreover, other strategies to improve the impedance bandwidth have been investigated [6-8]. The frequency range for UWB systems between 3.1–10.6 GHz will cause interference to the existing wireless systems for example the wireless local area network (WLAN) for IEEE 802.11a operating in 5.15–5.35 GHz and 5.725–5.825 GHz bands or 7.25-7.75 GHz for downlink of X-band satellite systems, so the UWB antenna with a band-notched function is required [9-15].

In this paper, a simple method for designing a novel and compact microstrip-fed slot antenna with band-stop performance and time domain reflectometry analysis for UWB applications has been presented. In the proposed antenna for bandwidth enhancement, based on defected ground structures (DGS) we use a pair of inverted U-shaped slots in the ground plane and also based on defected microstrip structures (DMS) theory, to generate a band-stop performance an M-shaped slot was inserted at feed-line [16]. Unlike other band-notched UWB antennas reported in the literature to date, this structure has an ordinary square radiating stub configuration. We also report their circuit models based on TDR analysis. The proposed band-notched UWB antenna has a compact size. Good VSWR and radiation pattern characteristics are obtained in the frequency band of interest. Simulated and measured results are presented to validate the usefulness of the proposed microstrip-fed slot antenna structure for UWB applications.

II. ANTENNA DESIGN

The presented slot antenna fed by a 50 Ω microstrip line is shown in Fig. 1, which is printed on an FR4 substrate of width W_{sub}=20 mm and length $L_{sub} = 20mm$, thickness 0.8 mm, permittivity 4.4, and loss tangent 0.018. The basic antenna structure consists of a square radiating stub, a feed line, and a ground plane. The radiating stub is connected to a feed line of width W_f=1.5 mm and length L_f=5 mm. The equivalent circuit model of the proposed design is illustrated in Fig. 2. The antenna is designed to work at the frequency range of from 3.03 to 13.21 GHz.

Submitted On: October 22, 2013
Accepted On: June 17, 2016

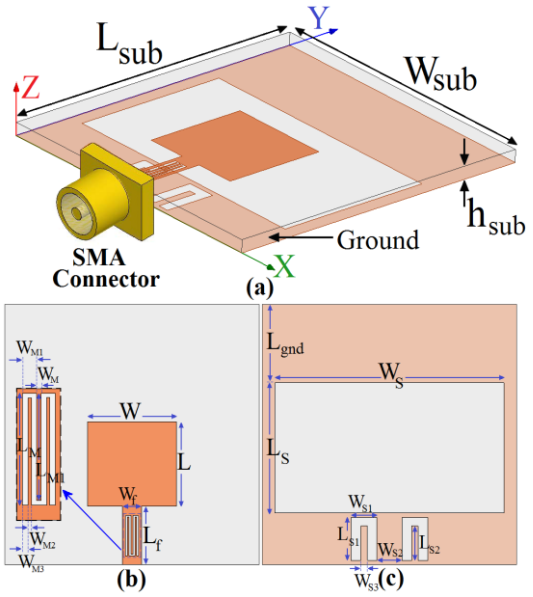

Fig. 1. Geometry of the proposed slot antenna: (a) side view, (b) top layer, and (c) bottom layer.

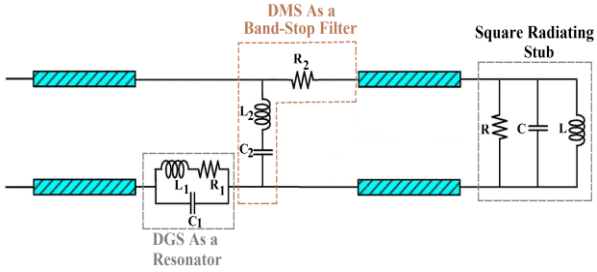

Fig. 2. The proposed antenna equivalent circuit model.

The proposed antenna is connected to a 50 Ω SMA connector for signal transmission. The final dimensions of the designed antenna are as follows:

$W_{sub} = 20mm$, $L_{sub} = 20mm$, $h_{sub} = 0.8mm$, $W = 7mm$, $L = 7mm$, $W_f = 1.5mm$, $L_f = 5mm$, $W_S = 18mm$, $L_S = 10mm$, $W_{S1} = 2mm$, $L_{S1} = 4.7mm$, $W_{S2} = 2mm$, $L_{S2} = 2.85mm$, $W_{S3} = 0.5mm$, $L_M = 3.7mm$, $W_M = 0.2mm$, $L_{M1} = 3.6mm$, $W_{M1} = 0.5mm$, $W_{M2} = 0.15mm$, and $L_{gnd} = 6mm$.

A. Defected structures (DGS and DMS) and these equivalent circuit models

Recently, defected ground plane structures (DGS) and defected microstrip structure (DMS) have been proposed for suppression of spurious response in the microstrip structures [17-18]. These configurations provide the band-stop characteristics.

The proposed DGS and DMS with their equivalent circuit models are shown in Fig. 3, which is printed on a FR4 substrate of thickness 0.8 mm, permittivity 4.4, and loss tangent 0.018. The corresponding geometrical parameters of the proposed structures are denoted in Fig. 3. This defected ground structures on the ground plane and feed-line will perturb the incident and return current and induce a voltage difference on the ground plane and microstrip feed-line. The proposed DGS can be modeled as a resonator with parallel LC circuit [19]. The resistance in equivalent circuits represents the loss of the slot and slit, which is small in general [20]. The proposed DMS act as a band-stop filter therefore can be modeled with series and parallel LC circuit.

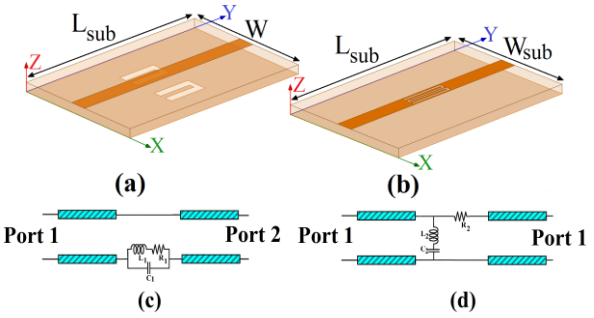

Fig. 3. The proposed defected structures, (a) DGS and (b) DMS with their equivalent circuit models in (c) and (d).

B. Time domain reflectometry analysis

In this section, the proposed defected structures with mentioned design parameters were simulated, and the TDR results of the input impedance for them in equivalent circuit and full-wave analysis cases are presented and discussed. The simulated full-wave TDR results are obtained using the Ansoft simulation software high-frequency structure simulator (HFSS) [21].

Figures 4 and 5 show the simulated reflection waveform observed at Port1 of the defected structures, as shown in Fig. 3 (a) and Fig. 3 (b), and with a 50 termination on Port2. The excitation source is a step wave with amplitude 1Volt and rise time of 30psec. The corresponding result predicted by the equivalent circuit model is also shown in these figures. As shown in Figs. 4 and 5, TDR curves have started with impedance just under 50 Ω. This is indeed the characteristic impedance of the microstrip line. At impedance discontinuities, part of the input signal is reflected. These reflections, after traveling back, reach terminal Port1 and are observed there [12]. From these observations, the characteristic impedances along the transmission line can be computed. The optimal dimensions of the equivalent circuit models parameters are specified in Table 1.

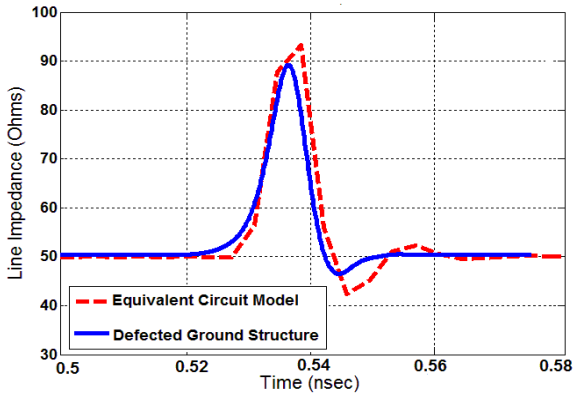

Fig. 4. The reflected waveforms simulated by HFSS and predicted by equivalent circuit model of the proposed defected ground structure.

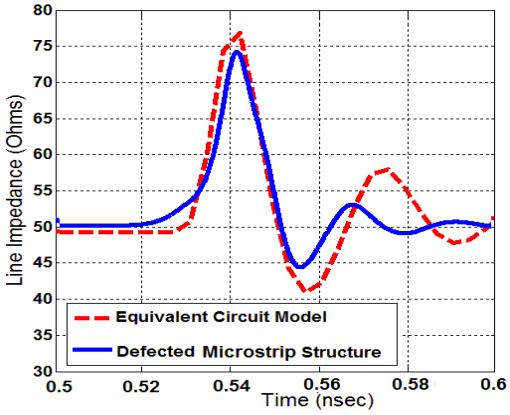

Fig. 5. The reflected waveforms simulated by HFSS and predicted by equivalent circuit model of the proposed defected microstrip structure.

Table 1: Equivalent circuit model parameters

Element	Value	Element	Value
L1	1.55 (nH)	L2	4.8 (nH)
C1	1.05 (pF)	C2	1.75 (pF)
R1	0.8 (Ω)	R2	2.1 (Ω)

C. TDR and genetic algorithm analysis

In order to calculate of the TDR results for the proposed equivalent circuits, we can write the reflection coefficient through defected structures as (1) which is observed at the source end, i.e., Port1:

$$\Gamma_Z(s)=\frac{Z(s)}{Z(s)+2Z_0}. \quad (1)$$

A step voltage source with rise time τ_r and amplitude V_0, can be expressed [15-16] as:

$$V_{in}(s)=\frac{V_0}{2\tau_r}\frac{1}{s^2}\left(1-e^{-\tau_r S}\right). \quad (2)$$

Therefore, the reflected waveform in Laplace domain can be written as:

$$V_{TDR}(s)=V_{in}(s)\Gamma_{DGS,DMS}(s). \quad (3)$$

In TDR measurements, the impedance follows from:

$$Z_{TDR}=Z_0\times\left(V_{in}(t)+V_{TDR}(t)\right)/\left(V_{in}(t)-V_{TDR}(t)\right), \quad (4)$$

where Z_0 is the characteristic impedance of the transmission line at the terminal.

In order to optimize TDR result with genetic algorithm results for the equivalent circuits, the impedance of these circuits in Laplace domain can be represented as follows:

$$z_{11}=\frac{V_1}{I_1}\Big|_{I_2=0}= \quad ,(5)$$

$$\left[\left(R_2+\frac{1}{C_2+S}+L_2S\right)\Big\|\left(L_3S\Big\|\frac{1}{C_3S}\right)+\frac{1}{C_1S}+L_1S\right]\Big\|R_1$$

$$\begin{cases} Z=(R_1+L_1S+\dfrac{1}{C_1S})\Big\|(L_3S\Big\|\dfrac{1}{C_3S})+L_2S+\dfrac{1}{C_2S} \\ Z_{12}=\dfrac{V_1}{I_2}\Big|_{I_1=0}=R_1\times\dfrac{R_2}{R_2+Z}\times\dfrac{L_3S\Big\|\dfrac{1}{C_3S}}{L_3S\Big\|\dfrac{1}{C_3S}+\dfrac{1}{C_1S}+L_1S+R_1} \end{cases}, \quad (6)$$

$$\begin{cases} Y=(R_2+L_2S+\dfrac{1}{C_2S})\Big\|(L_3S\Big\|\dfrac{1}{C_3S})+L_1S+\dfrac{1}{C_1S} \\ Z_{21}=\dfrac{V_2}{I_1}\Big|_{I_2=0}=R_2\times\dfrac{R_1}{R_1+Y}\times\dfrac{L_3S\Big\|\dfrac{1}{C_3S}}{L_3S\Big\|\dfrac{1}{C_3S}+\dfrac{1}{C_2S}+L_2S+R_2} \end{cases}, \quad (7)$$

$$z_{22}=\frac{V_2}{I_2}\Big|_{I_1=0}= \quad , \quad (8)$$

$$\left[\left(R_1+\frac{1}{C_1+S}+L_1S\right)\Big\|\left(L_3S\Big\|\frac{1}{C_3S}\right)+\frac{1}{C_1S}+L_2S\right]\Big\|R_2$$

$$S_{11}=\frac{(Z_{11}-Z_0)(Z_{22}+Z_0)-Z_{12}Z_{21}}{(Z_{11}+Z_0)(Z_{22}+Z_0)-Z_{12}Z_{21}}, \quad (9)$$

$$S_{21}=\frac{2Z_{21}Z_0}{(Z_{11}+Z_0)(Z_{22}+Z_0)-Z_{12}Z_{21}}. \quad (10)$$

Figures 6 and 7 show the simulated reflection waveforms observed at Port1 of the defected structures, as shown in Fig. 2, and with a 50 Ω termination on Port2, before and after optimization, respectively. The excitation source is a step wave with amplitude 1Volt and rise time of 30psec. The corresponding result

predicted by the equivalent circuit model is also shown in these figures. As shown in Figs. 6 and 7, TDR curves have started with impedance just under 50 Ω. This is indeed the characteristic impedance of the microstrip line. At impedance discontinuities, part of the input signal is reflected. These reflections, after traveling back, reach terminal Port1 and are observed there [22-23].

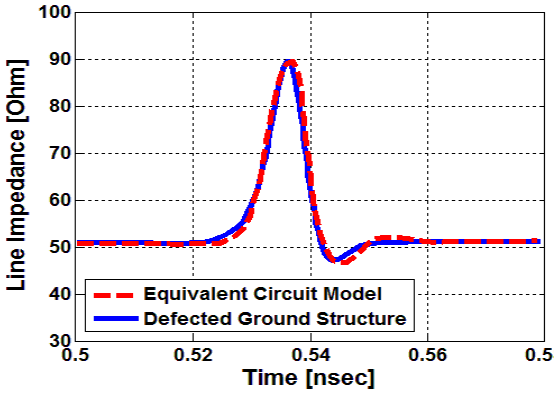

Fig. 6. The reflected waveforms simulated by HFSS and predicted by equivalent circuit model the proposed defected microstrip structure shown in Fig. 2 before optimization.

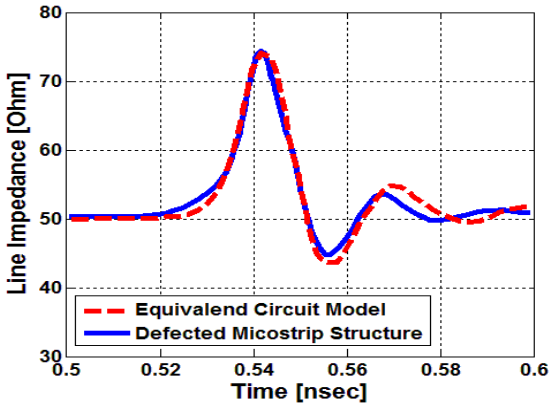

Fig. 7. The reflected waveforms simulated by HFSS and predicted by equivalent circuit model the proposed defected ground structure shown in Fig. 2 after optimization by GA.

From these observations, the characteristic impedances along the transmission line can be computed. From these formulas, the characteristic impedances along the transmission line can be computed. The optimal dimensions of the equivalent circuit models parameters calculated from ordinary TDR and modified TDR by genetic algorithm technique are specified in Table 2.

Table 2: The equivalent circuit models parameters calculated from ordinary TDR and modified TDR by genetic algorithm technique

Element	Before Optimization	After Optimization
L_1	1.55 (nH)	1.61 (nH)
C_1	1.05 (pF)	1.15 (pF)
R_1	0.8 (Ω)	0.76 (Ω)
L_2	4.8 (nH)	4.6 (nH)
C_2	1.75 (pF)	1.7 (pF)
R_2	2.1 (Ω)	2.05 (Ω)

III. RESULTS AND DISCUSSIONS

The proposed microstrip-fed slot antenna with various design parameters were constructed, and the numerical and experimental results of the input impedance and radiation characteristics are presented and discussed.

The configuration of the presented slot antenna was shown in Fig. 1. Geometry for the ordinary slot antenna (Fig. 8 (a)), with two inverted U-shaped slots in the ground plane (Fig. 8 (b)), and the proposed antenna (Fig. 8 (c)) structures are shown in Fig. 8. VSWR characteristics for the structures that were shown in Fig. 6 are compared in Fig. 9. As shown in Fig. 9, it is observed that the upper frequency bandwidth is affected by using the pair of inverted U-shaped slots in the ground plane and notched frequency bandwidth is sensitive to the M-shaped SIR slot.

To understand the phenomenon behind the bandwidth enhancement performance, simulated current distributions for the proposed antenna on the ground plane at 12 GHz is presented in Fig. 10 (a). It is found that by using two inverted U-shaped slots, an additional current path in the ground plane is generated and a new resonance at 12 GHz can be achieved. Another important design parameter of this structure is the M-shaped slot at the feed-line. Figure 10 (b) presents the simulated current distributions on the radiating stub and feed-line at the notched frequency (7.5 GHz). As shown in Fig. 10 (b), at the notched frequency the current flows are more dominant around of the M-shaped slot at feed-line.

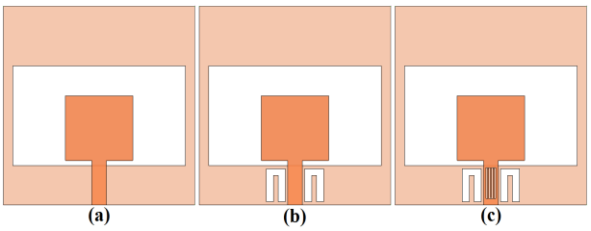

Fig. 8. (a) Ordinary slot antenna, (b) the antenna with a pair of inverted U-shaped slots, and (c) the proposed antenna.

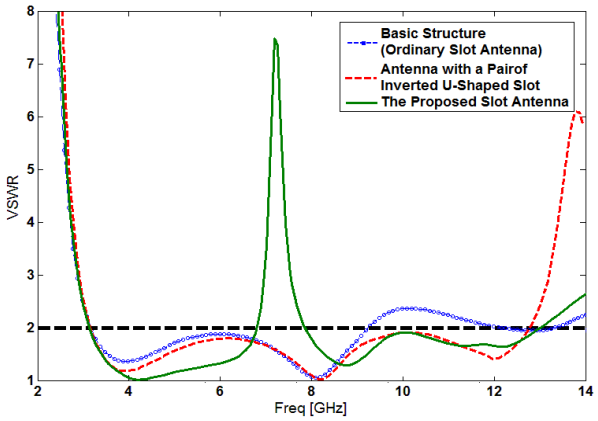

Fig. 9. Simulated VSWR characteristics for antennas shown in Fig. 6.

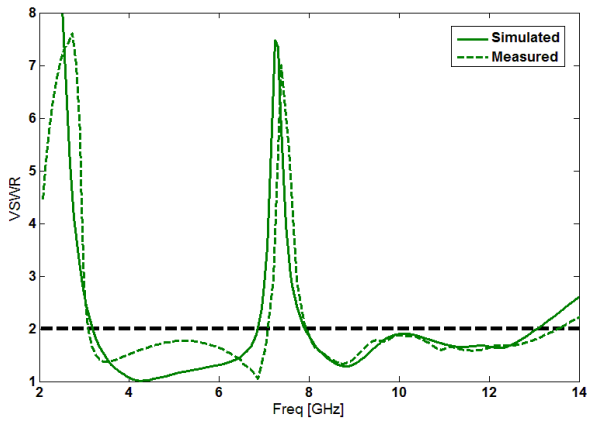

Fig. 11. Measured and simulated VSWR characteristics for the proposed antenna.

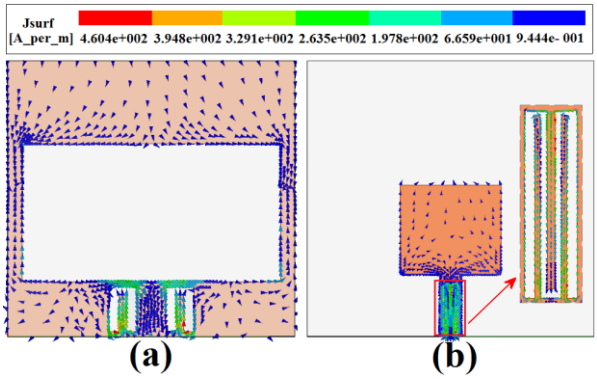

Fig. 10. Simulated surface current distributions for the proposed antenna: (a) on the ground at 12 GHz (new resonance frequency), and (b) on the square radiating stun and feed-line at 7.5 GHz (notched frequency).

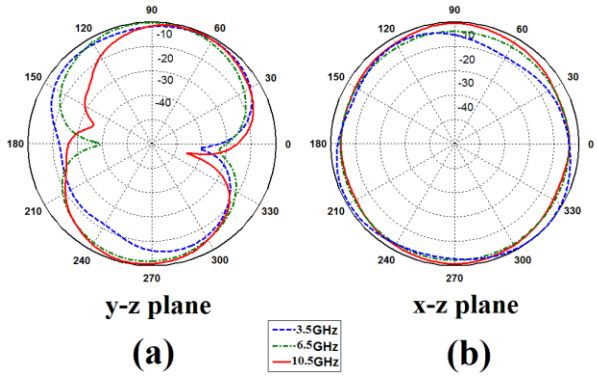

Fig. 12. Measured radiation patterns of the proposed antenna: (a) E-plane and (b) H-plane.

The proposed antenna with final design was built and tested. The measured and simulated VSWR characteristics of the proposed antenna were shown in Fig. 11. Fabricated antenna has the frequency band of 3.03 to 13.21 GHz with a band-notched performance around 7.22 to 7.81 GHz.

Figure 12 shows the measured radiation patterns including the co-polarization in the H-plane (x-z plane) and E-plane (y-z plane). The main purpose of the radiation patterns is to demonstrate that the antenna actually radiates over a wide frequency band. It can be seen that the radiation patterns in *x-z* plane are nearly omnidirectional for the three frequencies. The radiation patterns on the y-z plane are like a small electric dipole leading to bidirectional patterns in a very wide frequency band [24-25].

IV. CONCLUSION

In this paper, a novel band-notched slot antenna with a time domain method to extract the equivalent RLC of the defected structures for UWB applications has been proposed. The analytic formulations for the equivalent circuit models are obtained based on time-domain reflectometry theory. Furthermore, using Genetic Algorithm Optimization, the accuracy of the equivalent circuit models of the employed DGS and DMS have been improved significantly. The fabricated antenna covers the frequency range for UWB systems between 3.03 to 13.21 GHz with a band-notched characteristic in the frequency range of 7.25 to 7.75 GHz to avoid interference from X-band communication systems. The proposed band-notched UWB antenna has compact and simple configuration and is easy to fabricate. Experimental results show that the proposed antenna could be a good candidate for UWB applications.

ACKNOWLEDGMENT

The authors are thankful to the Microwave Technology (MWT) Company staff for their professional help (www.microwave-technology.com).

REFERENCES

[1] H. Schantz, *The Art and Science of Ultra Wideband Antennas*. Artech House, 2005.

[2] A. Dastranj and H. Abiri, "Bandwidth enhancement of printed E-shaped slot antennas fed by CPW and microstrip line," *IEEE Trans. Antenna Propag*., vol. 58, pp. 1402-1407, 2010.

[3] Y. W. Jang, "Experimental study of large bandwidth three-offset microstrip line-fed slot antenna," *IEEE Microw. Wireless Comp. Lett.*, vol. 11, pp. 425-426, 2001.

[4] N. Ojaroudi, "Bandwidth improvement of monopole antenna using π-shaped slot and conductor-backed plane," *International Journal of Wireless Communications, Networking and Mobile Computing*, vol. 1, pp. 14-19, 2014.

[5] N. Ojaroudi, "Compact UWB monopole antenna with enhanced bandwidth using rotated L-shaped slots and parasitic structures," *Microw. Opt. Technol. Lett*., vol. 56, pp. 175-178, 2014.

[6] M. K. Kim, Y. H. Suh, and I. Park, "A T-shaped microstrip line-fed wide-slot antenna," *in Proc. IEEE AP-S Int. Symp.*, pp. 1500-1503, 2000.

[7] K. Chung, T. Yun, and J. Choi, "Wideband CPW fed monopole antenna with parasitic elements and slots," *Electronics Letters*, vol. 40, no. 17, pp. 1038-1040, 2004.

[8] N. Ojaroudi and M. Ojaroudi, "Novel design of dual band-notched monopole antenna with bandwidth enhancement for UWB applications," *IEEE Antennas Wireless Propag. Lett.*, vol. 12, pp. 698-701, 2013.

[9] N. Ojaroudi, M. Ojaroudi, and N. Ghadimi, "UWB monopole antenna with WLAN frequency band-notched performance by using a pair of E-shaped slits," *Applied Computational Electromagnetics Society (ACES) Journal*, vol. 28, pp. 1244-1249, 2014.

[10] N. Ojaroudi, "A modified compact microstrip-fed slot antenna with desired WLAN band-notched characteristic," *American Journal of Computation, Communication and Control*, vol. 1, pp. 56-60, 2014.

[11] N. Ojaroudi, "Application of protruded strip resonators to design an UWB slot antenna with WLAN band-notched characteristic," *Progress in Electromagnetics Research C*, vol. 47, pp. 111-117, 2014.

[12] N. Ojaroudi and M. Ojaroudi, "Dual band-notched monopole antenna with multi-resonance characteristic for UWB wireless communications," *Progress in Electromagnetics Research C*, vol. 40, pp. 188-199, 2013.

[13] N. Ojaroudi and M. Ojaroudi, "A novel design of reconfigurable small monopole antenna with switchable band notch and multi-resonance functions for UWB applications," *Microw. Opt. Technol. Lett*., vol. 55, pp. 652-656, 2013.

[14] N. Ojaroudi, M. Mehranpour, S. Ojaroudi, and Y. Ojaroudi, "Application of the protruded structures to design an UWB slot antenna with band-notched characteristic," *Applied Computational Electromagnetics Society (ACES) Journal*, vol. 29, pp. 184-189, 2014.

[15] N. Ojaroudi, "Application of protruded Γ-shaped strips at the feed-line of UWB microstrip antenna to create dual notched bands," *International Journal of Wireless Communications, Networking and Mobile Computing*, vol. 1, pp. 8-13, 2014.

[16] N. Ojaroudi and M. Ojaroudi, "An UWB slot antenna with band-stop notch," *IET Microw. Antennas Propag*., vol. 10. pp. 831-835, 2013.

[17] A. B. Abdel-Rahman, A. K. Verma, A. Boutejdar, and A. S. Omar, "Control of bandstop response of Hi-Lo microstrip low-pass filter using slot in ground plane," *IEEE Trans. Microw. Theory Tech*., vol. 52, pp. 1008-1013, Mar. 2004.

[18] C.-S. Kim, J.-S Lim, J.-H. Kim, and D. Ahn, "A design of a miniaturized 2-pole bandpass filter by using slot and hair-pin line," *in IEEE MTT-S Int. Dig*., Fort Worth, TX, pp. 1983-1986, June 2006.

[19] C. H. Cheng, C. H. Tsai, and T. L. Wu, "A novel time domain method to extract equivalent circuit model of patterned ground structures," *IEEE Microw. Wireless Compon. Lett.*, vol. 17, pp. 486-488, 2010.

[20] X. Zeng, J. He, M. Wang, and M. Abdulla, "New closed-form formula for series inductance and shunt capacitance based on measured TDR impedance profile," *IEEE Microw. Wireless Compon. Lett*., vol. 17, pp. 781-783, 2007.

[21] Ansoft High Frequency Structure Simulator (HFSS), ver. 13, Ansoft Corporation, 2011.

[22] A. J. Kerkhoff, R. L. Rogers, and H. Ling, "Design and analysis of planar monopole antennas using a genetic algorithm approach," *IEEE Trans. Antennas Propag*., vol. 2, pp. 1768-1771, 2004.

[23] A. J. Kerkhoff and H. Ling, "Design of a band-notched planar monopole antenna using genetic algorithm optimization," *IEEE Trans. Antennas Propag.*, vol. 55, pp. 604-610, 2007.

[24] N. Ojaroudi and M. Ojaroudi, "Dual band-notched monopole antenna with multi-resonance characteristic for UWB wireless communications," *Progress in Electromagnetics Research C*, vol. 40, pp. 188-199, 2013.

[25] N. Ojaroudi, S. Amiri, F. Geran, and M. Ojaroudi,

"Band-notched small monopole antenna using triple E-shaped structures for UWB systems," *Applied Computational Electromagnetics Society (ACES) Journal*, vol. 27, no. 12, pp. 1022-1028, 2012.

A Novel Wideband End-Fire Conformal Antenna Array Mounted on a Dielectric Cone

Zengrui Li [1], Longdan Tan [2], Xiaole Kang [1], Jianxun Su [1], Qingxin Guo [1], Yaoqing (Lamar) Yang [3], and Junhong Wang [4]

[1] School of Information Engineering
Communication University of China, Beijing, 100024, China
zrli@cuc.edu.cn, darever1988@126.com, sujianxun_jlgx@163.com, qxguo@cuc.edu.cn

[2] Network Operation Center
Startimes Media Group, Beijing, 100024, China
tanld@startimes.com.cn

[3]Department of Electrical and Computer Engineering
University of Nebraska-Lincoln, Nebraska, 68182, USA
yyang3@unl.edu

[4] Institute of Lightwave Technology
Beijing Jiaotong University, Beijing, 100044, China
wangjunh@bjtu.edu.cn

Abstract ─ In this paper, a novel log-periodic antenna named quasi-second order Koch fractal log-periodic dipole array (QLPK^{2}DA) is presented for the conformal applications. The proposed antenna array shows wider operating bandwidth and small physical profile. In addition, the radiation characteristics of the proposed antenna array mounted on a dielectric cone are investigated. Results show that the cone curvature has an influence on the performance of the conformal antenna, both in terms of its bandwidth and radiation patterns. The thickness and permittivity of the dielectric cone have an effect on the bandwidth of the conformal antenna. The measured results show that the antenna has a wide band ranging from 2 GHz to 10 GHz and shows a typical end-fire radiation beam. Measurement results of both single antenna and conformal antenna array show a good agreement with simulated values.

Index Terms─ Conformal, Koch fractal, log-periodic antenna, wideband.

I. INTRODUCTION

Wideband antennas are required for many electromagnetic applications, such as radio astronomy and UWB technology. The printed log-periodic array antenna (LPDA) has attracted great attention in wideband wireless communication systems due to many advantages, such as simple in fabrication, low cross-polarization, wide frequency band and the end-fire beam [1]. It is a challenge to reduce the antenna size while maintaining its main performance characteristics. For the purpose of antenna miniaturization, different kinds of fractal geometries have been investigated in antenna design [2-10]. Among the previous research, Koch fractal is an important geometry studied by many antenna researchers [6-10]. In [7] and [8], two kinds of the printed Koch fractal log-periodic dipole arrays are proposed. However, these two antennas only use the first order Koch fractal technique to reduce the antenna size and the bandwidth is just from 2 GHz to 3 GHz. To reduce cross-polarization and further miniaturize the antenna, quasi-second order Koch fractal dipoles are proposed for antenna design in this paper.

On the other hand, conformal antennas are mainly used in aviation, radars and military systems. For these applications, conformal antennas need to cover a wide bandwidth and have end-fire radiation beam. A variety of conformal antennas have been investigated during the past two decades, including monopole antennas [11-12], slot antennas [13-14], leaky-wave antennas [15-16], microstrip antenna arrays [17-18], log-periodic antennas [19-20] and substrate integrated waveguide (SIW) antennas [21-22], etc. However, most of these antennas are mounted on metallic surfaces and have broadside radiation beam. There are few studies about end-fire conformal antennas in literatures [20-21].

Submitted On: September 22, 2015
Accepted On: February 26, 2016

In this paper, a quasi-second order Koch-fractal log-periodic antenna dipole array is proposed for conformal applications for the first time as far as we know. The contributions of our work are as follows:

1) The quasi-second order Koch fractal element is proposed for antenna design. Compared with LPDA, the proposed QLPK^{2}DA has smaller size and operates with a wider frequency band.

2) The proposed antenna can be easily mounted on a dielectric cone. The influences of cone curvature, cone thickness and cone permittivity on the conformal antenna's bandwidth and radiation performance are investigated. The curvature of cone has an influence on bandwidth and radiation patterns of conformal antenna. The thickness and dielectric constant of cone only affect the bandwidth of conformal antenna.

3) A prototype of the conformal antenna array with four antenna elements is fabricated. Measurement results are compared with simulated values to validate our proposed design.

II. ANTENNA DESIGN

In this section, a quasi-second order Koch fractal log-periodic antenna is proposed, as shown in Fig. 1. This antenna includes ten quasi-second Koch fractal dipoles, which are cross-fed by a parallel-strip transmission line and printed on both layers of a Teflon-F4B substrate with a dielectric constant of 3.5 and loss tangent of 0.003. The thickness of the substrate is 0.5 mm.

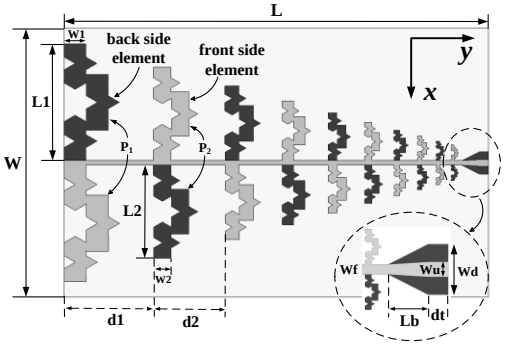

Fig. 1. Configuration of the proposed QLPK^{2}DA.

A. Design of the LPDA

A conventional printed log-periodic dipole array (LPDA) with Euclidean dipoles is designed, as shown in Fig. 2. To achieve a higher gain, the scaling factor τ and spacing factors σ of LPDA is set to be 0.84 and 0.14 respectively, based on the method described in [23-24]. The antenna's half-angle is $\alpha=30^\circ$. The number of the radiation dipoles are calculated to be $N=14$ to cover the desired bandwidth from 2 GHz to 10 GHz. In this design, $\tau=L_{i+1}/L_i=W_{i+1}/W_i=d_{i+1}/d_i$, where L_i and W_i are the length and width of the dipole P_i, d_i is the distance between dipole P_{i+1} and P_i.

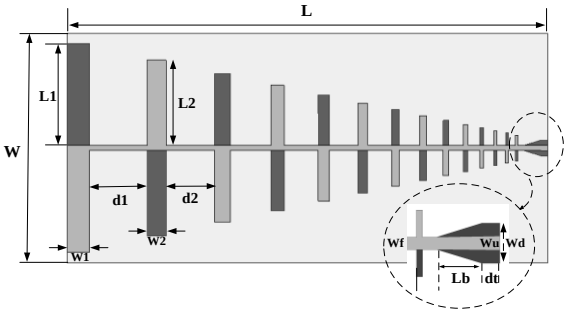

Fig. 2. Configuration of the LPDA.

B. Design of the QLPK^{2}DA

To realize the miniaturization of LPDA, Koch iteration is applied in this design. Generally, Euclidean elements are defined as Koch curves of 0th iteration (K0) while other order iterations are based on lower order Koch curves [9-10]. The Koch fractal monopoles, designed from K0 to K2, are depicted in Fig. 3. The characteristics of the antenna such as the primary resonant frequency, is directly related to the fractal dimension. For a given order, Koch elements with different indentation angles will also have different input impedances and resonant frequencies [10]. A typical indentation angle of $\theta=60^\circ$ is set to Koch fractal elements in this research.

However, it will bring complexity in design if Koch fractal element's width increases, especially on the higher order elements. Therefore, we propose a modified second order Koch fractal element named quasi-second order Koch fractal element. The middle part of each quasi-second order Koch fractal element is replaced by two rectangle patches "S1" and "S2", as shown in Fig. 4. This structure can also reduce the reverse current on each fractal element and reduce the cross-polarization, compared with second order Koch fractal antenna. Based on the above proposed LPDA, the QLPK^{2}DA can be realized by replacing Euclidean elements with quasi-second order Koch fractal elements, as shown in Fig. 1. A gradient microstrip balun at the end of the feeding line is designed to transform an unbalanced input signal to a balanced signal at the quasi-second order Koch fractal elements.

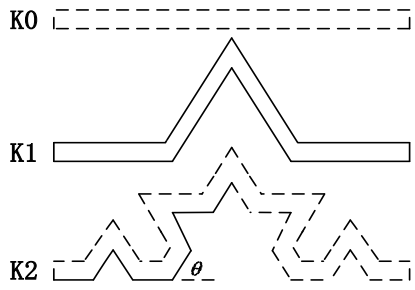

Fig. 3. Koch fractal monopoles, K0 to K2.

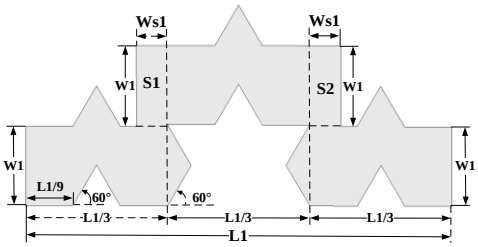

Fig. 4. Structure of quasi-second order Koch fractal element with $W_{s1}=1.9$ *mm*.

To cover the desired bandwidth (2 GHz-10 GHz), the LPDA and QLPK^{2}DA were simulated and optimized with the assistance of ANSYS High Frequency Structure Simulator (HFSS) Version 12. Figure 5 shows the simulated return loss of the two antennas. The efficiency of QLPK2DA is also simulated and achieves at least 76.7% over the entire band shown in Fig. 6. The dimensions of the designed LPDA and QLPK^{2}DA are listed in Table 1. The overall dimension of the LPDA is 66×137 mm^2, while the physical size of the QLPK^{2}DA is only 60×94.9 mm^2, which is 37% smaller than the LPDA. Apparently, the physical size of the antenna can be greatly reduced due to the quasi-second order Koch fractal structure.

The prototypes of the LPDA and QLPK^{2}DA are fabricated and shown in Fig. 7 and Fig. 8, respectively. The prototype antennas are measured by an Agilent E5071C Vector Network Analyzer in an anechoic chamber in Communication University of China (CUC).

Figure 9 and Fig. 10 show the comparisons between the simulated and measured return losses of the LPDA and QLPK^{2}DA, respectively. It is found that the measured results and simulated values of these two antennas agree with each other over the frequency band (return loss > 10 dB) ranging from 2 GHz to 10 GHz with a ratio about 5:1. In Fig. 10, the small deviation of the results in the higher frequency band may be caused by the imperfection of hand-soldering the SMA connector.

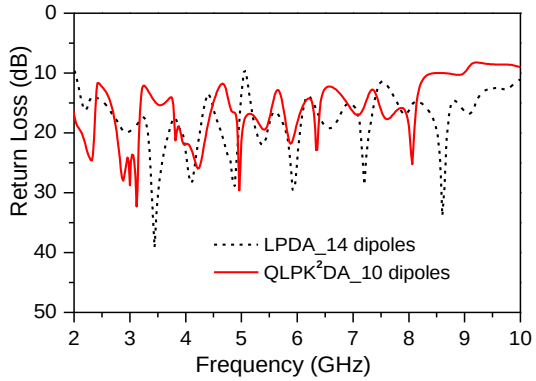

Fig. 5. Comparison of simulated return loss between LPDA and QLPK^{2}DA.

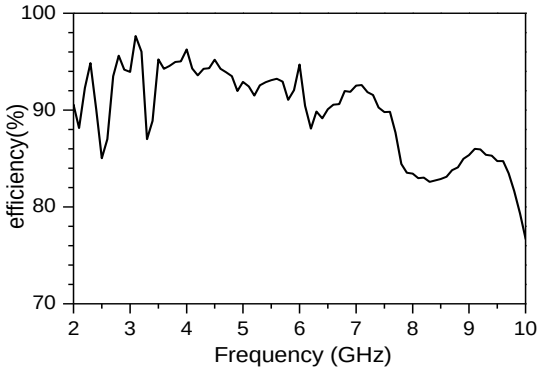

Fig. 6. Efficiency of QLPK2DA by simulation.

Table 1: Optimized parameters of LPDA and QLPK^{2}DA (In millimeters)

Parameters	L_1	W_1	d_1	W	L
LPDA	29.3	6.4	16.4	66	137
QLPK^{2}DA	26	4.9	20	60	94.9
Parameters	W_f	W_u	W_d	L_b	d_t
LPDA	1.4	1.6	5	5	2
QLPK^{2}DA	1	1.5	5	4	2

Fig. 7. Prototype of LPDA: (a) front view and (b) back view.

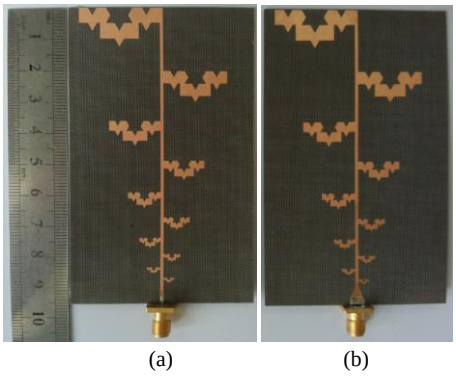

Fig. 8. Prototype of QLPK^{2}DA: (a) front view and (b) back view.

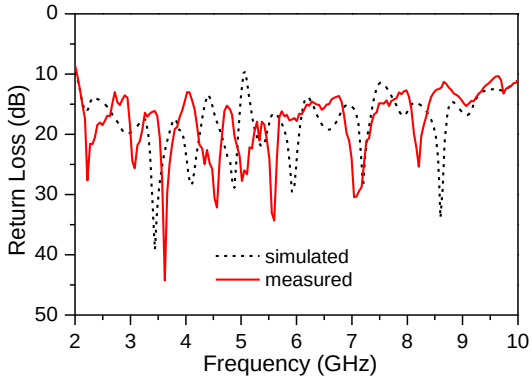

Fig. 9. Measured and simulated return loss of LPDA.

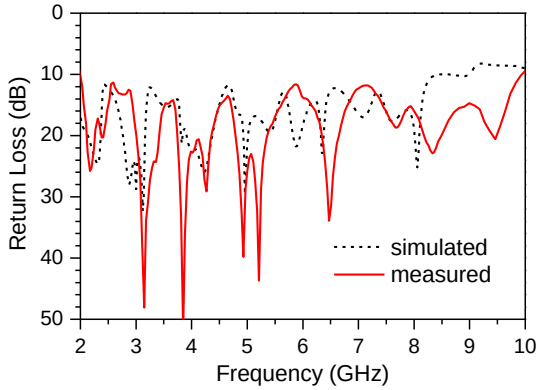

Fig. 10. Measured and simulated return loss of QLPK^{2}DA.

The far field radiation patterns in the E-plane (xoy plane) and H-plane (yoz plane) at different frequencies were measured and plotted in Fig. 11. The measured co-polarization radiation patterns and the simulated results show good agreement in both planes. However, the measured cross-polarization radiation patterns are wider than the simulated results. It may be caused by the deviation of the relative position between test antenna and reference antenna. The proposed antenna has end-fire radiation beams in both planes and the maximum radiation is in the direction of +y axis.

The measured half power beam-width and front-to-back ratios of the QLPK^{2}DA are listed in Table 2 and Table 3. Table 2 shows the beam-width in E-plane and H-plane vary from 42° to 72° and 54° to 94°. According to Table 3, the front-to-back ratios of the QLPK^{2}DA achieve more than 12 dB except few frequencies, which confirmed the end-fire characteristic of the antenna. Figure 12 shows the comparisons of the measured gains between LPDA and QLPK^{2}DA. It is observed that the gain of LPDA is higher than that of QLPK^{2}DA except a few frequency points. Within the operating frequency band, the measured gain of the QLPK^{2}DA in end-fire direction varies between 2.6 dBi and 8.7 dBi.

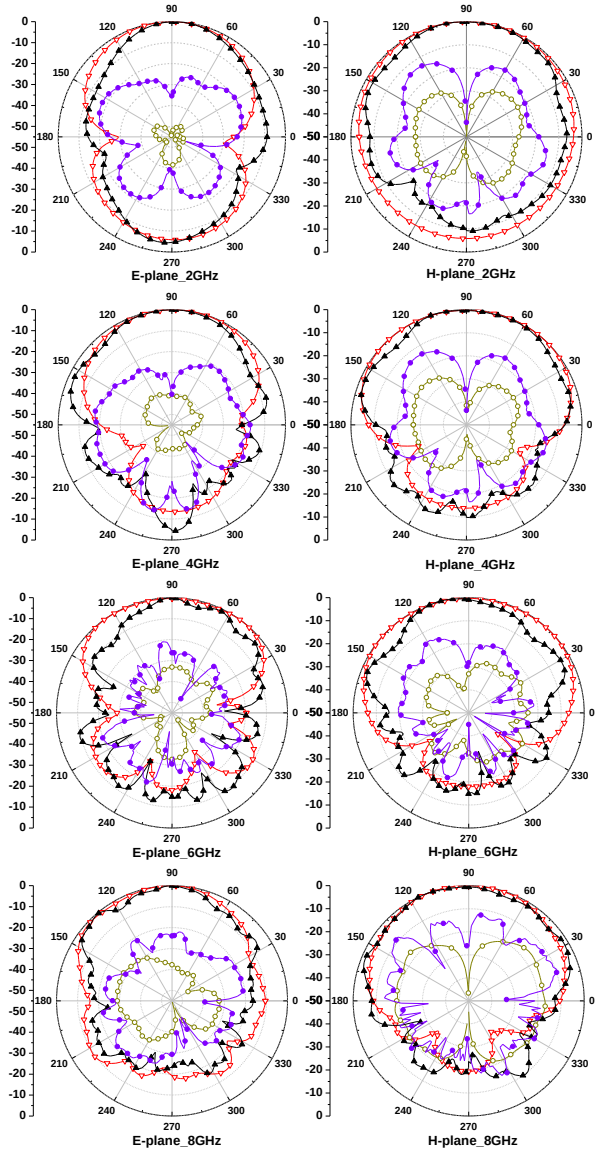

Fig. 11. Measured and simulated radiation patterns of QLPK^{2}DA. -▲- measured co-polarization, -●- measured cross-polarization, -▽- simulated co-polarization, -○- simulated cross-polarization.

Table 2: Measured half power beam-width of QLPK^{2}DA

Frequency (GHz)	2	4	6	8	10
E-plane (deg)	46	64	42	72	47
H-plane (deg)	86	68	54	94	50

Table 3: Measured front-to-back ratio of QLPK2DA

Frequency (GHz)	2	4	6	8	10
E-plane (dB)	8	8	17	23	20
H-plane (dB)	12	13	16	24	21

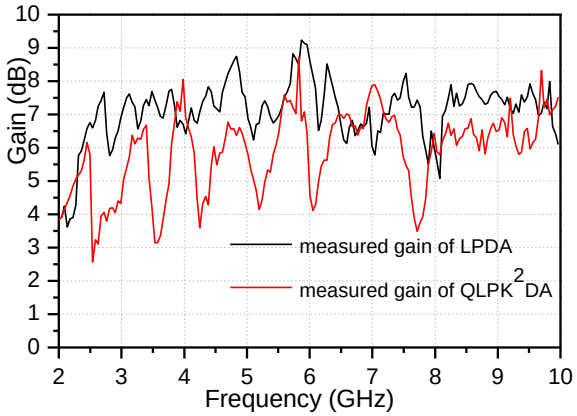

Fig. 12. Measured gain of LPDA and QLPK^{2}DA.

Since the linear phase response of the antenna in the time domain is one of the most important parameters in wideband systems, the group delay of two QLPK^{2}DA with a distance of 30 cm has also been measured. Figure 13 shows that the variation of the group delay is within 5ns across the entire frequency band, which indicates that the phase of the antenna shifts little within the operating frequency band. Thus, the proposed antenna has a desirable time domain characteristic.

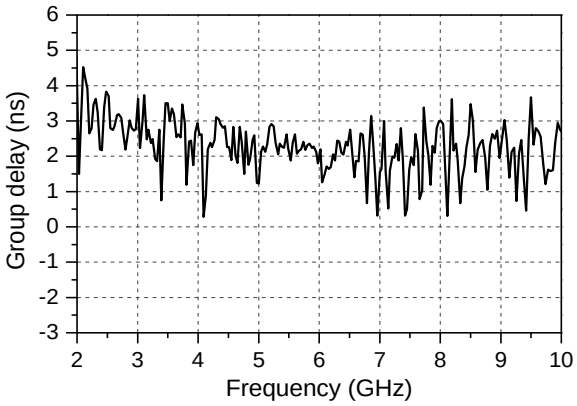

Fig. 13. Measured group delay of the proposed antenna.

III. CONFORMAL ANTENNA RESEARCH

A. Effects of cone curvature

The proposed QLPK^{2}DA is mounted on a dielectric cone to investigate the conformal antenna characteristics. The antenna is on dielectric cones with different curvatures, as shown in Fig. 14. The exterior diameters of the three cones' top/bottom surfaces are 300/360 mm, 190/210 mm, 130/150 mm, respectively. The height, thickness and dielectric constant of three cones are 350 mm, 0.5 mm and 2.1, respectively.

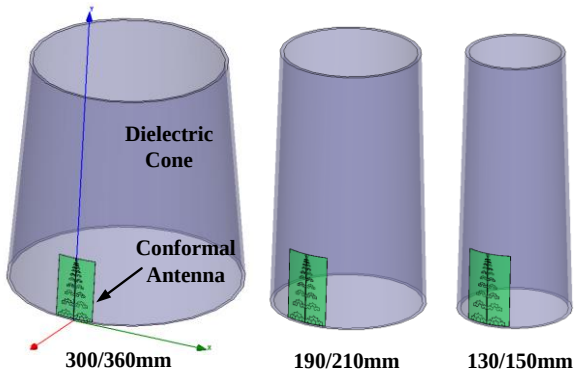

Fig. 14. Configuration of QLPK^{2}DA mounted on cones with different curvatures.

The simulated voltage standing wave ratio (VSWR) of the conformal antenna with different cone curvatures is shown in Fig. 15. It is observed that, with the increasing of cone curvature, the VSWR deteriorates especially in the middle and high frequency bands. The simulated radiation patterns of the conformal antenna with different cones curvatures at 2 GHz, 4 GHz, 6 GHz, and 8 GHz are plotted in Fig. 16. It can be seen that the variation of cone curvature has little effects on the co-polarization radiation patterns of the conformal antenna. Since the antenna is bent on the cone, there exists an extra electric current component in -*Z* direction. Therefore, the cross-polarization radiation patterns of the conformal antenna become larger with the increasing of cone curvature. The simulated half power beam-width of the conformal antenna is all less than 100 degree, as shown in Table 4.

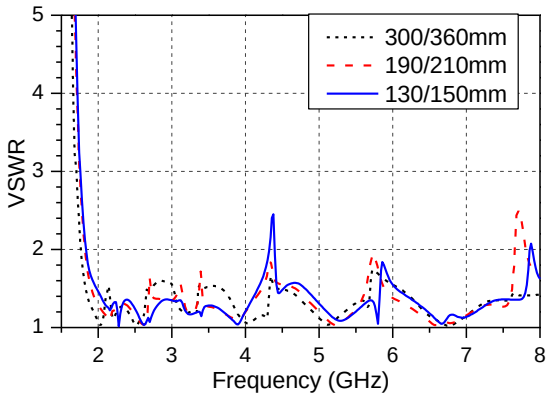

Fig. 15. Simulated VSWR of conformal antenna with different cone curvatures.

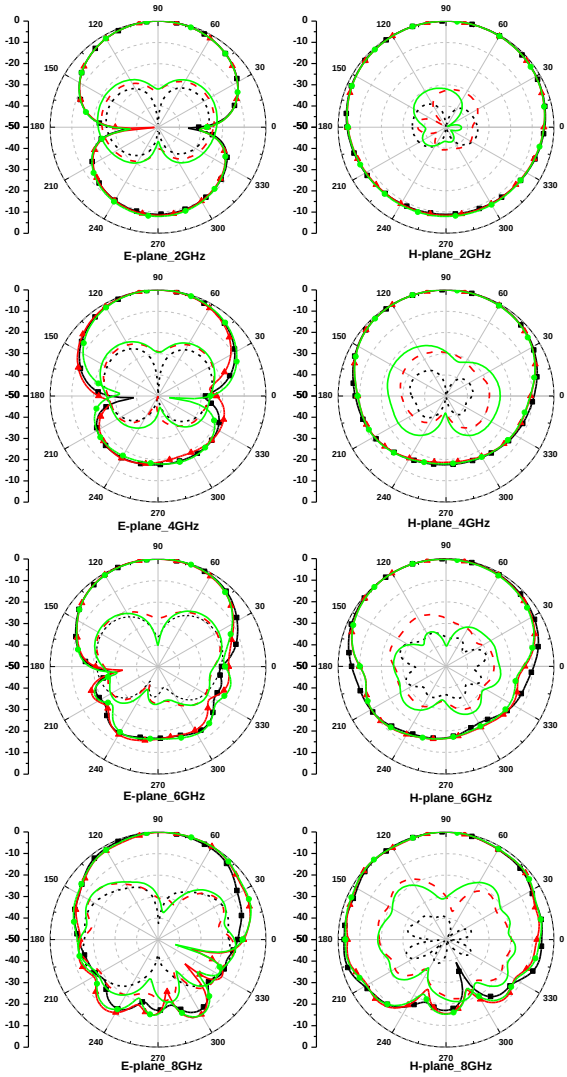

Fig. 16. Simulated radiation patterns of conformal antenna. -■- co-polarization (300/360 mm), --- cross-polarization (300/360 mm), -▲- co-polarization (190/210 mm), – – – cross-polarization (190/210 mm), -●- co-polarization (130/150 mm), — cross-polarization (130/150 mm).

Table 4: Simulated half power beam-width of QLPK^{2}DA mounted on different cones

Frequency (GHz)	2	3	4	5	6	7	8
E-plane (deg)	78	91	61	66	54	63	59
H-plane (deg)	97	79	85	92	79	83	74

B. Effects of cone thickness

In this subsection, the QLPK^{2}DA is mounted on cones with different thickness (5 mm, 7 mm, 10 mm) so as to examine the effect of the cone thickness on the characteristics of the conformal antenna. The outer diameter of cones' top and bottom surfaces is 190/210 mm. The height and dielectric constant of cones are 350 mm and 2.1, respectively.

The simulated VSWR of conformal antenna with different cone thickness is shown in Fig. 17. It is found that as the thickness increases, the VSWR becomes larger in the lower frequency band. The VSWR value varies between 1 and 3 in the whole operating band. The study on radiation performance indicates that the changes of cone thickness have little effect on far-field radiation patterns of conformal antenna.

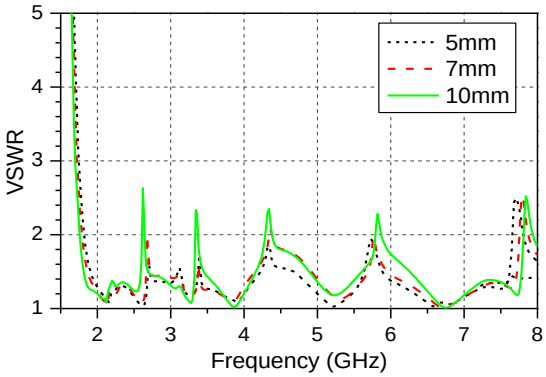

Fig. 17. Simulated VSWR of conformal antenna with different cone thickness.

C. Effects of cone dielectric constant

We also studied the performance of the antenna mounted on cones with different dielectric constants (2.1, 2.5, 3 and 3.5). The outer diameter of cones' top and bottom surfaces is 190/210 mm. The height and thickness of cones are 350 mm and 5 mm.

From Fig. 18, we can readily observe that cone dielectric constant has a significant effect on VSWR of conformal antenna. When the dielectric constant increases, the VSWR of conformal antenna deteriorates rapidly. It is found that when the dielectric constant is larger than 3, the VSWR will increase to be larger than 3, which is unacceptable for application. Studies show that the changes of cone dielectric constant have little effect on radiation performance of conformal antenna.

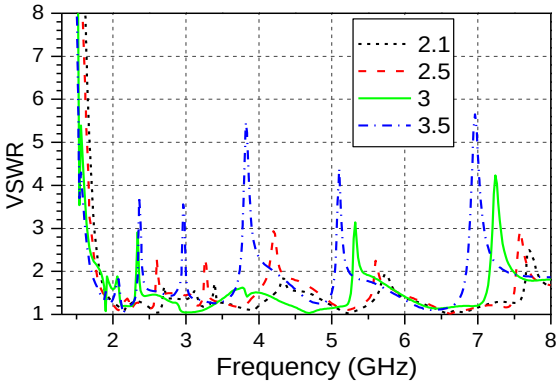

Fig. 18. Simulated VSWR of conformal antenna with different dielectric constants.

IV. EXPERIMENTAL RESULTS

A prototype of conformal antenna array is constructed by mounting four proposed QLPK^{2}DA on the surface of a polypropylene cone with a dielectric constant of 2.3, as shown in Fig. 19. The height, thickness, top and bottom surfaces' outer diameter of the cone are 274 mm, 3 mm, 188/204 mm, respectively. The prototype was measured by an Agilent E5071C Vector Network Analyzer in an anechoic chamber in CUC.

The measured and simulated return losses of the conformal antenna are shown in Fig. 20. It can be seen that the measured and simulated results are in good agreement. Because of the imperfection during building the antenna, the measured results shift a little bit towards the lower frequency band.

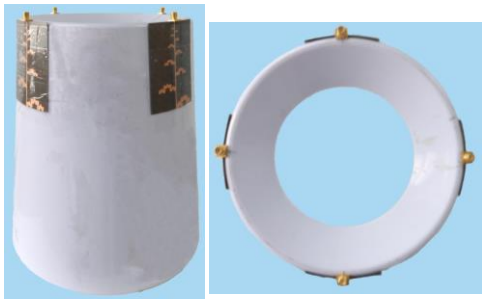

Fig. 19. Prototype of four QLPK^{2}DA mounted on a dielectric cone: (a) side view and (b) top view.

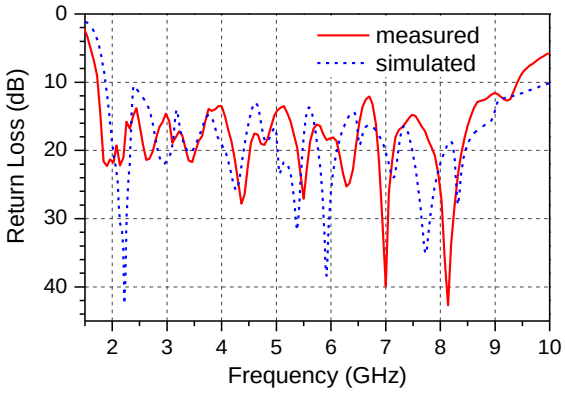

Fig. 20. Measured and simulated return loss of the conformal antenna.

Figure 21 shows the measured and simulated radiation patterns of the conformal antenna in both E-plane (xoy plane) and H-plane (yoz plane) at 2 GHz, 4 GHz, 6 GHz and 8 GHz. It is found that the conformal antenna has end-fire radiation beams in both planes. The measured radiation patterns have good agreement with simulated curves. The coupling between four ports of the conformal antenna is also investigated. Because the four QLPK^{2}DA are mounted evenly on the cone, $|S_{41}|$ is equal to $|S_{21}|$ and $|S_{42}|$ is equal to $|S_{31}|$. So we just consider $|S_{21}|$ and $|S_{31}|$ here. Figure 22 shows the measured $|S_{21}|$ and $|S_{31}|$ of the conformal antenna. It can be observed that the measured results are both less than -28 dB in the operating frequency band, which is good enough for the port coupling of the conformal antenna.

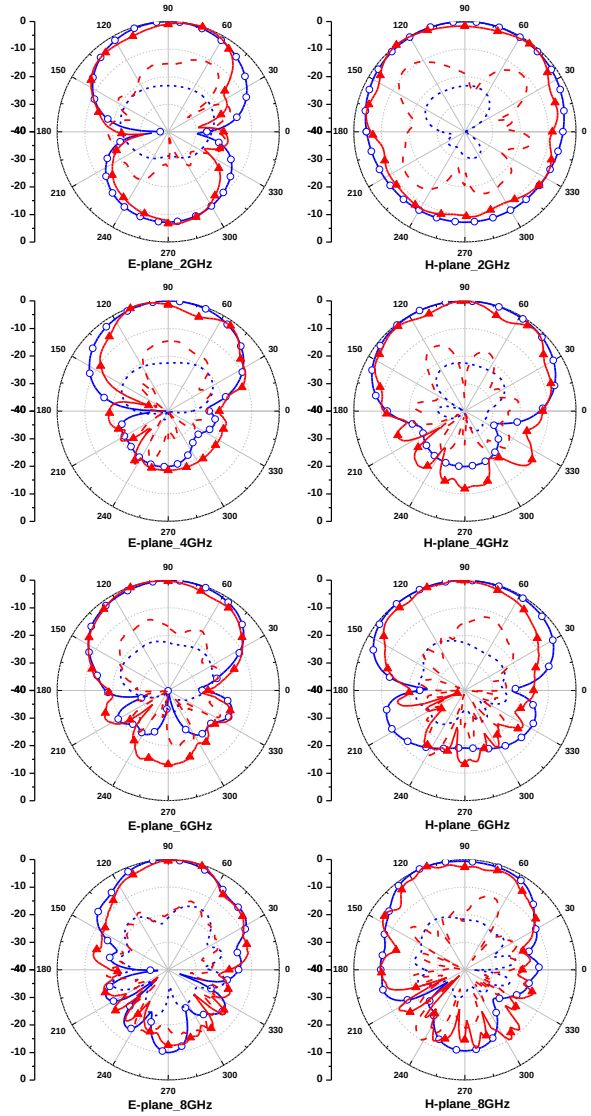

Fig. 21. Measured and simulated radiation patterns of conformal antenna. -○- simulated co-polarization, --- simulated cross-polarization, -▲- measured co-polarization, – – –measured cross-polarization.

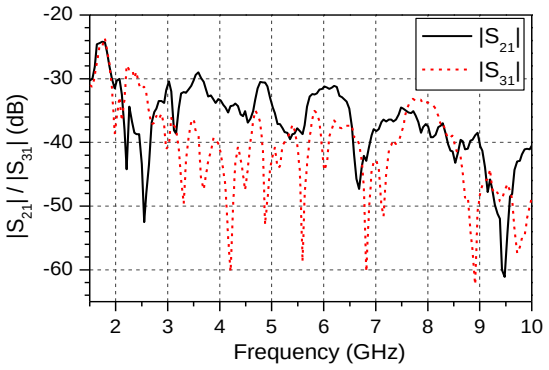

Fig. 22. Measured coupling of the conformal antenna.

V. CONCLUSION

This paper presented a novel wideband end-fire conformal antenna array mounted on a dielectric cone. A quasi-second order Koch fractal element is applied in conformal antenna research for the first time. The effects of cone curvature, thickness, dielectric constant on the performance of conformal antenna are investigated and some inspiring results for end-fire conformal antenna design have been obtained. Measured and simulated results of the prototype show the conformal antenna has wide frequency band, end-fire radiation patterns and wide half power beam-width. The proposed antenna array has a great potential to be used in conformal systems such as missiles, radars, aircrafts.

ACKNOWLEDGMENT

The work was supported in part by the National Science Foundation of China (NSFC) under grant No. 61331002, No. 61102011, No. 61201082, and in part by Excellent Innovation Team of CUC under grant No. yxtd201303.

REFERENCES

[1] C. A. Balanis, *Antenna Theory: Analysis and Design*. John Wiley and Sons. Inc., 2005.

[2] W. Chen, G. Wang, and C. Zhang, "Bandwidth enhancement of a microstrip-line-fed printed wide-slot antenna with a fractal-shaped slot," *IEEE Transactions on Antennas and Propagation*, vol. 57, no. 7, pp. 2176-2179, Jul. 2009.

[3] C. Puente-Baliarda, J. Romeu, R. Pous, and A. Cardama, "On the behavior of the Sierpinski multiband fractal antenna," *IEEE Transactions on Antennas and Propagation*, vol. 46, no. 4, pp. 517-524, Apr. 1998.

[4] A. Gorai, A. Karmakar, M. Pal, and R. Ghatak, "Multiple fractal-shaped slots-based UWB antenna with triple-band notch functionality," *Journal of Electromagnetic Waves and Applications*, vol. 27, no. 18, pp. 2407-2415, 2013.

[5] A. Azari, "A new ultra wideband fractal monopole antenna," *Applied Computational Electromagnetics Society (ACES) Journal*, vol. 26, no. 4, 2011.

[6] A. Sundaram, M. Maddela, and R. Ramadoss, "Koch-fractal folded-slot antenna characteristics," *IEEE Antennas and Wireless Propagation Letters*, vol. 6, pp. 219-222, 2007.

[7] D. E. Anagnostou, J. Papapolymerou, M. M. Tentzeris, and C. G. Christodoulou, "A printed log-periodic Koch-dipole array (LPKDA)," *IEEE Antennas and Wireless Propagation Letters*, vol. 7, pp. 4852-4856, 2009.

[8] H.-T. Hsu and T.-J. Huang, "A Koch-shaped log-periodic dipole array (LPDA) antenna for universal ultra-high-frequency (UHF) radiao frequency identification (RFID) handheld reader," *IEEE Transactions on Antennas and Propagation*, vol. 61, no. 9, pp. 2176-2179, Sep. 2013.

[9] S. R. Best, "On the resonant properties of the Koch fractal and other wire monopole antennas," *IEEE Antennas and Wireless Propagation Letters*, vol. 1, pp. 74-76, 2002.

[10] K. J. Vinoy, J. K. Abraham, and V. K. Varadan, "On the relationship between fractal dimension and the performance of multi-resonant dipole antennas using Koch curves," *IEEE Transactions on Antennas and Propagation*, vol. 51, no. 9, pp. 2296-2303, Sep. 2003.

[11] H.-Y. Liang, H.-C. Yang, and J. Zhang, "A cylindrical conformal directional monopole antenna for borehole radar application," *IEEE Antennas and Wireless Propagation Letters*, vol. 11, pp. 1525-1528, 2012.

[12] Z.-Q. Liu, Y.-S. Zhang, Z. Qian, Z. P. Han, and W. Ni, "A novel broad beamwidth conformal antenna on unmanned aerial vehicle," *IEEE Antennas and Wireless Propagation Letters*, vol. 11, pp. 196-199, 2012.

[13] S. Nikolaou, G. E. Ponchak, J. Papapolymerou, and M. M. Tentzeris, "Conformal double exponentially tapered slot antenna (DETSA) on LCP for UWB applications," *IEEE Transactions on Antennas and Propagation*, vol. 54, no. 6, pp. 1663-1669, Jun. 2006.

[14] G. E. Ponchak, J. L. Jordan, and C. T. Chevalier, "Characteristics of double exponentially tapered slot antenna (DETSA) conformed in the Longitudinal direction around a cylinder," *IEEE Antennas and Wireless Propagation Letters*, vol. 6, pp. 60-63, 2007.

[15] J. L. Gomez-Tornero, "Analysis and design of conformal tapered leaky-wave antennas," *IEEE Antennas and Wireless Propagation Letters*, vol. 10, pp. 1068-1071, 2010.

[16] A. J. Martinez-Ros, J. L. Gomez-Tornero, and G. Goussetis, "Conformal tapered substrate integrated waveguide leaky-wave antenna," *IEEE Transactions*

on Antennas and Propagation, vol. 62, no. 12, pp. 5983-5991, Dec. 2014.

[17] B. D. Braaten, S. Roy, S. Nariyal, M. Al Aziz, N. F. Chamberlain, I. Irfanullah, M. T. Reich, and D. E. Anagnostou, "A self-adapting flexible (SELFLEX) antenna array for changing conformal surface applications," *IEEE Transactions on Antennas and Propagation*, vol. 61, no. 2, pp. 655-665, Feb. 2013.

[18] K. Wincza, S. Gruszczynski, and K. Sachse, "Conformal four-beam antenna arrays with reduced sidelobes," *Electronics Letters*, vol. 44, no. 3, pp. 174-175, Jan. 2008.

[19] N. A. Bishop, J. Miller, D. Zeppettella, W. Baron, J. Tuss, and M. Ali, "A broadband high-gain bi-layer LPDA for UHF conformal load-bearing antenna structures (CLASs) applications," *IEEE Transactions on Antennas and Propagation*, vol. 63, no. 5, pp. 2359-2364, May 2015.

[20] X. Gao, Z. Shen, and C. Hua, "Conformal VHF log-periodic ballon antenna," *IEEE Transactions on Antennas and Propagation*, vol. 63, no. 6, pp. 2756-2761, Jun. 2015.

[21] Y. Zhao, Z. Shen, and W. Wu, "Conformal SIW H-plane horn antenna on a conducting cylinder," *IEEE Antennas and Wireless Propagation Letters*, vol. 14, pp. 1271-1274, 2015.

[22] Y. J. Cheng, H. Xu, D. Ma, J. Wu, L. Wang, and Y. Fan, "Millimeter-wave shaped-beam substrate integrated conformal array antenna," *IEEE Transactions on Antennas and Propagation*, vol. 61, no. 9, pp. 4558-4566, Sep. 2013.

[23] R. Carrel, "The design of log-periodic dipole antennas," *IRE International Convention Record*, vol. 9, no. 1, pp. 61-75, 1961.

[24] C. K. Campbell, I. Traboulay, M. S. Suthers, and H. Kneve, "Design of a stripline log-periodic dipole antenna," *IEEE Transactions on Antennas and Propagation*, vol. 25, no. 15, pp. 718-721, Sep. 1977.

Zengrui Li received the B.S. degree in Communication and Information System from Beijing Jiaotong University, Beijing, China, in 1984; the M.S. degree in Electrical Engineering from the Communication University of China, Beijing, China, in 1987; and the Ph.D. degree in Electrical Engineering from Beijing Jiaotong University, Beijing, China, in 2009. He is currently a Professor with the Communication University of China, Beijing, China. His research interests include the areas of computational electromagnetics, the Finite-Difference Time-Domain (FDTD) methods, electromagnetic modeling and simulation of antennas, and communication antennas. Li is a Senior Member of the Chinese Institute of Electronics.

Longdan Tan received the B.S. and M.S. degree in Electromagnetic Field and Microwave Technology from the Communication University of China, Beijing, China, in 2012 and 2015, respectively. He is currently working at Network Operation Center, Startimes Media Group, Beijing, China as a Communication Engineer. His research interests include conformal antennas, wideband antennas for wireless communications and RF circuits.

Xiaole Kang received the B.S. and M.S. degree in Electromagnetic Field and Microwave Technology from the Communication University of China, Beijing, China, in 2010 and 2013, respectively. From 2013 to 2014, she was an Assistant Engineer of Shandong Academy of Sciences, Jinan, China, where she was responsible for the design of UWB antenna for through-wall radar system. She is currently pursuing the Ph.D. degree in Electromagnetic Field and Microwave Technology at the Communication University of China. Her research interests include conformal antennas, wideband antennas for wireless communications and RF circuits.

Jianxun Su received the M.S. and the Ph.D. degree in Electromagnetic Field and Microwave Technology from the Communication University of China and Beijing Institute of Technology, Beijing, China, in 2008 and 2011, respectively. From 2011 to 2013, he was with East China Research Institute of Electronic Engineering (ECRIEE), where he engaged in phased-array research. He is currently working as Postdoctoral Fellow at Electromagnetic Laboratory, Communication University of China. His special research interests include integral equation methods for electromagnetic problems and periodic structure analysis.

Qingxin Guo received the B.S., M.S. and Ph.D. degrees in Electromagnetic Field and Microwave Technology from the Communication University of China, Beijing, China, in 1997, 2006 and 2013, respectively. From 1997 to 2002, he was an Engineer and Project Manager of the Xiamen Overseas Chinese Electronics Co., Ltd., Xiamen, China, where he was involved with the repeaters and the mobile phone for the GSM system. From 2002 to 2004, he was a Project Manager of the Beijing Gigamega Electronics Co., Ltd., Beijing, China, where he was responsible for the design of a high-power amplifier for UHF TV transmitter and FM transmitter. From 2004 to 2008, he was a Project Manager of the Beijing Filcom Technology Co. Ltd., Beijing, China, where he was responsible for the design of a high-power combiner and multiplexer. He joined the Communication University of China in 2006. From 2011 to 2012, he was a Visiting Researcher with the Electromagnetic Communication Laboratory (EMC Lab), which is affiliated with the Electrical Engineering Department, Pennsylvania State University, University Park. His research interests include antennas, microwave passive components, and RF circuits.

Yaoqing Yang received his B.S. degree from the Beijing Jiaotong University, China, in 1983, and his M.S. degree from the Communication University of China, China, in 1986, both in Electrical Engineering. He received his Ph.D. degree in the area of Wireless Communications and Networks from the University of Texas (UT) at Austin in 2006. He is now an Associate Professor in the Department of Electrical and Computer Engineering, University of Nebraska-Lincoln (UNL). His current research interests lie in wireless communications and networks with emphasis on radio channel characterizations, cognitive radio networks, and statistical signal processing. Yang is a Senior Member of IEEE.

Junhong Wang received the B.S. and M.S. degrees in Electrical Engineering from the University of Electronic Science and Technology of China, Chengdu, China, in 1988 and 1991 respectively, and the Ph.D. degree in Electrical Engineering from Southwest Jiaotong University, Chengdu, China, in 1994. In 1995, he joined the faculty of the Department of Electrical Engineering, Beijing Jiaotong University, Beijing, China, where he became a Professor in 1999. From January 1999 to June 2000, he was a Research Associate with the Department of Electric Engineering, City University of Hong Kong, Hong Kong, China. From July 2002 to July 2003, he was a Research Scientist with Temasek Laboratories, National University of Singapore, Singapore. He is currently with the Key Laboratory of ALL Optical Network and Advanced Telecommunication Network, Ministry of Education of China, Beijing Jiaotong University, and also with the Institute of Lightwave Technology, Beijing Jiaotong University. His research interests include numerical methods, antennas, scattering, and leaky wave structures.

Analysis of Radiation Characteristics of Conformal End-Fire Antenna Mounted on a Large Conducting Cylinder

Ping Wang

School of Communications and Information Engineering
Chongqing University of Posts and Telecommunications, Chongqing 400065, China
wangpingcqz@163.com

Abstract ─ An analysis on the effect of dielectric radome on radiation characteristics of conformal end-fire antenna mounted on a large conducting cylinder is presented in this paper. Ray theory firstly is used to characterize the effect of the planar dielectric layer on the incident electromagnetic wave with different polarizations, which predicts the physical behavior of radome-antenna system. Meanwhile, the paper shows a comparing analysis of the effect of dielectric radome on conformal end-fire antenna with different polarization when the antenna is located on the external surface of a hollow conducting cylinder. It is found that the radiation characteristics of end-fire antenna is significantly changed due to the presence of the dielectric radome, and the effect of dielectric radome on vertically polarized end-fire antenna is less than that on horizontally polarized end-fire antenna. Parametric studies of the proposed radome-antenna system are also presented in this paper to explore the interaction mechanism between the endfire antenna and dielectric radome, and provide brief guidelines for the antenna designers. These results may provide some useful insights in the design of the radome-antenna system in practical engineering.

Index Terms ─ Conformal antenna, dielectric radome, end-fire antenna, horizontally polarized antenna, vertically polarized antenna.

I. INTRODUCTION

Dielectric antenna radome consists of single layer or multilayer dielectric with arbitrary shape, and its existence will affect the performance of the antenna or array and degrades the quality or property of electronic systems inevitably. For a number of years extensive research has been conducted on radome-antenna system and efficient analysis techniques [1-5] had also been developed for the accurate prediction of the behavior of electromagnetic (EM) performance. Due to the geometrical complexity of the radome-antenna system, its analysis is usually based on some approximate approaches [6-11], such as the methods based on the high-frequency approximation [6], integral equation models solved by the method of moments [7], the finite difference time domain (FDTD) method combined with the reciprocity theorem [8], and 3-D ray-tracing in conjunction with aperture integration method [9], coupled surface integral equation (CSIE) [10] and various fast solvers like the multilevel fast multi-pole algorithm (MLFMA) [11]. A hybrid physical optics method of moments (PO-MoM) scheme was also proposed to solve very large antenna-radome systems with sharp tip regions [12]. These analysis methods for the antenna-radome system are concentrated on the aspect that the antenna is placed in the interior of the dielectric radome. However, limited interior space of dielectric radome can't accommodate all electric systems, especially the large size antenna array, and the strong reciprocal interference between many radiation sources degrades the working quality of electronic systems, thus the model that the antenna is placed on the exterior of the dielectric radome is desirable, and it is also meaning to research on the performance of radome-antenna system in this layout.

Through our former working in [13] had involved the research on the end-fire antenna-radome system, the working was not refer to the physical behavior of dielectric radome and research the effect of dielectric radome on end-fire antenna with different polarization. Therefore, the objective of this paper is to investigate the effect of dielectric radome on radiation characteristics of conformal end-fire antenna mounted on a large conducting cylinder. A parametric study showing the impact of various parameters of dielectric radome on the antenna performance is presented. The simulation and analysis for the complete model are performed using the commercial computer software package Ansoft high-frequency structure simulator (HFSS), which is based on the finite element method.

II. EFFECT OF PLANAR DIELECTRIC LAYER ON THE INCIDENT PLANAR WAVE

In order to take insight into the physical behavior of dielectric radome and for simplicity, the section only

Submitted On: December 27, 2014
Accepted On: June 17, 2016

considers the physical mechanism when a planar wave is incident on a planar dielectric layer and dielectric constant ε_2 of dielectric layer is chosen to be same as dielectric radome ($\varepsilon_2 = \varepsilon_r = 5.5$, $\varepsilon_1 = \varepsilon_3 = 1$), as shown in Fig. 1. If amplitude of the incident planar wave is one, a transmitted field with a value of $T_{12}T_{23}$ in area 3 is produced when the plane wave is incident on two interfaces. However, the incident wave also produces second reflection in the material interface between dielectric layer and area 3, and creates second transmitted field with amplitude of $T_{12}R_{23}R_{21}T_{23}$. Similarly, second incident wave also produces third reflection in the material interface between dielectric layer and area 3, where T_{12} and T_{23} denote the transmission coefficient, R_{12} and R_{23} denote the reflection coefficient on two material interfaces. This shows that when a uniform plane wave is incident on lossless material interfaces with an angle of α, the total transmitted field in area 3 is the superposition of all transmitted fields, where *d* is the thickness of dielectric layer, β is the angle of refraction, and θ is the angle between transmission field and *z*-axis. Suppose that the coordinates of incidence point are (0, *d*), and the incident field is denoted as $E^i(0, d)$, and the transmission distance of refracted electromagnetic wave is represented as *P* in dielectric layer. Thus, when the planar wave is transmitted from the point (0, *d*) to the distance *r* away from the origin of the coordinate system, the variation of phase is the quantity $k_2P+k_3(r-P\sin\beta\sin\theta)$, where k_2 and k_3 are the propagation constants of electromagnetic wave in dielectric and vacuum, respectively.

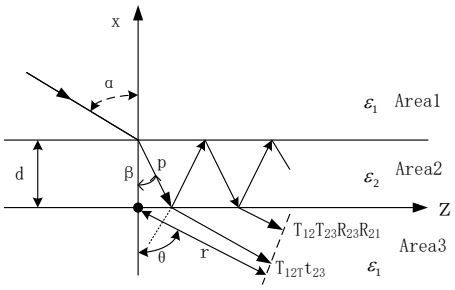

Fig. 1. EM wave is reflected and refracted many times in planar dielectric layer.

For simplicity, by setting $\Phi = k_2P - k_3P\sin\beta\sin\theta$, the phase of the first transmitted electromagnetic wave coming from a plane far away from the origin of the coordinate system with distance *r* can be expressed as $\Phi + k_3r$, the phase of the second transmitted electromagnetic wave coming from the same plane can be denoted as $3\Phi + k_3r$. Simultaneously, when it adds a reflection in the interior of substrate, the phase also adds a value of 2Φ . Therefore, the total field in area 3 can be denoted as:

$$\begin{aligned} E_{13} &= E^i(0,d)T_{12}T_{23}e^{(-j\Phi - jk_3r)}\left(1 + R_{21}R_{23}e^{-j2\Phi}\right. \\ &\quad \left. + (R_{21}R_{23})^2 e^{-j4\Phi} + (R_{21}R_{23})^3 e^{-j6\Phi} + \ldots\right) \\ &= E^i(0,d)T_{12}T_{23}e^{(-j\Phi - jk_3r)}\frac{1}{1 - R_{21}R_{23}e^{-j2\Phi}}. \end{aligned} \tag{1}$$

From Eq. (1), it can be seen that the total field is interrelated with the transmission coefficient and the reflection coefficient on two material interfaces. Setting the transmission coefficient of E-field as:

$$T_e = \frac{T_{12}T_{23}}{1 - R_{21}R_{23}e^{-j2\Phi}}, \tag{2}$$

where $\Phi = k_2P - k_3P\sin\beta\sin\theta = k_0d\sqrt{\varepsilon_2 - \varepsilon_1\sin^2\alpha}$.

Thus, the total E-field in area 3 can be expressed as;

$$E_{13} = E^i(0,d)T_e\exp(-j\Phi - jk_3r). \tag{3}$$

On the other hand, according to the different directions of electric field vector, the incident plane wave can be divided into two different polarization types:

(1) TE Wave: the electric field vector is normal to the incident plane.

We assume that the dielectric layer is parallel to the *yz*-plane, and is normal to the *x*-axis, so the direction of *y*-axis is that of E-field. The reflection coefficient of electric field can be given by [14]:

$$R_E^{TE} = \frac{\cos\alpha - \sqrt{\frac{\varepsilon_2\mu_1}{\varepsilon_1\mu_2}}\sqrt{1 - \frac{\varepsilon_1\mu_1}{\varepsilon_2\mu_2}\sin^2\alpha}}{\cos\alpha + \sqrt{\frac{\varepsilon_2\mu_1}{\varepsilon_1\mu_2}}\sqrt{1 - \frac{\varepsilon_1\mu_1}{\varepsilon_2\mu_2}\sin^2\alpha}}. \tag{4}$$

The transmission coefficient of electric field can be expressed as:

$$T_E^{TE} = 1 + R_E^{TE}, \tag{5}$$

and the reflection coefficient of magnetic field also can be written as $R_H^{TE} = R_E^{TE}$, the transmission coefficient of magnetic field is $T_H^{TE} = \eta_1/\eta_2 \times T_E^{TE}$, where $\eta_1 = \sqrt{\mu_1/\varepsilon_1}$ and $\eta_2 = \sqrt{\mu_2/\varepsilon_2}$ are the wave impedances of electromagnetic wave in medium and vacuum, respectively.

(2) TM Wave: the electric field vector is parallel to the incident plane.

According to the Ref. [14], the reflection coefficient of magnetic field will be:

$$R_H^{TM} = \frac{\cos\alpha - \sqrt{\frac{\varepsilon_1\mu_2}{\varepsilon_2\mu_1}}\sqrt{1 - \frac{\varepsilon_1\mu_1}{\varepsilon_2\mu_2}\sin^2\alpha}}{\cos\alpha + \sqrt{\frac{\varepsilon_1\mu_2}{\varepsilon_2\mu_1}}\sqrt{1 - \frac{\varepsilon_1\mu_1}{\varepsilon_2\mu_2}\sin^2\alpha}}. \tag{6}$$

The transmission coefficient of magnetic field can be expressed as $T_H^{TM} = 1 + R_H^{TM}$, and the reflection coefficient of electric field will be $R_E^{TM} = R_H^{TM}$ and the

transmission coefficient of electric field can be written as:

$$T_E^{TM} = \eta_2/\eta_1 \times T_H^{TM},$$

where $\eta_1 = \sqrt{\mu_1/\varepsilon_1}$ and $\eta_2 = \sqrt{\mu_2/\varepsilon_2}$ are the wave impedances of electromagnetic wave in medium and vacuum, respectively. Thus, it is clear from Eq. (3) that the power transmission coefficient $|T_e|^2$ can be calculated by using the transmission coefficient, the reflection coefficient and the value of Φ in any material interface as shown in Fig. 2.

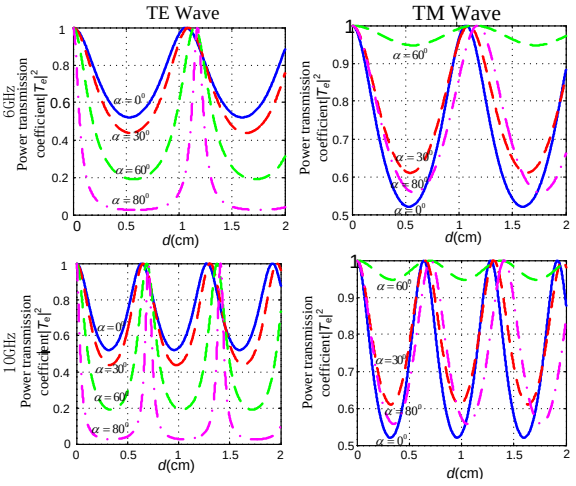

Fig. 2. Power transmission coefficient $|T_e|^2$ as a function of α, d and f.

It is obvious from Fig. 2 that when the thickness d of dielectric layer is close to zero and other parameters are chosen arbitrarily, the power transmission coefficient $|T_e|^2$ is close to one, which shows that the radome can be processed as thin dielectric layer by using unyielding dielectric to achieve higher transmission coefficient. It is also observed that for same incidence angle α the power transmission coefficient $|T_e|^2$ vary periodically with the thickness d of dielectric layer, and when the thickness d reaches a specific value the power transmission coefficient is close to one. As depicted in Fig. 1, choosing the phase difference between the two transmitted waves as $2\Phi = 2n\pi$, all transmitted waves will be superposed with same phase and the power transmission coefficient will reach its largest value. Thus the condition of achieving largest power transmission coefficient can be written as:

$$\Phi = k_0 d\sqrt{\varepsilon_2 - \varepsilon_1 \sin^2\alpha} = n\pi. \quad (7)$$

That is,

$$d = \frac{n\lambda}{2\sqrt{\varepsilon_2 - \varepsilon_1 \sin^2\alpha}}, \quad n=1,2,3,... \quad (8)$$

This shows that the power transmission coefficient has largest value when the thickness d of dielectric layer is selected by using Eq. (8).

III. EFFECT OF DIELECTRIC RADOME ON THE HORIZONTALLY POLARIZED ANTENNA

In this section, effect of dielectric radome on the horizontally polarized antenna based on balanced Vivaldi antenna (BAVA) is presented. The design of BAVA follows concepts described in [15], and it is designed to operate over 6–18 GHz frequency ranges. The proposed radome-antenna system is shown in Fig. 3. The antenna element is supported by using three dielectric cylinders, with height of h and dielectric constant 2.1, and is placed over a conducting cylinder surface of limited radius r=10 cm and length 15 cm. One end of three metal cylinder probes with radius of 0.6 mm is loaded by larger radius cylinder with thickness of 1 mm, whereas the other end firstly passes through dielectric cylinders with radius of 1.2 mm, and then is connected with the conducting cylinder surface, as shown in Fig. 3. The antenna surface is curved and is parallel to the cylinder surface, and the top edge of the antenna is parallel to the top edge of the conducting cylinder. A dielectric radome (dielectric constant $\varepsilon_r = 5.5$), whose generatrix is parabola curve and specifies in length P of 30 cm and thickness d of 5 mm, is presented. The generatrix equation can be expressed as:

$$\begin{aligned} x_o &= -az_0^{\,n} + r, \\ x_i &= -a_1 z_i^{\,n} + r - d, \end{aligned} \quad (9)$$

where a=r/P^n, a_1=(r-d)/(P-d)^n, n denotes the power index, x_0 is the distance between exterior generatrix and center line, z_0 is the variable value in z-direction, x_i is the distance between interior generatrix and center line, z_i is the variable value in z-direction.

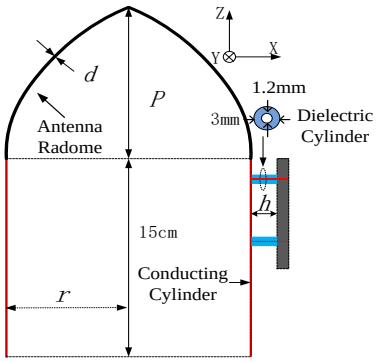

Fig. 3. Radome-antenna system based on balanced Vivaldi antenna.

Figure 4 shows the comparison of the radiation

patterns with two examples, i.e., without antenna radome and with antenna radome for both E_Φ and E_θ. It is seen clearly that when no antenna radome is used, the main beam of the antenna is directed to the end-fire direction and the antenna has low cross polarization of less than -20 dB. When the dielectric radome is placed on the top part of conducting cylinder, the electromagnetic wave from radiator will be reflected and refracted by the dielectric surface, which leads to the large beam direction angle in H-plane, such as at 6 GHz, beam direction angle is 27^0 and the 3 dB beam-width is 57^0 without dielectric radome, whereas the beam direction angle and 3 dB beam-width are 30^0 and 35^0 respectively with dielectric radome; at 12 GHz, beam direction angle is 0^0 and the 3 dB beam-width is 48^0 without dielectric radome, whereas the beam direction angle and 3 dB beam-width with dielectric radome become 130^0 and 100^0, respectively. The measured radiation pattern without dielectric radome also is presented to compare with simulated results, which shows that the simulation and measurement results generally agree, however a little discrepancy has been observed possibly due to the error of substrate parameters and manufacturing tolerances. Figure 5 shows the simulated E-field in H-plane (xz-plane), which demonstrates the impact of the dielectric radome on E-field. It is clearly seen from the figure that when an antenna radome is placed on the top part of conducting cylinder, for the low frequency the main energy is reflected by the surface of dielectric radome, whereas as the frequency is increased to 12 GHz a part of energy is transmitted through antenna radome. This is due to the fact that at 12 GHz the wavelength in air is 25 mm, but will be around 10.7 mm in material with dielectric constant ε_r=5.5, so the thickness of antenna radome is close to half-wavelength in dielectric. As a result, reflection coefficients in internal and external surfaces of dielectric radome have converse symbols, which lead to larger transmission coefficient.

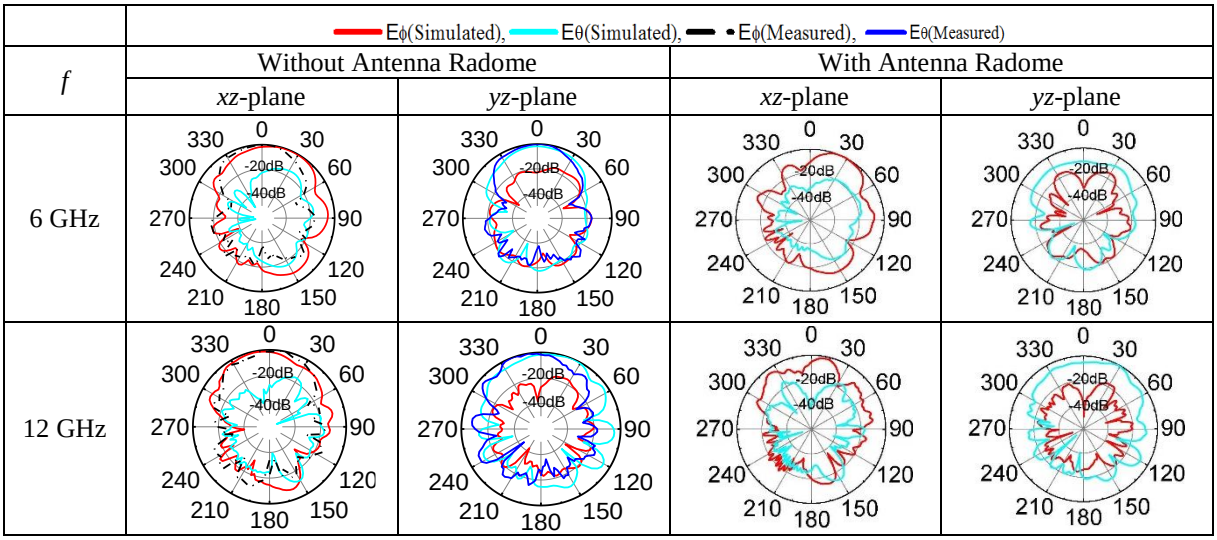

Fig. 4. Comparison of radiation pattern of the horizontal polarization antenna.

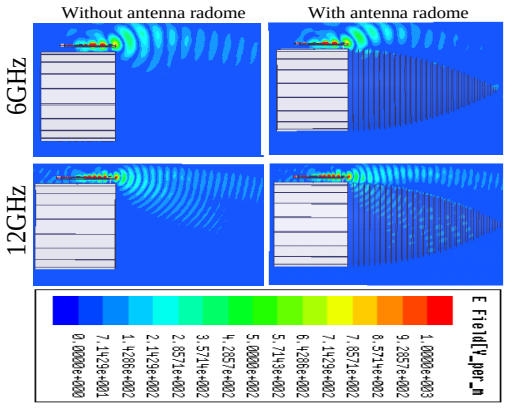

Fig. 5. Comparison of simulated radiated E-field of the horizontal polarization antenna in H-plane.

IV. EFFECT OF DIELECTRIC RADOME ON THE VERTICALLY POLARIZED ANTENNA

In order to meet the bandwidth requirement of 6-18 GHz a cascaded monopole log-periodic antenna configuration is selected, as shown in Fig. 6. The proposed antenna has a single-layer metallic structure and is printed on a substrate of thickness 0.724 mm, with the dielectric constant of 3.38, and is located above the metal conducting cylinder surface vertically. A 50 Ω coaxial cable is used as the feed source, whose outer conductor is directly soldered to metal ground plane, whereas the inner conductor is connected directly to the one end of cascaded folded microstrip-line, and other end is shorted to the ground plane for reducing the end reflection. As shown in Fig. 6, the geometry is specified by the following parameters: the height of the folded

microstrip-line P_1, the gap G_1, the vertically strip width and horizontally strip width in arm of first folded pairs w_1 and wf_1, and the transmission strip width s_1, the strip spacing in arm a_1, the transmission strip length b_1, and the scaling factor τ. All these parameters are decreased along the array by the scaling factor τ, which are expressed as:

$$\tau = \frac{P_2}{P_1} = \frac{w_2}{w_1} = \frac{a_2}{a_1} = \frac{wf_2}{wf_1} = \frac{b_2}{b_1} = \frac{G_2}{G_1} = \frac{s_2}{s_1}. \quad (10)$$

The length $(2P_1+a_1)$ of first folded microstrip-line is approximately half-wavelength at a frequency which is referred to as the lowest working frequency. The dielectric top edge of the proposed antenna is parallel to the top edge of conducting cylinder. Simulation and analysis of the radome-antenna system are performed using the package ANSYS high-frequency structure simulator (HFSS), and the optimized values are illustrated in Table 1.

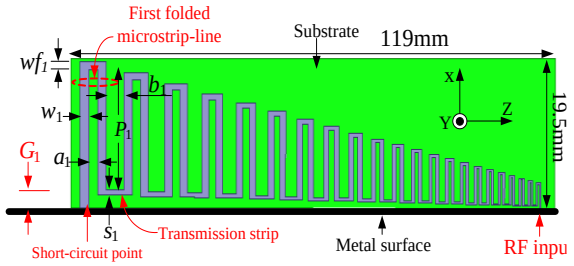

Fig. 6. Configuration of the proposed vertically polarized antenna.

Table 1: Parameters of the proposed antenna as Fig. 6

Parameter	P_1	G_1	w_1	wf_1
Values	12.5 mm	1 mm	4.76 mm	4.76 mm
Parameter	a_1	b_1	s_1	τ
Values	1.96 mm	1.76 mm	2.5 mm	0.88

Figure 7 shows the radome-antenna system based on cascaded monopole log-periodic antenna, which is same as the model presented in Fig. 3. It may also be mentioned that due to the radiated E-filed is vertical to the metal surface of conducting cylinder, thus the radiant electromagnetic wave of cascaded monopole log-periodic antenna can be approximated to the TM wave, and exhibits similar variations trend which has been presented in the theory analysis in Section II. Figure 8 only shows the radiation pattern of the vertically polarized antenna at two most influential frequencies. For other working frequencies, it is known from simulation that the dielectric radome has smaller effect on the radiation patterns of the vertically polarized antenna comparing to that of the horizontally polarized antenna, which is not presented in this paper owing to limited space. It is clearly seen from Fig. 8 that at 8 GHz the effect of the dielectric radome is very serious, which is due to the fact that as the frequency is increased, the effective radiation area is close to the top edge of conducting cylinder, the incidence angle of the radiant electromagnetic wave incident on the surface of dielectric radome becomes smaller (such as about 60^0). According to the theory of Section II, the power transmission coefficient also becomes larger, thus a radiated blind area will be appeared in end-fire direction. When the frequency is increased continuously which means that the incidence angle also becomes smaller, such as increasing to 12 GHz, but the radiation pattern is also subjected to the significant effect of the dielectric radome owing to the dielectric radome resonance.

Figure 9 shows the simulated radiated E-field in E-plane (xz-plane). It should be observed that without dielectric radome introduced, at low frequency the dominant currents are covered in whole folded metal microstrip-line, the metal surface has little influence on the radiation pattern, resulting in a main beam directed in the end-fire direction. When the antenna is worked in higher frequency range the resonant dominant currents are concentrated in the close proximity of the feed port, the main beam only is deviated from the end-fire direction slightly. However, due to the presence of the nearby dielectric radome, the radiated electromagnetic waves from the proposed antenna are significantly affected. It is also observed that a part of energy is transmitted through dielectric radome and deviated from its original radiant direction owing to refraction phenomena, which shows the similar behavior with horizontally polarized antenna.

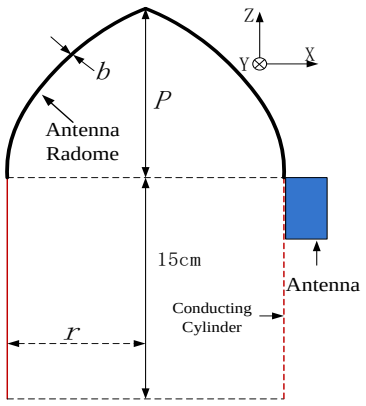

Fig. 7. Radome-antenna system based on cascaded monopole log-periodic antenna.

f	Without Antenna Radome		With Antenna Radome	
	xz-plane	*yz*-plane	*xz*-plane	*yz*-plane
8 GHz	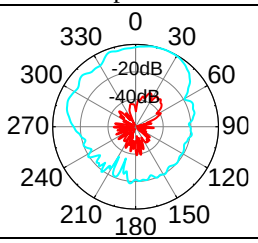	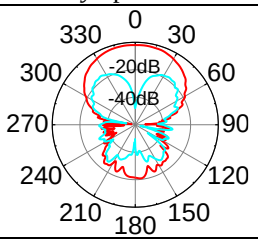	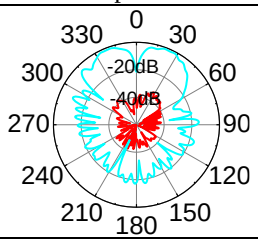	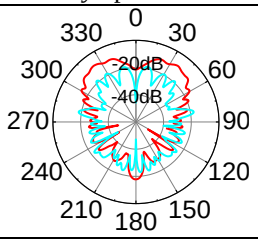
12 GHz	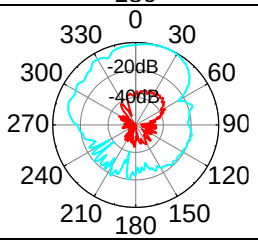	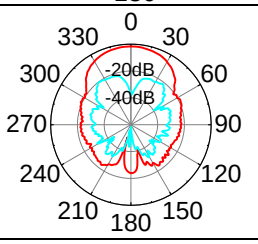	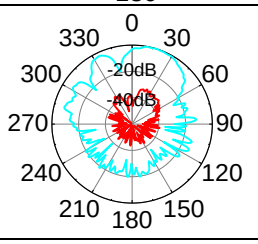	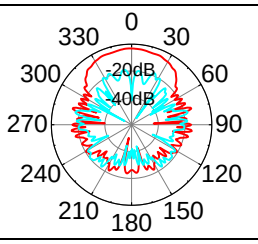

Fig. 8. Comparison of radiation pattern of the vertical polarization antenna. (— Eϕ; — Eθ)

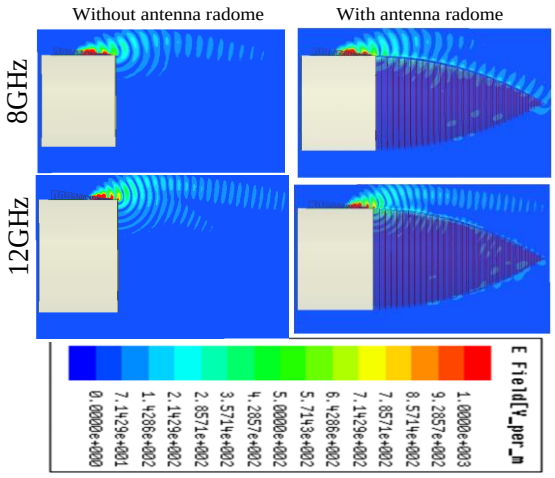

Fig. 9. Comparison of simulated radiated E-field of the vertical polarization antenna in E-plane.

V. PARAMETRIC STUDIES

In Section III and IV, a comparison of the effect of the dielectric radome on different polarization types is studied, which shows that the affect of dielectric radome on vertically polarized endfire antenna is less than that on the horizontally polarized endfire antenna, thus the vertically polarized endfire antenna is suitable for the proposed model. In this section, parametric studies about dielectric radome based on the cascaded monopole log-periodic antenna are presented. The parameters under study include the bottom plane radius r, height P, thickness b, power index n, and dielectric constant ε_r. To better understand the influence of the parameters on the radiation pattern, only one parameter at a time will be varied, while others are kept unchanged unless especially indicated.

A. Bottom plane radius *r* of dielectric radome

Figure 10 shows the effect of variation of the bottom plane radius r on the radiation pattern. It is obvious from the figure that in E-plane (*xz*-plane) the variation of radius r has little effect on the radiation pattern and the radiation pattern keeps low cross-polarization levels (<-30 dB). In H-plane (*yz*-plane) as the radius r is increased the front-back ratio of the antenna is also enhanced slightly. In the cross-polarization curves, the cross-polarization level is decreased by increasing radius r. This is due to the fact that smaller radius r of conducting cylinder will inspirit the higher mode, which leads to high cross-polarization levels.

B. Height *P* of dielectric radome

Figure 11 demonstrates the impact of varying the height P on the radiation pattern of the vertical polarization antenna. The figure shows that in E-plane (*xz*-plane) with increasing the height P from 10 to 30 cm, the antenna keeps low cross-polarization levels (<-30 dB), and the co-polarization curves almost keep invariable at working frequency, but in the co-polarization curve a deep blind area has been appeared in end-fire direction. In H-plane (*yz*-plane), the cross-polarization level becomes larger and the largest value varies around -20 dB. Moreover, the front-back ratio of the co-polarization curves is also increased slightly as the height P is increased. This is due to the fact that when the height P=30 cm, more energy is incident on the surface of dielectric radome, and the dielectric radome can enhance the directive function of the radiation field shown in Fig. 9. Results from the figure have revealed that in order to achieve a good radiation pattern a small height P needs

be adopted properly.

C. Thickness *b* of dielectric radome

The effect of varying the thickness *b* of dielectric radome on the radiation pattern is presented in Fig. 12. It is clearly seen from the figure that in E-plane (*xz*-plane) when the thickness *b* is decreased, the antenna keeps low cross-polarization levels, and shows better co-polarization curves. It may be noted that with increasing the thickness b, the dielectric radome resonance is pulled to the lower frequency band, thus the blind area will be appeared in co-polarization curves at lower frequency band. In H-plane (*yz*-plane), the variation of thickness *b* has significant effect on the cross- and co-polarization levels. As the thickness *b* is increased the cross-polarization levels become worse, whereas the cross-polarization levels in the end-fire direction is decreased slightly, generally less than -40 dB. For co-polarization curves, increasing thickness *b* will lead to higher front-back ratio. However, the radiation pattern is still almost symmetric with respect to the *z*-axis in *yz*-plane. It is also observed from the figure that smaller dielectric thickness *b* will produce smoother co-polarization curve. Thus, the antenna has good performance when the dielectric radome keeps small thickness *b*.

D. Power index *n* of the generatrix equation

Figure 13 shows the effect of varying the power index *n* on the radiation pattern. The results show that the variation of power index *n* has significant effect on the cross- and co-polarization levels. In E-plane (*xz*-plane), with increasing power index *n* the antenna also keeps low cross-polarization level, generally less than -30 dB. When the antenna is working in low frequency, the variation of power index *n* has little effect on the radiation pattern, but in high frequency as the power index *n* is increased, the co-polarization curve produces large variation and blind area of co-polarization curves becomes deeper. In H-plane (*yz*-plane), the cross-polarization levels, generally less than -30 dB. However, the co-polarization curve produces large variation and blind area of co-polarization curves becomes deeper as the power index *n* is increased. In H-plane (*yz*-plane), the cross-polarization level in end-fire direction is less than -40 dB, and has little variation as the index *n* is increased. However, the co-polarization curve in high frequency has large variation, and the front-back ratio is increased slightly with decreasing the power index *n*. Therefore, the antenna has good end-fire characteristics when the power index has smaller value.

E. Dielectric constant ε_r of dielectric radome

Figure 14 demonstrates the impact of varying dielectric constant ε_r on the radiation pattern. It is found that in E-plane (*xz*-plane) the variation of dielectric constant ε_r has little effect on the cross-polarization levels and the antenna also keeps low cross-polarization level, generally less than -30 dB. But the 3 dB beam-width of the co-polarization radiation field is decreased as the dielectric constant ε_r is increased, and the dielectric radome resonance is also produced in high frequency. This is also due to the fact that the thickness of dielectric radome is close to the half-wavelength when the antenna is working in higher frequency and leads to refraction phenomenon of a part of energy. In H-plane (*yz*-plane), the antenna also keeps low cross-polarization levels, and as the dielectric constant ε_r is increased the co-polarization curves still keep symmetric radiation pattern. It is obvious from the figure that smaller the dielectric constant ε_r better the radiation pattern will be.

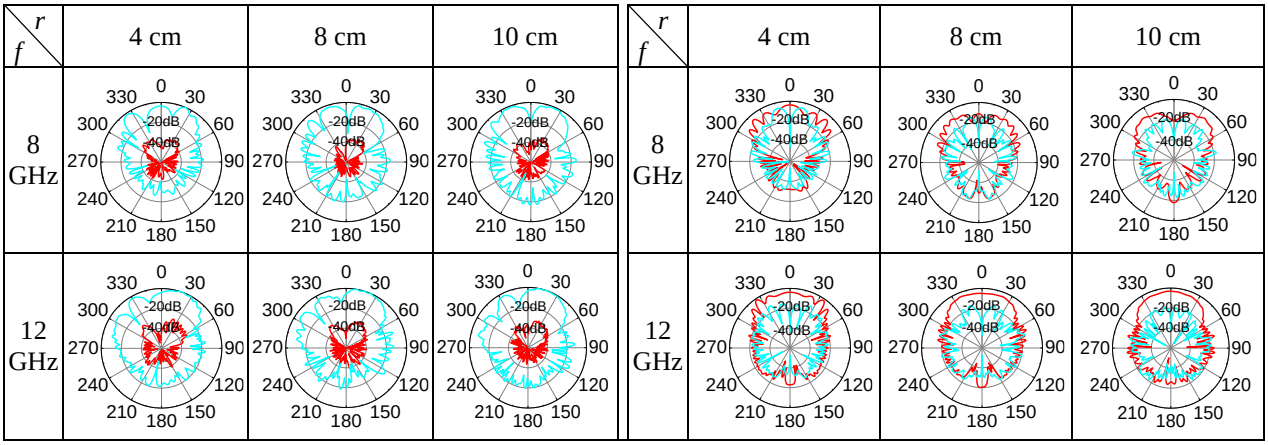

(a) *xz*-plane (b) *yz*-plane

Fig. 10. Effect of varying the bottom plane radius *r* on the radiation pattern. (— Eϕ; — Eθ)

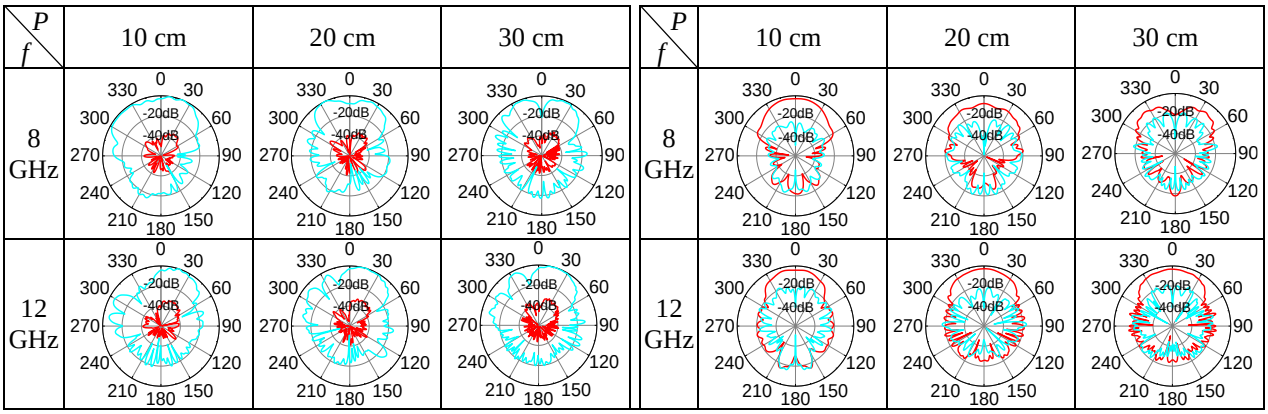

(a) *xz*-plane (b) *yz*-plane

Fig. 11. Effect of varying the height *P* on the radiation pattern. (— Eϕ; — Eθ)

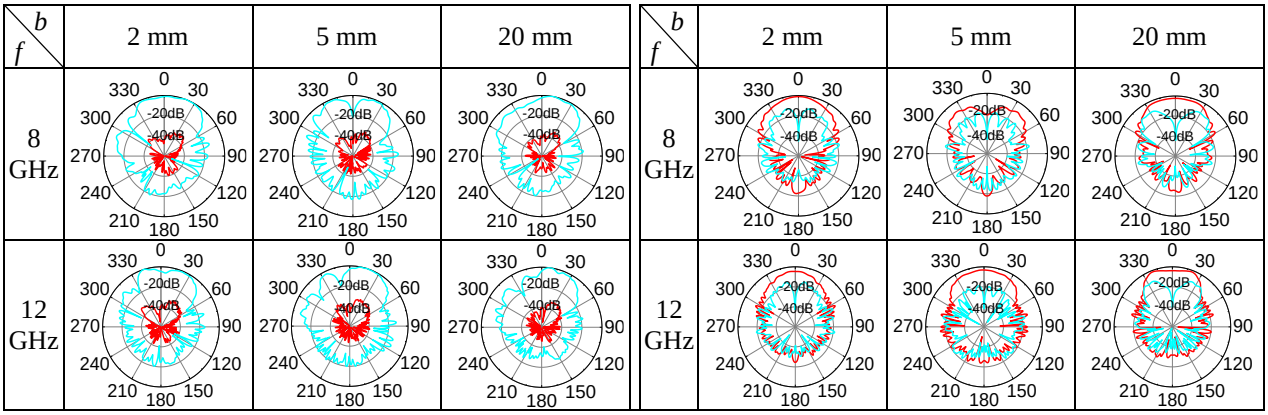

(a) *xz*-plane (b) *yz*-plane

Fig. 12. Effect of varying the thickness *b* on the radiation pattern. (— Eϕ; — Eθ)

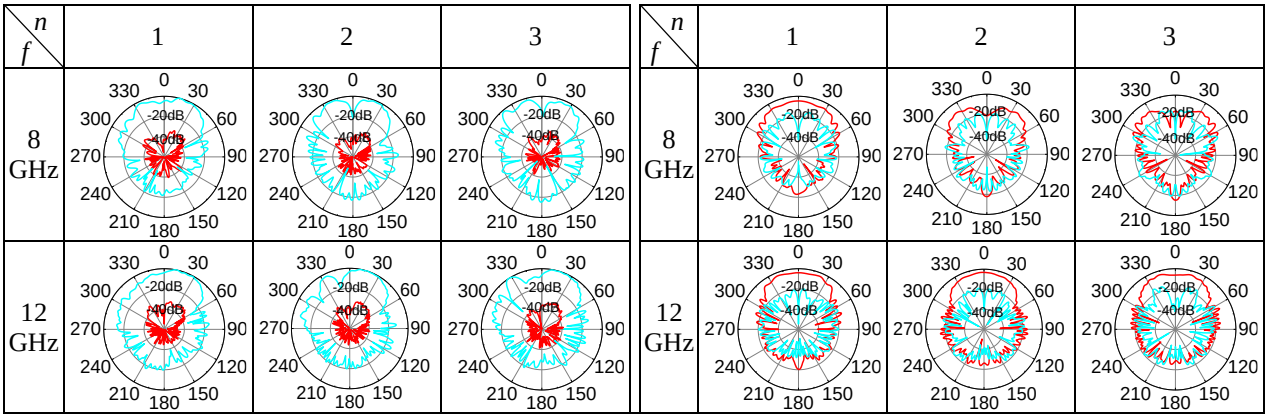

(a) *xz*-plane (b) *yz*-plane

Fig. 13. Effect of varying the power index *n* on the radiation pattern. (— Eϕ; — Eθ)

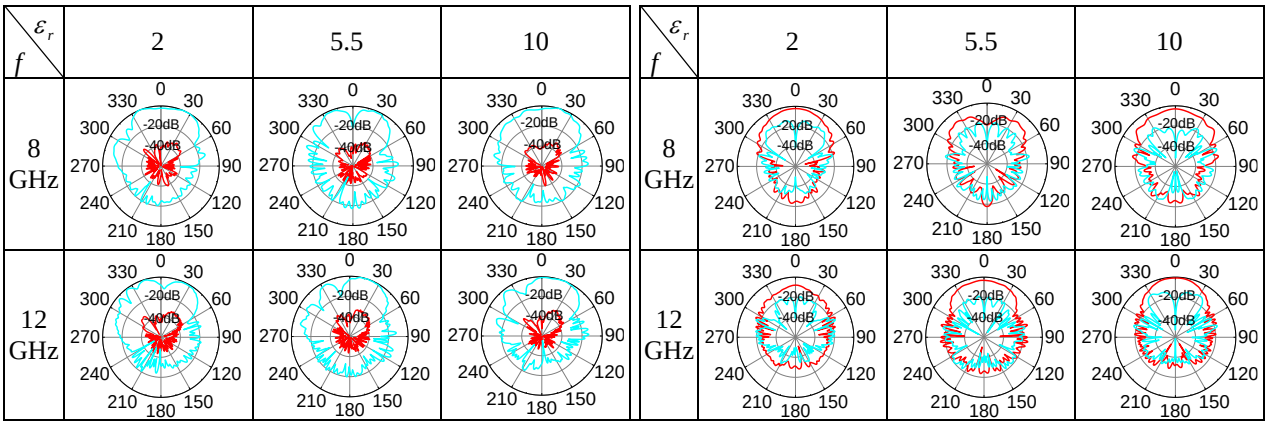

Fig. 14. Effect of varying the dielectric constant ε_r on the radiation pattern. (— Eφ; — Eθ)

VI. CONCLUSION

In this paper, an analysis on the effect of dielectric radome on radiation field of conformal end-fire antenna mounted on a large conducting cylinder is presented. The paper firstly analyzes the effect of planar dielectric layer on the plane wave with different polarizations, and gives the expression for the transmitted electric field and the power transmission coefficient to show their relation with thickness of dielectric layer and incidence angle. Then, a comparison of the effect of the dielectric radome on conformal end-fire antennas with different polarizations is presented. It has been found that the effect of the dielectric radome on the radiation pattern of the vertically polarized endfire antenna is less than that on the horizontally polarized endfire antenna. Finally, the effect of a nearby dielectric radome on the vertically polarized antenna's radiation characteristics has been examined, which show that with use of a larger radius *r*, smaller height *P*, smaller thickness *b*, smaller power index *n* and dielectric constant ε_r, a better end-fire radiation pattern can be achieved. The investigation should be helpful to the design of radome-antenna system.

ACKNOWLEDGMENT

This work is supported by the Changjiang Scholars and Innovative Research Team in University under Grant No. IRT1299, and Doctoral fund of Chongqing University of Posts and Telecommunications (A2015-08).

REFERENCES

[1] D. C. F. Wu and R. C. Ruduck, "Plane wave spectrum-surface integration technique for radome analysis," *IEEE Trans. Antennas Propag*., vol. 22, no. 3, pp. 497-500, 1974.

[2] S. W. Lee, M. S. Sheshadri, V. Jamnejad, and R. Mittra, "Wave transmission through a spherical dielectric shell," *IEEE Trans. Antennas Propag*., vol. 30, no. 3, pp. 373-380, 1982.

[3] X. J. Gao and L. B. Felsen, "Complex ray analysis of beam transmission through two-dimensional radomes," *IEEE Trans. Antennas Propag.*, vol. 33, no. 9, pp. 963-975, 1985.

[4] R. Orta, R. Tascone, and R. Zich, "Performance degradation of dielectric radome covered antennas," *IEEE Trans. Antennas Propag.*, vol. 36, no. 12, pp. 1707-1713, 1988.

[5] D. J. Kozakoff, *Analysis of Radome-Enclosed Antennas*. Norwood, MA: Artech House, 1997.

[6] X. J. Gao and L. B. Felsen, "Complex ray analysis of beam transmission through two-dimensional radomes," *IEEE Trans. Antennas Propag.*, vol. 33, no. 9, pp. 963-975, 1985.

[7] H. Mustacoglu, J. R. Mautz, and E. Arvas, "MoM analysis of an axisymmetric chiral radome," *Appl. Comp. Electromagnetics Society (ACES) Journal*, vol. 28, no. 3, Mar. 2013.

[8] B. Lin, S. Du, H. Zhang, and X. Ye, "Design and simulation of frequency-selective radome together with a monopole antenna," *Appl. Comp. Electro-magnetics Society (ACES) Journal*, vol. 25, no. 7, pp. 620-625, July 2010.

[9] R. U. Nair and R. M. Jha, "Electromagnetic performance analysis of a novel monolithic radome for airborne applications," *IEEE Trans. Antennas Propag.*, vol. 57, no. 11, pp. 3664-3668, 2009.

[10] M. He, "On the characteristics of radome enclosed archimedean spiral antennas," *IEEE Trans. Antennas Propag.*, vol. 56, no. 7, pp. 1867-1874, 2008.

[11] C. C. Lu, "A fast algorithm based on volume integral equation for analysis of arbitrarily shaped dielectric radomes," *IEEE Trans. Antennas Propag.*, vol. 51, no. 3, pp. 606-612, 2003.

[12] M. A. A. Moneum, Z. Shen, J. L. Volarjis, and O. Graham, "Hybrid PO-MoM analysis of large axi-symmetric radomes," *IEEE Trans. Antennas Propag.*, vol. 49, no. 12, pp. 1657-1665, 2001.

[13] P. Wang, G. J. Wen, H. B. Zhang, and Y. H. Sun, "A wideband conformal end-fire antenna array mounted on a large conducting cylinder," *IEEE Trans. Antennas Propag.*, vol. 61, no. 9, pp. 4857-4861, 2013.

[14] K. Q. Zhang and D. J. Li, *Electromagnetic Theory in Microwave and Optoelectronics*. Publishing House of Electronic Industry, China, 2001.

[15] J. D. S. Langley, P. S. Hall, and P. Newham, "Balanced antipodal vivaldi antenna for wide bandwidth phased arrays," *IEE Proc Microw. Antenna Propag.*, vol. 143, no. 2, pp. 97-102, 1996.

Ping Wang was born in Chongqing, China. He received his M.S. degree in Theoretical Physics from Chongqing University of China in 2008 and the Ph.D. degree in University of Electronic Science and Technology of China (UESTC) in 2013, respectively. Currently, he is working in Chongqing University of Posts and Telecommunications, China. His current research interests include patch antennas, wideband antennas, and arrays.

A Low Profile, Broadband Linearly and Circularly Polarized Cavity Backed Antenna Using Halved-Dual Mode SIW Cavity

Seyed A. Razavi and Mohammad H. Neshati

Ferdowsi University of Mashhad, 91779-48974, Mashhad, Iran
Alirazavi_parizi@yahoo.com, neshat@um.ac.ir

Abstract ─ In this paper, a low profile single fed cavity backed slot antenna producing both linear and circular polarizations at two different frequency is presented using a halved dual mode cavity. The proposed antenna has a planar structure using a single layer of printed circuit board (PCB) which allows for integrating the antenna to other planar circuits and provides straight forward connection to SMA connector. One prototype of the antenna is designed and fabricated and very good agreement between measurement and simulation results are obtained. Results show that the proposed antenna is able to present suitable radiation characteristics as both linearly polarized (LP) antenna and circularly polarized (CP) antenna.

Index Terms ─ Cavity backed antenna, half mode substrate integrated waveguide (HMSIW), linear and circular polarization.

I. INTRODUCTION

Nowadays, design of low profile planar antennas for use in compact wireless communications systems, is in large demand. Varieties of solutions have been presented for this purpose in literature. Microstrip patch antennas are a good candidate in these applications. They have usually simple structures which makes their fabrication process easy and low cost. However, they have some drawbacks including low impedance bandwidth and low radiation efficiency at high frequencies.

Cavity backed antennas provide high performance properties including high radiation efficiency and suppress surface waves effectively. The primary designs for this class of antennas using rectangular metallic waveguide are bulky, heavy and expensive [1-3]. Moreover, their integration with planar circuits is not easy.

Recently, substrate integrated waveguide (SIW) technology has been presented as a good and useful solution for planar implementation of different microwave components [4]. In [5-14], different SIW cavity backed antennas were presented. In [5], a linear polarized (LP) antenna is designed using a resonating slot on the broad wall of SIW cavity. In [6], by using a meandered slot, a LP cavity backed antenna with enhanced bandwidth is proposed. In [7], a circular polarized (CP) antenna is presented applying an annular slot and a shorting pin in a circular cavity. In [8], using a crossed slot, three antennas with different polarizations (LP, right handed CP and Left handed CP) are designed and investigated. The one with LP is designed and made in such a way that both vertical and horizontal polarizations depending on the frequency of operation are obtained. In [9], an inter-digital slot is used to develop a LP composite left/right handed (CRLH) SIW cavity backed antenna. In [10], a LP antenna with enhanced bandwidth (BW) up to 6.3% is presented by applying a long non-resonating slot on the surface of a rectangular cavity.

Despite all advantages of SIW technology, the size of these structures might be large in some applications, and therefore new methods for size reduction are needed. Half mode substrate integrated waveguide (HMSIW) is one effective solution for this purpose [11]. By this technique, size of the SIW structures is lowered up to 50% without affecting its performance. By using HMSIW technique to a non-radiating cavity in [12], a LP cavity backed antenna is designed and implemented. In [13], by applying HMSIW technique to a LP cavity backed slot antenna, a CP cavity backed antenna is developed; in which two orthogonal quarter-wavelength patch provide the circular polarization at far field of the structure. Also, in [14] perturbation technique in applied in a rectangular SIW cavity and its impedance bandwidth is improved in case of linear polarization. All the cavity backed antennas presented in [5-14] can radiate either LP wave or CP wave and none of them can generate both of LP and CP waves.

In this paper, HMSIW technique is used in conjunction with a dual mode cavity. A new cavity backed slot antenna with capability of producing both CP and LP wave is introduced. Based on the operating frequency of the structure, the proposed antenna radiates a LP or CP waves. The introduced structure is the modified version of the presented antenna in [13]. In [13], the slot length is chosen to be quarter of a

Submitted On: January 5, 2015
Accepted On: June 17, 2016

wavelength of resonant frequency. But, in this paper, the slot length is extended much more than a quarter of wavelength lead to exciting two resonating hybrid modes of the cavity. One of these hybrid modes generates LP wave, while the other one generates CP wave. LP wave is caused by the dominant radiation of the long slot, whereas the CP wave is radiated by two quarter wavelength patches. A prototype of the proposed antenna is designed, implemented, numerically studied and experimentally investigated. Results including reflection coefficient, radiation patterns and gain are reported.

II. ANTENNA STRUCTURE

The top view of the proposed antenna and its geometrical parameters are shown in Fig. 1. Its backside is totally metallic and acts as the ground of the microstrip structure. The introduced antenna consists of a halved rectangular cavity with length and width of a and b respectively. It is realized by two arrays of metallic vias and a magnetic wall of length b. A radiating slot of length l_s is also etched at the center of the upper side of the structure. An inset microstrip feed line is used to excite the cavity. This also simplifies planar integration and in turn SMA connector can be easily applied to the structure.

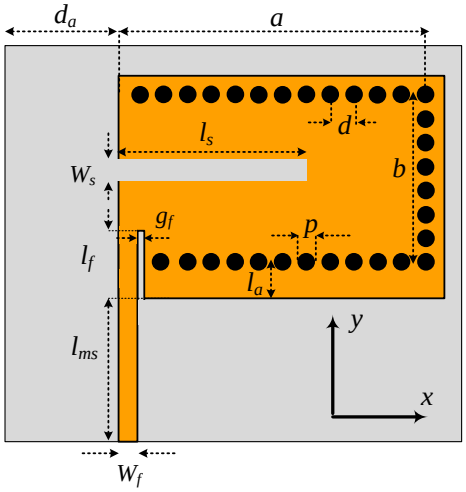

Fig. 1. Top view of the proposed antenna and its geometrical parameters.

III. THEORY OF OPERATION

The proposed structure is similar to that presented in [13], except the shape of the cavity and the slot length. These differences give to the antenna the capability of generating both LP and CP waves. In [13], the resonating slot with the length of quarter wavelengths is used on the broadside of the cavity, while in this paper a non-resonating slot with a length much more than a quarter wavelengths is used. So, the proposed antenna can only be implemented by rectangular cavity.

In the proposed structure, as discussed in [10], a dual mode cavity is used in which two hybrid modes including two different combinations of half TE_{110} and half TE_{120} modes, are excited. Choosing a non-resonant length for the slot, a dual mode cavity is obtained. In this antenna both magnetic wall and rectangular slot are radiating, while the rectangular slot produces co-polarized wave, whereas the magnetic wall produces cross-polarized one. Due to the large size of the slot, it radiates a LP wave by the lowest frequency hybrid mode, which is the 1st hybrid mode.

At the other resonant frequency of the cavity, both magnetic wall and a part of slot, which is equivalent to a quarter resonant wavelengths efficiently radiate. As a result, two quarter-wavelength patches, as shown in Fig. 2, are obtained. Two orthogonal E-fields with equal magnitudes are generated by these two quarter wavelength patches [13] and also 90° phase difference between orthogonal fields can be provided by tuning the slot length l_s. Therefore, a CP wave can be radiated.

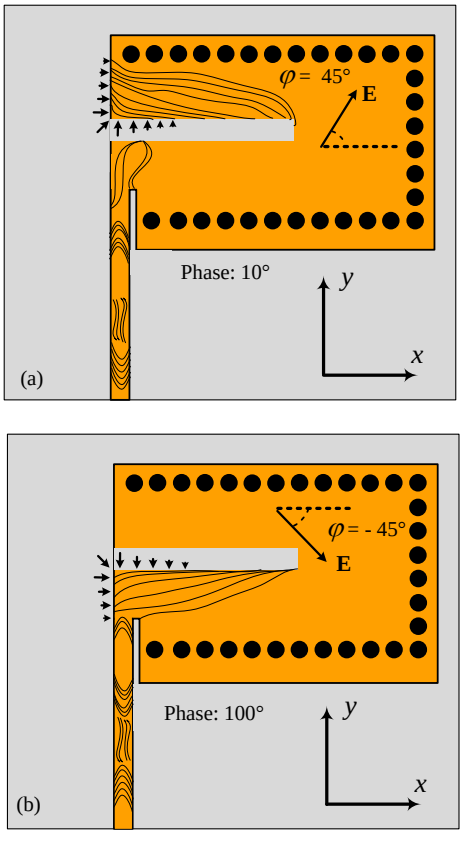

Fig. 2. E-field isolines of the proposed antenna at 10.53 GHz corresponding to the two orthogonal quarter-wavelength patch modes: (a) direction of radiated E-field at φ = +45°, and (b) direction of radiated E-field at φ = -45°.

In Fig. 2, the orthogonal quarter-wavelength patch modes and the radiated E-field caused by each one are illustrated at 10.53 GHz. As shown, the radiated fields are orthogonal, one is directed at φ = +45° and the other one at φ = -45°. At following, it is shown that this two quarter-wavelength patches are excited by higher hybrid mode (2st hybrid mode) of the cavity. In the proposed structure, in order to excite the two patches symmetrically and consequently provide circular polarization, the slot should be placed at the center of cavity.

The presented half mode cavity has the same frequency characteristics as that of the full cavity. However, it cannot support some resonating modes of the full one due to its half mode configuration. So, for the resonating modes that can be supported, the well-known formulation used for full mode cavity [15-16] can also be used here for calculation of the resonance frequencies. In SIW cavity, the conditions $d<2p$ and $p/\lambda_0<0.1$, where λ_0 is the free space wavelength, should be satisfied in order to effectively prevent power leakage through the side walls of the cavity [15-17].

IV. RESULTS AND DISCUSSION

To verify the operating conditions of the proposed antenna, a prototype of the cavity backed slot antenna is designed and implemented. The antenna structure is studied numerically using High Frequency Structure Simulator (HFSS) software based on Finite Element Method (FEM) and investigated experimentally. The geometrical parameters of the antenna are summarized in Table 1. It is made using Rogers Duroid 5880 substrate with electrical characteristics of ε_r = 2.2, thickness of 0.787 mm and tangent loss of 0.001. Photo of the fabricated antenna is illustrated in Fig. 3.

Simulated and measured results for reflection coefficient and axial ratio (*AR*) are illustrated in Fig. 4. Apart from a shift in frequency response, there is a good agreement between measured and simulated results. The difference between results is due to fabrication imperfection. It can be seen that reflection coefficient is less than -10 dB for frequency range from 9.43 GHz to 10.54 GHz, providing fractional bandwidth of 11.75%. Moreover, two distinct resonance frequencies are obtained at 9.65 GHz and 10.3 GHz, corresponding to the two different modes of the cavity. It can be seen that near the second one, proposed antenna radiates a CP wave at 10.3 GHz with minimum *AR* and 3 dB *AR* bandwidth of -0.35 dB and 180 MHz respectively.

From *AR* plot versus frequency, Fig. 4, it also can be observed that the proposed antenna radiates a LP wave at frequencies near to the frequency of its 1st hybrid mode. Also, near the frequency of its 2st hybrid mode, it radiates CP wave. Measured results indicate that the designed antenna provides LP wave from 9.43 GHz to 9.75 GHz. In case of CP, its *AR* bandwidth is from 10.11 GHz to 10.35 GHz.

Table 1: Geometrical parameters of the proposed antenna (units in mm)

Parameter	Value	Parameter	Value
d_a	7	l_{ms}	10
d	1.5	h	0.78
p	1	W_f	1.137
g_f	0.4	W_s	1
l_s	11.5	a	39
l_f	1	b	10.5
l_f	2.3		

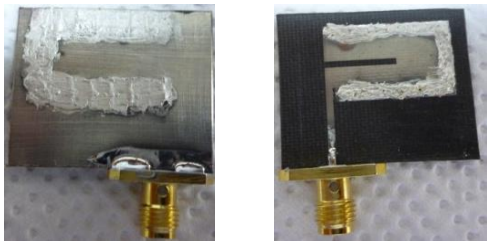

(a) (b)

Fig. 3: Photo of the fabricated antenna: (a) front view and (b) rear view.

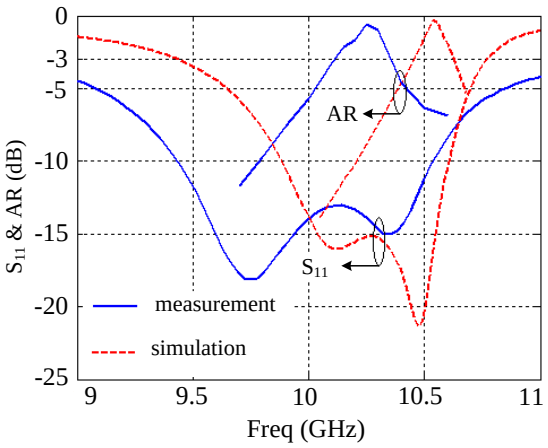

Fig. 4. Measured and simulated reflection coefficient and axial ratio of the proposed antenna.

The corresponding simulated field distribution inside the cavity for the two operating modes including TE_{120} and TE_{110} are shown in Fig. 5 (a) and 5 (b), in which vertical scale of 0-250 A/m is used for illustrating H-field vectors and red arrows represent the direction of H-vectors. Figure 5(a) shows H-vectors of the hybrid mods at 10.06 GHz is divided into an upper half part and a lower half cavity by the radiating slot. Also, field distribution at both sides of the slot is out of phase. Figure 5 (b) shows H-vectors of the hybrid mode at 10.47 GHz. It can be observed that field distribution at

both sides of the slot is in phase and field distribution at the upper side of the slot is dominant.

The schematic combination of TE_{110} and TE_{120} modes and generating 1st hybrid mode at 10.06 GHz is shown in Fig. 6 (a). Dominant E-filed isolines are shown by red and blue lines. The signs + and – represent the phase of the field distribution. It reveals that the hybrid mode at this frequency is the combination of strong TE_{120} mode and weak TE_{110} mode which makes field distributions at both sides of slot, out of phase and greatly different in magnitude. As a result the slot is able to radiate effectively. Figure 6 (b) shows that the generated 2nd hybrid mode at 10.47 GHz is the combination of strong TE_{110} and weak TE_{120} modes, and in turn field distributions at two sides of slot are in phase and greatly different in magnitude which also results in efficient radiation by the rectangular slot.

A parametric study is carried out and the effect of slot length, l_s, and dielectric aperture width on the radiation performance of the proposed antenna is investigated. The effect of slot length l_s on antenna parameters including co-polarized gain, the difference between co- and cross-polarized gain G_d, axial ratio and reflection coefficient is shown in Fig. 7 (a) and Fig. 7 (b) versus frequency. It can be seen that when the structure operates as a LP antenna, higher gain and lower cross polarized level (CPL) is achieved by extending the slot length. In fact, in this case its co-polarized gain is due to the efficient exciting of the applied slot and the cross-polarized gain is due to the magnetic wall of the cavity. As a result, by extending the slot length higher gain and lower CPL can be obtained. *AR* plot in Fig. 7 (c) shows by adjusting the slot length, 90° phase difference between orthogonal patch modes and consequently circular polarization at far field can be provided.

S_{11} plot in Fig. 7 (d) reveals that the slot length has also some effect on the location of the two resonate frequencies corresponding to the two hybrid modes. By extending the slot length, these two frequencies are departed from each other and broadband operating condition is obtained.

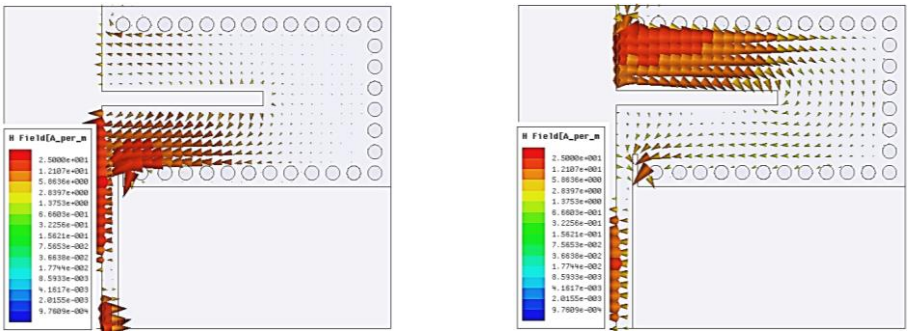

(a) (b)

Fig. 5. Simulated magnetic field distributions of the hybrid modes in half mode cavity: (a) H-vectors at 10.06 GHz, and (b) H-vectors at 10.47 GHz. Red arrows represent direction of H-vector.

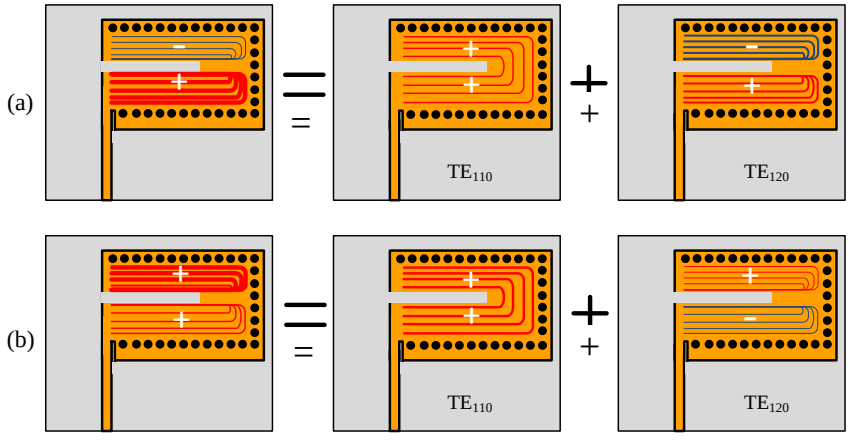

Fig. 6. Schematic combination of TE_{110} and TE_{120} modes and generating: (a) dominant E-filed isoline at 1st hybrid mode at 10.06 GHz, and (b) dominant E-filed isolines at 2nd hybrid at 10.47 GHz. Signs + and – represent phase of field distribution.

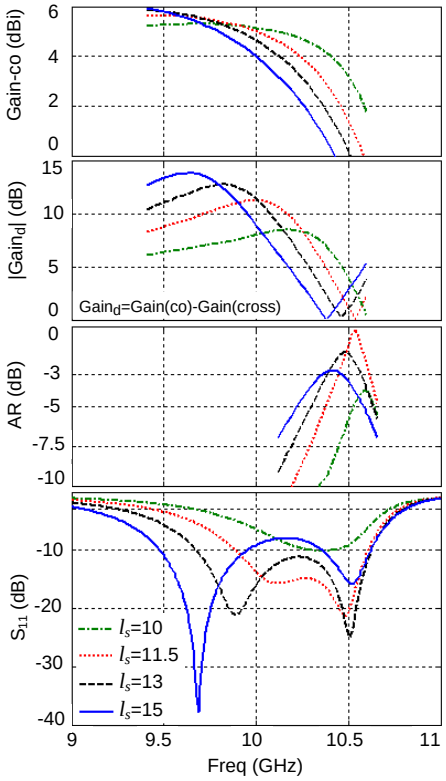

Fig. 7. The effect of slot length l_s on: (a) co-polarized gain, (b) difference between co- and cross-polarized gains, and (c) *AR*, d) S_{11}.

The effect of the dielectric aperture d_a on co-polarized gain (LP gain), gain difference G_d and gain in case of CP operation is depicted in Fig. 8. The co-polarized gain plot illustrates in case of LP operation, its gain is slightly enhanced by increasing d_a which also increases the antenna size. However, the gain difference G_d plot reveals that by increasing d_a, the frequency range in which the CPL is less than -10 dB (G_d>10 dB), is decreased. Figure 8 (b) reveals that in case of CP operation, higher gain can be achieved by increasing the dielectric aperture d_a.

Variations of co- and cross-polarization gains versus frequency at boresight direction are plotted in Fig. 9. Simulated result shows CPL is -11.2 dB at 10.06 GHz, which confirms that the structure is LP antenna at its lower resonate frequency. Also, measured result indicates that at the frequency range from 9.43 GHz to 9.75 GHz, CPL is less that -10 dB. Moreover, in case of LP antenna, measured gain is from 3.7 dBi to 5 dBi, which agree well with that obtained by simulation which is 4.5 dBi to 5.5 dBi in operating bandwidth.

Figure 9 also shows that at the vicinity of 10.25 GHz measured co- and cross-polarized gains are almost equal and CP wave is generated. Measured *AR* in Fig. 4 reveals that at the frequency range from 10.11 GHz to 10.35 GHz, the proposed antenna radiates CP wave. In this case, measured gain is 3.4 dBi, however simulated result shows gain is nearly 4 dBi. Table 2 summarizes simulated and measured radiation performance of the proposed antenna.

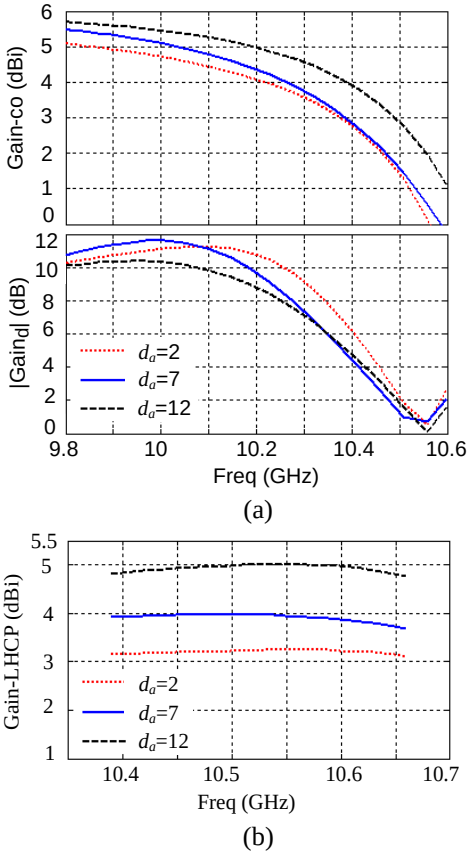

Fig. 8. The effect of d_a on antenna performance: (a) co-polarized, (b) difference G_d, and (c) gain for CP operating antenna.

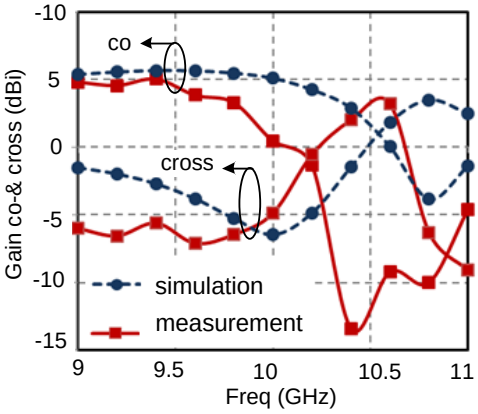

Fig. 9. Simulated and measured variation of co- and cross-polarization gains versus frequency.

In Fig. 10, measured radiation patterns of the proposed antenna are shown at two standard radiation planes. Figure 10 (a) shows radiation patterns at 9.5 GHz, in case of LP antenna. For CP operating condition of the antenna, radiation patterns at 10.25 GHz are shown in Fig. 10 (b). The measured cross polar level (CPL) at boresight direction is about -10 dB when antenna is LP and about -20 dB when it acts as a CP antenna.

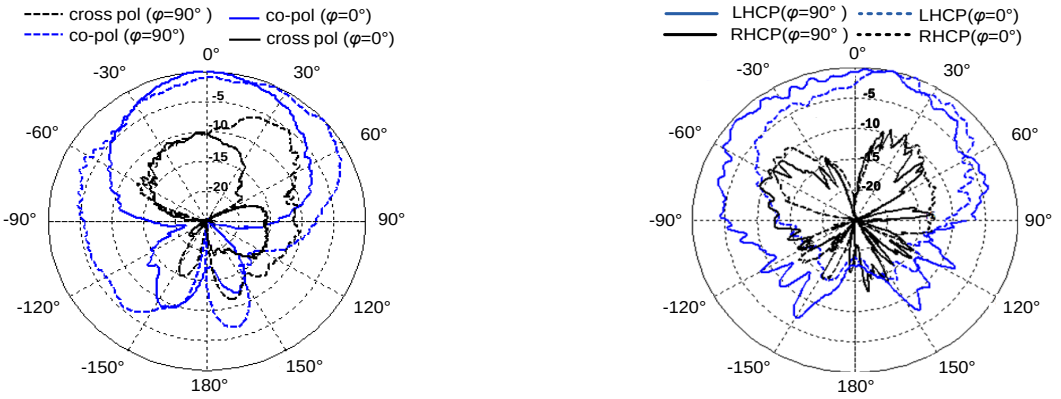

(a) (b)

Fig. 10. Radiation patterns of designed sample at φ=0˚ and φ=90˚ cut planes: (a) at 9.5 GHz and (b) at 10.25 GHz.

Table 2: Summary of the simulated and measured results of the proposed antenna

Parameter	Simulated	Measured
Impedance BW (GHz)	9.88 - 10.59 (6.9%)	9.43 - 10.54 (11.1%)
AR BW (GHz)	10.44 - 10.62 (1.7%)	10.11 - 10.35 (2.34%)
LP BW	9.7 - 10.17 (4.7%)	9.43 - 9.75 (3.3%)
CP BW	10.44 - 10.62 (1.7%)	10.11 - 10.35 (2.34%)
Maximum *AR (dB)*	-0.24	-0.59
Maximum *AR* freq (GHz)	10.54	10.25
LP Gain (dBi)	4.5~5.5	3.7~5
CP Gain (dBi)	≈ 4	≈ 3.4

The measured front to back ratio (FTBR) is almost about 15 dB for LP case, while it is nearly 17 dB in case of CP operation. Detailed radiation performance of the proposed antenna is summarized in Table 2.

V. CONCLUSION

A low profile planar cavity backed slot antenna which is able to produce both linear and circular polarizations depending on the frequency of operation is developed. This feature is not observed in the previous designs [1-13, 18] for planar cavity backed antennas. HMSIW technique is used in antenna topology which makes the antenna compact and also light weight. Moreover, the antenna has a single layer structure using a low cost PCB which makes it easy to integrate to other planar circuits. The proposed antenna has two resonating frequencies corresponding to the two hybrid modes of the halved rectangular cavity. In this antenna a long slot generates LP wave at the frequencies near to the lower resonate frequency. However, two quarter-wavelength patches produce CP wave at the frequencies near to the higher resonate frequency. A prototype of the proposed antenna is designed and fabricated. The radiation performance including radiation patterns and antenna gain were measured. Results show that the proposed antenna provides good radiation characteristics such as high gain, wide bandwidth comparable to the traditional antennas presented in literature [1-13, 18], but presenting the discussed advantages including double polarization tunability in addition to low cost single layer implementation.

REFERENCES

[1] Q. Li and Z. Shen, “An inverted microstrip-fed cavity-backed slot antenna for circular polarization,” *IEEE Antennas Wireless Propag. Lett.*, vol. 1, pp. 190-192, 2002.

[2] H. Morishita, K. Hirasawa, and K. Fujimoto, “Analysis of a cavity backed annular slot antenna with one point shorted,” *IEEE Trans. Antennas Propag.*, vol. 39, no. 10, pp. 1472-1478, Oct. 1991.

[3] D. Sievenpiper, H. Hsu, and R. M. Riley, “Low-profile cavity-backed crossed-slot antenna with a single-probe feed designed for 2.34-GHz satellite

radio applications," *IEEE Trans. Antennas Propag.*, vol. 52, no. 3, pp. 873-879, Mar. 2004.

[4] W. Hong, "Development of microwave antennas, components and subsystems based on SIW technology," *IEEE International Symp. Microwave Antenna Propagation and EMC Tech.*, Mape., pp. 14-17, 2005.

[5] G. Q. Luo, Z. F. Hu, L. X. Dong, and L. L. Sun, "Planar slot antenna backed by substrate integrated waveguide cavity," *IEEE Antennas Wireless Propag. Lett.*, vol. 7, pp. 236-239, 2008.

[6] J. C. Bohorquez, H. A. F. Pedraza, I. C. H. Pinzon, J. A. Castiblanco, N. Pena, and H. F. Guarnizo, "Planar substrate integrated waveguide cavity-backed antenna," *IEEE Antennas and Wireless Propagation Lett.*, vol. 8, pp. 1139-1142, 2009.

[7] D. Kim, J. W. Lee, C. S. Cho, and T. K. Lee, "X-band circular ring-slot antenna embedded in single-layer SIW for circular polarization," *IEEE Electronic Lett.*, vol. 45, no. 13, pp. 668-669, June 2009.

[8] G. Q. Luo, Z. F. Hu, L. Y. Yu, and L. L. Sun, "Development of low profile cavity backed crossed slot antennas for planar integration," *IEEE Trans. Antennas propag.*, vol. 57, no. 10, pp. 2972-2979, Oct. 2009.

[9] Y. Dong and T. Itoh, "Miniaturized substrate integrated waveguide slot antennas based on negative order resonance," *IEEE Trans. Antennas Propag.*, vol. 58, no. 12, 2010.

[10] G. Q. Luo, Z. F. Hu, W. J. Li, X. H. Zhang, L. L. Sun, and J. F. Zheng, "Bandwidth enhanced low profile cavity backed slot antenna by using hybrid SIW cavity modes," *IEEE Trans. Antennas Propag.*, vol. 60, no. 4, pp. 1698-1704, 2012.

[11] Q. Lai, C. Fumeaux, W. Hong, and R. Vahldieck, "Characterization of the propagation properties of the half-mode substrate integrated waveguide," *IEEE Trans. Microw. Theory Tech.*, vol. 57, no. 8, pp. 1996-2004, Aug. 2009.

[12] S. A. Razavi and M. H. Neshati, "Development of a linearly polarized cavity-backed antenna using HMSIW technique," *IEEE Antennas Wireless Propag. Lett.*, vol. 11, pp. 1307-1310, 2012.

[13] S. A. Razavi and M. H. Neshati, "Development of a low profile circularly polarized cavity backed antenna using HMSIW technique," *IEEE Trans. Antennas Propag.*, vol. 61, no. 3, pp. 1041-1047, 2012.

[14] E. Baghernia and M. H. Neshati, "Development of a broadband substrate integrated waveguide cavity backed slot antenna using perturbation technique," The *Applied Computational Electromagnetic Society Journal*, vol. 29, no. 11, pp. 847-855, 2012.

[15] F. Xu and K. Wu, "Guided-wave and leakage characteristics of substrate integrated waveguide," *IEEE Trans. Microw. Theory Tech.*, vol. 53, no. 1, pp. 66-73, Jan. 2005.

[16] G. Q. Luo, W. Hong, Q. H. Lai, K. Wu, and L. L. Sun, "Design and experimental verification of compact frequency selective surface with quasi-elliptic bandpass response," *IEEE Trans. Microw. Theory Tech.*, vol. 55, no. 12, pp. 2481-2487, Dec. 2007.

[17] H. Uchimura, T. Takenoshita, and M. Fujii, "Development of a "Laminated Waveguide"," *IEEE Trans Microwave. Theory Tech.*, vol. 46, no. 12, pp. 2438-2443, Dec. 1998.

[18] H. Dashti and M. H. Neshati, "Development of a low-profile patch and semi-circular SIW cavity hybrid antenna," *IEEE Trans. Antennas Propag.*, vol. 62, no. 9, pp. 4481-4488, 2014.

Seyed Ali Razavi was born in Kerman, Iran, 1985. He received the B.Sc. degree in Electrical Engineering from the University of Shahid Bahonar, Kerman, Iran, in 2006, the M.Sc. degree in Electrical Engineering from Ferdowsi University of Mashhad, Iran, in 2009 and Ph.D. degree in Electrical Engineering at Ferdowsi University of Mashhad, Mashhad, Iran in 2013. He is now with Graduate University of Advance Technology, Kerman, Iran as Assistant Professor. He has also collaboration with antenna group in Chalmers University of Technology. He is interested in microwave and millimeter-wave passive devices, antennas, electromagnetic wave scattering, SIW and gap-waveguide technologies.

Mohammad H. Neshati was born in Yazd, Iran. He received his B.Sc. in Electrical Engineering from Isfahan University of Technology, Isfahan, Iran; M.Sc. degree from Amir-Kabir University of Technology, Tehran, Iran and Ph.D. from the University of Manchester, UMIST, England in 2000. Since 2006 he has been with the Department of Electrical Engineering of Ferdowsi University of Mashhad, Mashhad Iran, where he is Associate Professor. His current research includes electromagnetic, antenna theory and design, microwave active and passive circuit design. Neshati is a Member of IEE AP, IEEE MTT and the Applied Computational Electromagnetic Societies.

A Compact Disc-Shaped Printed Antenna Using Parasitic Element on Ground Plane for Super Wideband Applications

M. M. Islam [1], M. R. I. Faruque [2], and M. T. Islam [3]

[1] Department of Software Engineering
Daffodil International University, Dhanmondi, Dhaka 1207, Bangladesh
mmoiislam@yahoo.com

[2] Space Science Centre (ANGKASA)
Universiti Kebangsaan Malaysia, 43600 UKM, Bangi, Selangor, Malaysia
rashedgen@yahoo.com

[3] Department of Electrical, Electronic and Systems Engineering
Universiti Kebangsaan Malaysia, 43600 UKM, Bangi, Selangor, Malaysia
titareq@gmail.com

Abstract ─ A microstrip line-fed monopole antenna is proposed and investigated using a structure of parasitic element for super-wideband applications. The parasitic element consists of 4 rectangular embedded slots on the ground plane. This parasitic element on the ground plane leads the UWB frequency band into the SWB frequency band. This proposed monopole antenna is fed by a microstrip line and is printed on low dielectric FR4 material of 1.6 mm thickness. All the simulations are performed using commercially available, finite element method (FEM) based Ansoft high-frequency structure simulator (HFSS) software and CST Microwave Studio. Measured results exhibit that the proposed disc-shaped antenna shows a wide bandwidth which covers from 2.90 GHz to more than 20 GHz, with a compact dimension of 25 mm × 33 mm for VSWR <2, observing an extended ultra-wideband frequency. A good combination is noticed between simulation and measurement. This proposed SWB antenna delivers impedance bandwidth covering the L, C, X, Ku bands and points out sharply surface current flow and nearly omnidirectional radiation patterns, which is appropriate for UWB or SWB applications.

Index Terms ─ Microstrip line, parasitic element, Super Wide Band (SWB), Ultra-Wide Band (UWB).

I. INTRODUCTION

The Federal Communications Commission (FCC) introduced the announcement of 3.1-10.6 GHz frequency band for commercial application of UWB technology [1]. The UWB antenna is the dominant figure of wireless communication and UWB technology. The utilization and the research of UWB antennas have been rising sharply with the demand of the integration and miniaturization and the improvement of high-speed integrated circuits. Owing to various merits such as high data rate, high salvation to multi path interference, large band width, small emission power, remote sensing applications and low cost for short range access. Major differences are observed between UWB and SWB antennas. In the information warfare, SWB antenna plays an important role as a key component of electronic counterwork equipment, while UWB antenna is extensively applied in communication and impulse radar systems. UWB covers the frequency range from 3.1 to 10.6 GHz with a ratio bandwidth of 3.4:1, while more than 8:1 or 10:1 is the ratio bandwidth of the SWB antenna.

In the recent years, several ultra-wideband antennas have been reported [2-10]. These antennas have various designs of monopole structures, such as triangular [2], square [3-4], rectangular [5] semi-circle [6], and circular disc [7] monopole antennas. Some of these UWB antennas are not appropriate to be integrated with associated UWB electronics and some do not have simple structure and are not suitable to be integrated. And the typical feeding techniques include simple microstrip lines [8], CPW feeds [9], and slotted structures [10]. For these antenna design structures, the operations of the antenna are usually limited within 3.1-10.6 GHz UWB frequency range. In order to attain super wide frequency band, different methods and techniques have already been proposed. Recently, there are various literatures on SWB microstrip antennas [11-22]. For instance, in [11], a compact super wideband antenna was proposed with switchable dual band-notched characteristics for 3 to 33 GHz band. However, this

Submitted On: July 7, 2014
Accepted On: May 22, 2016

antenna contained no validation experimentally. A compact semielliptical antenna was proposed, which was fed by a tapered coplanar waveguide [12]. The mentioned antenna is appropriate to cover from 0.46 GHz to 9.07 GHz frequency with a measured bandwidth ratio of 19.7: 1. In [13], a circular shaped asymmetrical dipole antenna was presented. This reported antenna attained an operating frequency band covering from 0.79 to 17.46 GHz with a dimension of 90 mm × 135 mm. A novel SWB antenna was proposed, which achieved a frequency band from 5 GHz to 150 GHz in [14].Although huge bandwidth exists, it is not appropriate for lower frequency bands such as S band communication and WiMAX. A half circular antenna of antipodal slot was designed with a range of 0.8 GHz to 7 GHz super wide band frequencies [15]. An asymmetrical dipole antenna of super-wideband was stated in [16]. A planar super wide band antenna of disc shape was designed with C-like slots in [17]. This mentioned antenna obtained bandwidth covering within 3-32 GHz with an overall dimension of 30 mm × 29:1 mm. An extremely wideband monopole antenna was designed with triple-band notched characteristics in [18]. The reported antenna acquired a bandwidth covering from 0.72-25 GHz with a size of 150 mm × 150 mm. In [19], a monopole antenna was presented for SWB applications. However, it's three dimensional structure makes it difficult to be integrated into portable devices. The peak gain is high but the antenna structure is too large. In addition, the reported [17-19] antennas do not cover K-band which introduces a new arena to design antenna that covers S, C, X, Ku, K and Ka bands. A monopole antenna was proposed for SWB applications [20]. This antenna covers the UWB demands including gain and bandwidth. At lower frequencies (2-2.5 GHz), the input impedance is not matched properly and the dimension is too large, that is 35×77 mm^2. A SWB antenna was proposed with printed patch and tapered feed region in ref. [21]. The input impedance being mismatched at 18-19 GHz frequencies creates variant group delay and the antenna structure is too large, 40×30 mm^2. A printed SWB antenna was presented and studied [22]. The overall antenna dimension is too large. A printed wideband antenna was narrated for multi-band wireless systems [23]. This antenna acquired wide bandwidth covering from 1:08 to 27:4 GHz, with a dimension of 124 mm × 120 mm × 1:5 mm. A monopole antenna of compact disc was designed for future UWB applications where operating bandwidth 3:5-31:9 GHz with a dimension of 35 mm × 30 mm × 0:8 mm [27]. An ultra-wideband antenna was proposed using capacitively loaded loop (CLL) with band-notched characteristics where covering bandwidth from 3 to 11 GHz with a dimension of 34 mm × 27 mm × 0:8 mm [25]. A printed ultra-wideband antenna was presented using inverted L-slit with band-notched characteristics where executing frequency band 2:82-13:95 GHz with a dimension of 30 mm × 36 mm × 0:4 mm [26].

In this paper, a disc-shaped printed microstrip antenna with the parasitic element on the ground plane that attains a compact SWB profile physically belonging to nearly omni-directional radiation characteristics, gain and reasonable current distribution is presented. The mentioned disc-shaped SWB antenna is made of circular radiating patch and the ground plane containing the parasitic element on the upper portion, generating a super wide bandwidth ranging from 2.90 to more than 20 GHz. The antenna formation is smooth with simple design and comfortable fabrication. The parasitic element structure is inserted on the upper portion of the ground plane to generate super frequency band for SWB applications. By virtue of significant selection of the parasitic element structure, it is observed that the reported antenna can obtain the operating SWB frequency band.

II. ANTENNA DESIGN ARCHITECTURE AND OPTIMIZATION

The geometrical outline of the proposed disc-shaped SWB antenna is demonstrated in Fig. 1, which is printed on both sides of a low cost dielectric, 1.6 mm thick FR4 substrate material belonging to permittivity of 4.6 and loss tangent 0.02. Finite element method (FEM) based Ansoft high-frequency structure simulator (HFSS) software, which is commercially available, has been used for all the simulations in this research. The reported SWB antenna has been designed following the UWB antenna1 indicated Fig. 2. This antenna is made of a disc-shaped radiating patch with a radius of R. The partial ground plane with the parasitic element is printed on the lower part of the substrate, where on the upper portion of the substrate; the disc-shaped radiator is printed using a microstrip line feeding.

The width and length of the microstrip line are stable with a view to attaining the 50 Ω input impedance. The port of the microstrip feed line is attached to a Sub Miniature version A (SMA) connector. The gap between the parasitic element and the partial ground plane is denoted using g_1.$W_{sub} \times L_{sub} \times H_{sub}$ is the thorough size of the proposed SWB antenna. The parasitic element is implanted on the upper position of the partial ground plane to create super frequency band. The parasitic element is made of four embedded rectangular slots to achieve the characteristics of super wideband. However, the position of the parasitic element plays an important role in order to determine the super frequency band of the proposed SWB antenna. In case of SWB antenna structure, the function of the resonator is to create and control super wide frequency band sharply. Because of exhibiting these properties, this parasitic element is a perfect resonator structure. In spite of implanting this

parasitic structure, the thorough antenna size is unchanged where, for the perfect resonator structure, excessive space is no longer required.

The optimized value of the antenna design parameters are identified in Table 1. The proposed SWB antenna is positioned in the x-y plane as well as the normal direction is leaded as parallel to the z-axis in Fig. 1 (c). Basically, the patch was circular and some modifications were performed on the ground plane. To enhance the impedance bandwidth, the following measures are used as shown in Fig. 2.

a) Adding a rectangular slot of about 30^0 angles, length of l_1, and width of 0.87 mm on the upper part of the ground plane as a parasitic element.
b) Embedding a slot with length of w_1, width of 1 mm horizontally.
c) Attaching a slot of about 330^0 with length of l_2, width of 1 mm.
d) Adding a slot of 30^0 with length of 10.1 mm, width of 1.1 mm

By choosing the optimized parameters reported in Table 1, the proposed SWB antenna can be tuned for operating in SWB applications.

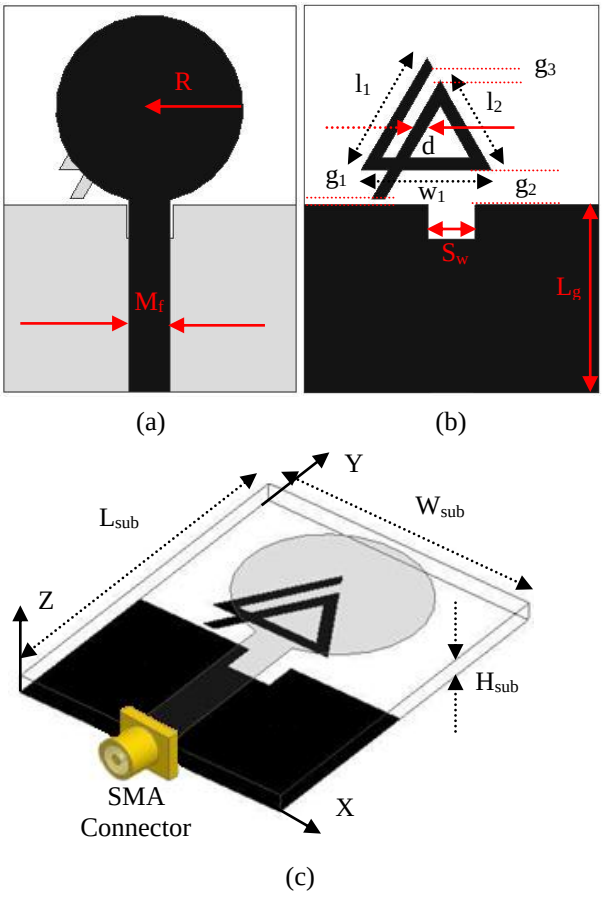

Fig. 1. The geometry of the proposed antenna: (a) top layer, (b) bottom layer, and (c) side view.

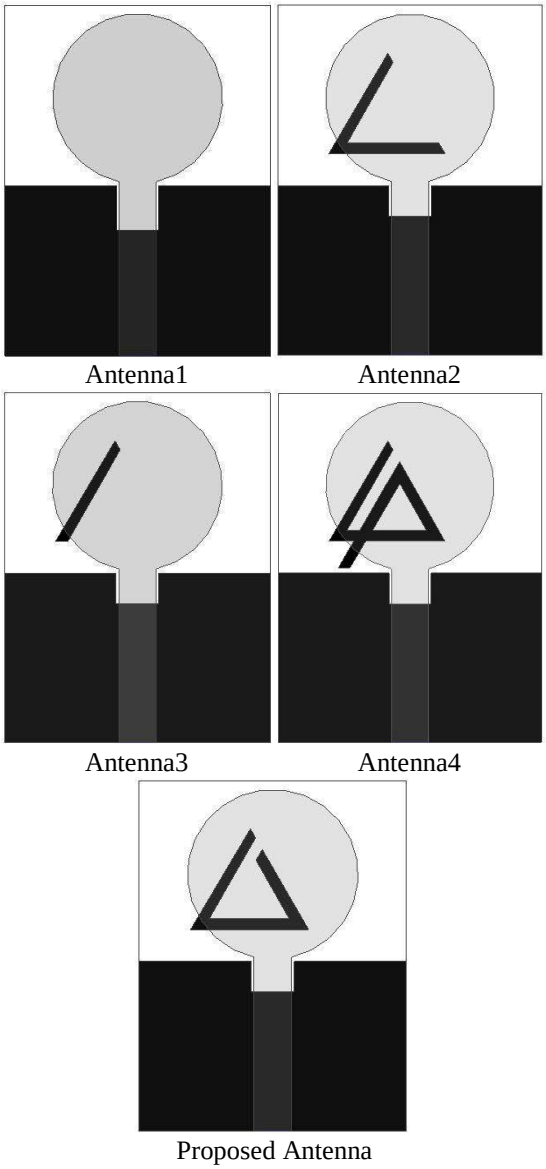

Fig. 2. The proposed design evolution with parasitic element.

Table 1: Optimized dimensions of the proposed SWB antenna

Para.	L_{sub}	W_{sub}	H_{sub}	l_1	l_2	g_1	g_2
mm	25	33	1.6	11	8.7	.5	3
Para.	g_3	d	w_1	R	M_f	L_g	S_w
mm	1.1	1.23	11.05	8	3.5	16	4

Figure 3 illustrates the input impedance of the various antenna structures with real values and the input impedance of the various antenna structures with imaginary values is indicated in Fig. 4. This SWB antenna is fed using a microstrip line of property impedance, which is referred before. It can be easily observed from the Fig. 3 that the impedance of the

proposed antenna with real values approaches to 50 Ω among all the antenna structures such as antenna 1, antenna 2, antenna 3 and antenna 4. On the other hand, it can be clearly seen from the Fig. 4 that the impedance of the proposed antenna with imaginary values approaches to zero among all the antenna structures such as antenna 1, antenna 2, antenna 3 and antenna 4. When the antenna impedance and the microstrip line property impedance approaches to both 50 Ω, the microstrip line impedance is matched with the load impedance. It can be found that this antenna impedance is well matched. The Fig. 5 shows the fabricated photograph of the proposed SWB antenna.

The simulated reflection coefficient property of various antenna structures is shown in Fig. 6. Antenna 1 covers frequency band from 2.9 GHz to 10.6 GHz and after that, covers 12.35 to 16.50 GHz. Antenna 2 covers 2.9-10.7 GHz frequency range and then again starts to operate from 12.1 GHz. Antenna 3 operates ranging from 2.9 to 4 GHz, 4.4 to 10.7 GHz and 12.2 to 18.9 GHz. Antenna 4 covers band from 3.08-10.7 GHz, 12.1-18.8 GHz and 19.4 GHz to more than 20 GHz. On the other hand, the proposed disc-shaped antenna covers from 2.9 GHz to more than 20 GHz, provides a reasonable wider impedance bandwidth in SWB applications in comparison to antenna 1, antenna 2, antenna 3 and antenna 4.

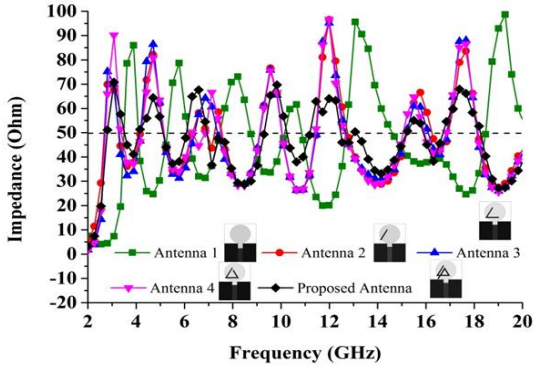

Fig. 3. Input impedance of the various antenna structures with real values.

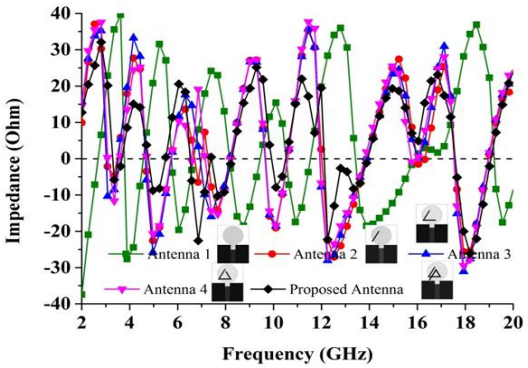

Fig. 4. Input impedance of the various antenna structures with imaginary values.

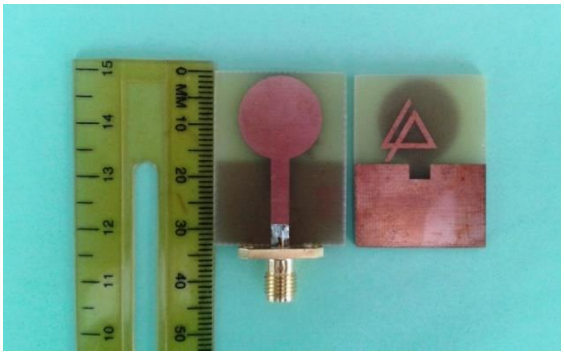

Fig. 5. The photograph of the top and bottom view of the proposed antenna.

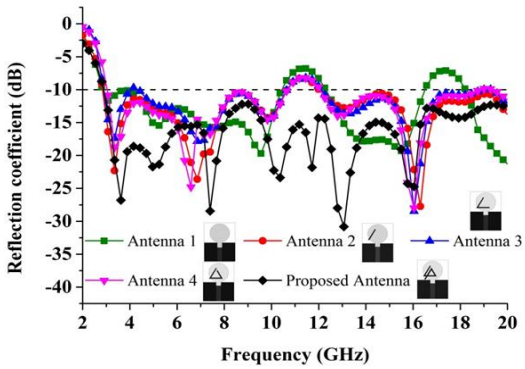

Fig. 6. simulated reflection coefficient properties of various antenna structures.

III. RESULTS AND DISCUSSIONS

The performance characteristics of the proposed disc-shaped SWB antenna are explained, studied, and optimized using HFSS. The proposed disc-shaped antenna with the parasitic element on the ground plane is prototyped in the PCB LPKF (S63) prototyping machine to obtain a physical test model, which is illustrated in Fig. 7 (a). An anechoic chamber is acted as the most effective electromagnetic measurement system. The results of the proposed SWB antenna prototype are measured in a rectangular shaped anechoic chamber of dimensions 5.5 m × 5 m × 3.5 m. As a reference antenna, a double ridge guide horn antenna is adopted. During measurement this prototyped antenna is located face to face in respect to the reference antenna. Figure 7 (b) demonstrates the photograph of the anechoic chamber. A pyramidal-shaped electrically thick foam absorber is adopted on the wall, ceiling, and floor with less than −60 dB reflectivity at normal incidence. A turntable of dimension 1.2 m diameter is applied in order to rotate the testing antenna with the specification, 3600 rotation angle, 1 RPM rotation speed was connected with a 10 meter cable among the controllers. An Agilent vector network analyzer (VNA E8362C) that covers up to 20 GHz is applied for the testing procedure.

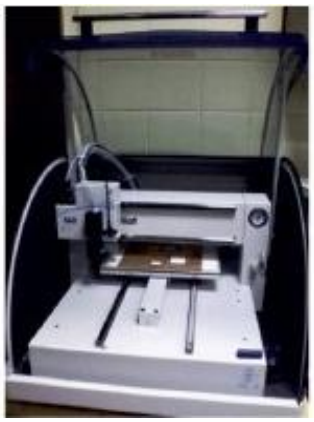

(a)

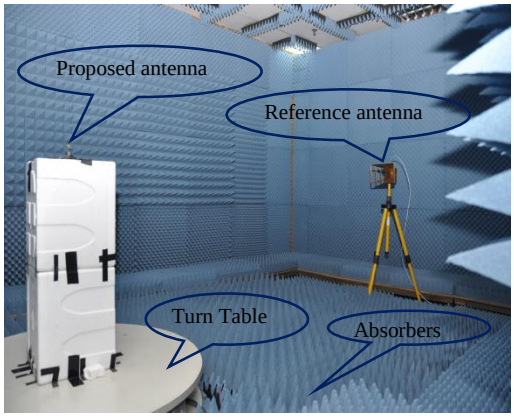

(b)

Fig. 7. (a) The LPKF machine and (b) the anechoic chamber for the proposed SWB antenna.

The simulated and measured reflection coefficient of the proposed SWB antenna is shown in Fig. 8. The measured results exhibit that the proposed disc-shaped antenna shows a broadband impedance matched properties which covers from 2.90 GHz to more than 20 GHz The little discordance between the measurement and simulation results is owing to fabrication tolerance, extended ground effect and the effect of improper soldering of the SMA connector. However, the measured results are also almost coincidence with the expected results, so these results are adoptable.

The surface current distribution on the ground plane and the patch of the proposed SWB antenna at frequencies 3.5 GHz, 4.25 GHz, 9.9 GHz, 11.5 GHz, 13.3 GHz, and 17.75 GHz is illustrated respectively in Fig. 9 and Fig. 10. From Fig. 9, it is observed that the parasitic element on the upper portion of the ground plays an important to create resonances and achieve super frequency bands. The parasitic element has a major effect at frequencies 3.5 GHz, 4.25 GHz, 11.5 GHz, and 13.3 GHz on the ground plane. This conducts to ensure that the performance of this SWB antenna is dependent on the parasitic element on the ground plane. Besides, the amount of current flow exists also around the slot on the ground plane at frequencies 3.5 GHz, 4.25 GHz, 9.9 GHz and 11.5 GHz. The feeding line keep role to flow current sharply.

The surface current distribution on the patch at six frequencies is demonstrated in Fig. 10. It can be seen clearly from Fig. 10 that the microstrip feeding is a dominant figure and the disc-shaped patch also plays role to flow currently sharply. The surface current maintains a harmonic order flow both the patch and the ground plane. As a result, super wide frequency band is generated.

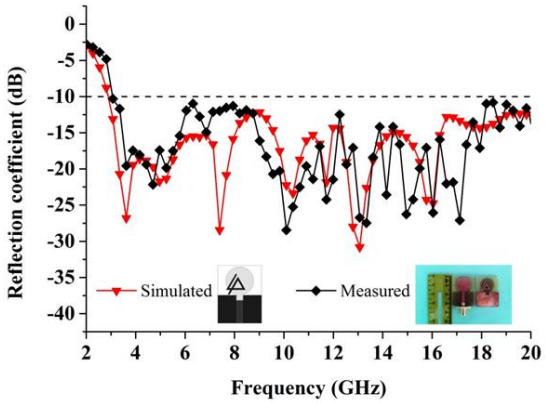

Fig. 8. Simulated and measured reflection coefficient of the proposed SWB antenna.

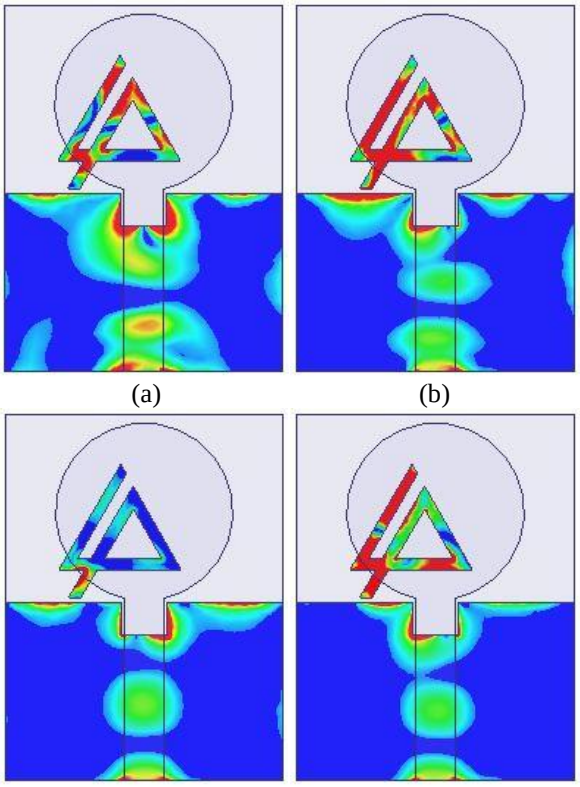

(a) (b)

(c) (d)

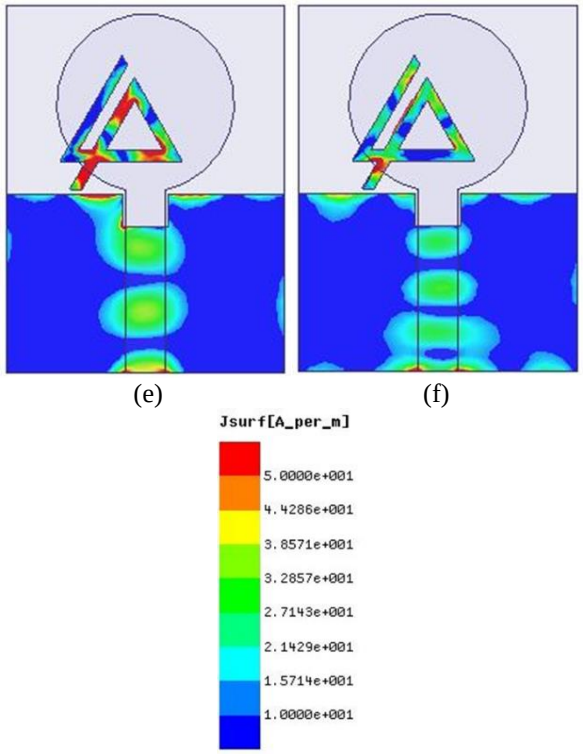

Fig. 9. Surface current distribution on the ground plane at frequencies: (a) 3.5 GHz, (b) 4.25 GHz, (c) 9.9 GHz, (d) 11.5 GHz, (e) 13.3 GHz, and (f) 17.75 GHz.

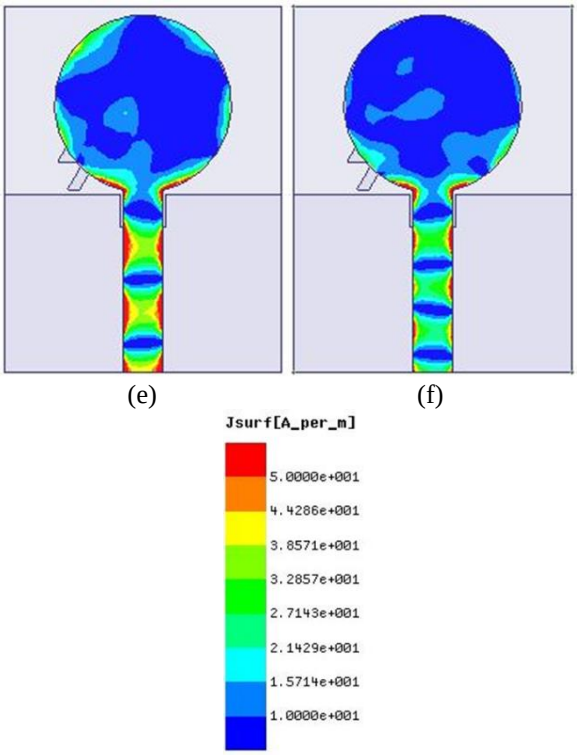

Fig. 10. Surface current distribution on the patch at frequencies: (a) 3.5 GHz, (b) 4.25 GHz, (c) 9.9 GHz, (d) 11.5 GHz, (e) 13.3 GHz, and (f) 17.75 GHz.

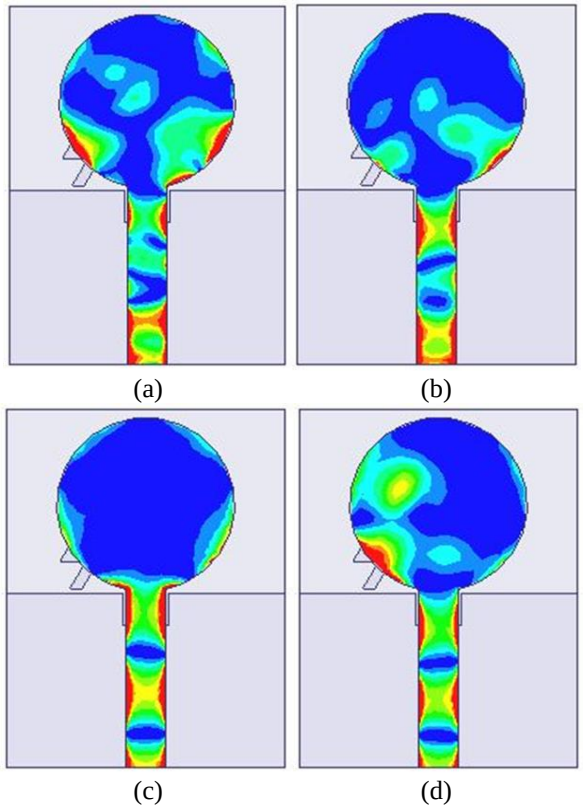

The measured normalized radiation pattern of the proposed disc-shaped SWB antenna is illustrated in Fig. 11 for (a) 3.5 GHz, (b) 4.25 GHz, (c) 9.9 GHz, (d) 11.5 GHz, (e) 13.3 GHz, and (f) 17.75 GHz on the both E-plane and H-plane, respectively. Two-dimensional (2D) radiation patterns are applied to indicate cross and co-polarization. To denote the co-polar and cross-polar, E_θ and E_φ are applied, respectively, where x-z plane is considered as H-plane and y-z plane is considered as E-plane. Cross-polarization is lower than co-polarization, which is the characteristic of standard radiation pattern. The cross-polarization has a higher effect on frequencies 11.5 GHz, 13.3 GHz at E-plane and frequencies 9.9 GHz, 17.75 GHz at H-plane. It is observed that the proposed SWB antenna exhibits better broadside radiation features, considerable front-to-back ratio with low cross polarization, which leads to symmetric and nearly omni-directional radiation pattern along both the E-plane and the H-plane.

The proposed SWB antenna exhibits linear polarization, since the level of cross-polarization is lower than that of co-polarization in the radiation pattern. For this nearly omni-directional radiation pattern characteristic, some reasonable merits are found. One merit is that the radiation pattern is more stable on the covering frequency. Resonances are not shifted all on a

sudden for various directions, so a stable amount of power exists in the direction of the broadside beam. The cross-polarization is comparatively higher in the radiation pattern, which may be happened due to the diffractions from the edges of the ground plane and the patch. These radiation patterns are appropriate for SWB applications.

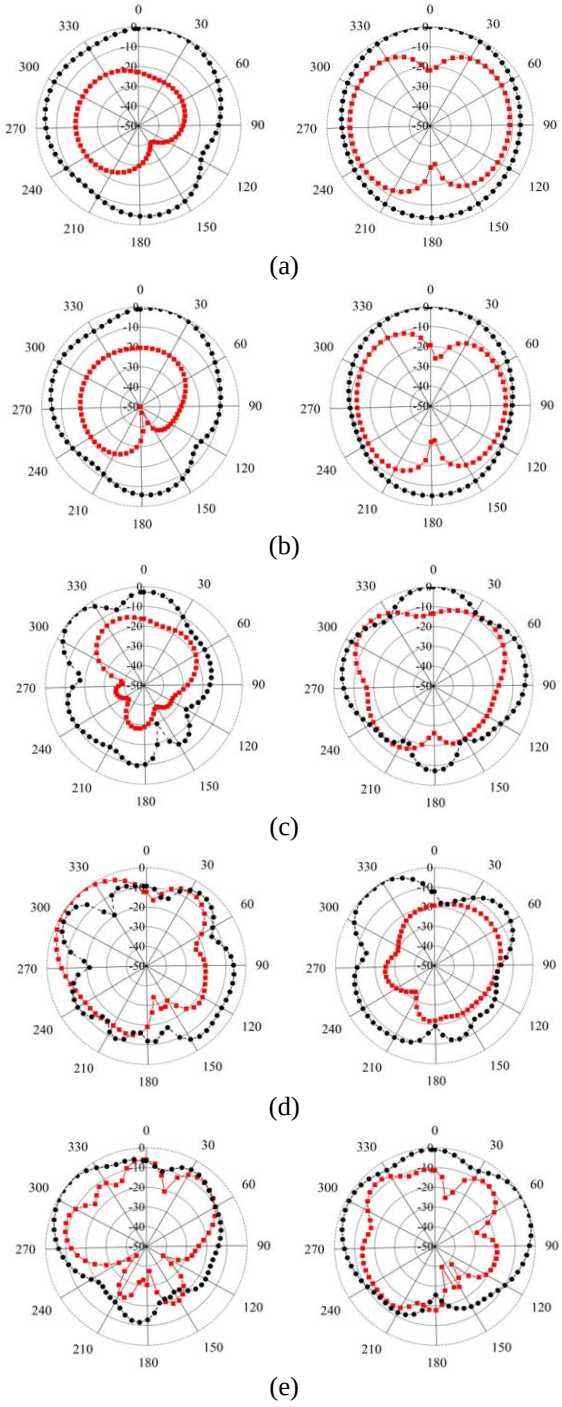

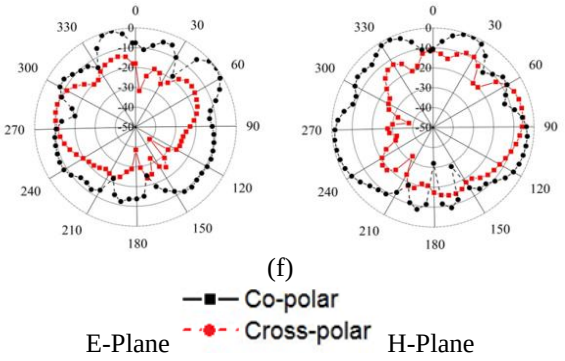

Fig. 11. Measured radiation pattern at frequencies: (a) 3.5 GHz, (b) 4.25 GHz, (c) 9.9 GHz, (d) 11.5 GHz, (e) 13.3 GHz, and (f) 17.75 GHz.

The measured gain of the proposed disc-shaped SWB antenna is exhibited in Fig. 12.

A standard three-antenna system is used for measuring gain with two identical horn antennas. It is known to the gains of the two identical horn antennas, and a gain with two identical horn antennas that follows well-known equations is applied in case of three antennas. The gain of the three antennas (under test) can be calculated following the below equations, because P_r is the radiated power, the gains of two horn antennas are known, and R is the distance between the two antennas.

Antenna 1 (horn) and Antenna 2 (horn):

$$G_1 + G_2 = 20log_{10}\left(\frac{4\pi R}{\lambda}\right) + 10log_{10}\left(\frac{P_{r2}}{P_{r1}}\right). \quad (1)$$

Antenna 1 (horn) and Antenna 3 (under test):

$$G_1 + G_3 = 20log_{10}\left(\frac{4\pi R}{\lambda}\right) + 10log_{10}\left(\frac{P_{r3}}{P_{r1}}\right). \quad (2)$$

Antenna 2 (horn) and Antenna 3 (under test):

$$G_2 + G_3 = 20log_{10}\left(\frac{4\pi R}{\lambda}\right) + 10log_{10}\left(\frac{P_{r3}}{P_{r2}}\right). \quad (3)$$

For directivity D, the following equation [41] is used in which U is the radiation intensity and *Prad* is the total radiated power:

$$D = \frac{4\pi U}{P_{rad}}. \quad (4)$$

It can be observed clearly from the Fig. 12 that the average gain of the proposed SWB antenna is 3.78 dBi where the maximum peak gain is 6.22 dBi, which is accepted for SWB applications.

The phase value of the proposed disc-shaped SWB antenna is shown in Fig. 13. It can be observed from the graph that this phase values imply that all the frequency components of the signal belongs to the same pulse distortion due to the same propagation delay. As a result, the phase variation of this proposed SWB antenna is linear across the entire covering frequency bands 2.90 GHz to more than 20 GHz. Table 2 contains the comparison between the proposed and existing antennas.

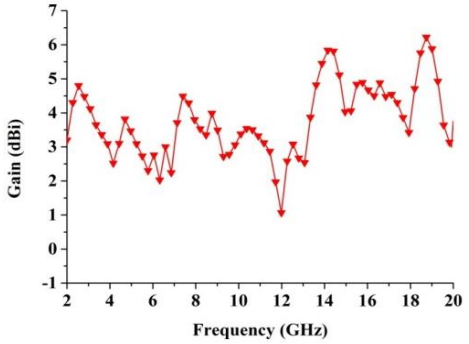

Fig. 12. Measured gain of the proposed disc-shaped SWB antenna.

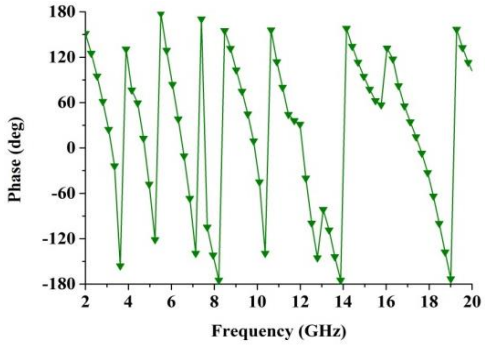

Fig. 13. The phase value of the proposed disc-shaped SWB antenna.

Table 2: Comparison between the proposed SWB and some existing antennas

Literature	Dimensions (mm^2)	Pass Band (GHz)	Measured Gain (dBi)
[13]	90×135	0.7986-17.4663	-20 to 5
[20]	35×77	1.44-18.8	1 to 7
[21]	30×40	2.5-≥25	2 to 6
[23]	120×124	1.08-27.4	Not mentioned
[24]	25×35	3.5-31.9	-0.8 to 8
Proposed	25×33	2.90-≥20	3.20-6.22

IV. CONCLUSION

A disc-shaped monopole antenna is proposed and investigated with a design evolution analysis, implanting the parasitic element on the ground plane for SWB applications. This antenna comprises a disc-shaped radiating patch and a partial ground plane with the parasitic element and has an overall dimension of 25 mm × 33 mm. For planar structure, this proposed SWB antenna design is straight, comfort to fabricate, and very compatible to integrate into microwave circuitry. The parasitic element is used on the ground plane to achieve SWB frequency bands with nearly omni-directional radiation characteristics and smooth current distribution. It is realized experimentally that this antenna is matched properly for SWB frequency ranging from 2.90 to more than GHz. The radiation patterns, low profile, stable gain and small dimension characteristics of the proposed antenna give the validation that, the reported antenna is a promising candidate of SWB applications.

REFERENCES

[1] Federal Communications Commission Revision of Part 15 of the Commission's Rules Regarding Ultra-Wideband Transmission System from 3.1 to 10.6 GHz, in Federal Communications Commission: ET-Docket, pp. 98-153, 2002.

[2] C.-C. Lin and H.-R. Chuang, "A 3-12 GHz UWB planar triangular monopole antenna with ridged ground-plane," *Progress In Electromagnetics Research*, vol. 83, pp. 191-198, 2008.

[3] N. Ojaroudi, M. Ojaroudi, N. Ghadimi, and M. Mehranpour, "UWB square monopole antenna with omni-directional radiation patterns for use in circular cylindrical microwave imaging systems," *Applied Computational Electromagnetics Society (ACES) Journal*, vol. 28, no. 2, pp. 123-129, 2013.

[4] N. Ojaroudi, M. Ojaroudi, and N. Ghadimi, "Square monopole antenna with band-notched characteristic for UWB communications," *Applied Computational Electromagnetics Society (ACES) Journal*, vol. 28, no. 8, pp. 712-718, 2013.

[5] R. Azim, M. T. Islam, and N. Misran, "Design of a planar UWB antenna with new band enhancement technique," *Applied Computational Electromagnetics Society (ACES) Journal*, vol. 26, no. 10, 2011.

[6] S. Lin, R.-N. Cai, G.-L. Huang, and J.-X. Wang, "A miniature UWB semi-circle monopole printed antenna," *Progress In Electromagnetics Research Letters*, vol. 23, pp. 157-163, 2011.

[7] N. Ojaroudi, M. Ojaroudi, N. Ghadimi, "Disc shaped monopole antenna with dual band-notched function for UWB applications," *Applied Computational Electromagnetics Society (ACES) Journal*, vol. 28, no. 6, pp. 528-534, 2013.

[8] M. M. Islam, M. T. Islam, M. Samsuzzaman, and M. R. I. Faruque, "Compact metamaterial antenna for UWB applications," *Electronics Letters*, vol. 51, pp. 1222-1224, 2015.

[9] C. M. Li and L. H. Ye, "Improved dual band notched UWB slot antenna with controllable notched bandwidths," *Progress In Electromagnetics Research*, vol. 115, pp. 477-493, 2011.

[10] M. T. Partovi, N. Ojaroudi, and M. Ojaroudi, "Small slot antenna with enhanced bandwidth and band-notched performance for UWB applications," *Applied Computational Electromagnetics Society (ACES) Journal*, vol. 27, no. 9, pp. 772-778, 2012.

[11] M. Almalkawi, M. Westrick, and V. Devabhaktuni, "Compact super wideband monopole antenna with

switchable dual band-notched characteristics," *Proceedings of the Asia-Pacific Microwave Conference*, Taiwan, pp. 723-725, 2012.

[12] X. R. Yan, S. S. Zhong, and X. X. Yang, "Compact printed monopole antenna with super-wideband," *Proceedings of the International Symposium on Microwave, Antenna, Propagation and EMC Technologies for Wireless Communications*, China, pp. 605-607, 2007.

[13] S. Barbarino and F. Consoli, "UWB circular slot antenna provided with an inverted-L notch fillter for the 5 GHz WLAN band," *Progress In Electromagnetics Research*, vol. 104, pp. 1-13, 2010.

[14] D. Tran, A. Szilagyi, I. E. Lager, P. Aubry, L. P. Ligthart, and A. Yarovoy, "A super wideband antenna," *Proceedings of the 5th European Conference on Antennas and Propagation*, Italy, pp. 2656-2660, 2011.

[15] W. Lu and H. Zhu, "Super-wideband antipodal slot antenna," *Proceedings of the Asia Pacific Microwave Conference*, Singapore, pp. 1894-1897, 2009.

[16] X. H. Jin, X. D. Huang, C. H. Cheng, and L. Zhu, "Super-wideband printed asymmetrical dipole antenna," *Progress In Electromagnetics Research Letters*, vol. 27, pp. 117-123, 2011.

[17] M. S. Mahmud and S. Dey, "Design and performance analysis of a compact and conformal super wide band textile antenna for wearable body area applications," *Proceedings of the 6th European Conference on Antennas and Propagation*, Czech Republic, pp. 1-5, 2012.

[18] J. K. Liu, P. Esselle, S. G. Hay, and S. S. Zhong, "Study of an extremely wideband monopole antenna with triple band-notched characteristics," *Progress In Electromagnetics Research*, vol. 123, 143-158, 2012.

[19] K. L. Lau, K. C. Kong, and K. M. Luk, "Super-wideband monopolar patch antenna," *Electronics Letters*, vol. 44, no. 12, pp. 716-718, 2008.

[20] K.-R. Chen, C.-Y.-D. Sim, and J.-S. Row, "A compact monopole antenna for super wideband applications," *IEEE Antennas and Wireless Propagation Letters*, vol. 10, pp. 488-491, 2011.

[21] M. Manohar, R. S. Kshetrimayum, and A. K. Gogoi, "Printed monopole antenna with tapered feed line, feed region and patch for super wideband applications," *IET Microwaves, Antennas and Propagation*, vol. 8, pp. 39-45, 2014.

[22] Y. Dong, W. Hong, L. Liu, Y. Zhang, and Z. Kuai, "Performance analysis of a printed super-wideband antenna," *Microwave and Optical Technology Letters*, vol. 51, pp. 949-956, 2009.

[23] J. Liu, K. P. Eselle, and S. S. Zhong, "A printed extremely wideband antenna for multi-band wireless systems," *Antennas Propagation Society Symposium*, Toronto, Canada, July 2010.

[25] M. N. Srifi, S. K. Podilchak, M. Essaaidi, and Y. M. M. Antar, "Compact disc monopole antennas for current and future ultra-wideband (UWB) applications" *IEEE Transactions on Antennas and Propagation*, vol. 59, no. 12, pp. 4470-4480, 2011.

[25] C. C. Lin, P. Jin, and R. W. Ziolkowski, "Single, dual and tri-band-notched ultra-wideband (UWB) antennas using capacitively loaded loop (CLL) resonators," *IEEE Transactions on Antennas and Propagation*, vol. 60, no. 1, pp. 102-109, 2012.

[26] C. Yoon, W.-J. Lee, W.-S. Kim, H.-C. Lee, and H.-D. Park, "Compact band-notched ultra-wide band printed antenna using inverted L-slit," *Microwave and Optical Technology Letters*, vol. 54, no. 1, pp. 143-144, 2012.

[27] C. A. Balanis, *Antenna Theory: Analysis and Design*. 3rd ed., Wiley-Interscience: New York, NY, USA, 2012.

Md. Moinul Islam was born in Jhenidah, Bangladesh in 1983. He received B.Sc. and M. Sc. degrees in Information and Communication Engineering from Islamic University, Kushtia, Bangladesh in 2005 and 2006, respectively and a Ph.D. degree in Space Science from the Universiti Kebangsaan Malaysia (UKM), Malaysia in 2016. He has authored or co-authored over 35 referred journals and conference papers. He is currently a Senior Lecturer at the Department of Software Engineering, Daffodil International University, Dhaka, Bangladesh. His research interests include antenna and wireless communications, metamaterials, medical imaging and sensing, satellite communications and radio frequency (RF).

Mohammad Rashed Iqbal Faruque was born in Chittagong, Bangladesh in 1974. He received the B.Sc. and M.Sc. degree in Physics from University of Chittagong, Chittagong, Bangladesh in 1998 and 1999, respectively, and a Ph.D. degree in Telecommunication Engineering from the Universiti Kebangsaan Malaysia (UKM) in 2012. From July 2000 to until 2007, he worked as a Lecturer at Chittagong University of Engineering and Technology (CUET), Chittagong. From June 2007 to November 2008, he was an Assistant Professor at University of Information Technology and Sciences (UITS), Chittagong. He has authored or co-authored approximately 60 referred journals and conference

papers. He is currently a Senior Lecturer at the Institute of Space Science (ANGKASA), UKM, Malaysia. His research interests include the RF, electromagnetic field and propagation, FDTD analysis, electromagnetic radiation, metamaterials applications and electromagnetic compatibility.

Mohammad Tariqul Islam is a Professor at the Institute of Space Science of the Universiti Kebangsaan Malaysia (UKM). He is also the Group Leader of Radio Astronomy Informatics Group at UKM. Prior to joining UKM, he was a Lecturer in Multimedia University, Malaysia. He is a Senior Member of the IEEE. He is serving as the Editor-in-Chief of the International Journal of Electronics & Informatics (*IJEI*). He has been very promising as a researcher, with the achievement of several International Gold Medal awards, a Best Invention in Telecommunication Award and a Special Award from Vietnam for his research and innovation. He has been awarded "Best Researcher Award" in 2010 and 2011 at UKM. His professorial interests include the areas of communication antenna design, radio astronomy antennas, satellite antennas, and electromagnetic radiation analysis. He has published over 150 journal papers and few book chapters on various topics related to antennas, microwaves and electromagnetic radiation analysis. He also has filled 6 patent applications on communication antennas. Thus far, his publications have been cited 810 times, and the H-index is 18 (Source: Scopus). He is now handling many research projects from the Ministry of Science, Technology and Innovation (MOSTI), Ministry of Higher Education Malaysia (MOHE) and some International research grants from Japan.

Asymmetrical Single Cell Multiband Uni-Planar Mushroom Resonant Antenna

Navid Amani and Amir Jafargholi

Institute of Space Science and Technology
Amirkabir University of Technology, 424 Hafez Ave., P.O. Box: 15875-4413, Tehran, Iran
N.Amani@live.com, Jafargholi@ieee.org

Abstract ─ A new asymmetrical zeroth-order resonant antenna with improved efficiency and widened impedance bandwidth is proposed. It comprises a rectangular patch, two shorted stub and coplanar waveguide (CPW) feed to have composite right/left handed (CRLH) features and easy fabrication process. The asymmetry helps to combine three resonance frequencies and extends the bandwidth up to 31%. The efficiency of the proposed antenna is greater than 94% over the entire bandwidth of 4.2 to 6.2 GHz. The proposed antenna has compact size, which can provide omnidirectional radiation pattern suitable for wireless applications. The proposed antenna has also a low frequency miniaturized resonance at GPS standard 1.57 GHz, while the second frequency band covers 802.11a/h/j/n/ac and 802.11p WLAN, dynamic frequency selection (DFS) and transmit power control (TPC) applications.

Index Terms ─ Composite right/left-handed transmission line (CRLH TL), multiband antenna, zeroth-order resonant antenna (ZORA).

I. INTRODUCTION

In recent years, introducing metamaterials (MTMs) opened the way for many researcher groups to enhance the antenna performances [1]-[4]. Due to unique electromagnetic properties, MTMs have been widely considered in microstrip antennas to improve their performance; however, the narrow bandwidth of the proposed structures is the main limiting factor for their engineering applications. In addition to these resonance structures, some researchers proposed the other type of MTMs known as composite right/left handed (CRLH) structures which is based on an equivalent circuit approach, [5]. The most famous CRLH resonator is a mushroom structure which employs a patch and via as a unit-cell [6]. Although, periodicity is preferred for computational convenience, applying an element such as unit cell of MTM in antenna structure as a metamaterial-inspired antenna have been proposed and unusual properties of MTM have been achieved [7]-[10]. Based on CRLH resonator theory, 2*N*-1 resonance frequencies are expected from an *N*-cell mushroom resonator [11]. In the case of one unit-cell, it is expected to have only zeroth-order mode (ZOR); however, the TM_{10} mode of the patch is excited in addition to zeroth-order metamaterial inspired resonance frequency [12]. Although, the TM_{10} mode occurs at a frequency above zeroth-order mode and does not satisfy metamaterial cell size criteria, this is useful especially in one-unit cell mushroom resonator due to dual band operation.

In [8-9] and [12]; the theoretical aspects of CRLH single cell patch antenna is discussed. Here the main focus of the paper is to optimize these designs to have a miniaturized/broadband low-profile antenna. Thus at first the antenna structure is described very briefly, and after that two conventional method to have broadband structure is applied to the proposed antenna, i.e., stepped and tapered structures. In this paper, a new asymmetrical zeroth-order resonant antenna with improved efficiency and widened impedance bandwidth is proposed. It comprises a rectangular patch, two shorted stub and coplanar waveguide (CPW) feed to have CRLH features and easy fabrication process. The asymmetry helps to combine three resonance frequencies and extends the antenna bandwidth. These features are verified by CST Microwave Studio and compared with experimental results.

II. DESIGN PROCEDURE

TL discontinuities are common in microwave circuits and microstrip antennas [13]. T-junction equivalent circuit is nearly similar to CRLH structure. A CRLH unit cell may be achieved just by paralleling the capacitance of the T-junction with the total inductance of the junction and stub, and also introducing a capacitance (C_L) series with RH inductance (L_R). As ground planes are coplanar in CPW, it facilitates easy shunt as well as series. The shunt elements are provided by connecting the stub of the T-junction to CPW ground as a shorted stub. The total inductance of the junction and stub becomes parallel with the total capacitance of the structure.

Submitted On: August 16, 2015
Accepted On: May 22, 2016

In addition, the gap existence between CPW central strip and main line of the T-junction introduces a LH capacitance C_L. Three different configuration of a single cell uni-palanar mushroom CRLH resonant antenna based on T-junction discontinuity and ungrounded CPW feed are realized. In the case of one unit cell there is neither left-hand capacitance nor negative–order modes. Nonetheless, zeroth-order and TM_{10} modes are achievable and dual-band operation is applicable. Asymmetrical configuration provides another resonance frequency below both the zeroth-order and TM_{10} modes; therefore, tri-band functionality is provided. We consider step and linear taper in the main line of the T-junction to combine zeroth-order and TM_{10} modes and enhance the antenna bandwidth.

A. Zeros order mode

Zeroth-order resonance frequency can be achieved by the following:

$$\omega sh = \frac{1}{\sqrt{L_L C_R}}, \quad (1)$$

where L_L and C_R are the left-hand inductance and right-hand capacitance, respectively. The right-hand capacitance is achieved through the gap between the rectangular strip and CPW ground planes. Left-hand inductance which is introduced by the means of shorted stub is determined by the width and length of the stub. These are influential parameters in ZOR frequency.

B. Positive- and negative-order modes

In contrast to zeroth-order mode, both positive- and negative-order modes are affected by the cells number, [11]. Simulations show that the number of resonance frequencies for these right- and left-handed regions are dependent on the number of cells, cell types and feeding configuration.

In general, CRLH structure is a band-pass filter due to the lowpass nature of the right-handed (RH) elements and the highpass nature of the LH elements. In a periodic CRLH TL net rejection commonly occurs from the structure, due to satisfaction of Bragg condition at both ends of the Brilluoin zone. In a periodic CRLH resonator, the resonance frequencies obtained by [11]:

$$\beta_n p = \frac{n\pi}{N} (n = 0, \pm 1, \ldots, \pm N), \quad (2)$$

where n is the mode number and N is the number of unit cells. Therefore, $2N+1$ resonances (i.e., N RH, N LH and one as zeroth-order mode) may be achieved in a CRLH resonator. When $|n|=N$, the dispersion diagram reaches to the edges of Brillouin zone where the period of the structure is equal to $|\lambda/2|$. Thus, there is a potential to satisfy Bragg condition with in-phase reflections from unit cells with sizes of $|\lambda/2|$. In this condition no energy transmits to the structure and consequently the corresponding resonances, known as Bragg frequencies, are eliminated. Generally, there are two Bragg frequencies in a multi-cell CRLH resonator, a resonance occurred in RH region and the other is located in LH region. Therefore, $2N$-1 resonance frequencies may be obtained. By reducing the number of cells, in-phase reflections from the adjacent cells will become progressively weaker. Eventually, in a single-cell CRLH resonator due to periodicity elimination, there is not any in-phase reflection from the adjacent cells and it causes to disappear Bragg gaps, which is consequently leads to obtain two additional resonance frequencies. It is worth nothing that the amount of bandgap decreasing at the RH region is greater than LH which is due to harmonic nature of the structure.

Simulation shows that this condition is much sensitive and strongly dependent to cell-types and feeding structure. As a result, a single-cell CRLH resonant antenna performs tri-band characteristic while occupying less area than a multi-cell CRLH resonant antennas and further miniaturization is achievable without missing multiband functionality.

In [9] it is shown that the ZOR frequency which is derived from dispersion diagram is equal for a single-cell and multi-cells CRLH resonators. Although zeroth-order resonance frequency in an open-ended CRLH resonator is independent of the series elements, any changes in shunt elements will shift all negative-, zeroth- and positive-order resonance frequencies. The width and location of the stub have determinative role in resonance frequencies, due to changes in shunt capacitance/ inductance values.

III. ANTENNA REALIZATION

A. Simple T-antenna

To have preferable impedance matching condition, a 50 Ω input impedance ungrounded CPW line is designed. The widths of the main line and central strip of the CPW have major effect on antenna matching. In order to achieve more coupling and better matching condition, the central strip of the CPW is designed wider at the end of the line ($W_2 > W_1$). To realize shunt elements, the stub of the junction is connected to the CPW ground plane. Shorted stub and gap dimensions between main line of the T-junction and CPW ground plane determine shunt parameter values and ZOR frequency of the structure. The schematic of the proposed CRLH resonant simple T-antenna and the manufactured prototype are shown in Fig. 1 (a).

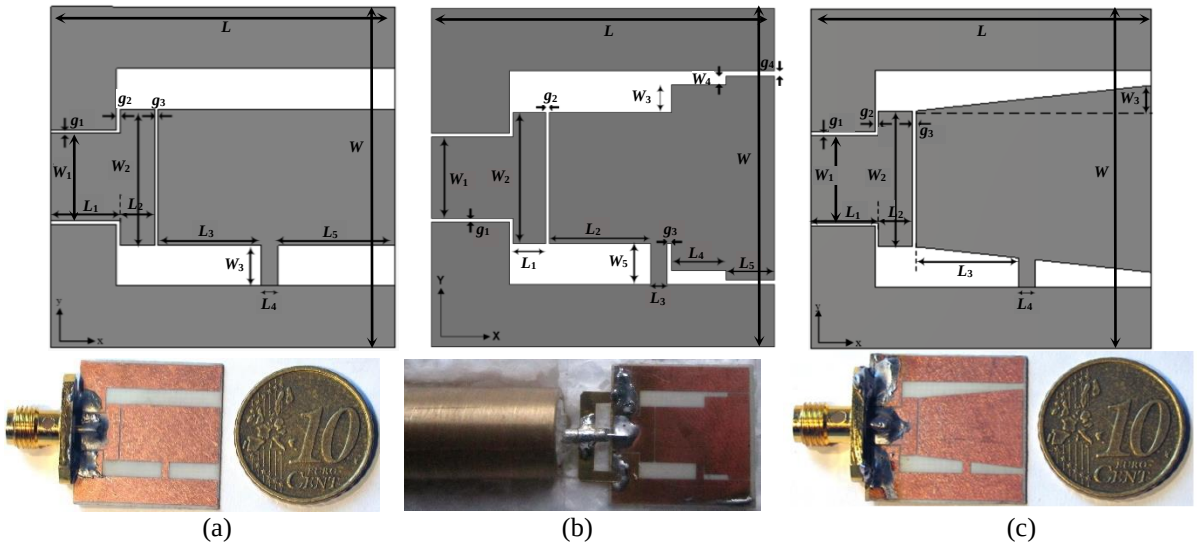

Fig. 1. Schematic of the proposed single-cell: (a) simple, (b) step tapered, and (c) linear tapered T-shape CRLH resonant antenna based on the T-junction discontinuity and CPW feed structure. Photograph of the manufactured prototype. All dimensions are (in mm): W=L=20, W_1=5.15, W_2=8, g_1=g_2=g_4=0.2, W_4=0.6, W_5=2.375; for simple type antenna: W_3=2.375, L_1=4, L_2=2, L_3=6, L_4=1, L_5=6.8, g_3=0.2; for step tapered T-antenna: W_3=1.575, L_1=2, L_2=6, L_3=1, L_4=3.42, L_5=3.16, g_3=0.22, for linear tapered antenna: W_3=1.

To show the effects of the shorted stub and the CRLH characteristics of the proposed structure, simulated impedance diagram of the simple T-antenna is compared with a CPW-fed simple patch without shorted stub (Fig. 2). According to this figure, the fundamental resonance frequency of a simple rectangular patch antenna is obtained around 5.8 GHz, while the proposed simple T-antenna has a little shift to upper frequencies at this mode and provides two additional resonances below this TM_{10} mode. Figure 3 demonstrates the simulated and measured reflection coefficient of the proposed T-antenna. However, zeroth-order mode of the proposed antenna is obtained at approximately 4.22 GHz. The measured asymmetry and TM_{10} modes occurred at 1.72 and 5.8 GHz, respectively. At the asymmetry mode the overall antenna dimensions is 20mm×20mm×0.508mm (0.11λ×0.11λ×0.003λ). The measured -10 dB bandwidth at asymmetry, zeroth-order and TM_{10} modes are 3.08%, 15.17% and 8.33%, respectively. In order to delineate the tri-band functionality of the proposed structure, the tangential electric field distribution of the proposed simple T-antenna at asymmetry, zeroth-order and TM_{10} modes are depicted in Fig. 4. It seems that there is a strong coupling between CPW feed and the radiating T-shape patch at all three modes that preserves the efficiency of the antenna. Owing to asymmetry of the patch, asymmetrical electric field distribution in CPW feed region are clearly observed at both asymmetry and zeroth-order modes while it is more symmetrical in TM_{10} mode.

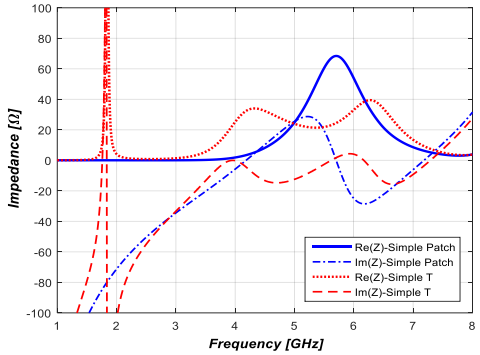

Fig. 2. Comparison of input impedance of the proposed single-cell CRLH resonant T-antenna with the simple rectangular patch without shorted stub.

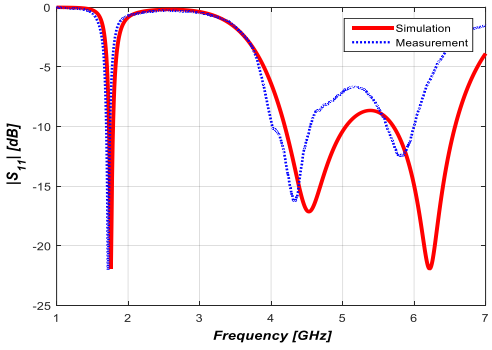

Fig. 3. Simulated and measured reflection coefficients of the proposed single-cell CRLH resonant T-antenna.

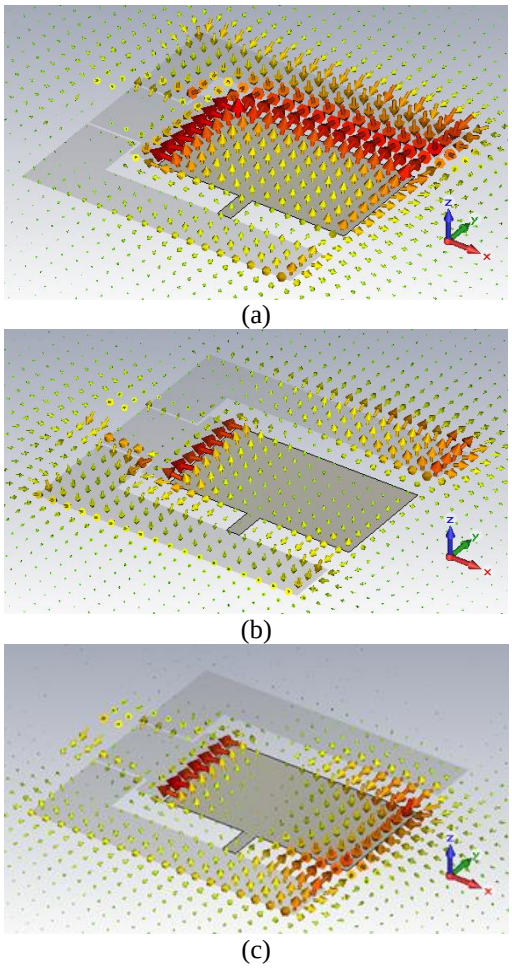

Fig. 4. Electric-field distribution of the simple T-antenna: (a) n=-1 mode, (b) n=0 mode, (c) n=+1 mode; asymmetrical electric field distribution in CPW feed region at both n=-1, 0 modes and symmetrical electric field distribution in n=+1.

B. Step tapered T-antenna

Accordant to impedance diagram of the simple T-antenna, Fig. 2, there is a great potential to combine zeroth-order and TM_{10} modes with small changes in the orginal structure. One common way to improve matching condition is to use reactive elements. It is well-known that microwave discontinuities can introduce reactive elements. Multiple step discontinuities with different length and width, generally used to improve impedance matching [14]. The schematic of the proposed step tapered single-cell uniplanar mushroom resonant antenna and its manufactured prototype are shown in Fig. 1 (b). The return loss diagram of the proposed antenna is shown in Fig. 5. Here, the miniaturization band or assymetry mode reduced to 1.57 GHz. At this frequency, the antenna dimension is approximately $0.1\lambda\times0.1\lambda\times0.0026$, while the measured bandwidth is about 31.4 MHz.

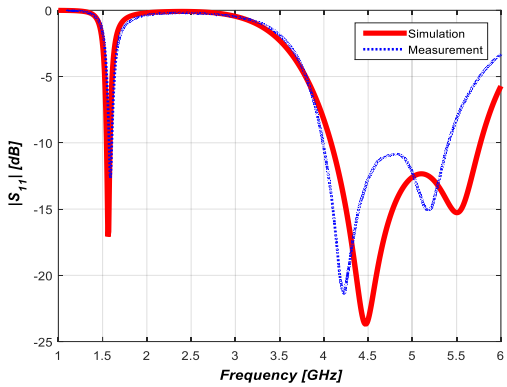

Fig. 5. Simulated and measured reflection coefficients of the single-cell step tapered CRLH resonant T-antenna.

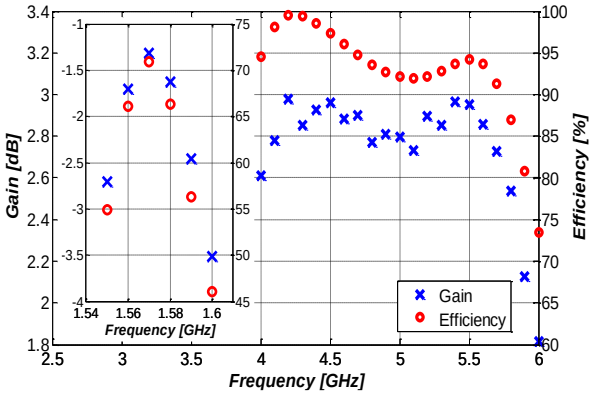

Fig. 6. Measured gain and simulated efficiency of the single-cell step tapered CRLH resonant T-antenna: (a) miniaturized lower, and (b) higher frequencies.

With the aid of two step discontinuities zeroth-order and TM_{10} modes became closer together and combined with significant 30.8% measured impedance bandwidth. The proposed antenna has -1.3 dB gain and considerable 70.8% total efficiency in miniaturization band due to integrated structure. Antenna dimension in the middle of its upper band is $0.3\lambda\times0.3\lambda\times0.0077$ with increased efficiency and extended bandwidth. The measured gain and simulated efficiency of the proposed antenna are plotted in Fig. 6.

The CST-predicted and measured far-field radiation patterns of the proposed tri-band single-cell uni-planar mushroom resonant antenna are also shown in Fig. 7 at f=1.5 and 4.2 GHz. To measure the antenna radiation pattern, the sleeve balun is used which is designed and fabricated to measure the radiation at a single resonance frequency due to its narrowband behavior [9]. For the sake of brevity we omit the results, however for all three types of proposed antenna the measurements have done using sleeve balun as described and depicted here. As expected, the results show that the proposed antenna has fairly good omnidirectional radiation patterns at the *XZ*-

plane (φ=0) and *YZ*-plane (φ=90).

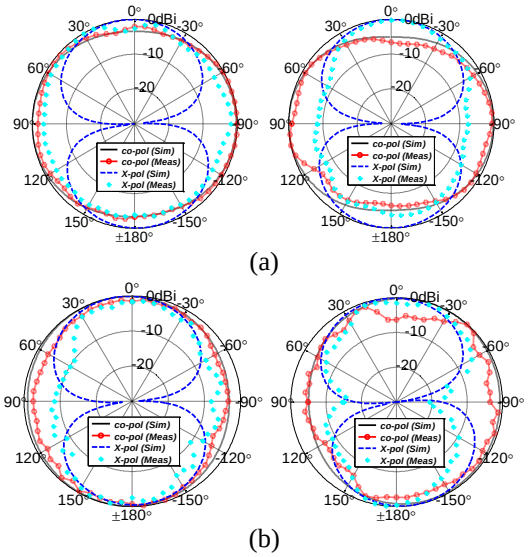

Fig. 7. Comparison of CST-predicted and measured radiation patterns, XZ-Plane (left) and YZ-Plane (right), for dualband step tapered CRLH resonant T-antenna: (a) 1.5 GHz and (b) 4.2 GHz.

Because the size of the proposed antenna in the highest resonance frequency is less than 0.5λ (about 0.38λ), omnidirectionality of radiation patterns is preserved in the entire impedance bandwidth at all three modes.

According to the applications of the proposed miniaturized tri-band antenna in mobile communication systems, the level of cross-polarized radiation pattern is not critical.

C. Linear tapered T-antenna

Continuous step discontinuities with differential length and width extension transform to tapered line. The schematic of the proposed linear tapered CRLH resonant antenna and the manufactured prototype are shown in Fig. 1 (c). The zeroth-order mode shifted up to 4.5 GHz. Reflection coefficient diagram of the proposed linear tapered T-antenna shows better impedance matching in the frequency range between zeroth-order and TM_{10} modes, Fig. 8, and in upper band, remarkable 37.97%, for -10 dB measured impedance bandwidth is achieved. The measured antenna bandwidth at the miniaturized frequency is about 44 MHz where the antenna dimension is 0.11λ×0.11λ×0.003λ.

Table 1 shows the overall performance of the proposed step tapered T-antenna in comparison with the recently reported ZOR antennas [15], [16], [17], [18]. Deficiencies of the reference antennas are highlighted in the table. In [15] and [16] two and three unit cells are used, respectively while dipole-like pattern is achieved. The proposed single-cell ZOR antenna in [17] suffers from narrow bandwidth. Although, another single-cell ZOR antenna is presented in [18], the proposed antenna becomes 3-dimensional and bulky due to folded mushroom structure.

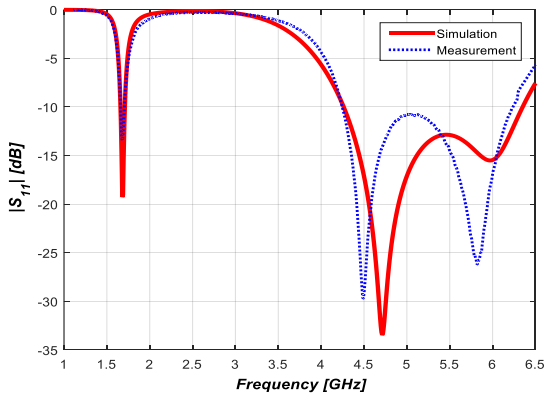

Fig. 8. Simulated and measured reflection coefficients of the single-cell linear tapered CRLH resonant T-antenna.

Table 1: Summary of antenna performances for the proposed and reference antennas

	Step Tapered T-Antenna		[15]	[16]	[17]	[18]
Frequency (GHz)	Lower band (1.57)	Upper band 4.2-6.2 (f_c=4.59)	2.03	2.78	2.67	3.58
Antenna footprint (λ_0)	0.1×0.1×0.0026	0.3×0.3×0.007	0.17×0.14×0.01	0.46×0.24×0.01	0.22×0.33×-	0.36×0.23×0.18
Number of cells	1		2	3	1	1
Antenna type	Miniaturized	Low profile	Low profile	Low profile	Low profile	3-Dimensional
Bandwidth (%)	2	30.8	6.8	70.5	0.6	68.3
Efficiency (%)	70.8	94	62	82	-	>80
Gain (dB)	-0.59	2.9	1.35	2	1.22	>3
Pattern type	Omni-directional	Omni-directional	Dipole-like	Dipole-like	Omni-directional	Omni-directional

IV. CONCLUSION

A new asymmetrical uni-planar resonant antenna which comprises of simple patch, shorted rectangular strip and ungrounded CPW feed has been proposed. Using step and linear tapered structures, a dual-band antenna which has a miniaturized lower-band resonance

frequency, at GPS standard 1.57 GHz, as well as wideband upper-band frequencies, from 4.2 to 6.2 GHz, have been proposed. The effects of unit cell number on the zeroth-order bandgap and the number of resonance frequencies in a CRLH resonator is illustrated here. It is shown that reducing the number of cells does not have considerable effects on the zeroth-order mode. In the other word, to design a miniaturized single-cell CRLH resonant antenna, someone may assume a periodic boundary condition, in order to extract the relative dispersion diagram and zeroth-order resonance frequency. To address simultaneously a compact multiband CRLH resonant antenna with high efficiency, a single-cell T-junction based CPW-fed antenna is proposed. In contrast to other ZORAs, a good impedance matching in all resonances is achieved while the antenna efficiency is high. The proposed antenna is implemented on a single layer thin substrate without via process resulting in a simple fabrication. Based on mentioned theoretical concepts, two types of proposed structure have been utilized, i.e., tri-band and dual-band CRLH resonant antennas.

REFERENCES

[1] L. Liu, C. Caloz, and T. Itoh, "Dominant mode leaky-wave antenna with backfire-to-endfire scanning capability," *Electron. Lett*., vol. 38, no. 23, pp. 1414-1416, Nov. 2002.

[2] M. Rafaei Booket, M. Veysi, Z. Atlasbaf, and A. Jafargholi, "Ungrounded composite right/left handed metamaterials: Design, synthesis, and applications," *IET Microwave Antenna Propag.*, vol. 6, no. 11, pp. 1259-1268, 2012.

[3] A. Jafargholi and M. H. Mazaheri, "Broadband microstrip antenna using epsilon near zero metamaterials," *IET Microwave Antenna Propag.*, accepted, 2015.

[4] A. Jafargholi, M. Kamyab, and M. Veysi, "Artificial magnetic conductor loaded monopole antenna," *IEEE Antennas Wireless Propag. Lett.*, vol. 9, pp. 211-214, 2010.

[5] A. Sanada, C. Caloz, and T. Itoh, "Novel zeroth-order resonance in composite right/left-handed transmission line resonators," *Proc. Asia-Pacific Microw. Conf.*, vol. 3, pp. 1588-1591, 2003.

[6] D. Sievenpiper, L. Zhang, R. F. J. Broas, N. G. Alexopolous, and E. Yablonovitch, "High-impedance electromagnetic surfaces with a forbidden frequency band," *IEEE Trans. Antennas Propag.*, vol. 47, no. 11, pp. 2059-2074, Nov. 1999.

[7] A. Erentok and R. W. Ziolkowski, "Metamaterial-inspired efficient electrically small antennas," *IEEE Trans. Antennas Propag.*, vol. 56, no. 3, pp. 691-707, 2008.

[8] N. Amani, A. Jafargholi, M. Kamyab, and A. Vaziri, "Asymmetrical wideband zeroth-order resonant antenna," *Electron. Lett.*, vol. 50, no. 2, pp. 59-60, 2014.

[9] N. Amani, M. Kamyab, A. Jafargholi, A. Hosseinbeig, and J. S. Meiguni, "Compact tri-band metamaterial-ispired antenna based on CRLH resonant structures," *Electron. Lett*., vol. 50, no. 12, pp. 847-848, 2014.

[10] M. Rafaei Booket, A. Jafargholi, M. Kamyab, H. Eskandari, M. Veysi, and S. M. Mousavi, "Compact multi-band printed dipole antenna loaded with single-cell metamaterial," *IET Microw. Antennas Propag.*, vol. 6, pp. 17-23, 2012.

[11] C. Caloz and T. Itoh, *Electromagnetic Metamaterials: Transmission Line Theory and Microwave Applications*. New York: Wiley, 2006.

[12] N. Amani, M. Kamyab, and A. Jafargholi, "Zeroth-order and TM_{10} modes in one-unit cell CRLH mushroom resonator," *IEEE Antennas Wireless Propag. Lett.*, vol. 14, pp. 1396-1399, 2015.

[13] K. C. Gupta, R. Garg, I. Bahl, and P. Bhartia, *Microstrip Lines and Slotlines*. 2nd ed., Artech House, 1996.

[14] G. V. Eleftheriades, A. K. Iyer, and P. C. Kremer, "Planar negative refractive index media using periodically L–C loaded transmission lines," *IEEE Trans. Microw. Theory Tech*., vol. 50, no. 12, pp. 2702-2712, Dec. 2002.

[15] T. Jang, J. Choi, and S. Lim, "Compact coplanar waveguide (CPW)-fed zeroth-order resonant antennas with extended bandwidth and high efficiency on vialess single layer," *IEEE Trans. Antennas Propag.*, vol. 59, no. 2, pp. 363-372, 2011.

[16] B. Niu and Q. Feng, "Bandwidth enhancement of CPW-fed antenna based on epsilon negative zeroth- and first-order resonators," *IEEE Antenna Wireless Propag. Lett.*, vol. 12, pp. 1125-1128, 2013.

[17] T. G. Kim and B. Lee, "Metamaterial-based compact zeroth-order resonant antenna," *Electronics Letters*, vol. 45, no. 1, pp. 12-13, Jan. 2009.

[18] S. Ko and J. Lee, "Wideband folded mushroom zeroth-order resonance antenna," *IET Microw. Antennas Propag.*, vol. 7, pp. 79-84, 2013.

A Dual Frequency Monopole Antenna with Double Spurlines for PCS and Bluetooth Applications

Niwat Angkawisittpan [1*] and Apirat Siritaratiwat [2]

[1] Computational Electromagnetics and Optical Systems Research Unit (CEMOS), Faculty of Engineering
Mahasarakham University, Kantarawichai, Maha Sarakham 44150, Thailand
niwat.a@msu.ac.th*

[2] Department of Electrical Engineering, Faculty of Engineering
Khon Kaen University, Muang, Khon Kaen 40002, Thailand

Abstract ─ Design of a simple and compact dual frequency monopole antenna for applications in PCS (Personal Communication System) and Bluetooth system is presented. The first operating frequency is achieved from a traditional monopole antenna structure for the frequency of 1.9 GHz for PCS application while the second operating frequency is obtained from two spurline structures etched on the traditional monopole antenna structure for the frequency of 2.4 GHz for Bluetooth application. Both simulated and experimental results, such as reflection coefficients and VSWR (Voltage Standing Wave Ratio), are presented and discussed. The radiation pattern measurements are also performed. From the measured results, the first operating band covers between 1.851 and 1.98 GHz, and the second operating band covers between 2.28 and 2.53 GHz. The proposed antenna is compact and suitable to be used for applications in the PCS and Bluetooth system.

Index Terms ─ Double spurlines, dual frequency, monopole antennas.

I. INTRODUCTION

Printed antennas have become popular since the last decade. The design of printed antennas has received the attention of communication research community due to their applications in wireless communications and their major advantages such as low profile, ease of manufacture, low manufacturing cost, light weight, and compatibility with monolithic microwave integrated circuits (MMICs) [1-11], etc. Modern communication systems (GPS, PCS, WLAN, RFID, Bluetooth, etc.) often require antennas with compactness and low cost. Besides, the antenna structure should be simple and the fabrication technology should be uncomplicated.

Many printed antennas are reported in the literature for wireless communications. Remarkable antenna structures among them are: dual band planar branched monopole antenna [12], internal planar monopole antenna for mobile phones [13], CPW-fed L-shaped slot planar monopole antenna for triple band operation [14], dual band CPW-fed strip-sleeve monopole antenna [15], CPW-fed dual frequency monopole antenna [16], Y-shaped planar monopole antenna [17], dual band and 9-shaped monopole antenna for RFID and WLAN applications [18], multifrequency printed antennas with metamaterial particles [19], etc. Various antenna applications require different frequency bands for their wireless communication systems. For examples, PCS requires 1.85-1.99 GHz band for communication [20]. WLAN employs the 2.4 GHz and 5.2 GHz bands [21], and the 2.3-2.55 GHz band is used for Bluetooth applications [22]. The antenna size from the aforementioned antenna designs is large and some techniques are complicated. Also, wireless communication systems (PCS, GPS, WLAN, RFID, Bluetooth, etc.) require antenna structure with low cost and compactness. Therefore, the simpler antenna design and the compact antenna size are necessary for modern communication systems such as dual band antenna systems, and ultra-wideband antenna systems, etc.

Among the microstrip filter designs, spurline is a simple structure with the smallest structure compared to other structures [23]. Spurline is a defected microstrip structure (DMS) with L-shaped slot etched in the microstrip feed line. It provides resonance property with its compact size. Examples of spurline structures in microwave devices are: microstrip spurline filter with miniaturization and electronic tuning technique [24], miniaturized bandstop filter using meander spurline and capacitively loaded stubs [25], compact microstrip bandstop filter with spurline structures covering S-band to Ku-band [26], microwave coupled line filter from spurline structures [27], and harmonic suppression of microstrip ring resonator using double spurlines [28], etc.

In this paper, a novel approach to achieve a compact dual band printed monopole antenna is introduced. The

Submitted On: July 13, 2015
Accepted On: May 22, 2016

attributes of compact size and resonance property of spurline structures are applied to the conventional printed monopole antenna for designing a novel compact dual band monopole antenna. The proposed monopole antenna can be tuned to completely operate in the following bands of PCS application (1.9 GHz) and Bluetooth communication system (2.4 GHz). The proposed antenna is simulated using an in-house Finite-Difference Time-Domain (FDTD) technique for reflection coefficients. Then, the VSWR is calculated from the reflection coefficients. The experimental results of the fabricated antenna prototype are presented and compared with the simulated results. The radiation pattern measurements of the proposed antenna are also performed.

This paper is organized as follows. In Section 2, an explanation on the design of the novel compact dual frequency monopole antenna is given. The results are presented and discussed in Section 3 followed by the conclusions in Section 4.

II. ANTENNA DESIGN

In the antenna design, FDTD is used to simulate our antenna design. FDTD is a simple electromagnetic simulation tool used to analyze the antenna from the time-dependent Maxwell's equations. The details of FDTD technique are available in [29]. FDTD's code is created using FORTRAN language.

A sketch of the spurline structure on microstrip line is shown in Fig. 1 (a) [23]. Usually, the narrow line provides the inductance (L) while the slot gap exhibits the capacitance (C) [25]. A simple circuit model with a parallel RLC circuit is shown in Fig. 1 (b). The radiation effect and loss are represented by a resistor (R). The resonant characteristics are modeled by L and C. Based on the transmission line theory [25], the circuit parameters can be determined using the following equations:

$$R = 2Z_0\left(\frac{1}{|S_{21}|} - 1\right), \tag{1}$$

$$C = \frac{\sqrt{0.5(R + 2Z_0)^2 - 4Z_0^2}}{2.83\pi Z_0 R \Delta f}, \tag{2}$$

$$L = \frac{1}{(2\pi f_0)^2 C}, \tag{3}$$

where Z_0 is the 50 Ω characteristic impedance of the transmission line, f_0 is the resonant frequency, S_{21} is the transmission coefficient at the resonant frequency, and Δf is the -3 dB bandwidth of S_{21}. Due to the resonance obtained from the spurline structure and the compactness of the structure, the spurline structure is employed to design the proposed antenna.

The radiating element of the proposed antenna is designed by using the conventional monopole antenna theory for the first frequency band at 1.9 GHz for PCS, and then the second frequency band at 2.4 GHz for bluetooth application is designed by adding the spurline structures to the conventional monopole antenna.

The initial design for the first frequency band is designed with the length of one quarter wavelength at the frequency of 1.9 GHz. The initial length is 39.5 mm. The antenna is fabricated on an ARLON AD260A dielectric substrate of thickness of 1 mm, relative permittivity of 2.60, and loss tangent of 0.0017 [30]. The antenna is fed by a 50-microstrip line of length of 15 mm (G) and width of 2.8 mm (W_f). The second frequency band is designed with spurline structures etched on the conventional monopole antenna. The length of the spurline structures is equal to 24.5 mm (L2), one quarter wavelength at the frequency of 2.4 GHz.

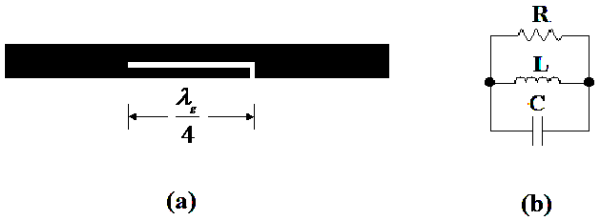

Fig. 1. Sketch of a spurline structure on a microstrip line and its RLC equivalent circuit.

After the proposed antenna is initially designed, its dimensions are optimized to obtain the operating frequencies of 1.9 GHz and 2.4 GHz. The geometrical configuration of the proposed antenna is shown in Fig. 2. The geometrical parameters are carefully adjusted and the proposed antenna dimensions are finally obtained. The prototype of the antenna is fabricated using the printed circuit board etching technology following the parameters given in Table 1. A photograph of the proposed antenna is shown in Fig. 3.

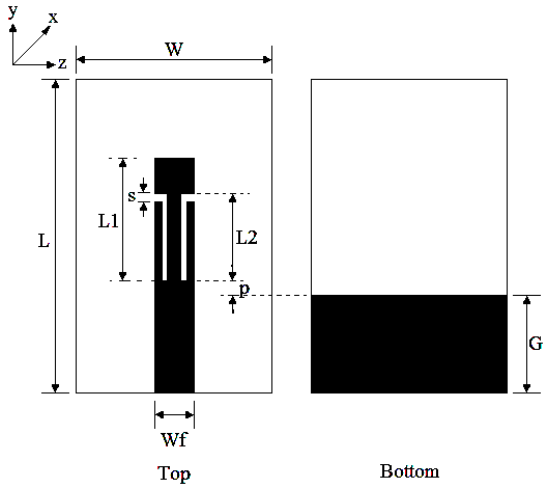

Fig. 2. Sketch of the proposed antenna.

Table 1: Dimensions of the proposed antenna

Parameters	W	L	G	W_f	L1	L2	s	p
Value (mm)	30	60	15	2.8	30	24.5	0.5	2

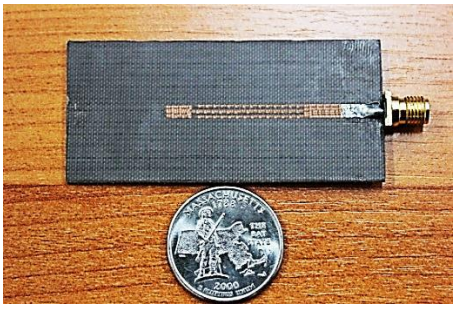

Fig. 3. A photograph of the proposed antenna.

III. RESUTS AND DISCUSSIONS

Figure 4 shows the simulated and measured reflection coefficients (S_{11}) against frequency for the proposed monopole antenna. It is quite clear that there are two resonant frequencies at 1.9 GHz and 2.4 GHz from the results. The reflection coefficient measurements are performed using the Agilent HP-E5071B vector network analyzer. The measured lower resonant mode achieves a -10 dB impedance bandwidth of ranging from 1.851 GHz to 1.98 GHz with respect to the center frequency of 1.915 GHz, and the measured upper resonant impedance bandwidth ranges from 2.28 GHz to 2.53 GHz with respect to the center frequency of 2.38 GHz. From the graph, it is clearly seen that the measured results for the proposed antenna are in good agreement with the simulated results.

The VSWR of the proposed antenna is obtained through the FDTD simulations and the experimental measurements. As shown in Fig. 5, the measured VSWR are in good agreement with the simulated VSWR. The simulated and measured VSWRs achieve a 1:2 ranging from 1.85 GHz to 1.98 GHz for the first resonant frequency and ranging from 2.28 GHz to 2.53 GHz for the second resonant frequency.

The far-field range is the minimum distance that reduces the phase variation across the proposed antenna enough to obtain a good radiation pattern for the antenna. The far-field radiation patterns for the proposed monopole antenna are also examined as the following setup in Fig. 6. The distance between the horn antenna and the proposed antenna is 25 cm. The measured radiation patterns of the proposed monopole antenna at 1.9 GHz and 2.4 GHz are illustrated in Fig. 7 and Fig. 8, respectively. It is noticed that the proposed antenna exhibits a traditional dipole antenna pattern at Y-Z plane, and an omni-directional pattern at the X-Z plane for both resonant frequencies.

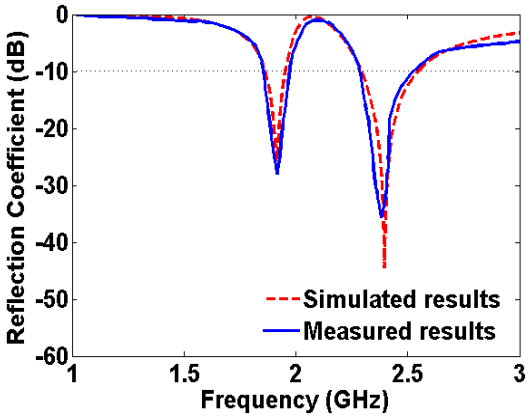

Fig. 4. Reflection coefficients of the proposed antenna.

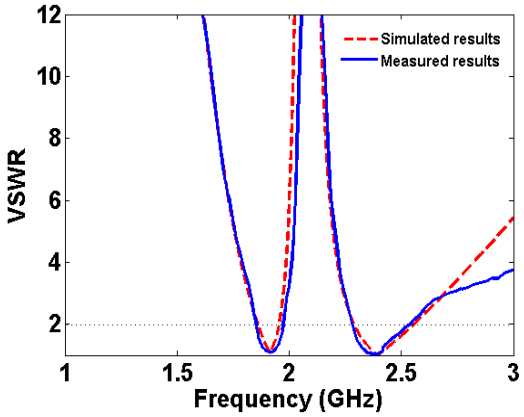

Fig. 5. VSWR of the proposed antenna.

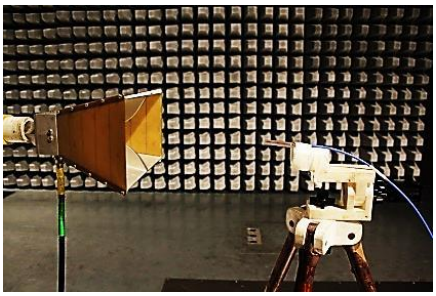

Fig. 6. Radiation pattern measurement setup.

Figure 7 plots the measured radiation patterns of the proposed antenna at 1.9 GHz with the measured antenna gain of 2.11 dBi, while Fig. 8 illustrates the measured radiation patterns of the proposed antenna at 2.4 GHz with the measured antenna gain of 2.15 dBi.

The size of the proposed antenna is compared with other antennas in Table 2. From Table 2, it is found that the size of the proposed antenna is smaller than other antennas.

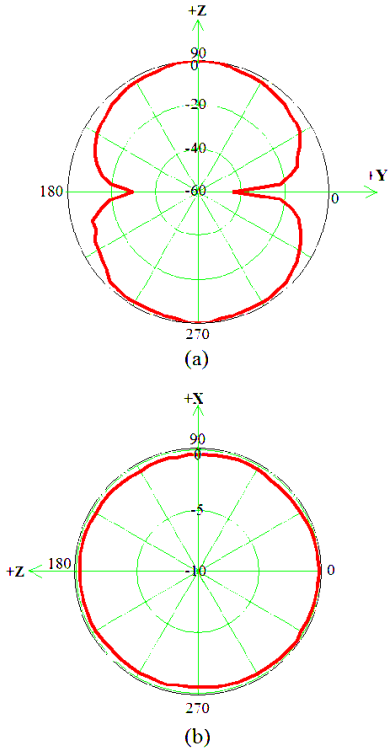

Fig. 7. Radiation patterns of the proposed antenna at 1.9 GHz: (a) Y-Z plane and (b) X-Z plane.

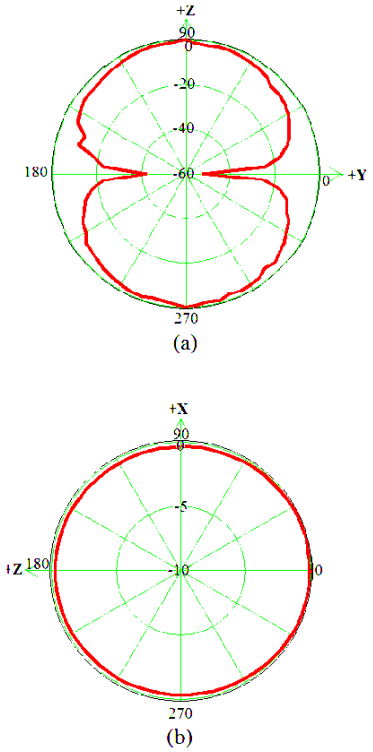

Fig. 8. The Radiation patterns of the proposed antenna at 2.4 GHz: (a) Y-Z plane and (b) X-Z plane.

Table 2: Size comparison for antennas

Antenna	Overall Dimension	Operating Frequency (GHz)
Antenna in [13]	40 mm x 65 mm	1.8
Antenna in [14]	57 mm x 68 mm	0.9, 1.87, 2.18
Antenna in [15]	50 mm x 110 mm	0.9, 1.8
Antenna in [16]	56 mm x 60 mm	1.80, 2.46
Proposed antenna	30 mm x 60 mm	1.9, 2.4

IV. CONCLUSION

A new design of compact dual frequency monopole antenna constructed by a traditional monopole antenna structure and two spurline structures is proposed. The lower operating frequency (1.9 GHz) is obtained from the traditional monopole antenna while the upper operating frequency (2.4 GHz) is obtained from the spurline structures etched on the traditional monopole antenna. The measured results such as reflection coefficients and VSWR are obtained and compared with the simulated results. Moreover, the radiation pattern measurements are also performed. The proposed antenna exhibits a traditional dipole antenna pattern at Y-Z plane, and an omni-directional pattern at the X-Z plane for both 1.9 GHz and 2.4 GHz. The proposed antenna covers dual bands for PCS and Bluetooth applications. The proposed antenna is simple in design and compact in size. Hence, the proposed antenna may be a suitable candidate for the dual frequency operations in PCS and Bluetooth applications. This technique can be applied to other operating frequency bands for various dual band applications.

ACKNOWLEDGMENT

This work is financially supported by the Faculty of Engineering, Mahasarakham University, Thailand. Also the author would like to thank the Electrical and Electronic Product Testing Center (PTEC), King Mongkut's Institute of Technology Ladkrabang (KMITL), Bangkok, Thailand for the assistance in the experimental measurements of the proposed antenna.

REFERENCES

[1] X. H. Jin, X. D. Huang, C. H. Cheng, and L. Zhu, "Super-wideband printed asymmetrical dipole antenna," *Progress in Electromagnetics Research Letters*, vol. 27, pp. 117-123, 2011.

[2] S. Lin, S. Luan, Y. Wang, X. Luo, X. Han, X. Q. Zhang, Y. Tian, and X. Y. Zhang, "A printed log-periodic tree-dipole antenna (Plptda)," *Progress in Electromagnetics Research M*, vol. 21, pp. 19-32, 2011.

[3] J. R. Panda and R. S. Kshetrimayum, "A printed 2.4GHz/5.8GHz dual-band monopole antenna with a protruding stub in the ground plane for WLAN and RFID applications," *Progress in Electro-*

magnetics Research, vol. 117, pp. 425-434, 2011.

[4] S. Papantonis and E. Episkopou, "Compact dual band printed 2.5-shaped monopole antenna for WLAN applications," *Progress in Electromagnetics Research C*, vol. 24, pp. 57-68, 2011.

[5] I. T. Tang, C. M. Li, and C. Y. Lin, "Printed dipole antenna with back to back asymmetric dual-C shape uniform strips for Dtv applications," *Progress in Electromagnetics Research C*, vol. 22, pp. 73-83, 2011.

[6] M. Abu, M. K. A. Rahim, O. B. Ayop, and F. Zubir, "Triple-band printed dipole antenna with single-band Amc-His," *Progress in Electromagnetics Research B*, vol. 20, pp. 225-244, 2010.

[7] Y. S. Hu, M. Li, G. P. Gao, J. S. Zhang, and M. K. Yang, "A double-printed trapezoidal patch dipole antenna for UWB applications with band-notched characteristic," *Progress in Electromagnetics Research*, vol. 103, pp. 259-269, 2010.

[8] T. Sedghi, V. Rafii, and M. Moosazadeh, "UWB monopole antenna with compact polygon-shaped patch for portable devices," *Applied Computational Electromagnetics Society Journal*, vol. 29, no. 1, pp. 67-70, 2014.

[9] M. Naser-moghadasi and S. F. Qotolo, "A novel switchable double band-notch antenna for ultra-wideband application," *Applied Computational Electromagnetics Society Journal*, vol. 29, no. 10, pp. 763-770, 2014.

[10] B. Heydari, Z. Sanaati, V. Waladi, and Y. Zehforoosh, "A novel fractal monopole antenna with wide bandwidth enhancement for UWB applications," *Applied Computational Electromagnetics Society Journal*, vol. 29, no. 11, pp. 923-927, 2014.

[11] N. Ojaroudi, M. Ojaroudi, and N. Ghadimi, "UWB monopole antenna with WLAN frequency band-notched performance by using a pair of E-shaped slits," *Applied Computational Electromagnetics Society Journal*, vol. 28, no. 12, pp. 1244-1249, 2013.

[12] M. N. Suma, R. K. Raj, M. Joseph, P. C. Bybi, and P. Mohanan, "A compact dual band planar branched monopole antenna for DCS/2.4-GHz WLAN applications," *IEEE Microwave and Wireless Components Letters*, vol. 16, no. 5, pp. 275-277, 2006.

[13] C. A. Shen and K. H. Lin, "A broadband internal planar monopole antenna for mobile phone," *Microwave and Optical Technology Letters*, vol. 48, no. 4, pp. 768-769, 2006.

[14] W. C. Liu and C. C. Huang, "A CPW-fed L-shaped slot planar monopole antenna for triple-band operations," *Microwave and Optical Technology Letters*, vol. 44, no. 6, pp. 510-512, 2005.

[15] C. H. Cheng, W. J. Lv, Y. Chen, and H. B. Zhu, "A dual-band strip-sleeve monopole antenna fed by CPW," *Microwave and Optical Technology Letters*, vol. 42, no. 1, pp. 70-73, 2004.

[16] H. D. Chen and H. T. Chen, "A CPW-fed dual-frequency monopole antenna," *IEEE Transactions on Antennas and Propagation*, vol. 52, no. 4, pp. 978-982, 2004.

[17] J. S. Mandeep and T. C. How, "Design of a dual monopole antenna with wideband frequency," *Progress in Electromagnetics Research C*, vol. 3, pp. 119-128, 2008.

[18] J. R. Panda, A. S. R. Saladi, and R. S. Kshetrimayum, "A compact printed monopole antenna for dual-band RFID and WLAN applications," *Radio-engineering*, vol. 20, no. 2, pp. 464-467, 2011.

[19] D. Segovia-vargas, F. J. Herraiz-martinez, E. Ugarte-munoz, J. Montero-de-paz, V. Gonzalez-posadas, and L. E. Garcia-munoz, "Multifrequency printed antennas loaded with metamaterial particles," *Radioengineering*, vol. 18, no. 2, pp. 129-143, 2009.

[20] C. Mahatthanajatuphat, S. Saleekaw, P. Akkaraekthalin, and M. Krairiksh, "A rhombic patch monopole antenna with modified Minkowski fractal geometry for UMTS, WLAN, and Mobile WIMAX application," *Progress in Electro-magnetics Research*, vol. 89, pp. 57-74, 2009.

[21] W. Ren, "Compact dual-band slot antenna for 2.4/5 GHz WLAN applications," *Progress in Electro-magnetics Research B*, vol. 8, pp. 319-327, 2008.

[22] P. C. Ooi and K. T. Selvan, "A dual-band circular slot antenna with an offset microstrip-fed line for PCS, UMTS, IMT-2000, ISM, Bluetooth, RFID and WLAN applications," *Progress in Electro-magnetics Research Letters*, vol. 16, pp. 1-10, 2010.

[23] R. N. Bates, "Design of microstrip spur-line band-stop filters," *IEE Journal on Microwave, Optics and Acoustics*, vol. 1, no. 6, pp. 209-214, 1977.

[24] M. Chongcheawchamnan, M. F. Shafique, and I. D. Robertson, "Miniaturisation and electronic tuning techniques for microstrip spurline filters," *IET Microwaves, Antennas and Propagation*, vol. 5, no. 1, pp. 1-9, 2011.

[25] H. Liu, R. H. Knoechel, and K. F. Schuenemann, "Miniaturized bandstop filter using meander spurline and capacitively loaded stubs," *ETRI Journal*, vol. 29, no. 5, pp. 614-618, 2007.

[26] K. Singh and K. Nagachenchaiah, "Very wideband, compact microstrip bandstop filter covering S-band to Ku-band," *International Journal of Microwave Science and Technology*, vol. 2010, pp. 1-4, 2010.

[27] J. R. Loo-yau, O. I. Gomez-pichardo, and F. Sandoval-ibarra, "Spurline structures and its application on microwave coupled line filter,"

Revista Mexicana De Fisica, vol. 57, no. 3, pp. 184-187, 2011.

[28] N. Angkawisittpan, "Harmonic suppression of microstrip ring resonator using double spurlines," *International Journal of the Physical Sciences*, vol. 7, no. 1, pp. 31-36, 2012.

[29] A. Taflove and S. Hagness, *Computational Electrodynamics: The Finite-Difference Time-Domain Method*. 2nd ed., Norwood: Artech House, 2000.

[30] Arlon Electronic Materials Division, Rancho Cucamonga, CA, USA.

Niwat Angkawisittpan was born in Khon Kaen, Thailand. He received his B.Eng. in Electrical Engineering with honors from Khon Kaen University, Thailand in 1997. He received his M.Sc. in Electrical & Computer Engineering from Purdue University, Indiana, USA in 2003. Also he received his Ph.D. in Electrical Engineering from University of Massachusetts Lowell, Massachusetts, USA in 2009. Since 2009, he has been with the Department of Electrical Engineering, Faculty of Engineering, Mahasarakham University, Maha Sarakham, Thailand as a Lecturer. He has authored or co-authored a number of papers in scientific journals and conference proceedings. His research interests include compact microstrip devices, Metamaterial applications for RF and microwave circuits, and electromagnetic material characterization.

Apirat Siritaratiwat received his B.Eng. (EE) from Khon Kaen University in 1992. After working in the industry for few years, he joined the Department of Electrical Engineering, Khon Kaen University in 1994 and continued his post-graduate study at the University of Manchester, UK, between 1995-1999. He has served in many managerial positions such as Head of Department, Assistant to President for Research Affairs, etc. He has done researches in HDD and been one of pioneer researchers of ESD/EOS and EMI in recording heads. Since his researches are mainly jointed with HDD industry, it leaded to the establishment of the KKU-Seagate Cooperation Research Laboratory and the I/U CRC in HDD Component where he was Director. He has published more than 80 articles and held 4 pending patents.

Full-Wave Analysis of Indoor Electromagnetic Pollution from Base-Station Antennas

Xunwang Zhao, Zhongchao Lin, Huanhuan Zhang, Sio-Weng Ting, and Yu Zhang

School of Electronic Engineering
Collaborate Innovation Center of Information Sensing and Understanding
Xidian University, Xi'an, Shaanxi 710071, China
zhanghuanajkd@outlook.com, xdzxw@126.com

Abstract ─ Three-dimensional (3D) intricately detailed models for base-station antennas and buildings are created. Indoor radiation from antennas is accurately analyzed using the higher-order basis functions (HOBs) in the context of method of moments (MoM). The use of HOBs reduces the number of unknowns in MoM compared with the use of piecewise Rao-Wilton-Glisson basis functions (RWGs). To significantly improve the capability of MoM, an efficient parallel algorithm is developed based on a block-cyclic matrix distribution scheme. Taking radiation power, main-beam pointing and materials into account, the electric-field distribution inside buildings is simulated to determine the indoor radiation level, which may be beyond the safety limit. The numerical results are verified through comparison with the measured results.

Index Terms ─ Base-station antennas, buildings, radiation safety, method of moments, parallel technique.

I. INTRODUCTION

More and more base stations for mobile communication systems are built to achieve better signal coverage, as shown in Fig. 1. On the other hand, the strength of electromagnetic field from base stations can be too strong to exceed the safety limit, which is referred to as electromagnetic pollution. It is an electromagnetic compatibility (EMC) problem becoming a matter of concern for more and more people. Therefore, it is necessary to assess the radiation in urban buildings.

Since measurements with electromagnetic meters or other tools are costly to identify the radiation level [1, 2], the approach based on electromagnetic simulation can be applied. Moreover, the use of computational methods can calculate the field strength at a point where measurement is difficult to be undertaken. Among various methods, the ray-tracing technique is widely used for predicting channel capacity or path loss in indoor environment because this kind of high-frequency asymptotic method is low-cost in simulation of electrically large structures [3, 4]. However, as is known, it is not accurate for complex models including thin geometric structures.

Fig. 1. Base-station antennas on a building.

To obtain accurate results, full-wave methods, such as the method of moments (MoM) [5] and the finite-difference time-domain (FDTD) method [6], are also employed for indoor channel capacity [7–9]. This kind of methods requires a large amount of data regarding geometries, building locations, materials, and so on, and is computationally intensive. It is not convenient for FDTD to simulate open-region problems because FDTD needs absorbing boundary condition. Due to the high computational complexity and memory requirement, it is difficult for MoM to solve electrically large problems. Therefore, the MoM-based fast algorithm, namely multilevel fast multipole algorithm (MLFMA), has been utilized to compute electric-field (E-field) distribution in indoor environment [10]. However, since buildings contain complex structures and multiple dielectrics, low convergence or even divergence usually occurs for MLFMA.

In addition, there is a kind of empirical (statistical) methods including Hata model, COST-231-Walfisch-Ikegami model and dual-slope model. The interested readers are referred to [4, 11] for a summarization of these methods for indoor propagation. These methods are based on the statistical characterization of the received signals. They are easier to implement and require less computational effort, but less accurate than

Submitted On: March 6, 2016
Accepted On: May 27, 2016

numerical methods.

Previous works mainly deal with two-dimensional (2D) buildings and focused on channel capacity and path loss. In this paper, we use MoM with the higher-order basis functions (HOBs) to analyze indoor E-field distribution and extend full-wave analysis to 3D scenarios. The concern is the safety of indoor radiation rather than channel capacity and path loss. The high-performance parallel computing technique is utilized to greatly improve the capability of MoM. Multiple factors including radiation power, main-beam pointing and materials are taken into account to determine whether the radiation level exceeds the safety limit or not.

II. PARALLEL HIGHER-ORDER METHOD OF MOMENTS

A. Integral equations

Base-station antennas and buildings contain metallic and dielectric materials, and a general form of the Poggio–Miller–Chang–Harrington–Wu (PMCHW) formulation is utilized [12, 13], which is solved in frequency domain for equivalent electric and magnetic currents over dielectric boundary surfaces and electric currents over perfect electric conductors (PECs). The set of integral equations are solved by using MoM, specifically the Galerkin's method.

For the case when one of the two domains sharing a common boundary surface is a PEC, the magnetic currents are equal to zero at the boundary surface and therefore, the PMCHW formulation degenerates into the electric field integral equation (EFIE).

B. Higher-order basis functions

Higher-order polynomials over bilinear quadrilateral patches are used as basis functions over relatively large subdomains [12],

$$\boldsymbol{F}_{ij}(p,s) = \frac{\boldsymbol{\alpha}_s}{\left|\boldsymbol{\alpha}_p \times \boldsymbol{\alpha}_s\right|} p^i s^j,\ -1 \le p \le 1,\ -1 \le s \le 1, \quad (1)$$

where, p and s are local coordinates, i and j are orders of basis functions, and $\boldsymbol{\alpha}_p$ and $\boldsymbol{\alpha}_s$ are covariant unitary vectors. A quadrilateral patch is illustrated in Fig. 2.

The orders can be adjusted according to the electrical size of a geometric element. The orders increase as the element becomes larger. The electrical size of a geometric element can be as large as two wavelengths. Typically, the number of unknowns for HOBs is reduced by a factor of 5–10 compared with that for traditional piecewise basis functions, e.g. Rao-Wilton-Glisson basis functions (RWGs) [14], and thus the use of HOBs drastically reduces the computational amount and memory requirement. Note that the polynomials can also be used as basis functions for wire structures. In this case, truncated cones are used for geometric modeling [12].

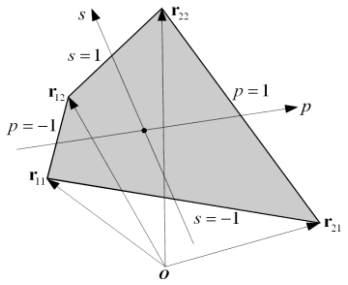

Fig. 2. Bilinear quadrilateral patch defined by four vertices with the position vectors $\boldsymbol{r}_{11}$, $\boldsymbol{r}_{21}$, $\boldsymbol{r}_{12}$ and $\boldsymbol{r}_{22}$.

C. Parallel technique

The parallel scheme for MoM is partitioning the dense complex matrix. The large dense MoM matrix is divided into a number of smaller block matrices that are nearly equal in size and distributed among all participating processes, assuming that each parallel process runs on one CPU core here. The distribution manner of the blocks is chosen appropriately according to the parallel LU decomposition solver to minimize the communication between processes. Specifically, a block-cyclic matrix distribution is used among processes. Two factors, process grid and block size, significantly affects the performance of the parallel algorithm [15]. Setting the shape of process grid $P_r \times P_c$ as square as possible, with P_c slightly larger, enables the algorithm implementation to be most efficient. The block size depends on the CPU cache size and needs to be tested on computational platforms to determine the optimum value. The typical value of the block size for modern CPUs is 128.

III. SAFETY LIMIT OF BASE-STATION RADIATION

The International Commission on Non-Ionizing Radiation Protection (ICNIRP) has defined the guideline for limiting electromagnetic radiation exposure and provided protection against known adverse health effects, which is a popular reference standard in many countries. The ICNIRP standard in the frequency range from 400 MHz to 2000 MHz is given in Table 1. According to this standard, the threshold of E-field strength at 900 MHz is 41.2 V/m corresponding to 4.5 W/m^2. An even tougher standard is adopted in China, which is 12.0 V/m corresponding to 0.4 W/m^2, as shown in Table 1.

Table 1: Threshold of radiation level

Country/Region	E-field Strength (V/m)	Power Density (W/m^2)
ICNIRP (400 MHz−2000 MHz)	$1.375\, f^{1/2}$	$f/200$
China (30 MHz−3000 MHz)	12.0	0.4

IV. ANALYSIS OF E-FIELD DISTRIBUTION IN BUILDINGS

A base-station antenna working at 944 MHz is created first. Then the E-field distribution generated by two base-station antennas inside a smaller apartment (denoted by Apartment I) is simulated and compared with the measured results for verification. Finally, two base-station antennas radiating E-field inside a larger apartment (denoted by Apartment II) are simulated and analyzed.

A. Modeling of the base-station antenna

The base-station antenna consists of five cross-dipole elements and a back plate, as shown in Fig. 3. The tilt angle of the dipole is ±45°. The length of each dipole is 0.168 m and the distance between two neighboring antenna elements is 0.246 m. Each dipole is excited by a delta-gap voltage source. The working frequency of the antenna is 944 MHz. The red arrows in Fig. 3 denote the locations of the sources. The radiation patterns of the antenna are simulated by the proposed higher-order MoM and the FEKO software [16]. Note that FEKO uses the traditional piecewise basis functions, such as the RWG basis functions. The number of unknowns for HOBs is 831 and that for FEKO is 4000. Since the antenna is a small model, we do not use the parallel algorithm in this simulation. The total simulation time for HOBs is 16.4 s and that for FEKO is 37.0 s. The radiation patterns of the antenna are compared in Fig. 4. The results from HOBs agree well with those from FEKO, but the number of unknowns and simulation time for HOBs are much lower. Figure 5 shows the 3D radiation pattern of the antenna that will be used in the following examples.

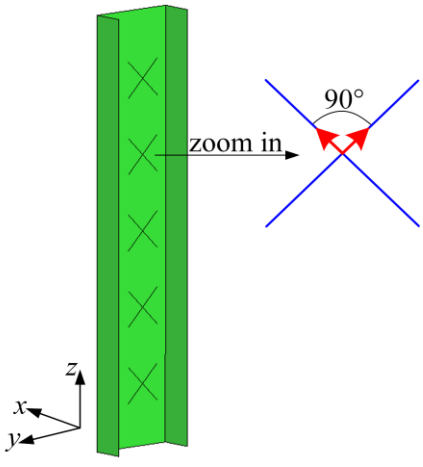

Fig. 3. Base-station antenna and its cross-dipole elements.

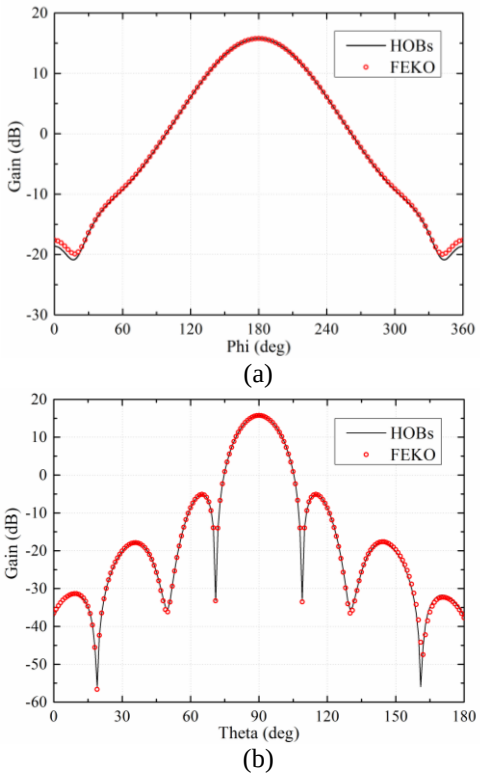

Fig. 4. Radiation patterns of the base-station antenna in: (a) the *xoy* plane and (b) the *xoz* plane.

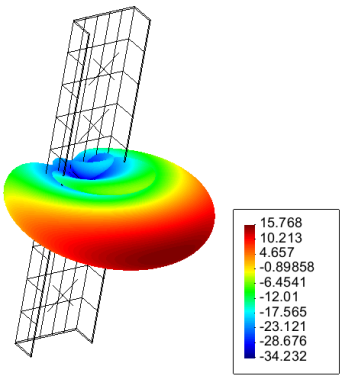

Fig. 5. 3D radiation pattern of the base-station antenna.

B. E-field distribution in Apartment I

Two base-station antennas are installed in front of an apartment denoted by Apartment I [17], which is a real building located at University of Macau. The main-lobes of the two antennas are pointed to different directions, as shown in Fig. 6 (a). In detail, the main-lobe direction of Antenna 1 is ϕ=45° and θ=90°, and that of Antenna 2 is ϕ=0° and θ=102°. The radiation power of each antenna is 365 mW. The antenna

locations and the apartment dimensions are demonstrated in Fig. 6 (b). The wall, ceiling and floor of the apartment are assumed to be homogeneous dielectrics. They are made of concrete with equivalent permittivity ε_r=3.916 and have a thickness of 0.2 m. The thickness of the door and windows, which are made of glass (ε_r=2.37), is 0.012 m.

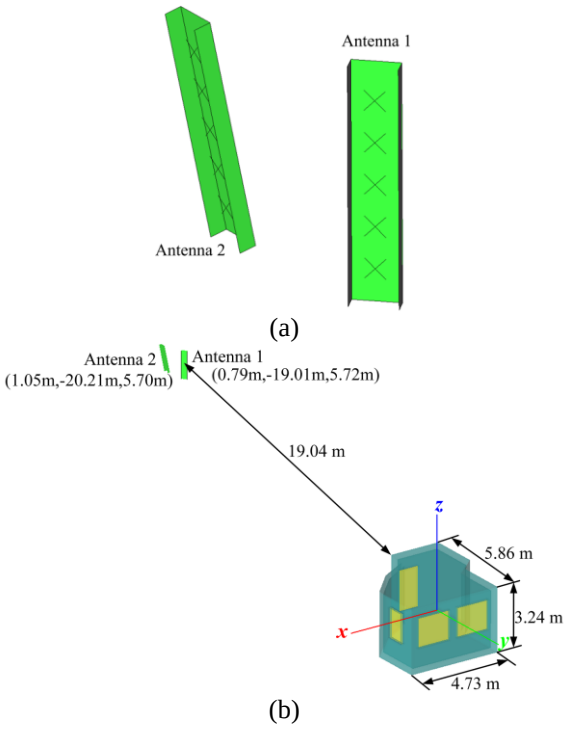

Fig. 6. Two base-station antennas in front of Apartment I: (a) two base-station antennas with different main-beam directions and (b) locations of the base-station antennas and dimensions of Apartment I. The wall, ceiling and floor of the apartment are in dark green color, and the door and windows in yellow color.

The number of unknowns for this model is 311,261. The computing platform used in this simulation is the Magic Cube with 1450 nodes at Shanghai Supercomputer Center (SSC), and each node has four quad-core 1.9 GHz processors and 64 GB memory (http://www.ssc.net.cn/en/ resources_1.aspx). The total simulation time is about 11.8 hours when 512 CPU cores are used and the memory required is about 1.4 TB. The radiation pattern and E-field distribution are shown in Fig. 7. The E-field at four points inside the apartment is compared with the measured results, as listed in Table 2. The tool for measurement was a mobile phone installed with a commercial mobile network measurement software called NEMO [18]. From comparison, it is observed that the computed and measured fields agree with each other.

It can be seen from Fig. 7 that the maximum value of E-field strength is approximately 1.4 V/m, which is below both the ICNIRP and China standards. There are several factors that affect the indoor radiation level: (1) radiation power of antennas, (2) gain of antennas, (3) distance between antennas and buildings and (4) materials of buildings. In this simulation, the radiation power is low and the main lobe is not directly pointed to the apartment, and therefore, the indoor radiation is weak.

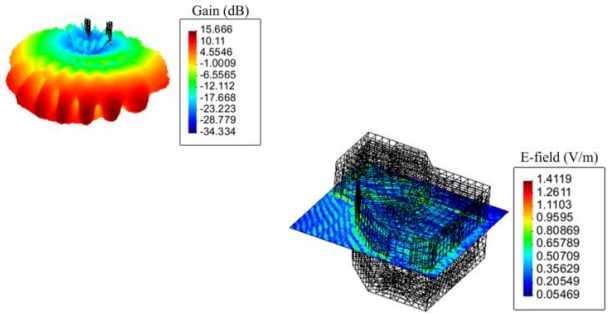

Fig. 7. Radiation pattern of the base-station antennas and the E-field distribution on a cut-plane at a height of 1.70 m inside and around Apartment I.

Table 2: Comparison of simulated and measured E-field in Apartment I

Location (m)	Simulation (V/m)	Measurement (V/m)
(3.24, 2.98, 1.70)	0.38	0.536
(4.55, 4.47, 1.70)	0.34	0.393
(1.75, 4.36, 1.70)	0.45	0.474
(1.09, 1.69, 1.70)	0.88	0.927

C. E-field distribution in Apartment II

Consider two base-station antennas in front of a larger apartment denoted by Apartment II. The distance between the two antenna centers is 1.28 m and both the antennas are tilted 12° in the vertical plane, as shown in Fig. 8 (a). The radiation power of each antenna is 10 W, which is much higher than that in last section. The locations of the antennas and the dimensions of the apartment are demonstrated in Fig. 8 (b). The thickness of the wall, ceiling and floor is 0.16 m, and that of the door and windows is 0.003 m. The dielectric permittivity of the apartment is the same as that in last section, but the conductivity of the wall, ceiling and floor is set as 0.002 S/m.

The number of unknowns is 1,179,986, which is challenging for MoM. To facilitate the simulation, we set the *xoz* plane as a symmetry plane and the number of unknowns is reduced by half. The computing cluster used here has 136 nodes at Xidian University, and each

node has two 12-core 2.2 GHz processors and 64 GB memory. The total simulation time is about 6 hours when 2400 CPU cores are used and the memory required is about 5.1 TB.

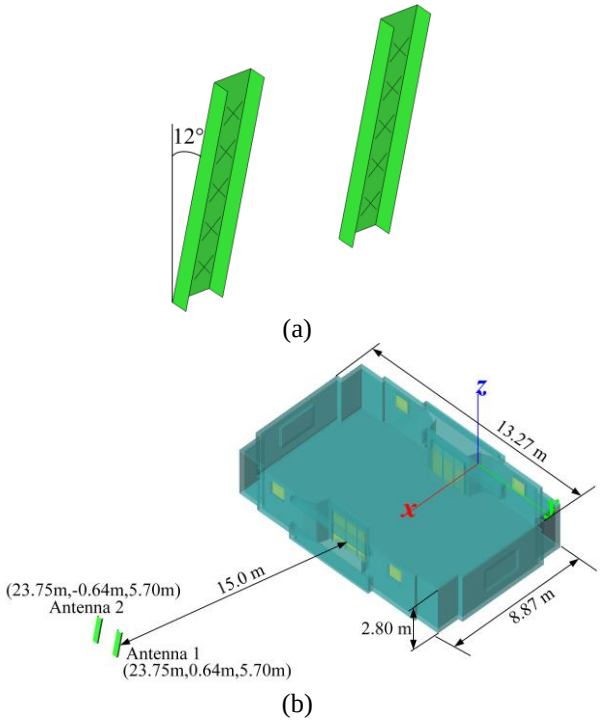

Fig. 8. Two base-station antennas in front of Apartment II: (a) attitude of the two base-station antennas and (b) locations of the base-station antennas and dimensions of Apartment II. The wall, ceiling and floor of the apartment are denoted in dark green color, and the doors and windows in yellow color.

The radiation pattern and E-field distribution are shown in Fig. 9. It is obvious that the maximum value of E-field strength is nearly 26 V/m, which is still below the ICNIRP standard. However, it is higher than twice the China standard.

To reduce the E-field strength inside Apartment II, a simple approach is to reduce the radiation power of antennas. However, it would reduce the signal coverage of base stations. Instead, we change the main-lobe directions by rotating the antennas in the azimuth plane, which is equivalent to the reduction of the antenna gain. As shown in Fig. 10, the angle is denoted by α. We consider three different azimuth angles that are 15°, 30°, and 45°. The E-field distribution is given in Fig. 11. As expected, the E-field strength inside the apartment decreases with increase of α. When α is 45°, the maximum value of E-field strength reaches the critical value of 12 V/m.

Due to the fact that many buildings are constructed of reinforced concrete, larger conductivities, namely 0.01 S/m and 0.1 S/m, are considered for the wall, ceiling and floor. Take the angle of 45° for example, the E-field distribution is shown in Fig. 12. It is obvious that the E-field strength also decreases with increase of conductivity and the maximum value of E-field strength goes down below 12 V/m.

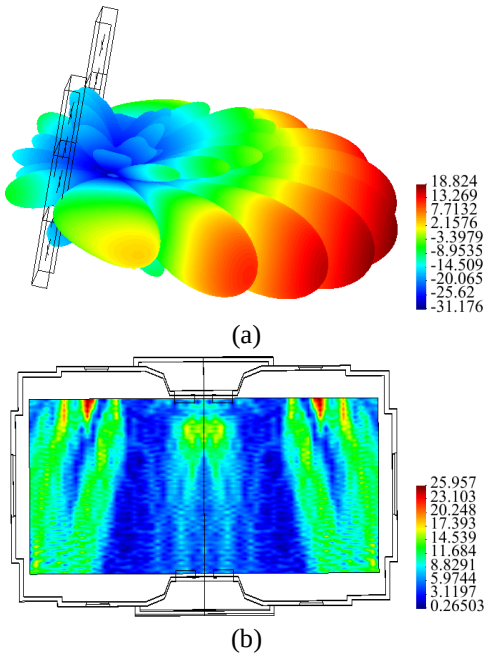

Fig. 9. Radiation pattern of the base-station antennas (a) and the E-field distribution on a cut-plane at a height of 1.70 m inside Apartment II (b).

Fig. 10. Main-lobe directions of base-station antennas in the *xoy* plane.

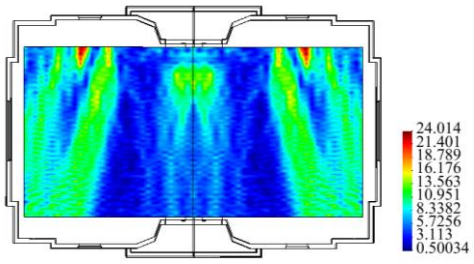

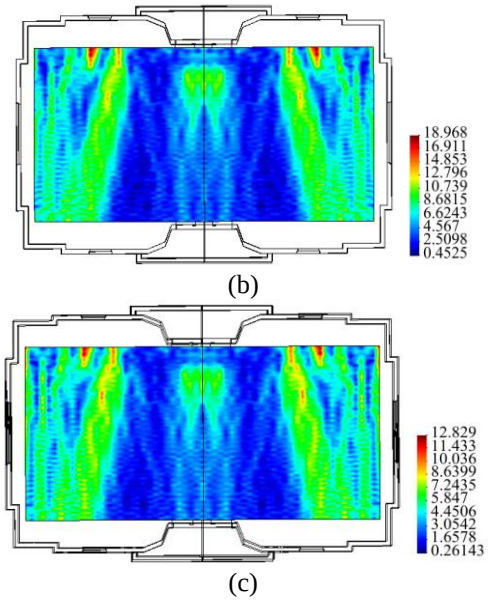

Fig. 11. E-field distribution generated by two base-station antennas with the azimuth angle of: (a) 15°, (b) 30° and (c) 45°. The cut-plane is at a height of 1.70 m inside Apartment II.

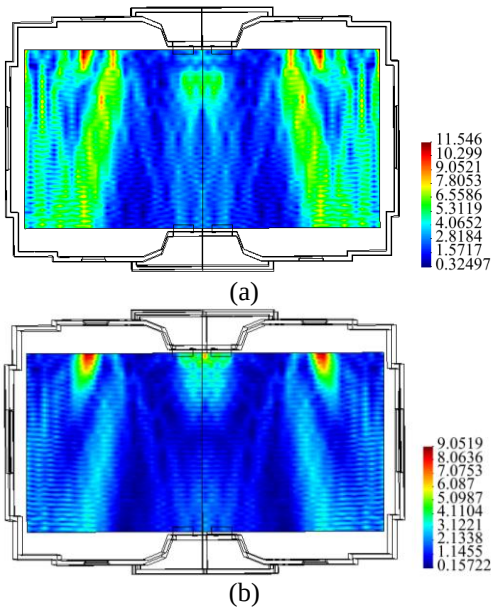

Fig. 12. E-field distribution generated by two base-station antennas with the conductivities of: (a) 0.01 S/m and (b) 0.1 S/m for the wall, ceiling and floor. The cut-plane is at a height of 1.70 m inside Apartment II.

V. CONCLUSION

We propose a parallel higher-order method of moments for assessing the indoor radiation level. The electric-field distribution is simulated inside three-dimensional buildings and the accuracy of the numerical simulations is confirmed by the measurements. Because different radiation safety standards are adopted in the world, one should use the local standard for assessment. The future work will focus on the improvement of the proposed method to simulate larger models, such as the electric-field distribution in a tall building.

ACKNOWLEDGMENT

This work is supported by the NSFC (61301069), the program for New Century Excellent Talents in University of China (NCET-13-0949), the Fundamental Research Funds for the Central Universities (JB160218), and the National High Technology Research and Development Program of China (863 Program) (2012AA01A308).

REFERENCES

[1] A. Bamba, W. Joseph, J. B. Andersen, E. Tanghe, G. Vermeeren, D. Plets, J. O. Nielsen, and L. Martens, "Experimental assessment of specific absorption rate using room electromagnetics," *IEEE Trans. Electromagn. Compat.*, vol. 54, no. 4, pp. 747-757, August 2012.

[2] O. Cerezci1, A. Y. Citkaya, S. S. Seker, and Z. S. Citkaya, "Determination of the electromagnetic pollution in a district and recommendations to decrease exposure levels," in *30th Annual Review of Progress in Applied Computational Electro-magnetics*, Jacksonville, USA, , pp. 697-702, 23-27 March 2014.

[3] K. A. Remley, H. R. Anderson, and A. Weisshar, "Improving the accuracy of ray-tracing techniques for indoor propagation modeling," *IEEE Trans. Veh. Technol.*, vol. 49, no. 6, pp. 2350-2358, November 2000.

[4] N. Tran-Minh and T. Do-Hong, "Application of raytracing technique for predicting average power distribution in indoor environment," in *Second International Conference on Communications and Electronics*, Hoi an, Vietnam, pp. 121-125, 4-6 June 2008.

[5] R. F. Harrington, *Field Computation by Moment Methods*, in IEEE Series on Electromagnetic Waves. New York: IEEE, 1993.

[6] K. S. Yee, "Numerical solution of initial boundary value problems involving Maxwell's equations in isotropic media," *IEEE Trans. Antennas Propag.*, vol. 14, no. 3, pp. 302-307, May 1966.

[7] A. Alighanbari and C. D. Sarris, "Parallel time-domain full-wave analysis and system-level modeling of ultrawideband indoor communication systems," *IEEE Trans. Antennas Propag.*, vol. 57, no. 1, pp. 231-240, January 2009.

[8] X. P. Yang, Q. Chen, and K. Sawaya, "Numerical analysis of wall effect on indoor MIMO channel capacity by using MoM-FDTD hybrid technique,"

in *Proc. IEEE Antennas Propag. Soc. Int. Symp.*, Albuquerque, USA, pp. 2979-2982, 9-14 July 2006.

[9] V. Pham-Xuan, I. Kavanagh, M. Condon, and C. Brennan, "On comparison of integral equation approaches for indoor wave propagation," in *IEEE-APS Topical Conference on Antennas and Propagation in Wireless Communications (APWC)*, Aruba, pp. 796-799, 3-9 August 2014.

[10] J. Fostier and F. Olyslager, "An asynchronous parallel MLFMA for scattering at multiple dielectric objects," *IEEE Trans. Antennas Propag.*, vol. 56, no. 8, pp. 2346-2355, August 2008.

[11] Ç. Kurnaz, "An empirical modeling of electromagnetic pollution on a university campus," *ACES Express Journal*, vol. 1, no. 2, pp. 76-79, February 2016.

[12] Y. Zhang and T. K. Sarkar, *Parallel Solution of Integral Equaton Based EM Problems in the Frequency Domain*. Hoboken, NJ: Wiley, 2009.

[13] B. M. Kolundzija and A. R. Djordjevic, *Electromagnetic Modeling of Composite Metallic and Dielectric Structures*. Norwood: Artech House, 2002.

[14] S. M. Rao, D. R. Wilton, and A. W. Glisson, "Electromagnetic scattering by surfaces of arbitrary shape," *IEEE Trans. Antennas Propag.*, vol. 30, no. 3, pp. 409-418, May 1982.

[15] Y. Zhang, Z. Lin, X. Zhao, and T. K. Sarkar, "Performance of a massively parallel higher-order method of moments code using thousands of CPUs and its applications," *IEEE Trans. Antennas Propag.*, vol. 62, no. 12, pp. 6317-6324, December 2014.

[16] http://www.feko.info/

[17] C. K. Chio, S.-W. Ting, X. W. Zhao, T. K. Sarkar, Y. Zhang, and K.-W. Tam, "Prediction model for radiation from base-station antennas using electromagnetic simulation," in *Proc. of Asia-Pacific Microwave Conference*, Kaohsiung, Taiwan, pp. 1082-1084, 4-7 December 2012.

[18] http://www.anite.com/businesses/network-testing

Palladium Decorated SWCNTs Sensor for Detecting Methane at Room Temperature Based on UWB-RFID

Jian Liu and Ping B. Li

School of Communication and Information Engineering
Xi'an University of Science and Technology, Xi'an, 710054, China
liujian2@xust.edu.cn, lbp90128@xust.edu.cn

Abstract ─ A chipless sensor in the protocol of ultra wideband radio frequency identification (UWB-RFID) is proposed in the paper. This sensor, used to detect methane at room temperature, is configured by a planar patch antenna plus a U slot on which interdigitated fingers electrodes (IDE) with load of palladium decorated single walled carbon nanotubes (Pd-SWCNTs) are embedded. The sensor can cover the entire UWB spectrum except for the band that produce band-gap. The amplitudes and frequencies of the band-gap are designated as the signatures modulated and reflecting the status quo of methane retrieved by Pd-SWCNTs. The sensor is validated by an approximate combination of the analytical and numerical method. Results show that if the concentration of methane is increased from 0 ppm to 100 ppm at room temperature, the *identifiable sensitivity* can be achieved by -9.32 dB in terms of the scheme of the amplitude modulation of band-gap frequency; or, the *identifiable sensitivity* can be achieved by -11.30 dB in terms of the scheme of the frequency modulation of band-gap frequency.

Index Terms ─ Chipless tag, methane sensor, nano-technology, room temperature, ultra-wideband radio frequency identification (UWB-RFID).

I. INTRODUCTION

The exploration of safe and accurate method to detect methane at room temperature is a critical issue due to the fact that methane, once concentrated in air by 4%, can cause combustion, or even explosion. Some traditional methods like the catalytic beads, the metal oxides and the infrared flame ionizations are readily used to detect the concentration of methane, but they needs to consume a large amount of energy, and the required environmental temperature is usually high up to 500°C [1]. This situation is changed since the single walled carbon nanotubes (SWCNTs) was invented in 1990s. It is these sensors that are decorated by the single walled carbon nanotubes can really make detecting methane at room temperature possible [2].

Additionally, the detection of methane in the consideration of safety issue is firmly relevant to the way of contactless intrusion to the methane's molecule, the protocol of wireless communication is therefore a pivotal in this regards. Commonly, the wireless sensor networks (WSN) is an amazing choice for its longer lifetime and lower complexity, and it is more specific if the sensor node is the sort of chipless type (tag) that is nothing but to be interrogated by reader passively or semi-actively [3].

On this account, the radio frequency identification (RFID) is a more appropriate protocol for the WSN in specific for the case that all the sensors are the type of chipless tags. A few of such applications have been implemented and released in recent literatures [4-7]. However, we find that all the RFID mentioned here are the narrow band circumstances borne with narrow band characteristics, for example, the interrogation signals are the sort of standardized continuous waves. As a result, these systems are common in weakness in canceling the multipath effects; and the sensor tags are more vulnerable in fighting against narrowband and multiuser interference with lower security. So, the narrow band RFID is not regarded as a promising wireless framework for the future identification where higher level reliability for real-time identification and intensive accuracy for positioning in sub-meters level are awfully required [8].

However, this narrow band RFID could be replaced by broader band counterpart if combing RFID with the technology of ultra-wide band, known as UWB-RFID. In a UWB-RFID system, a very short pulse will take over the standard continuous wave to conduct tag interrogation. This way could make transceiver in UWB-RFID to consume less power on one hand; the other hand, it could make tags serve to positioning in accuracy of sub-meter level. Furthermore, tags in UWB-RFID perform more robustness in fighting against multipath interference and have large coverage area, low detection probability and solid security. In the meanwhile, they can be more effective in improving the accessibility of multiple channels and making interference be mitigated a great deal [9].

In theory, when a UWB-RFID uses a very short

Submitted On: September 22, 2015
Accepted On: May 3, 2016

pulse as the signal of interrogation, it will leave two types of pulses existed in the backscattering waves with one called the structural mode; and another the antenna mode. Referring to the investigations unveiled in recent literatures [10-12], we can find that almost all the tags concerned are governed solely by the antenna mode or by the spectrum of backscattering signals, few of them are purely on the structural mode even if the structural mode has been verified to be possess of less pulse deformation against the waveform of interrogation pulse, and the amplitude of structural mode is accordingly larger than that of the antenna mode [13].

So, in this paper, we propose a design of UWB-RFID chipless tag in specific for detecting methane at room temperature. The mechanism of the detection is based on the signature intended in the structural mode only. The configuration of tag is a combination of a metallic portrayed electromagnetic interface with a sensor head made from interdigitated fingers electrodes (IDE) loaded by palladium decorated single walled carbon nanotubes (Pd-SWCNTs). The performance of the tag is described by the parameter of *identifiable sensitivity* that will be defined and derived in the paper.

II. UWB-RFID SENSOR SYSTEM

A typical UWB-RFID sensor system consists of a reader and a sensor node, as shown in Fig. 1. The sensor node is the chipless type that is interrogated by reader passively or semi-actively. If the frequency is *f*, the modulus of $S_{11}(f)$ will represent the reflection coefficient of the reader antenna, $D_t(\theta_t, \emptyset_t)$ will represent the directivity of the reader antenna where θ_t and $\emptyset_t$ are the elevation and azimuth angle along which the interrogation signal is transmitted. Also shown in Fig. 1, the chipless tag consists of a sensor head and an antenna, the modulus of $S_{22}(f)$ represents the reflection coefficient of the tag antenna, $D_r(\theta_r, \emptyset_r)$ represents the directivity of the tag antenna where θ_r and $\emptyset_r$ are the elevation and azimuth angle along which the backscattering signal is received [14].

In Fig. 1, T_{rs} represents the structural mode, T_{rt} represents the antenna mode. In principle, the amplitude, frequency and time on both structural mode and antenna mode can be the candidate signatures used to convey the sensed information.

For achieving structural mode only, the load of the tag should be impedance match to the feed line. If P_t represents the power emitted by reader, P_r represents the power received by reader [15], we have:

$$\frac{P_r}{P_t} = e_t\left(1-\left|S_{11}(f)\right|^2\right)\frac{D_t(\theta_t,\phi_t)}{4\pi R_1^2} \times \sigma\frac{\lambda^2}{4\pi}\frac{D_r(\theta_r,\phi_r)}{4\pi R_2^2}e_r\left(1-\left|S_{22}(f)\right|^2\right), \tag{1}$$

where e_t and e_r are the loss coefficients that are associated with the performance of insertion loss and antenna efficiency. R_1 is the distance from reader to tag, R_2 is the reverse distance from tag and reader, λ is the wavelength, σ is the radar cross section (RCS).

For simplicity, the antenna in reader is same for transmission and reception, and it is also polarization matching to the tag antenna. R_1 is equal to R_2 denoted by R, $D_t(\theta_t, \emptyset_t)$ is equal to $D_r(\theta_r, \emptyset_r)$, then the structural mode $Y_S(f)$ is approximated to:

$$\begin{aligned} Y_S(f) \approx X(f)&\sqrt{\left(1-\left|S_{11}(f)\right|^2\right)} \\ &\times\sqrt{e_tD_t(\theta_t,\phi_t)}\frac{1}{\sqrt{4\pi}R}e^{-2j\pi f\frac{Rt}{c}} \\ &\times\sqrt{\sigma}\frac{c}{\sqrt{4\pi}|f|}\sqrt{e_rD_r(\theta_r,\phi_r)}\frac{1}{\sqrt{4\pi}R}e^{-2j\pi f\frac{Rt}{c}} \\ &\times\sqrt{\left(1-\left|S_{22}(f)\right|^2\right)}, \end{aligned} \tag{2}$$

where $X(f)$ is the pulse transmitted by reader in the domain of frequency, *c* is the wave velocity in free space.

The above equation can be rewritten as:

$$\begin{aligned} Y_S(f) \approx X(f)&\eta_T\sqrt{\left(1-\left|S_{11}(f)\right|^2\right)}H_F(f) \\ &\times\eta_L H_R(f)A(f)\eta_R\sqrt{\left(1-\left|S_{22}(f)\right|^2\right)}, \end{aligned} \tag{3}$$

where $\eta_T = \sqrt{e_tD_t(\theta_t,\phi_t)}$, $\eta_R = \sqrt{e_rD_r(\theta_r,\phi_r)}$, $H_F(f) = H_R(f) = (1)/(\sqrt{4\pi}R)e^{-2j\pi f(R)/(c)t}$, and $\eta_L = \sqrt{\sigma}$. The effective aperture of the antenna is $A(f) = c/(\sqrt{4\pi}|f|)$.

In (3), η_L and $\sqrt{\left(1-\left|S_{22}(f)\right|^2\right)}$ are the terms associated with the characteristics of tag. All the variants there can be designated as the signatures used to convey the sensed information including the intended information of the tag: the status quo of concentration of methane.

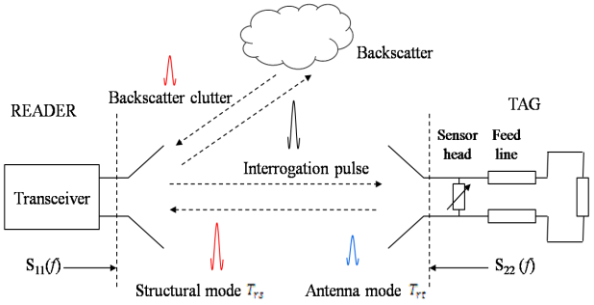

Fig. 1. The illustration of the mechanism of backscattering for the emitted pulse to interrogate chipless tag passively and semi-actively with presence of scatters.

III. UWB-RFID CHIPLESS TAG FOR DETECTING METHANE

It is evidence that the RCS σ and the reflection coefficient $|S_{22}(f)|$ are of importance to determine the

structure and the performance of the sensor tag. For chipless type, the sensor tag is usually composed of an electromagnetic interface and a sensor head. The electromagnetic interface is used to receive and backscatter the interrogation signal; however the sensor head is used to realize the specified sensing mechanism that will give the interrogation signal a kind of manipulation. So, the signatures dedicated by the electromagnetic interface should be capable of responding sensor head with a broad dynamic range so as to make tag be with of good sensitivity.

A. Electromagnetic interface

In the design, the electromagnetic interface is grown on a substrate that is a thinly filmed structure in order to facilitate geometry conformal to target object. The antenna of the electromagnetic interface is a planar patch with an arc typed edge, and the feed is micro-strip line connected by a load, as shown in Fig. 3 and Fig. 4 [16].

In the middle of the antenna plane, there is a U-slot etched to create a band-gap frequency in the backscattering spectrum [17]. The RCS $\sigma$and $|S_{22}(f)|$ are the function of the spectrum that are influenced by the depth (amplitude) and the location (frequency) of this band-gap frequency. If the signature is selected as the *amplitude* of the band-gap frequency, we define it the sensing scheme of the amplitude modulation of band-gap frequency; and if the signature is selected as the *frequency* of the band-gap frequency, we define it the sensing scheme of the frequency modulation of band-gap frequency.

Given $d(t)$ representing the function of the concentration of methane versus time, $Y_s(f)$ is the structural mode related both to the band-gap frequency *f* and $d(t)$ denoted by $Y_s[f, d(t)]$, the amplitude of band-gap frequency $Y_s[f, d(t)]$ can be expressed as:

$$Y_S[f, d(t)] \approx X(f)\eta_T\sqrt{(1-|S_{11}(f)|^2)}H_F(f) \times \eta_L[d(t)]H_R(f)A(f)\eta_R\sqrt{(1-|S_{22}[f, d(t)]|^2)}, \quad (4)$$

where $|S_{22}(f)|$ is replaced by $|S_{22}[f, d(t)]|$, indicating that the modulus of the reflection coefficient is dependent on the concentration of methane; $\eta_L = \sqrt{\sigma}$ is replaced by $\eta_L[d(t)] = \sqrt{\sigma[d(t)]}$, also indicating that the RCS is dependent on the concentration of methane.

The above equation can be rewritten as:

$$Y_S[f, d(t)] \approx X_f(f)Y_d[f, d(t)], \quad (5)$$

where $X_f(f) \approx X(f)\eta_T\sqrt{(1-|S_{11}(f)|^2)}H^2(f)A(f)\eta_R$ indicating the terms that are irrelevant to the concentration of methane. $Y_d[f, d(t)] = \eta_L[d(t)]\sqrt{(1-|S_{22}[f, d(t)]|^2)}$, indicating the terms that are really related to the concentration of methane.

At the beginning time t_0, the concentration of methane is assumed to be 0 ppm denoted by $d(t_0) = 0$. In this case, at the specified frequency *f*, there is no band-gap, the amplitude of t is $Y_d[f, d(t_0)]$. At the moment *t*, the concentration of methane is increased to $d(t)$, in this case, at the specified frequency *f*, there is band-gap, and the amplitude of the band-gap is turned to be $Y_d[f, d(t)]$. The *identifiable sensitivity* of the sensor tag in terms of the amplitude modulation of band-gap frequency is defined as:

$$S_{amp}[d(t)](dB) = 20\lg\{\frac{Y_d[f, d(t)] - Y_d[f, d_0(t)]}{Y_d[f, d_0(t)]}\}. \quad (6)$$

Similarly at the beginning t_0, the concentration of methane is 0 ppm denoted by $d(t_0) = 0$, in this case, at the specified frequency f_0, there is band-gap, the value $Y_d[f_0, d(t_0)]$ is minimum as $f_0\{Y_d[f_0, d(t_0)]_{\min}\}$. At the moment *t*, the concentration of methane is increased to $d(t)$, in this case, at the specified frequency *f*, there is band-gap, the value $Y_d[f, d(t)]$ is minimum denoted by $f\{Y_d[f, d(t)]_{\min}\}$. The *identifiable sensitivity* of the sensor tag in terms of the frequency modulation of band-gap frequency is defined as:

$$S_{freq}[d(t)](dB) = 20\lg\{\frac{f\{Y_d[f, d(t)]_{mim}\} - f_0\{Y_d[f_0, d(t_0)]_{mim}\}}{f_0\{Y_d[f_0, d(t_0)]_{mim}\}}\}. \quad (7)$$

B. Sensor head

As the characteristics of the electromagnetic interface mentioned above, the sensor head should be the kind that can control either the amplitude or the frequency of the band-gap frequency according to the data of the concentration of methane in its vicinity. However, since the molecule of the methane (CH_4) is lower in the quality of polarity, it is difficult to find an exact mechanism used to detect methane through the way of molecule absorption and desorption [18], [19] till the time that a few of innovative solutions had been reported in some recent literatures [20-22]. The most interesting contribution was dedicated by Lu *et al.* who dispersed a Pd-SWCNTs bundle onto an interdigitated finger electrodes (IDE), delivering an architecture of sensor head that is qualified for detecting methane at room temperature. When this sensor head is exposed to methane gas, the materials of Pd-SWCNTs commence to interact with the methane's molecule, the equivalent conductance of the Pd-SWCNTs and the corresponding current across IDE electrodes as results can be changed with the change of the concentration of methane. The curve plotted in Fig. 2 shows that the current will be increased from 1.80 mA to 1.91 mA when the the concentration of methane is increased from 0 ppm to 100 ppm [22].

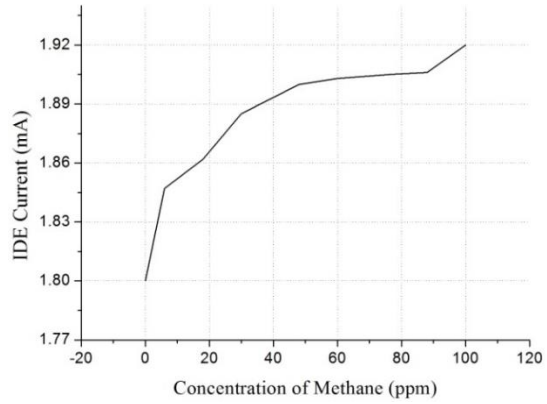

Fig. 2. Current flowing IDE versus the concentration of methane

IV. GEOMETRY OF CHIPLESS TAG

As discussed above, the intended sensor tag is the combination of an electromagnetic interface with a sensor head made from IDE loaded by Pd-SWCNTs. As shown in Fig. 3, there is one sensor head embedded in the middle location of the U-slot with one IDE electrodes soldered on the metallic plane close to the upper edge, and another IDE electrode soldered on the metallic plane close to the low edge of the U-slot. This implementation of the sensor tag is based on the scheme of the amplitude modulation of band-gap frequency. The size of this geometry guarantees the sensor tag be able to cover the entire UWB band with range from 3.1 GHz to 10.6 GHz; in the meanwhile, it has a band-gap at 5 GHz.

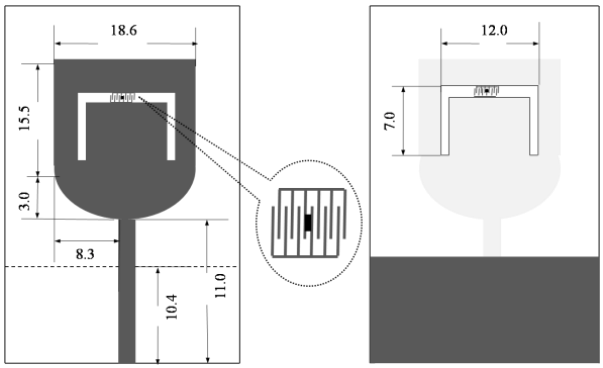

Fig. 3. (a) The front geometry of the proposed tag that the IDE loaded by Pd-SWCNTs is embedded in the middle of the U-slot, detecting methane based on the scheme of amplitude modulation of band-gap frequency. (b) Back of the proposed tag. (unit: mm)

Similarly, two identical sensor heads are embedded in the vertical arms of the U-slot symmetrically with a few distances away from the slot terminal ends, as shown in Fig. 4. This implementation of the sensor tag is based on the scheme of the frequency modulation of band-gap frequency. The size of this geometry guarantees the sensor tag to cover the entire UWB band, and having a band-gap frequency that can be shifted from 5 GHz to 5.25 GHz to reflect the concentration of methane increased from 0 ppm to 100 ppm.

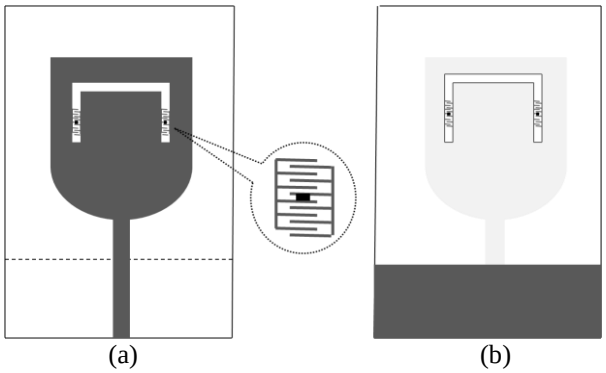

Fig. 4. (a) The front geometry of the proposed tag that the IDE loaded by Pd-SWCNTs is embedded in the vertical arms of the U-slot, detecting methane based on the scheme of frequency modulation of band-gap frequency. (b) Back of the proposed tag.

V. NUMERICAL APPROXIMATES, ANALYSES AND VALIDATION

The performance of the proposed sensor tags are described by the parameters of *identifiable sensitivity* as defined above. The process will be an approximate combination of the analytical and numerical method. In the analytical expression (6) and (7), the RCS σ and S_{22} will be achieved by numerical method or by real-field measurement.

The IDE with load of Pd-SWCNTs is regarded as a standalone component in the simulation model that will be replaced by an equivalent resistance achieved by simulation on the band-gap frequency. The simulation model of the sensor tag is based the fast multipole method algorithm (FMMA) in the consideration of that the operating frequency of the sensor tag is UWB band with range from 3.1 GHz to 10.6 GHz, the minimum wavelength is around 3 mm, comparatively smaller than the average size of the antenna dimension; Moreover, the FMMA can be applied to accelerate the iterative solver in the method of moments (MOM) as applied to the scattering problems about the computational electro-magnetic such as the computation of the RCS σ as it is required in this design [23].

With respect to the sensor tag illustrated in Fig. 3, the curve of the modulus of S_{22} versus frequency is shown in Fig. 5. It can be seen that there is a band-gap at 5 GHz. The modulus of S_{22} at the band-gap frequency is -7.73 dB, indicating the concentration of methane is 0 ppm (solid black line); while the modulus of S_{22} is changed to

-9.98 dB, indicating the concentration of methane is increased to 100 ppm (dash dot red line), the discrepancy is achieved by 2.25 dB.

The curve of RCS versus frequency is shown in Fig. 6. When the concentration of methane is 0 ppm, the RCS at the band-gap frequency is -32.59 dBsm (solid black line); however, when the concentration of methane is increased to 100 ppm, this RCS is decreased to -31.61 dBsm (dash dot red line), the discrepancy is 0.98 dB.

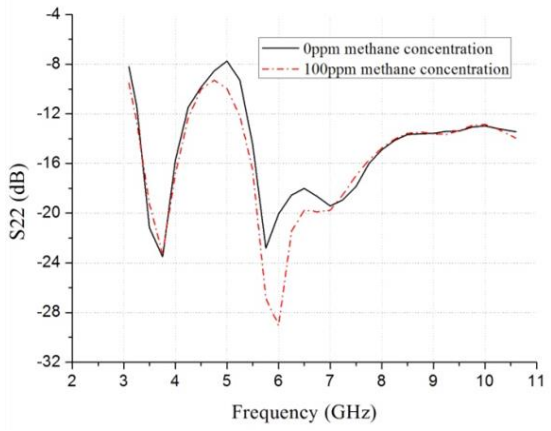

Fig. 5. S_{22} versus the concentration of methane and the frequency upon the scheme of amplitude modulation of band-gap frequency.

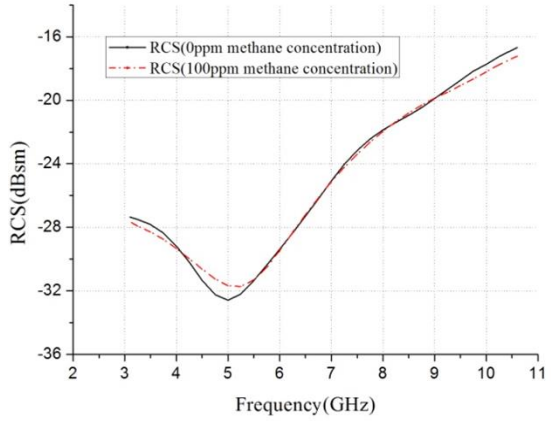

Fig. 6. RCS versus the concentration of methane and the frequency upon the scheme of amplitude modulation of band-gap frequency.

Substituting these values into (6), we can achieve the parameter of the *identifiable sensitivity* by -9.32 dB to specify that the concentration of methane is 100 ppm, as shown in Fig. 7.

With respect to the sensor tag illustrated in Fig. 4, the curve of the modulus of S_{22} versus frequency is shown in Fig. 8. The band-gap is at 5 GHz for the concentration of methane by 0 ppm (solid black line). This band-gap is moved to 5.25 GHz for the concentration of methane increased to 100 ppm (dash dot red line). When the concentration of methane is increased from 0 ppm to 100 ppm, the minimum RCS is moved from 6.45 GHz to 6.75 GHz, as shown in Fig. 9.

Substituting all these values into $Y_d[f, d(t)] = \eta_L[d(t)]\sqrt{1 - |S_{22}[f, d(t)]|^2}$, we can get $Y_d[f, d(t)]$ versus frequency as shown in Fig. 10. When the concentration of methane is 0 ppm, the minimum $Y_d[f, d(t)]$ is achieved at the frequency of 6.25 GHz (solid black line); but when the concentration is increased to 100 ppm, the minimum $Y_d[f, d(t)]$ is moved to the frequency of 6.75 GHz (dash dot red line).

Substituting these values into (7), we can achieve the *identifiable sensitivity* by -11.30 dB for the methane concentrated by 100 ppm, as shown in Fig. 11.

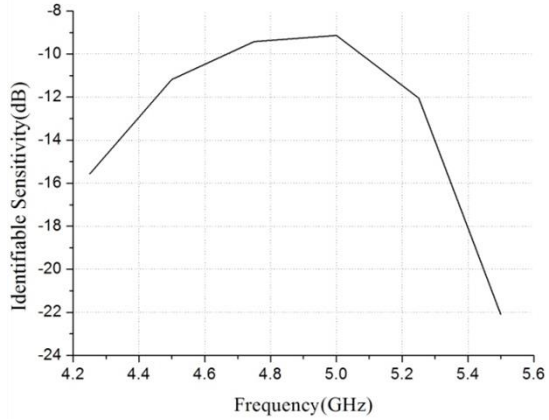

Fig. 7.The identifiable sensitivity for the concentration of methane of 100 ppm upon amplitude modulation of band-gap frequency.

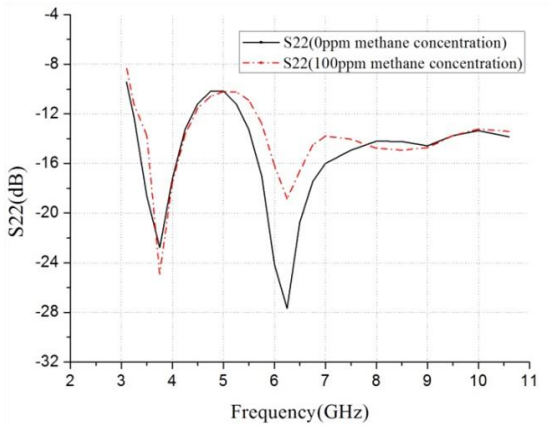

Fig. 8. S_{22} versus the concentration of methane and frequency in terms of the scheme of frequency modulation of band-gap frequency.

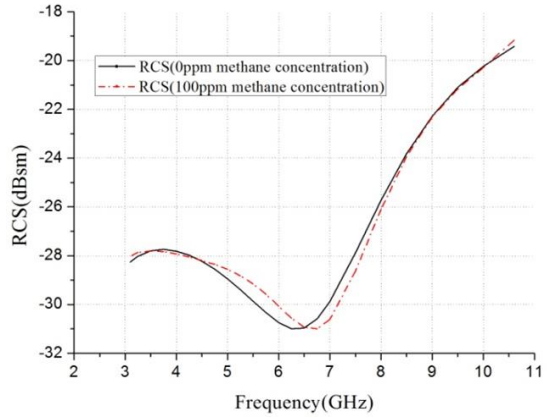

Fig. 9. RCS versus the concentration of methane and the frequency in terms of the scheme of frequency modulation of band-gap frequency.

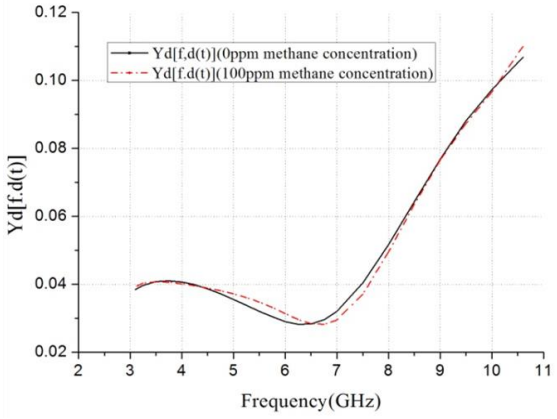

Fig. 10. $Y_d[f, d(t)]$ versus the concentration of methane and the frequency in terms of the scheme of frequency modulation of band-gap frequency.

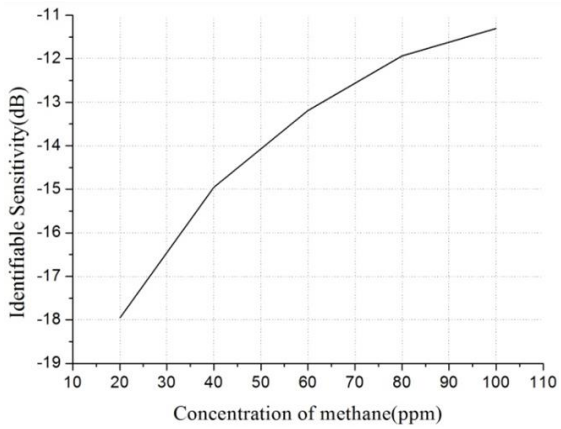

Fig. 11. The identifiable sensitivity achieved in terms of the scheme of the frequency modulation of band-gap frequency.

VI. CONCLUSION

It can be concluded form this design that the Pd-SWCNTs enabled UWB-RFID chiplees sensor can be used to conduct the detection of concentration of methane at room temperature. Based on the structural mode of the backscattering signal, the geometry of sensor tag is simple and the detection procedure is cost efficient.

It can be seen that band-gap can be introduced by etching U-slot on the planar antenna of UWB. The band-gapped frequency can be designated as the sensing signature. If the amplitude of the band-gap frequency is manipulated by the data of the concentration of methane, it forms the scheme of the amplitude modulation of band-gap frequency; and if the frequency of band-gap frequency is manipulated by the data of the concentration of methane, it forms the scheme of the frequency modulation of band-gap frequency.

The performance of the proposed sensor tag is validated by a method combing the analytical and numerical computation with deliverables of the parameter of *identifiable sensitivity* that is achieved by -9.32 dB in terms of the scheme of amplitude modulation of band-gap frequency, or by -11.30 dB in terms of the scheme of frequency modulation of band-gap frequency, indicating the methane concentrated by 100 ppm at room temperature.

It is evidence that the dynamic range of the identifiable sensitivity is quite constraint due to the limitation of Pd-SWCNTs. The performance of the sensor tag would be improved when more advanced nano-materials in specific for the detection of methane can be available in future.

REFERENCES

[1] D. Kohl, "Function and application of gas sensors," *J. Phys. D Appl. Phys.*, vol. 34, pp. 125-149, 2001.

[2] C. Occhiuzzi, A. Rida, G. Marrocco, and M. Tentzeris, "RFID passive gas sensor integrating carbon nanotubes," *Microwave Theory and Techniques, IEEE Transactions on*, vol. 59, no. 10, pp. 2674-2684, Oct. 2011.

[3] V. Chawla and D. S. Ha, "An overview of passive RFID," *IEEE Commun. Mag.*, vol. 45, no. 9, pp. 11-17, Sep. 2007.

[4] V. Plessky and L. Reindl, "Review on SAW RFID tags," *IEEE Trans. Ultrason. Ferroelectr. Freq. Contro.*, vol. 57, no. 3, pp. 654-668, 2010.

[5] D. Girbau, J. Lorenzo, A. Lazaro, C. Ferrater, and R. Villarino, "Frequency coded chipless RFID tag based on dual-band resonators," *IEEE Antennas and Wireless Propagation Letters*, vol. 11, pp. 126-128, 2012.

[6] I. Balbin and N. C. Karmakar, "Phase-encoded chipless RFID transponder for large-scale low-cost

applications," *IEEE Microwave Wireless Compon. Lett.*, vol. 19, no. 8, pp. 509-511, Aug. 2009.

[7] B. Shao, Q. Chen, R. Liu, and L. R. Zheng, "Design of fully printable and configurable chipless RFID tag on flexible substrate," *Microwave and Optical Technology Letter*, vol. 54, no. 1, pp. 226-230, 2012.

[8] K. Finkenzeller, *RFID Handbook: Fundamentals and Applications in Contactless Smart Cards and Identification*. 2nd ed., New York: Wiley, 2004.

[9] D. Dardari, R. D'Errico, C. Roblin, A. Sibille, and M. Z. Win, "Ultrawide bandwidth RFID: The next generation?," *Proc. IEEE*, vol. 98, no. 9, pp. 1570-1582, Sep. 2010.

[10] S. Hu, Y. Zhou, C. L. Law, and W. Dou, "Study of a uniplanar monopole antenna for passive chipless UWB-RFID localization system," *IEEE Trans. Antennas Propag.*, vol. 58, no. 2, pp. 271-278, Feb. 2010.

[11] D. Girbau, Á. Ramos, A. Lázaro, S. Rima, and R. Villarino, "Passive wireless temperature sensor based on time-coded UWB chipless RFID tags," *IEEE Trans. Mircow. Theory Tech.*, vol. 60, no. 11, pp. 2623-2632, Nov. 2012.

[12] Y. F. Weng, S. W. Cheung, T. I. Yuk, and L. Liu, "Design of chipless UWB RFID system using a CPW multi-Resonator," *IEEE Antennas. Propag. Mag.*, vol. 55, no. 1, pp. 13-31, Feb. 2013.

[13] A. Ramos, A. Lazaro, D. Girbau, and R. Villarino, "Time-domain measurement of time-coded UWB chipless RFID tags," *Progress in Electromagnetics Research*, vol. 116, pp. 313-331, 2011.

[14] Federal Communications Commission, Revision of Part 15 of the Commission's Rules Regarding Ultra-Wideband Transmission Systems, First Rep. Order (ET Docket98–153), Adopted Feb. 14, 2002. Released Apr. 22, 2002.

[15] Z. Chen, X. Wu, H. Li, N. Yang, and M. Y. W. Chia, "Considerations for source pulses and antennas in UWB radio systems," *IEEE Trans. Antennas Propag.*, vol. 52, no. 7, pp. 1739-1748, July 2004.

[16] C. A. Balanis, *Antenna Theory Analysis and Design*. 3rd ed., Hoboken, NJ: Wiley, 2005.

[17] E. A. Daviu, M. C. Fabrés, M. F. Bataller, and V. M. R. Peñarrocha, "Modal analysis and design of band-notched UWB," *IEEE Trans. Antennas Propag.*, vol. 58, no. 5, pp. 1453-1467, May 2010.

[18] R. Bogue, "Nanomaterials for gas sensing: A review of recent research," *Sensor Review*, vol. 34, no. 1, pp. 1-8, 2014.

[19] J. Chen, M. A. Hamon, H. Hu, Y. Chen, A. M. Rao, P. C. Eklund, and R. C. Haddon, "Solution properties of single-walled carbon nanotubes," *Science*, vol. 282, pp. 95-98, 1998.

[20] Z. P. Li, J. F. Li, X. Wu, S. M. Shuang, C. Dong, and M. M. F. Choi, "Methane sensor based on nanocomposite of palladium/multi-walled carbon nanotubes grafted with 1,6-hexanediamine," *Sensors and Actuators B*, vol. 139, pp. 453-459, 2009.

[21] A. Biaggi-Labiosa, F. Sola, M. Lebron-Colon, L. J. Evans, J. C. Xu, G. W. Hunter, G. M. Berger, and J. M. Gonzalez, "A novel methane sensor based on porous SnO2 nanorods: Room temperature to high temperature detection," *Nanotechnol.*, vol. 23, pp. 455-501, 2012.

[22] Y. Lu, J. Li, J. Han, H. T. Ng, C. Binder, C. Partridge, and M. Meyyappan, "Room temperature methane detection using palladium loaded single-walled carbon nanotube sensors," *Chem. Phys. Lett.*, vol. 391, pp. 344-348. 2004.

[23] E. Nader, D William, V. R. Murphy, O. Ladimir, and V. Marius, "The fast multipole method for electromagnetic scattering computation," *IEEE Transactions on Antennas and Propagation*, vol. 40, pp. 634-641, 1992.

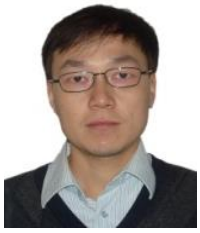

Jian Liu was born in Xi'an, Shaanxi, in 1967. He received the B.S. and M.S. degrees in the Electromagnetic Field Engineering from Xidian University, Xi'an, in 1990 and 1996. From 1990 to 1996, he was an Assistant Professor with the Communication Engineering Department, Xi'an Mining Institute. From 1997 to 1998, he was an Electrical Engineer with RF & Wireless Laboratory, ZTE. From 1998 to 2000, he was a Lecturer with the Communication Engineering Department, Xi'an Science and Technology College. From 2000 to 2003, he was the Senior Scientist and Project Leader with Philips Research Laboratory. From 2004 to 2010, he was Department Head of PTCC, Panasonic Research and Development Cooperation Limited. Since 2010, he has been a Lecturer with the School of Communication and Information Engineering, Xi'an University of Science and Technology. He is the author of 1 text book, more than 10 articles, and holds 7 patents. His research interests include Computational Electromagnetism, Antenna, RF & Microwave Communication and Sensors.

Baiping Li received the B.S., M.S. and Ph.D. in 1985, 1997 and 2011 from Chongqing University, Liaoning Technical University and Xi'an University of Science and Technology, respectively. She is now the Professor and the Head of the School of Communication and Information Engineering, Xi'an University of Science and Technology. She is the author of six books, and more than 40 articles. Her research interests include the key technologies on Wireless Communications and Sensor Networks.

Transformer-Based Dual-Mode VCO for Multi-Mode Multi-Standard Receiver

Xiangning Fan, Xiaoyang Shi, and Li Tang

Institute of RF&OE-ICs, School of Information Science and Engineering
Southeast University, Nanjing, 210096, China
xnfan@seu.edu.cn

Abstract ─ The proposed VCO in this paper is used for multi-mode multi-standard wireless transceiver. The overall scheme includes two VCOs, each VCO adopts transformer-based structure. On-chip transformer which uses coplanar central tap structure and adopts the top metal winding is present. The primary and secondary inductances adopt octagon differential structure. Electromagnetic field (EM) simulation is carried out by using ADS Momentum. Negative conductance unit adopts the current reuse of cross coupled MOSFET. Oscillation mode can be chosen by switch. The primary and secondary inductances of the transformer are connected with 4 bit binary switches capacitor arrays and varactors under different oscillation modes to extend the range of frequency adjustment. Measurement results show that the frequency range is from 1.2 to 7.3 GHz and the phase noise at 1 MHz offset is less than -80 dBc/Hz in the whole frequency range.

Index Terms ─ Dual-mode VCO, transformer, wideband.

I. INTRODUCTION

The ever-increasing demand for the wide range wireless services is continuously generating new standards, which often come with new frequency bands or new modulation schemes [1-5]. Wireless receivers capable for supporting multi-mode multi-standard applications are highly desirable, and have become a hot spot. Phase-locked loop (PLL), as one of the most critical building blocks in RF front-end, is widely used in wireless systems. As the core of the PLL, the voltage-controlled oscillator (VCO), together with frequency-extension circuits, should be continuously tunable within a wide frequency range to fulfill the requirement of the ubiquitous connectivity and the new emerging standards. It is one of the main bottlenecks of achieving fully integrated multi-mode multi-standard receivers.

Owing to the low phase noise performance, LC-VCOs are preferred rather than ring oscillators, but their frequency range is limited owing to the low C_{max}/C_{min} ratio of the varactor. To widen the frequency range, most LC-VCOs use switched capacitors [6] or inductors [7]. However, these approaches suffer from the channel resistance and parasitic capacitance of the switch, which tend to degrade the phase noise performance and frequency tuning range. Recently, a transformer-based resonator that is able to generate two distinct frequency bands was exploited to realize dual-band VCOs or wideband VCOs [8]. In this paper, we propose a new transformer-based VCO that adopts a current-reused configuration, and apply it to the multi-mode multi-standard wireless receivers.

The rest of this paper is organized as follows. Circuit architecture and transformer design are shown in Section II. Measurement results are given in Section III, with the conclusion in Section IV.

II. CIRCUIT ARCHITECTURE AND TRANSFORMER DESIGN

Multi-mode multi-standard wireless applications need a larger frequency range, but it can typically not be achieved in traditional resonant tanks with a sufficient quality factor and phase-noise. In principle, we use two VCOs (VCOH and VCOL) to achieve the whole frequency range, and each VCO adopts transformer-based structure.

A. Oscillation frequency

Figure 1 (a) shows the general model of the one-port dual-band oscillator. Resistive components are added in series with the inductors and capacitors to account for the loss of the network, which can be typically compensated for oscillation by employing a negative transconductance cell at Port-1 or Port-2. The component Qs are defined as $Q_{L1}=\omega_{L1}/R_{L1}$, $Q_{C1}=1/(\omega C_1 R_{C1})$, $Q_{L2}=\omega_{L2}/R_{L2}$, and $Q_{C2}=1/(\omega C_2 R_{C2})$.

To facilitate the calculation of the tank impedance, the transformer is replaced by an equivalent network as shown in Fig. 1 (b), and the impedance Z_{L1} can be derived as (1)-(3), where Z_{L1} contains an equivalent inductor L_1 in series with a resistor ΔR_{L1}, and the angle frequencies ω_1 and ω_2 are given by $\omega_1 = 1/\sqrt{L_1 C_1}$, and $\omega_2 = 1/\sqrt{L_2 C_2}$:

Submitted On: September 28, 2015
Accepted On: June 17, 2016

$$Z_{L1} = \Delta R_{L1} + j\omega L_1^{'}, \tag{1}$$

$$\Delta R_{L1} = \frac{\frac{L_1}{k^2 L_2}(R_{L2}+R_{C2})(\omega L_1)^2}{[\frac{L_1}{k^2 L_2}(R_{L2}+R_{C2})]^2 + (\frac{\omega L_1}{k^2})^2[1-(\frac{\omega_2}{\omega})^2]^2}, \tag{2}$$

$$L_1^{'} = \frac{[\frac{L_1}{k^2 L_2}(R_{L2}+R_{C2})]^2 + (\frac{\omega L_1}{k^2})^2[1-(\frac{\omega_2}{w})^2][1-k^2-(\frac{\omega_2}{\omega})^2]}{[\frac{L_1}{k^2 L_2}(R_{L2}+R_{C2})]^2 + (\frac{\omega L_1}{k^2})^2[1-(\frac{\omega_2}{\omega})^2]^2} L_1. \tag{3}$$

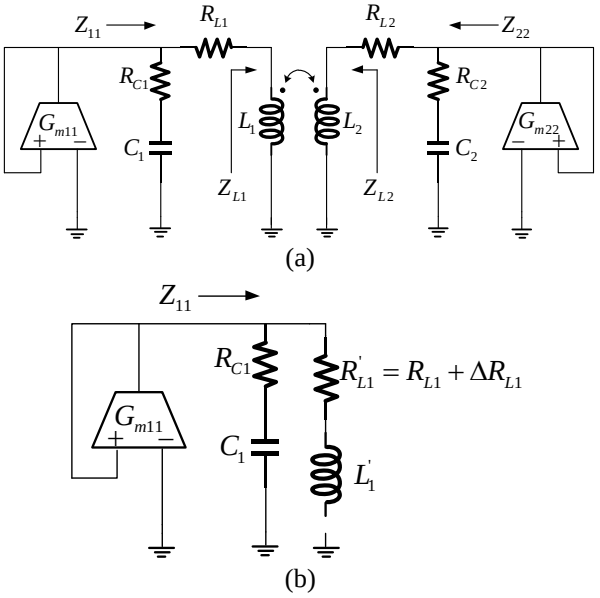

Fig. 1. Models of one port oscillators: (a) general model, and (b) simplified network for Z11 calculation.

Without loss of generality, let's define $L_1=mL_2=mL$, $C_1=nC_2=nC$ and assume in all the following discussions that $k>0$ and $mn>1$, so that $\omega_1<\omega_2$. Z_{11} can be considered as a simplified LC tank as shown in Fig. 1 (b). The frequency response of Z_{11} can be quickly estimated by assuming a low-loss case, in which case Z_{11} can be derived as:

$$Z_{11} \approx (1/sC_1) \,||\, (sL_1^{'}) = \frac{j\omega_1^2 L_1 \omega[(1-k^2)\omega^2 - \omega_2^2]}{(k^2-1)\omega^4 + (\omega_1^2+\omega_2^2)\omega^2 - \omega_1^2\omega_2^2}. \tag{4}$$

Because of the symmetry of the network in Fig. 1 (a), Z_{22} can be directly rewritten from Z_{11} as:

$$Z_{22} = \frac{j\omega_2^2 L_2 \omega[(1-k^2)\omega^2 - \omega_1^2]}{(k^2-1)\omega^4 + (\omega_1^2+\omega_2^2)\omega^2 - \omega_1^2\omega_2^2}. \tag{5}$$

From (4) and (5), Z_{11} and Z_{22} have exactly the same two peak frequency located at:

$$\omega_{H/L}^2 = \frac{\omega_1^2+\omega_2^2 \pm \sqrt{(\omega_1^2-\omega_2^2)^2 + 4k^2\omega_1^2\omega_2^2}}{2(1-k^2)}. \tag{6}$$

Besides the zero frequency, there is only one notch frequency $\omega_{1,notch}$ in Z_{11}, and similarly, there exits only one notch frequency $\omega_{2,notch}$ in Z_{22}, which are given by:

$$\omega_{1,notch} = \frac{\omega_1}{\sqrt{1-k^2}}, \tag{7}$$

$$\omega_{2,notch} = \frac{\omega_2}{\sqrt{1-k^2}}. \tag{8}$$

B. Start up conditions

Figure 2 (a) and Fig. 2 (b) plot the magnitude and phase response of Z_{11} and Z_{22} with high-Q components. The phase shift begins from 90° at low frequency, cross 0° at the first peak frequency, returns to 90 after either $\omega_{1,notch}$ in Z_{11} or $\omega_{2,notch}$ in Z_{22}, and cross 0° again at the second peak frequency.

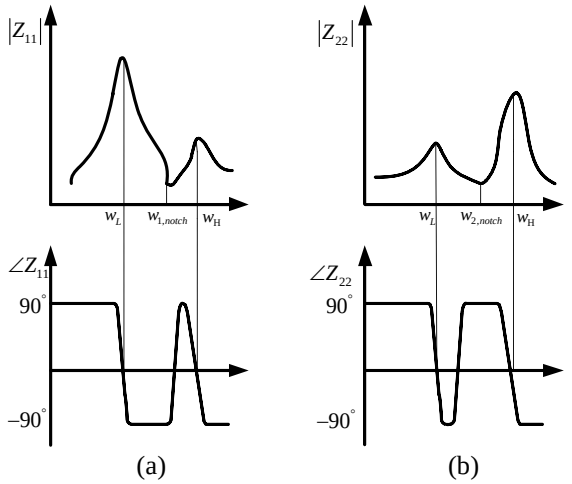

Fig. 2. Frequency response of the fourth-order LC tank of: (a) Z_{11} and (b) Z_{22}.

The start-up conditions of the one-port oscillator shown in Fig. 1 (a) are given by:

$$G_{m11} > \frac{1}{real\{Z_{11}\}}, \tag{9}$$

$$imag\{Z_{11}=0\}. \tag{10}$$

If the tank Q is high enough, from (9), the minimum G_m for oscillation can be expressed as:

$$G_{m11,\min} = \frac{(R_{L1}^{'}+R_{C1})C_1}{L_1^{'}}. \tag{11}$$

Putting (2) and (3) into (11), it can be derived that:

$$G_{m11,\min}=\frac{1}{A_1\omega_{osc}L_1}[\frac{1}{A_1}\frac{1}{Q_{L1}}+\frac{1}{Q_{C1}}+\lambda(\frac{1}{A_2}\frac{1}{Q_{L2}}+\frac{1}{Q_{C2}})], \quad (12)$$

where $A_1=\omega_1^2/\omega_{osc}^2$, $A_2=\omega_2^2/\omega_{osc}^2$, and $\lambda=(A_2(A_1-1))/(A_1(A_2-1))$.

Symmetrically, $G_{m22,\min}$ can be easily rewritten from (12) as:

$$G_{m22,\min}=\frac{1}{A_2\omega_{osc}L_2}[\frac{1}{A_2}\frac{1}{Q_{L2}}+\frac{1}{Q_{C2}}+\lambda^{-1}(\frac{1}{A_1}\frac{1}{Q_{L1}}+\frac{1}{Q_{C1}})]. \quad (13)$$

At both the potential oscillation frequencies ω_L and ω_H, the phase shift is 0°, and thus (10) is satisfied, and the necessary and sufficient conditions for start-up oscillation at ω_L or ω_H would become $G_{m11}>G_{m11,\min}(\omega_L)$ or $G_{m11}>G_{m11,\min}(\omega_H)$, respectively. If G_{m11} is large enough to satisfy the two conditions, the oscillator can potentially oscillator at either frequency ω_L or ω_H or concurrently oscillator at both frequencies. The final steady-state oscillation depends on detailed configuration of the high-order LC tank and specific form nonlinearity of the active device [9].

In general, $|k|\to 0$ is undesirable in terms of the chip area as the two coils of the transformer need to be completely decoupled from each other. It would be more desirable to make $mn\to\infty$, which is equivalent to $\omega_2>>\omega_1$. With different value of ω_2/ω_1 and k, the transconductance ratio is always larger than 1, which implies that if the cross-coupled G_m cell placed Port 1 to compensate the loss of the tank, the VCO always prefers to oscillator at the lower peak frequency ω_L. Moreover, the larger the ratio ω_2/ω_1 is, the more stable the oscillation becomes. In order to enable stable oscillation at ω_H, the oscillator can be designed such that $G_{m22,\min}(\omega_H)<G_{m22}<G_{m22,\min}(\omega_L)$. In this case, the values of $\sqrt{mn}$ and k need to be properly chosen.

Figure 3 gives out the architecture of the proposed VCO. It consists of a transformer-based resonator and two switched differential transistor pairs. The resonator includes two identical LC tanks coupled by the transformer, and has two resonator frequencies.

The two differential pairs (MN1, MP1 and MN2, MP2) can be switched to simulate a desired oscillation mode and damps the other. When switches SW_L (SW_H) are turned on and SW_H (SW_L) are turned off, the cross-coupled transistors MN1(MN2) and MP1(MP2) generate negative resistance to compensate the loss of the transformer-based resonator. Thus, the VCO operates as a two-port oscillators at low (high) band ω_L (ω_H). Since no lossy switches are added to the resonator, it does not degrade the phase noise performance while mode switching. In each mode, switched capacitor arrays which are controlled by 4-bit digital control code, and varactors which are tuned by V_T, are adopted for coarse and fine tuning, respectively. Note that, each differential pair is constructed by series stacking of an NMOS and a PMOS. This solution offers three advantages. First, the current consumption can be reduced by half with respect to the traditional VCOs while providing the same negative resistance [10]. Secondly, it is inherently immune to the phase noise degradation caused by second-harmonic terms since no common-source node exists. Thirdly, less transistors connected to the resonator means low parasitic capacitance, which is beneficial to the frequency tuning range.

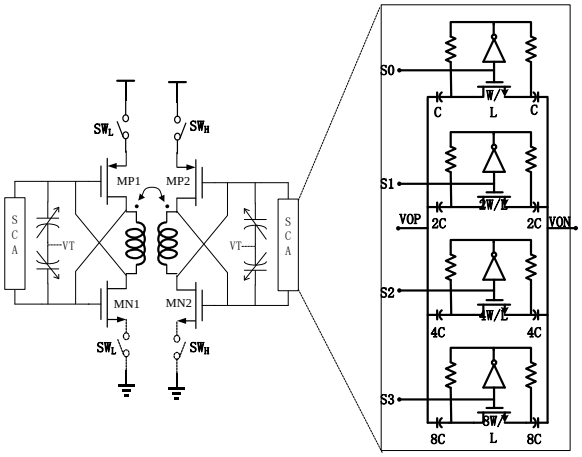

Fig. 3. Schematic of the proposed VCOs: VCOH and VCOL.

A major challenge is the implementation of the transformer. In the design of the transformer, two issues have to be addressed: (1) two ports should be on the same side to facilitate connection with capacitors; (2) two coils are weakly coupled. To achieve these goals, we design the transformers as shown in Fig. 4. The geometry size of the transformer used in VCOH in Fig. 4 (a) is shown below: two-turn primary coil has an inner radius of 125μm, the width and spacing is 18μm and 4μm, two-turn secondary coil has an inner radius of 65μm, the width and spacing is 12μm and 4μm, each coil is placed in a common-centric configuration and is implemented using the top thick mental6 layer (2.34μm) in the used technology. Electromagnetic simulation results using ADS Momentum are shown in Fig. 5. The geometry size of the transformer used in VCOL in Fig. 4 (b) is shown below: two-turn primary coil has an inner radius of 250μm, the width and spacing is 28μm and 4μm, two-turn secondary coil has an inner radius of 125μm, the

width and spacing is 28μm and 4μm, each coil is placed in a common-centric configuration and is implemented using the top thick mental6 layer (2.34μm) in the used technology. Electromagnetic simulation results using ADS Momentum are shown in Fig. 6.

As the simulation result shows, the coupling coefficient is small enough to ensure the two coils of the transformer is weakly coupled. The quality factor Q is high enough in the working band of the VCO.

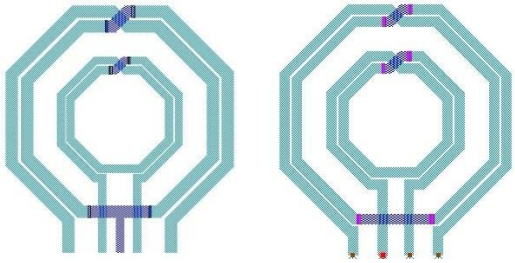

(a) (b)

Fig. 4. Transformer layout: (a) transformer in VCOH, and (b) transformer in VCOL.

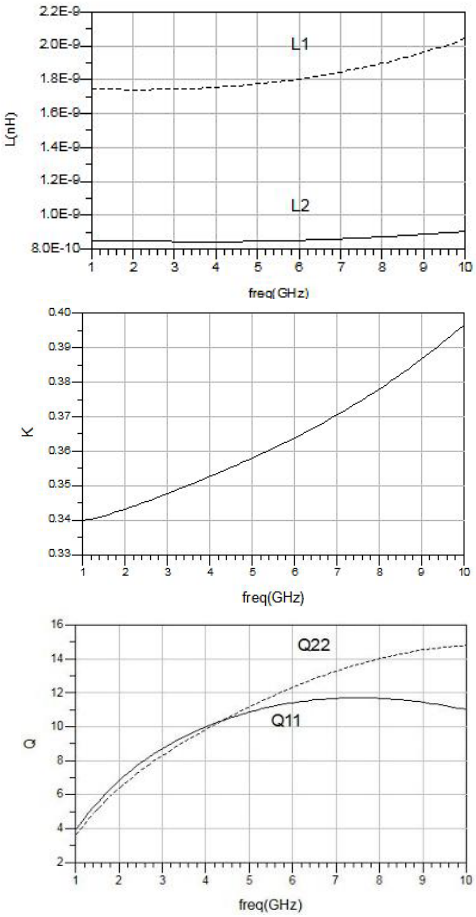

Fig. 5. Transformer EM simulation results of VCOH.

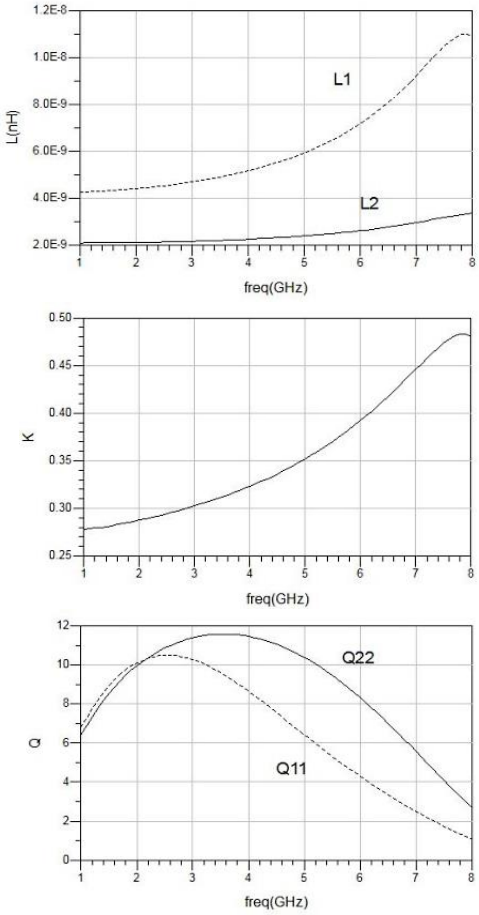

Fig. 6. Transformer EM simulation results of VCOL.

III. MEASURENMENT RESULTS

The proposed VCOs are implemented using 0.18μm CMOS technology. Figure 7 shows the micrograph of the VCOs.

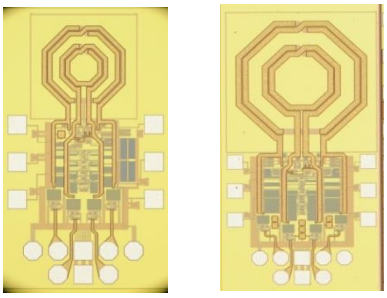

(a) (b)

Fig. 7. Die micrograph of the proposed VCOs: (a) VCOH and (b) VCOL.

VCOH covers an area of 1084μm×616μm, and VCOL covers an area of 1420μm×710μm. The performances of the fabricated VCOs are evaluated on wafer by

employing a Cascade Microtech probe station. The output spectrum and phase noise of the VCOs are measured by an Agilent E4440A spectrum analyzer.

Figure 8 shows the measured tuning curves of VCOH. The measured phase noise is shown in Fig. 9.

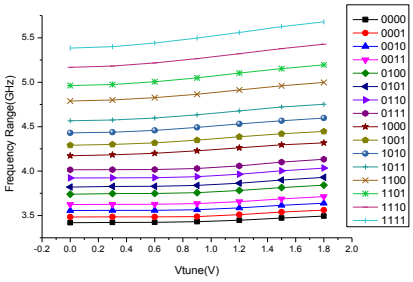

(a)

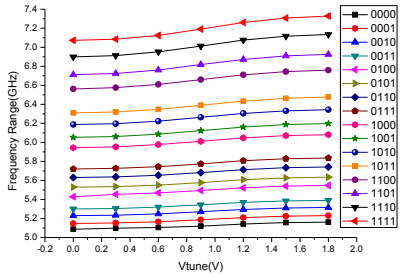

(b)

Fig. 8. Tuning curves of VCOH: (a) low band in VCOH, and (b) high band in VCOH.

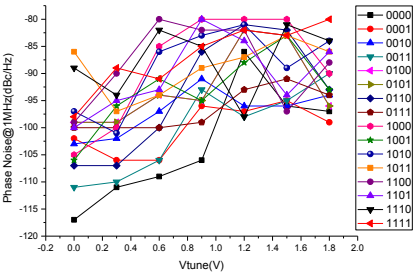

(a)

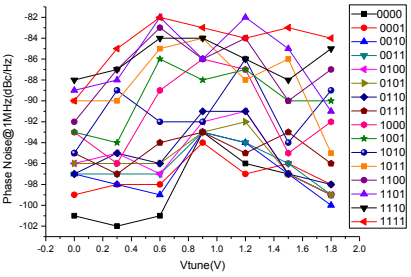

(b)

Fig. 9. Phase noise@1MHz of VCOH: (a) low band in VCOH, and (b) high band in VCOH.

As the figures show, VCOH is tunable from 3.42 to 5.67 GHz at low band and from 5.12 to 7.33 GHz at high band, resulting in a tuning range of from 3.42 to 7.33 GHz that meets the demand. The phase noise in the whole frequency is less than -80 dBc/Hz but not good enough.

Figure10 shows the measured tuning curves of VCOL. The measured phase noise is shown in Fig. 11.

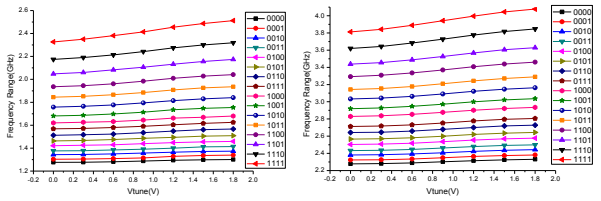

(a) (b)

Fig. 10. Tuning curves of VCOL: (a) low band in VCOL, and (b) high band in VCOL.

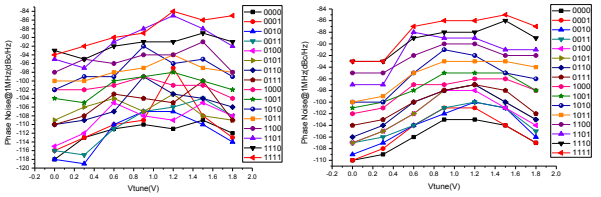

(a) (b)

Fig. 11. Phase noise @1MHz of VCOL: (a) low band in VCOL, and (b) high band in VCOL.

As the figures show, VCOL is tunable from 1.28 to 2.55 GHz at low band and from 2.29 to 4.03 GHz at high band, resulting in a tuning range of from 1.28 to 4.03 GHz that meets the demand. The phase noise in the whole frequency is less than -84 dBc/Hz.

In Table 1, performance of the present VCO is summarized and compared with recently published dual-band VCOs.

Table 1: Comparison between dual-band VCOs

	Tech. (CMOS)	Supply (V)	Power (mW)	Frequency Range (GHz)	PN (dBc/Hz)
[5]	0.18 μ m	1.2	13	0.83-3.72	-104
[7]	0.18 μ m	1.0	8	3.4-7.0	-101
[9]	0.18 μ m	2.5	15	0.79-0.85 1.75-1.87	-134
[10]	0.18 μ m	1.0	10	3.27-5.02 9.48-11.36	-112
This work	0.18 μ m	1.8	14.4	3.42-7.3	-84

IV. CONCLUSION

In this paper we use two transformer-based VCOs for the multi-mode multi-standard wireless receivers. The proposed VCOs are fabricated with 0.18μm CMOS technology. Measurement results show that VCOH

exhibits a frequency tuning range of 3.42-7.33 GHz, and the phase noise is less than -80 dBc/Hz at 1 MHz offset from the carrier, VCOL exhibits a frequency tuning range of 1.28-4.03 GHz, and the phase noise is less than -84 dBc/Hz at 1 MHz offset from the carrier.

ACKNOWLEDGMENT

This work is supported by the Priority Academic Program Development of Jiangsu Higher Education Institutions and Graduate Innovation Project of Jiangsu Province.

REFERENCES

[1] S. A. Osmany, F. Herzel, and J. C. Scheytt, "An integrated 0.6–4.6 GHz, 5–7 GHz, 10–14 GHz, and 20–28 GHz frequency synthesizer for software-defined radio applications," *IEEE Journal of Solid-State Circuits*, vol. 45, no. 9, pp. 1657-1668, 2010.

[2] J. Kim, J. Shin, S. Kim, and H. Shin, "A wide-band CMOS LC VCO with linearized coarse tuning characteristics," *IEEE Trans. Circuits Syst. II*, vol. 55, no. 5, pp. 399-403, 2008.

[3] W. Zou, X. Chen, K. Dai, and X. Zou, "Switched-inductor VCO based on tapped vertical solenoid inductors," *Electron. Lett.*, vol. 48, no. 9, pp. 509-511, 2008.

[4] Y. Takigawa, H. Ohta, Q. Liu, S. Kurachi, N. Itoh, and T. Yoshimasu, "A 92.6% tuning range VCO utilizing simultaneously controlling of transformers and MOS varactors in 0.13 μm CMOS technology," *IEEE Radio Frequency Integrated Circuits Symp., (RFIC)*, Boston, MA, USA, pp. 83-86, 2009.

[5] J. T. Xu, C. E. Saavedra, and G. Chen, "An active inductor-based VCO with wide tuning range and high DC-to-RF power efficiency," *IEEE Trans. Circuits Syst. II*, vol. 58, no. 8, pp. 462-466, 2011.

[6] M. Demirkan, S. P. Bruss, and R. R. Spencer, "Design of wide tuning-range CMOS VCOs using switched coupled-inductors," *IEEE Journal of Solid-State Circuits*, vol. 43, no. 5, pp. 1156-1163, 2008.

[7] A. Bevilacqua, F. P. Pavan, C. Sandner, A. Gerosa, and A. Neviani, "A 3.4-7 GHz transformer-based dual-mode wideband VCO," *IEEE Eur. Solid-State Circuit Conference.(ESSCRIC)*, pp. 440-443, 2006.

[8] A. Bevilacqua, F. P. Pavan, C. Sandner, A. Gerosa, and A. Neviani, "Transformered-based dual-mode voltage-controlled oscillators," *IEEE Trans. Circuit Syst. II: Express Briefs*, vol. 54, no. 4, pp. 293-297, 2007.

[9] N. Tchamov, S. Broussev, I. Uzunov, and K. K. Rantala, "Dual-band LC VCO architecture with a fourth-order resonator," *IEEE Trans. Circuit Syst. II: Exp. Briefs*, vol. 54, no. 3, pp. 277-281, 2007.

[10] S. Rong and H. C. Luong, "A 1V 4 GHz-and-10 GHz transformer-based dual-band quadrature VCO in 0.18μm CMOS," *Proc. IEEE Custom Integr. Circuit Conference. (CICC)*, vol. 38, no. 8, pp. 1325-1332, 2003.

Xiangning Fan received the B.S. and M.S. degrees both from Nanjing University of Posts and Telecommunications in 1985 and 1988 respectively. From 1997, he became a part time Ph.D. in National Communications Research Laboratory (NCRL), Southeast University and received the Ph.D. degree in 2005 with Grade A.

Since 1988, he works in Southeast University and now he is a Full Professor in Institute of RF-&-OE-ICs, School of Information Science and Engineering, Southeast University. Fan has finished more than 20 national projects on WSN, UWB, and 3G/4G Mobile Systems, and published more than 130 papers in IEEE T-CAS, IEEE COMM. Letters, Signal Processing, IET Radar, Sonar & Navigation, Electronic Letters, Sensor Letters, Springer AICASP, etc. with about 100 papers SCI/Ei indexed. His current research interests include RF ICs, receiver design and signal processing of wireless systems.

Xiaoyang Shi received the B.S. degree in Information Science and Engineering and the M.S. degree in Circuits and System at Southeast University, in 2012 and 2015. His present research interests include frequency synthesizers and RF circuit design.

Li Tang received the B.S. and M.S. degrees in Micro-electronics from Beijing Institute of Technology, China, in 2010 and 2013. He now is currently working towards the Ph.D. degree at Institute of RF-&OE-ICs, Southeast University, China. His research interests include RF integrated circuit design and receiver design.

Design of a 0.7~1.5 GHz Wideband Power Amplifier in 0.18-μm CMOS Process

Xiangning Fan, Zhou Yu, Jiakai Lu, and Zaijun Hua

Institute of RF&OE-ICs, School of Information Science and Engineering
Southeast University, Nanjing, 210096, China
xnfan@seu.edu.cn

Abstract ─ A power amplifier (PA) for multi-mode multi-standard transceiver which is implemented in a TSMC 0.18-μm CMOS process is presented. The proposed PA improves bandwidth using matching compensation, lossy matching network and negative feedback technique. Measurement results show that the working frequency range of the wideband PA is 0.7~1.5GHz, with the maximum output power of 18.2~22.3dBm. The output P1dB during test is 16.6~21.4 dBm, and the corresponding power added efficiency (PAE) is 7.7%~23.4%. The power gain within the working frequency is larger than 16dB and the S11 is less than -13dB. According to the test results, the proposed PA can cover the frequency of more than one octave. The linearity and power gain of the PA is satisfactory within the working frequency.

Index Terms ─ CMOS power amplifiers, lossy matching network, wideband amplifier, wideband matching.

I. INTRODUCTION

In the past decade, with the development of wireless communication technology, more and more modern wireless communication standards and applications emerged. An integrated multi-standard RF front-end which can cover GSM, LTE, WLAN, Bluetooth and GPS is required in this information era. Therefore, a fully integrated multi-mode multi-standard mobile front-end increasingly attracts the focus of industry and research [1].

However, conventional multi-mode transceivers are often implemented with some narrow band PAs for each frequency band [2], which increases the chip area and power cost. With the growing number of standards which the transceiver needs to support, wideband PAs draw more and more attention. Compared with narrow band Pas, wideband PAs have advantages of high integration and low cost.

Common methods of wideband matching network designing contain two major directions. Some wide band PAs are designed with tunable matching network of which the resonance frequency is tunable by switches [3], switched capacitors [4] or variable inductors. Another design method is a single wideband matching network which can directly cover the whole working bands [5].

Nowadays, most of RF PA is implemented in GaAs technology for its superior device performance [6]. However, CMOS process, which has the merit of high integration level and low cost, becomes a choice for designing PAs. In this work, a 0.7-1.5GHz CMOS power amplifier is designed in TSMC 0.18μm process.

The outline of this paper is as follows. Section II introduces the main techniques used in the design, i.e., wideband matching technology. Section III describes the circuit design of the proposed wideband PA. Measurement results are given in Section IV. Finally, summary of this work follows in Section V.

II. WIDEBAND MATCHING TECHNOLOGY

To ensure a good performance over whole frequency range of 0.7~1.5GHz, the power amplifier should have wideband matching network features.

In common structures of multi-mode power amplifier, wideband design and multi-band combination are two major design directions. Conventional multi-mode transceivers are often implemented with some narrow band PAs for each frequency band, which increases the chip area and power cost.

With the growing number of communication standards, wideband design becomes more attractive. Some wideband PAs are designed with tunable matching network of which the resonance frequency is tunable by switches, switched capacitors or variable inductors. Another design method is a single wideband matching network which can directly cover the whole working bands.

The wideband matching technique mainly adopts in this design include matching compensation technique, lossy matching network and negative feedback.

A. Matching compensation technique

Parasitic capacitances of MOS tube result in gain of power transistor rolls off at a rate of 6dB per octave.

Submitted On: September 30, 2015
Accepted On: June 17, 2016

Matching compensation technique is often applied for matching the output impedance of driver stage and the input impedance of power stage at the high frequency band. The mismatch at low frequency results in gain attenuation. Therefore, the flat gain across the whole frequency range can be expected, as shown in Fig. 1.

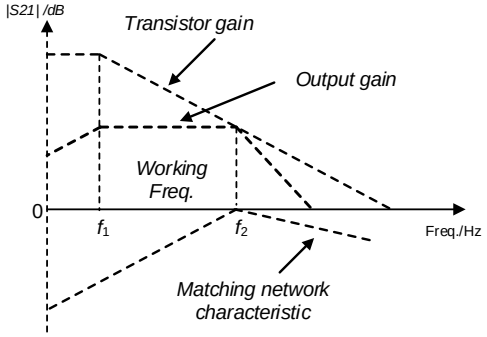

Fig. 1. Matching compensation of inter-stage network.

B. Lossy matching network

Lossy matching structure is shown in Fig. 2. Similar to mathing compensation technique, lossy mathing network attenuates the low-frequency gain by introducing resistance. In Fig. 2 (a), in the low frequency range, the inductor can be seen as a short circuit, and signal flows to the ground through the resistor, which absorbs low frequency energy. While in the high frequency range, the impedance of the inductor is so large that signal cannot pass through. In Fig. 2 (b), in the low frequency range, the capacitor branch can be seen as open, and signal flows through the resistor. Thus, these matching networks can adjust the low frequency gain and improve the bandwidth.

When designing wideband PA, the impedance may change rapidly in a wide frequency range. By adding resistor, the input matching can be realized easily. But for maximum output power, the resistors cannot be used in output matching network.

Furthermore, it can greatly improve the stability of the amplifier. Though it increases the noise factor of amplifier, it is still widely used in wideband matching for PA.

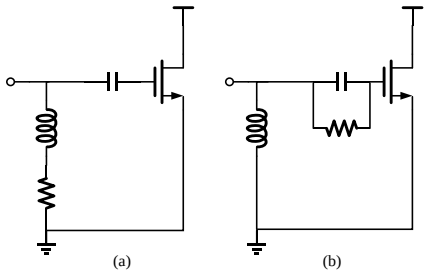

Fig. 2. Lossy matching network.

C. Negative feedback

The bandwidth of amplifier is restricted to the gain bandwidth product (GBW). Negative feedback is suitable for designing wideband amplifier which calls for flat gain performance. It can also improve the linearity of amplifier [7] and simplify the design of matching network.

Considering the power stage in Fig. 3. The resistor R_f is designed to adjust the gain of transistor, and the capacitor C_f blocks DC signal. When there is no feedback path on the transistor, the output power is expressed by:

$$P_O = V_o^2 / R_L = (g_m V_1)^2 R_L. \quad (1)$$

With the RC feedback path, the output power is changed to P_{ofb}, which can be expressed by:

$$P_{ofb} = V_o^2 / R_L = (g_m V_1)^2 R_L g(\frac{1\text{-}1/ g_m R_f}{1+R_L / R_f})^2. \quad (2)$$

Therefore, the power loss caused by the negative feedback can be expressed by:

$$\frac{P_{ofb}}{P_o} = (\frac{1\text{-}1/ g_m R_f}{1+R_L / R_f})^2. \quad (3)$$

When $R_f >> R_L$, the power loss can be expressed by:

$$\frac{P_{ofb}}{P_o} \approx 1 - \frac{2R_L}{R_f}. \quad (4)$$

As shown in (4), the feedback resistor R_f will cause the power loss of the PA. Negative feedback can also influence the stability of amplifier [1].

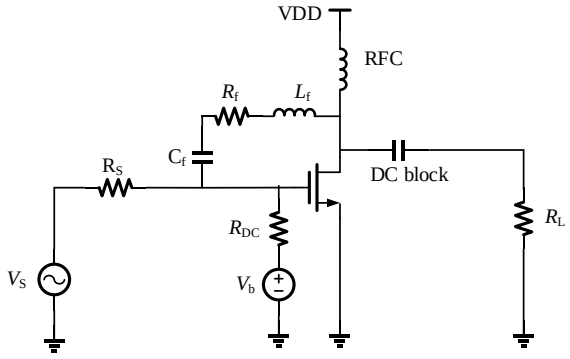

Fig. 3. Feedback amplifier structure.

D. Low-Q multi-stage matching network

Usually, simple single stage lumped components matching network cannot reach large bandwidth impedance transformation and is only used in the narrow-band matching. The output matching network is realized by low Q multi-stage impedance matching network, as shown in Fig. 5. The Q value, working bandwidth and center frequency can be expressed as:

$$Q = f_0 / BW. \quad (5)$$

Maximum Q factor of network is:

$$Q_{\max} = \sqrt{f_H \times f_L} / BW. \quad (6)$$

For wideband power amplifier, the impedance conversion ratio between the optimum impedance and the 50Ω port impedance is very large, which means a long distance between two impedance points on Smith chart. The Q factor of the network will limit the values of matching components.

Figure 4 (a) shows the scheme of using a single L type matching network, while Fig. 4 (b) using a multi-stage L type matching network. Apparently, by using multi-stage L type matching network, the Q factor can be smaller and the band extended. R_1 and R_2 are virtual resistances for matching, their values are between R_S and R_L. For n-stage L type matching network, assume $R_S > R_L$, when the ratio of the adjacent resistors is equal, the optimal bandwidth can be achieved [8]:

$$\frac{R_S}{R_1} = \frac{R_1}{R_2} = \cdots = \frac{R_{n-1}}{R_L}, \quad (7)$$

$$\begin{aligned} R_1 &= (R_S R_2)^{1/2} \\ R_2 &= (R_1 R_3)^{1/2} \\ &\vdots \\ R_{n-1} &= (R_{n-2} R_L)^{1/2}. \end{aligned} \quad (8)$$

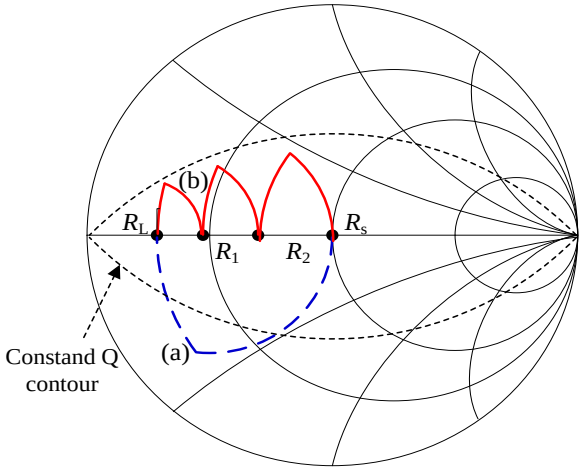

Fig. 4. Smith chart impedance transformation: (a) single L type matching network, and (b) multi-stage L type matching network.

III. WIDEBAND PA CIRCUIT DESIGN

The proposed wideband PA is used for multi-mode multi-standard transceiver. It calls for the performance of PA on linearity, power gain and working frequency. Additionally, because the transceiver needs to handle non-constant envelop signal, the PA should be designed to work in linear regime.

As shown in Fig. 5 (a), the power amplifier employs a two-stage topology structure, i.e., the driver and output stage, to have sufficient power gain. Both driver stage and output stage are biased as a Class-A amplifier to get maximum linearity. The driver stage is designed to provide high gain and the power stage should have sufficient power-handling capability.

Both input matching network and inter-stage matching network are realized with lossy network which introduces resistance element in the matching network. Resistance absorbs energy in low frequency range, thus the gain of low frequency and high frequency are equal.

The inter-stage matching network is designed to match the output impedance of driver stage and the input impedance of power stage at the high frequency band. The mismatch between the two impedances at low frequency range reduces the low frequency gain. Therefore, it can be expected that the flat gain across the whole frequency range, as shown in Fig. 5 (b).

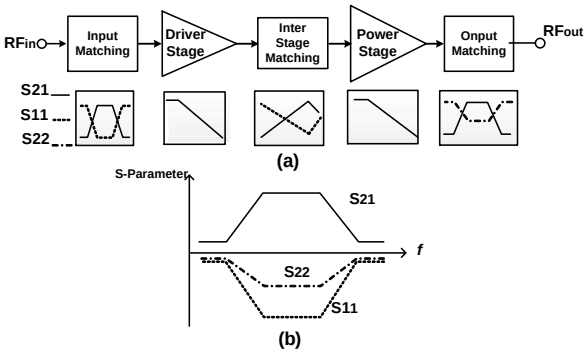

Fig. 5. Wideband power amplifier: (a) schematic diagram and (b) S-parameters.

All components outside of the dotted line frame in Fig. 6 are placed off-chip, including RF chokes and output matching network. L_{bond} is the equivalent inductance of bonding wire. The driver stage exploits a cascode structure to ensure sufficient gain. The cascode structure also improve the input-output isolation, thus simplified the design of matching network.

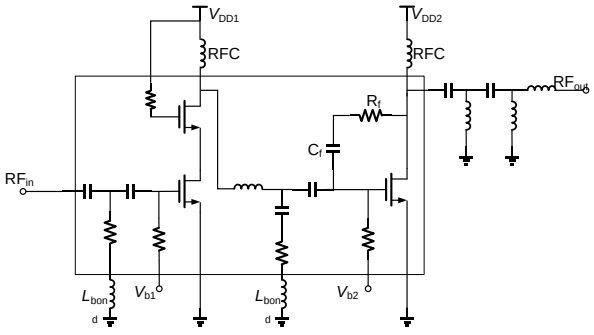

Fig. 6. Schematic diagram of two-stage wideband power amplifier.

TSMC 0.18μm CMOS process provides both thick-oxide transistor and thin-oxide transistor. In the power stage, with the supply voltage of 3.3V, a thick-oxide transistor is used to sustain a large-voltage swing across the drain and the gate. The supply voltage of driver stage is 2V, so the devices in driver stage are both thin-oxide transistors.

The output matching network is realized by low Q multi-stage impedance matching network. Load-pull simulation results show that the optimum load impedance R_{opt} changes a little across working band. The low Q matching network transforms load impedance of 50Ω close to R_{opt} over the working band so that the power stage has sufficient power-handling capability. The output impedance transformation is shown in Fig. 7. The real part of the impedance at the drain of output transistor is around 15Ω, and the magnitude of the impedance is between 15Ω and 20Ω.

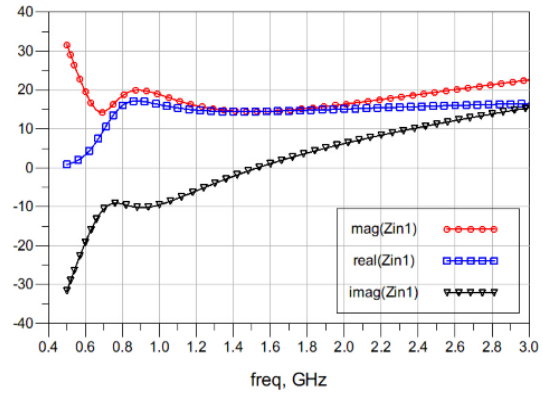

Fig. 7. Impedance transformation of output matching network.

Negative feedback technique is used in power stage to expand bandwidth of the amplifier. It is important to choose proper resistance that makes balance between power gain, bandwidth and stability.

IV. MEASURENMENT RESULTS

The proposed PA has been fabricated in TSMC 0.18μm process. The chip size of the PA is 0.98mm×0.46mm. Output matching network and RF choke inductors are off the chip. The photograph of the wideband PA is shown in Fig. 8.

According to the measurement results, the DC current of the driver stage and power stage are 32mA and 158mA, respectively. So the DC power consumption is about 585mW.

In the working band of 0.7~1.5GHz, the PA is set to be working at 9 frequency points. Figure 9 shows the measured output power of the PA at 700MHz. According to the relationship of input power and output power in Fig. 9, the power gain, 1dB compression points and efficiency can be calculated.

Figure 10 shows the measured power gain, maximum output power and S11 of the wideband PA. And Fig. 11 shows the measured output 1dB compression points and corresponding PAE (Power Added Efficiency).

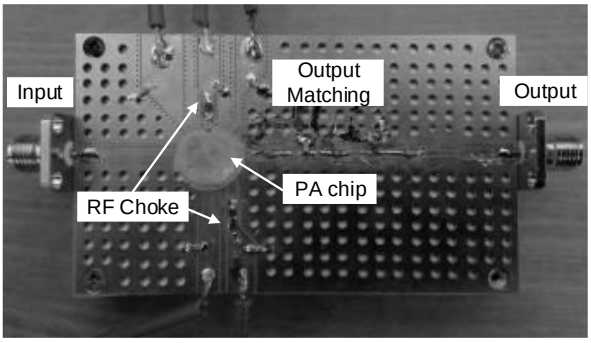

Fig. 8. Photograph of fabricated wideband PA.

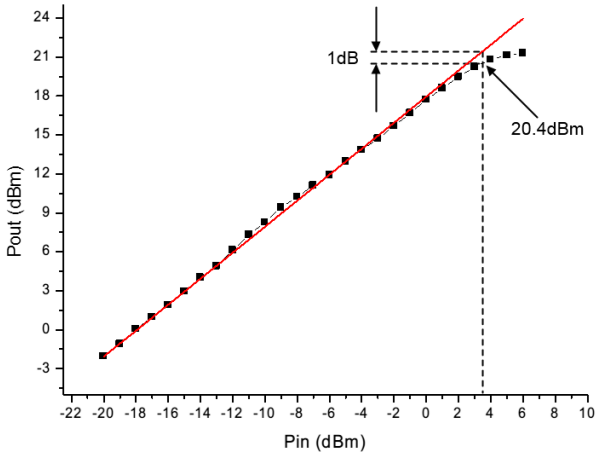

Fig. 9. Measured output power at 700MHz.

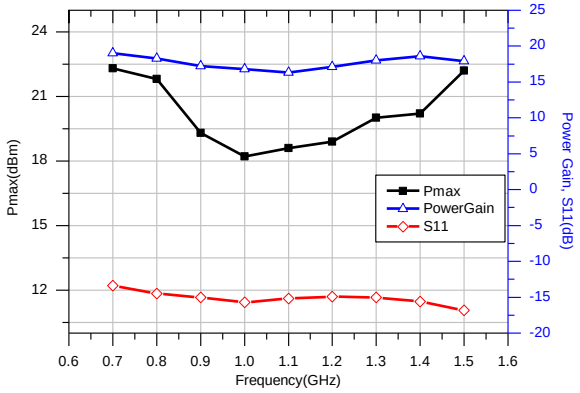

Fig. 10. Measured power gain, maximum output power and S11.

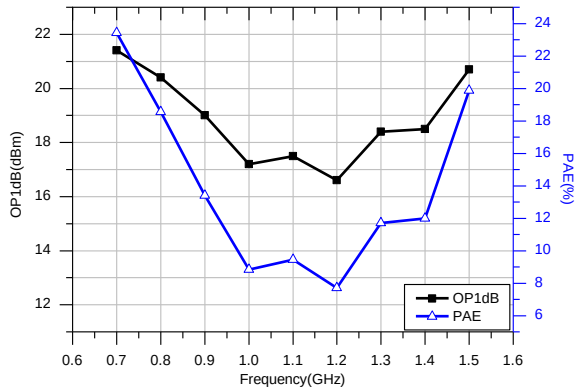

Fig. 11. Measured OP1dB and PAE @ OP1dB.

Within the frequency range of 0.7-1.5GHz, the PA can deliver maximum output power of more than 18dBm with the power gain between 16.3dB and 19dB. The small signal S-parameters of S11 is under -13dB across the frequency range. The OP1dBis between 16.6dBm and 21.4dBm and the PAE at OP1dB is 7.7%~23.4% through the working band. The overall performance of the designed PA with the recent state-of-the art results are summarized in Table 1.

Table 1: Summary of PA performance and comparison with proposed designs

Ref.	[7]	[8]	[9]	[10]	This Work
Freq. (GHz)	6~10	3~7.5	0.5~5	0.9~3.0	0.7~1.5
S11 (dB)	<-8	<-5	<-15	—	<-13
Gain (dB)	8.5	10	10~15	12~17	>16
OP_{1dB} (dBm)	5	>0	10~17	17~21	16.6~22
Psat (dBm)	—	>5	14~21	20~21	18.2~22
PAE (%)	14.4	12	3~16	11~23	8~23.4
CMOS Tech (μm)	0.18	0.18	0.13	0.18	0.18

V. CONCLUSION

This work presents a wideband two-stage linear power amplifier operating from 0.7GHz to 1.5GHz. Lossy matching network, matching compensation and negative feedback are used to improve bandwidth. The measurement results show that the PA demonstrate the maximum output power of more than 18dBm with the power gain of 16.3~18dB within the working band. From 0.7GHz to 1.5GHz, the output 1dB compression point is more than 16.6dBm and can be above 21dBm at 700MHz. At the OP1dB, the PA can achieve 7.7%~23.4% power added efficiency. According to the test results, the proposed PA can cover the frequency of more than one octave with satisfactory power gain and linearity. This PA applies to multi-standard wireless communication applications, and can be used in multi-mode multi-standard transceiver.

ACKNOWLEDGMENT

This work is supported by the Priority Academic Program Development of Jiangsu Higher Education Institutions and Graduate Innovation Project of Jiangsu Province.

REFERENCES

[1] S. S. Hyuk, Y. K. Woo, Y. J. Joo, et al., "A fully integrated CMOS class-E power amplifier for reconfigurable transmitters with WCDMA/WiMAX applications," *Proceedings of the 2013 26th International Conference on VLSI Design and 2013 12th International Conference on Embedded Systems*, pp. 169-172, 2013.

[2] J. P. Young and N. Cheng, "Multimode multiband power amplifier optimization for mobile applications," *VLSI Technology, Systems, and Applications (VLSI-TSA)*, pp. 1,3, Apr. 2013.

[3] K. Sungyoon, K. Unha, K. Youngwoo, et al., "A multi-mode multi-band reconfigurable power amplifier for low band GSM/UMTS handset applications," *Power Amplifiers for Wireless and Radio Applications (PAWR)*, pp. 16-18, Jan. 2013.

[4] H. Wang, C. Sideris, and A. Hajimiri, "A CMOS wideband power amplifier with a transformer-based high-order output matching network," *IEEE Journal on Solid-State Circuits*, vol. 45, no. 12, pp. 2709-2722, Dec. 2010.

[5] A. Grebennikov, *RF and Microwave Power Amplifier Design*. Publishing House of Electronics Industry, pp. 258-260, 2005.

[6] A. Fukuda, T. Furuta, H. Okazaki, et al., "Low-loss matching network design for band-switchable multi-band power amplifier," *IEICE Transactions on Electronics*, vol. E95-C, pp. 1172-1181, July 2012.

[7] H.-W. Chung, C.-Y. Hsu, C.-Y Yang, K.-F. Wei, and H.-R. Chuang, "A 6-10-GHz CMOS power amplifier with an inter-stage wideband impedance transformer for UWB transmitters," *Proceedings of the 38th European Microwave Conference*, pp. 305-308.

[8] S. A. Z. Murad, R. K. Pokharel, H. Kanaya, and K. Yoshida, "A 3.0–7.5 GHz CMOS UWB PA for group 1~3 MB-OFDM application using current reused and shunt-shunt feedback," *The 2009 International Conference on Wireless Communication & Signal Processing*, pp. 1-4, 2009.

[9] J. Roderick and H. Hashemi, "A 0.13μm CMOS

power amplifier with ultra-wide instantaneous bandwidth for imaging applications," *IEEE ISSCC Dig. Tech. Papers*, pp. 374-375, Feb. 2009.

[10] D. Imanishi, K. Okada, and A. Matsuzawa, "A 0.9-3.0 GHz fully integrated tunable CMOS power amplifier for multi-band transmitters," *IEEE Asian Solid-State Circuits Conference*, pp. 1-4, Nov. 16-18, 2009.

Xiangning Fan received the B.S. and M.S. degrees both from Nanjing University of Posts and Telecommunications in 1985 and 1988 respectively. From 1997, he becomes a part time Ph.D. in National Communications Research Laboratory (NCRL), Southeast University and received the Ph.D. degree in 2005 with Grade A. Since 1988, he works in Southeast University and now he is a Full Professor in Institute of RF-&-OE-ICs, School of Information Science and Engineering, Southeast University. Fan has finished more than 20 national projects on WSN, UWB, and 3G/4G Mobile Systems, and published more than 130 papers in IEEE T-CAS, IEEE COMM. Letters, Signal Processing, IET Radar, Sonar & Navigation, Electronic Letters, Sensor Letters, Springer AICASP, etc. with about 100 papers SCI/Ei indexed. His current research interests include RF ICs, receiver design and signal processing of wireless systems.

Zhou Yu received the B.S. degree in Information Science and Engineering and the M.S. degree in Integrated Circuit Engineering at Southeast University, in 2012 and 2015. His present research interests include frequency transmitter and RF circuit design.

Jiakai Lu received the B.S. degree in Micro-electronics and the M.S. in integrated circuit engineering at Southeast University, in 2012 and 2015. His present research interests include RF integrated circuit design and transmitter design.

Zaijun Hua was born in Jiangyan, Jiangsu Province, in 1983. He received the B.S. and M.S. degrees in Telecommunication Engineering from Beijing Jiaotong University, Beijing, China, in 2006 and 2008, respectively, and is currently working toward the Ph.D. degree at Southeast University. His research interests are RF transceivers.